

FAST solid-state synthesis on a minute scale

Dissertation

zur Erlangung des akademischen Grades eines
„Doktor der Naturwissenschaften“

am Fachbereich

Chemie, Pharmazie, Geographie und Geowissenschaften

Der Johannes Gutenberg – Universität Mainz

Im Promotionsfach Chemie

vorgelegt von:

Martin Alexander Lange

Geboren am 25.02.1990 in Mainz

Mainz, März 2021

Dekan:



1. Berichterstatter:



2. Berichterstatter:



Tag der mündlichen Prüfung: XX / XX / XXXX

Declaration:

The presented dissertation was prepared between November 2016 and March 2021 under the direction of [REDACTED] at the Department Chemistry of the Johannes Gutenberg University Mainz.

I hereby declare that I wrote the presented dissertation independently and without outside help. All used references and resources are completely indicated.

Erklärung:

Die vorliegende Arbeit wurde in der Zeit November 2016 bis März 2021 unter der Betreuung von [REDACTED] im Department Chemie der Johannes Gutenberg-Universität Mainz durchgeführt.

Hiermit erkläre ich, dass die vorliegende Arbeit selbstständig verfasst und keine anderen als die angegebenen Quellen und Hilfsmittel verwendet wurden. Alle Stellen, die wörtlich oder sinngemäß aus Quellen übernommen wurden sind als solche gekennzeichnet.

Mainz, März 2021

Martin Alexander Lange

Acknowledgements

[REDACTED]

Table of Content

Chapter 1 Introduction.....	1
Chapter 1.1 Field-Assisted Sintering techniques	2
Chapter 1.1.1 Mechanisms of field activated sintering	5
Chapter 1.1.2 Application of field activated sintering.....	11
Chapter 1.1.2.1 Deformation, densification and coarsening	12
Chapter 1.1.2.2 Synthesis and phase control.....	13
Chapter 1.1.3 Advanced field activated sintering methods	14
Chapter 1.1.3.1 Flash Sintering	14
Chapter 1.1.3.2 Flash Spark Plasma Sintering	15
Chapter 1.1.3.3 Pressureless Spark Plasma Sintering	15
References.....	17
Authorship contributions.....	25
Chapter 2 Solid State Fluorination on the Minute Scale: Synthesis of WO_{3-x}F_x with Photocatalytic Activity.....	27
Chapter 2.1 Motivation	28
Chapter 2.2 Results and Discussion.....	29
Chapter 2.2.1 SPS Synthesis and Chemical Analysis	29
Chapter 2.2.2 Phase Analysis	31
Chapter 2.2.3 Structure determination by ADT	34
Chapter 2.2.4 Local structure by ¹⁹ F MAS-NMR spectroscopy.....	37
Chapter 2.2.5 Electronic structure and composition of cubic WO _{3-x} F _x by XPS spectroscopy	42
Chapter 2.3 Photocatalytic properties	42
Chapter 2.4 Summary	44
Chapter 2.5 Experimental details	45
References.....	48

Authorship contributions	53
Chapter 3 A Generalized Method for High-Speed Fluorination of Metal Oxides by Spark Plasma Sintering Yields Ta₃O₇F and TaO₂F with High Photocatalytic Activity for Oxygen Evolution from Water	55
Chapter 3.1 Motivation.....	56
Chapter 3.2 SPS reaction and chemical analysis.....	58
Chapter 3.2.1 Phase composition.....	59
Chapter 3.2.2 Micro- and local structure of Ta ₃ O ₇ F and TaO ₂ F.....	62
Chapter 3.2.3 Band structure, charge carrier concentration and charge transfer	64
Chapter 3.3 Photoelectrochemical water splitting.....	67
Chapter 3.3.1 Photoconversion efficiency	69
Chapter 3.3.2 Water splitting	70
Chapter 3.4 Summary	71
Chapter 3.5 Experimental Methods.....	72
References	75
Authorship contributions	79
Chapter 4 Photocatalysts for water splitting from plastic scrap: Ultrafast spark plasma synthesis of NbO₂F and Nb₃O₇F by solid state .. fluorination of Nb₂O₅	81
Chapter 4.1 Motivation.....	82
Chapter 4.2 Results and Discussion	84
Chapter 4.2.1 SPS Reaction and Chemical Analysis	84
Chapter 4.2.2 Phase analysis	84
Chapter 4.2.3 Micro and local structure of NbO ₂ F and Nb ₃ O ₇ F.....	87
Chapter 4.3 Band Gap and Photoelectrochemical Water Splitting	90
Chapter 4.3.1 Photoelectrochemical water splitting mechanism	91
Chapter 4.3.2 Photoconversion Efficiency.....	92
Chapter 4.4 Summary	94
Chapter 4.5 Experimental methods	95
References	97

Authorship contributions.....	101
Chapter 5 Rapid Topochemical Nitridation of Ta₂O₅ with Vacancy-.....	
Assisted N³⁻/O²⁻ Exchange	103
Chapter 5.1 Motivation	104
Chapter 5.2 Synthesis	106
Chapter 5.3 Results and Discussion.....	107
Chapter 5.3.1 Diffraction Study.....	107
Chapter 5.3.2 Neutron diffraction analysis	110
Chapter 5.3.3 Electron microscopy.....	111
Chapter 5.3.4 UV/Vis diffuse reflectance spectroscopy	113
Chapter 5.3.5 XPS analysis.....	113
Chapter 5.4 Conclusion.....	115
Chapter 5.5 Experimental Methods	115
References.....	117
Chapter 6 Conclusions	123
Chapter 7 Supplementary Information	127
Authorship contributions	129
Chapter 7.1 Supplementary Information from Chapter 2	131
Authorship contributions	145
Chapter 7.2 Supplementary Information from Chapter 3	147
Authorship contributions	167
Chapter 7.3 Supplementary Information from Chapter 4	169
Authorship contributions	183
Chapter 7.4 Supplementary Information from Chapter 5	185
List of Figures	a
List of Tables.....	f
List of Symbols and Notations.....	h

Abstract

Solid-state reactions often proceed slowly, since atom diffusion through the involved crystalline phases involved is the rate-determining. For this reason, a successful reaction requires heat treatment over days or weeks, which is linked to enormous energy consumption. Metal oxides require particularly high temperatures, due to their high melting points. However, their high stability makes them very popular materials for a wide range of applications. Sustainability, energy efficiency and economic profitability are factors of increasing importance in industry. 7% of primary energy in Germany is used for high-temperature processes of metals and ceramics, making the search for new energy-efficient sintering processes all the more important. Field activated sintering (FAST) offers a simple, fast and cost-effective way to produce exceptionally structured materials (e.g. nanostructured, composites or gradient materials). This process represents a modified sintering process in which a sample is heated by means of an electric current via conductive pressing tools. The use of electricity allows very fast heating and cooling rates and thus very short process cycles. However, the exact mechanism of FAST is still far from being completely understood. The primary effect of electricity is assumed to be heat from electricity, but the influence of other and especially non-thermal effects cannot be ruled out. Although FAST has already enabled new possibilities in the sintering of materials, its direct application to solid-state syntheses is still not widespread.

The first objective of this dissertation was the modification of metal oxides and their transfer to a FAST process. Due to the similar ionic radii of fluorine, nitrogen and oxygen, fluorination and nitridation, respectively, are obvious model reactions. Common methods, such as the use of binary fluorides, hydrofluoric acid, or ammonia gas, carry the disadvantages of either being poorly controllable, the requirement of extreme and cumbersome reaction conditions, or being limited to small-scale approaches. Newer methods of fluorination, such as the use of perfluorinated polymers like Teflon, offer the possibility to use industrial waste products for simple syntheses. For this reason, fluorination with Teflon was first tested on tungsten oxide and subsequently on niobium and tantalum oxide. The optimum reaction conditions determined by screening various FAST program parameters showed that, with the aid of FAST, the reaction time can be reduced from 24 hours to 10 minutes and the same program parameters can be applied to all the oxides investigated. The resulting oxyfluoride phase is determined solely by the amount of Teflon used and the type of mixing of the reactants. A new phase of tungsten oxyfluorides could be discovered, dissolved and characterized. Comparison of material

properties revealed that FAST shrinks the optical band gap and introduces a large degree of disorder into the crystal structure. Materials synthesized via FAST exhibit lower long-range order than corresponding references. Similarly, it was observed that FAST treatment inhibits grain growth. It could be concluded that FAST, due to the very short reaction time and more extreme conditions, "freezes" the materials in a metastable state of large disorder because there is not enough time for sufficient thermal equilibration.

As another method, nitridation was investigated using the reaction of oxides with magnesium nitride. This new method, based on analogous fluorinations, requires sample preparation under clean room conditions and leads to oxynitrides and magnesium oxide as a by-product, which can be easily washed out of the product powder. Via conventional furnace synthesis, all known tantalum oxynitride and tantalum nitride phases can be synthesized. FAST allows nitrogen to be incorporated into the tantalum oxide structure while maintaining the structure or forming a superstructure. Only a further heating step leads to the formation of known oxynitride phases.

The photocatalytic activity of the samples in terms of dye decomposition and water splitting was investigated both in internal cooperation with the working group and in cooperation with King Fahd University in Saudi Arabia. Remarkably, powder samples prepared via FAST are significantly more active than comparable materials prepared via conventional furnace synthesis. This proves the potential within direct FAST synthesis of materials.

Zusammenfassung

Festkörperreaktionen verlaufen oft langsam, da die Atom-Diffusion durch die beteiligten kristallinen Phasen den geschwindigkeitsbestimmenden Schritt darstellt. Aus diesem Grund ist für eine erfolgreiche Reaktion eine Wärmebehandlung über Tage oder Wochen notwendig, was mit einem enormen Energieverbrauch verbunden ist. Metalloxide erfordern hierbei, bedingt durch ihre hohen Schmelzpunkte, besonders hohe Temperaturen. Sie sind jedoch aufgrund ihrer hohen allgemeinen Stabilität sehr beliebte Materialien für vielfältige Anwendungen. Nachhaltigkeit, Energieeffizienz und wirtschaftliche Rentabilität sind Faktoren von zunehmender Bedeutung in der Industrie. 7% der Primärenergie in Deutschland wird für Hochtemperaturprozesse von Metallen und Keramiken aufgewandt, umso wichtiger ist die Suche nach neuen energieeffizienten Sinterprozessen. Feldaktivierte Sintertechnik (FAST) bietet hier eine Möglichkeit auf einfachem, schnellem und kostengünstigem Weg außergewöhnlich strukturierte Materialien herzustellen (z.B. Nanostrukturiert, Komposite oder Gradienten-Werkstoffe). Dieser Prozess stellt einen modifizierten Sinterprozess dar, bei dem über leitfähiges Presswerkzeug eine Probe mithilfe von elektrischem Strom geheizt wird. Die Verwendung von Strom erlaubt sehr schnelle Heiz- und Kühlraten und somit sehr kurze Prozesszyklen. Allerdings ist der genaue Mechanismus von FAST noch weit davon entfernt, vollständig verstanden zu sein. Als primärer Effekt des Stroms wird Stromwärme angenommen, der Einfluss von weiteren und insbesondere nicht-thermischen Effekten kann hierbei jedoch nicht ausgeschlossen werden. Obwohl FAST bereits neue Möglichkeiten beim Sintern von Materialien ermöglicht hat, ist die direkte Anwendung auf Festkörpersynthesen noch wenig verbreitet.

Eine erste Zielsetzung dieser Dissertation war die Modifikation von Metalloxiden und deren Übertragung auf einen FAST-Prozess. Aufgrund der ähnlichen Ionenradien von Fluor, Stickstoff und Sauerstoff, sind die Fluorierung bzw. Nitridierung als Modellreaktionen naheliegend. Übliche Methoden, wie die Verwendung von binären Fluoriden, Flusssäure oder Ammoniakgas tragen die Nachteile mit sich entweder schlecht kontrollierbar zu sein, extreme und umständliche Reaktionsbedingungen zu benötigen oder sind auf kleine Ansätze beschränkt. Neuere Methoden zur Fluorierung, wie die Verwendung von perfluorierten Polymeren wie Teflon, bieten die Möglichkeit auch industrielle Abfallprodukte nutzbringend für einfachen Synthesen zu verwenden. Aus diesem Grund wurde die Fluorierung mit Teflon zunächst anhand

von Wolframoxid und darauffolgend an Niob- und Tantaloxid getestet. Die über ein Screening verschiedener FAST-Programmparametern ermittelten optimalen Reaktionsbedingungen zeigten, dass mithilfe von FAST die Reaktionszeit von 24 Stunden auf 10 Minuten reduziert werden kann und dieselben Programmparameter für alle untersuchten Oxide anwendbar sind. Die resultierende Oxyfluorid-Phase wird hierbei allein über die eingesetzte Menge Teflon, sowie die Durchmischung der Edukte, festgelegt. Dabei konnte eine neue Phase von Wolframoxyfluoriden in entdeckt, gelöst und charakterisiert werden. Vergleich von Materialeigenschaften ergab, dass die optische Bandlücke durch FAST schrumpft und eine großer Grad an Fehlordnung in die Kristallstruktur gebracht wird. Über FAST synthetisierte Materialien weisen eine geringere Fernordnung auf als entsprechende Referenzen. Ebenso konnte beobachtet werden, dass FAST-Behandlung das Körnerwachstum inhibiert. Daraus ließ sich schließen, dass FAST, bedingt durch die sehr kurze Reaktionszeit und extremeren Bedingungen, die Materialien in einem metastabilen Zustand großer Unordnung „einfriert“, da nicht genug Zeit für ausreichende thermische Equilibrierung vorhanden ist.

Als weitere Methode wurde die Nitridierung anhand der Reaktion von Oxiden mit Magnesiumnitrid untersucht. Diese neue, an analoge Fluorierungen angelehnte, Methode erfordert eine Probenpräparation unter Reinraumbedingungen und führt zu Oxynitriden und Magnesiumoxid als Nebenprodukt, welches leicht aus dem Produktpulver gewaschen werden kann. Über konventionelle Ofensynthese sind so alle bekannten Tantaloxynitrid und -nitrid Phasen herstellbar. FAST ermöglicht hierbei einen Einbau des Stickstoffs in die Tantaloxidstruktur unter Strukturerehalt bzw. Ausbildung einer Überstruktur. Erst ein weiterer Heizschritt im Anschluss führt zur Ausbildung bekannter Oxynitrid Phasen.

Sowohl in Arbeitskreis interner Kooperation und in Kooperation mit der King Fahd University in Saudi-Arabien konnte die photokatalytische Aktivität der Proben in Bezug auf Farbstoffzersetzung und Wasserspaltung untersucht. Bemerkenswerterweise sind über FAST dargestellte Pulverproben deutlich aktiver als vergleichbare, über herkömmliche Ofensynthese hergestellte Materialien. Dies beweist das Potenzial der direkten FAST-Synthese von Materialien.

Chapter 1 | Introduction

Chapter 1.1 Field-Assisted Sintering techniques

The sintering of materials is a well-known and important technique for mankind which, throughout history, proved to be very crucial for the advancement of many civilizations all over the world. It is assumed that sintering was already known to mankind several thousands of years before humans became sedentary more than 12 000 years ago, even earlier than the currently oldest known “artificially” made material: the Venus of Vestonice.^[1] An application of sintering is well known for old civilizations, like the Mesopotamian civilization 6000 BC where clay bodies were burnt in open fireplaces to obtain valuable tools. More examples can be found in ancient Egypt, 3000 BC, where sintering of ceramics and metal was commonplace, and even in South Africa, where sintering was carried out for gold and jewelry in Inca civilizations. Here, significant advancements of low temperature sintering can already be observed, like the first use of glazes.^[2] Over time, the mostly empirical developed techniques for sintering allowed mass-production of stable and high-quality ceramics, as done in Egypt and Greece, in form of porcelain in China, and later in the near east and in Europe. The name “ceramic” itself shows the strong link of this technique to open fires, originating from the ancient Greek word “κεραμος”, which means “burnt”. First scientific approaches to improve and investigate the mechanisms of sintering techniques started in the early 20th century and lead to a first wave of reports looking into the basic phenomena and mechanisms of mass transport. In the following, and due to the huge industrial importance of sintering, many methods were devised to improve the sintering process, offering some well-established advantages. Firstly, in comparison to casting, lower temperatures can be used, making sintering suitable for materials which would decompose before melting. Secondly, sintering can be applied to a broad range of materials, which otherwise cannot be easily shaped due to their hardness. Thirdly, sintering opens up the production of nanostructured materials, and lastly, it allows the rapid production of net shape components, reducing waste and processing times compared to alternative manufacturing routes.^[3] Even if sintering enjoyed a widespread application, the technique itself remained largely untouched by innovation for nearly 25 000 years till H.W. Volaston reported the first experiments applying pressure to the sintering process, which in turn stimulated many ideas on how to improve sintering further^[4]. One of these ideas was the application of electric currents in various ways to sintering, being patented as early as 1906^[5,6], 1933^[7] and 1937^[8], but technical limitations hindered the widespread use, even if first experiments date back to 1922.^[9] The technological advancement only allowed first scientific and industrial tests of current-

assisted sintering methods around 1970. Since then, different ways to enhance sintering by the application of an electric current have been developed, establishing the field of electronic current activated sintering techniques. A sketch of the history of sintering is shown in Figure 1.1, adapted from Biesuz et al.^[10] Reports on the historic evolution of sintering can be found in detail by various authors.^[3,11-13]

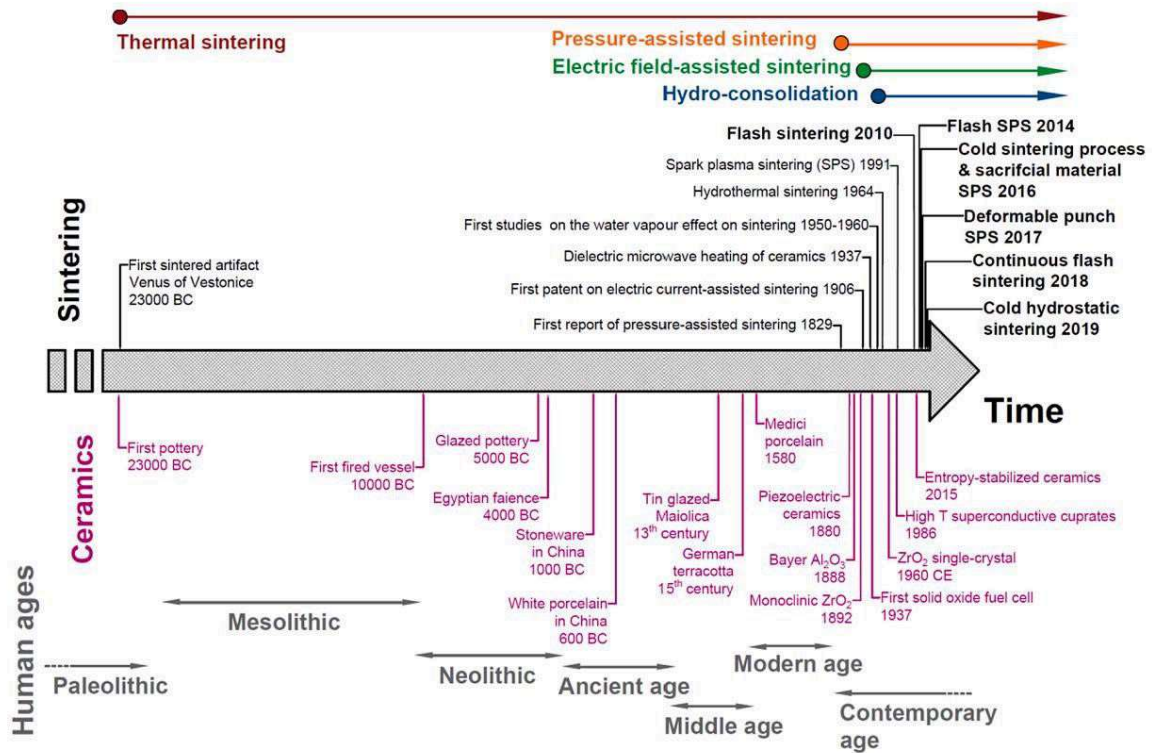


Figure 1.1. History of sintering through human history in comparison with ceramic development. The development of non-conventional sintering techniques almost exclusively happened in the last 120 years. Adapted from Biesuz et al.^[10]

Due to very subtle differences in the type and use of current, the exact distinction between single methods proves difficult and complicates the exact reproduction of results. Orrù et al.^[14], Anselmi-Tamburini et al.^[15] and Grasso et al.^[16] give simplified overviews and categorizations of primary differences. The main differentiations being either the use of very high currents and voltages over very short time periods (< 1 s), called “electric discharge sintering”, or the use of low voltages (~ 10 V) and only a couple of kA currents, called “resistive sintering”. One very common method in the field of “resistive sintering” is the so-called “field activated sintering technique” (FAST), also known as “spark-plasma sintering” (SPS). The term spark-plasma sintering originates from the hypothesis that during the sintering process, electric discharge between particles of the sintered powders leads to the brief presence of a “discharge plasma”,

but since this phenomenon could never be observed, it is widely agreed on as being disproven.^[17-19] Still, the term SPS remains firmly linked to the process, proven by the large number of uses for publications as shown in Figure 1.2A, adapted from Yamanoglu.^[20] During FAST, in addition to the application of pressure to the sintered material, also called green body, an electric current is applied to the sample through conducting pressing tools, which are connected to water-cooled, metallic electrodes (Figure 1.2B).^[21, 22] This method makes use of the heat dissipated due to energy loss caused by the electric resistance of the tools and green body, making Joule heat the primary mean to reach the sintering temperatures. Usually low voltage, in the range of a couple of Volts, is used, while the applied pulsed or direct current is in the kilo-Ampère range. This allows heating materials with heating rates up to a thousand degree Kelvin per minute and cooling rates up to a couple hundred degree Kelvin per minute. In addition, the heating process takes place in a much more uniform way compared to standard sintering processes, where the heating elements are located around the sinter-body. Heating via FAST is achieved in direct proximity of the sinter body in case of non-conductive samples and even, in parts, directly in the sample in case of conductive sample material.

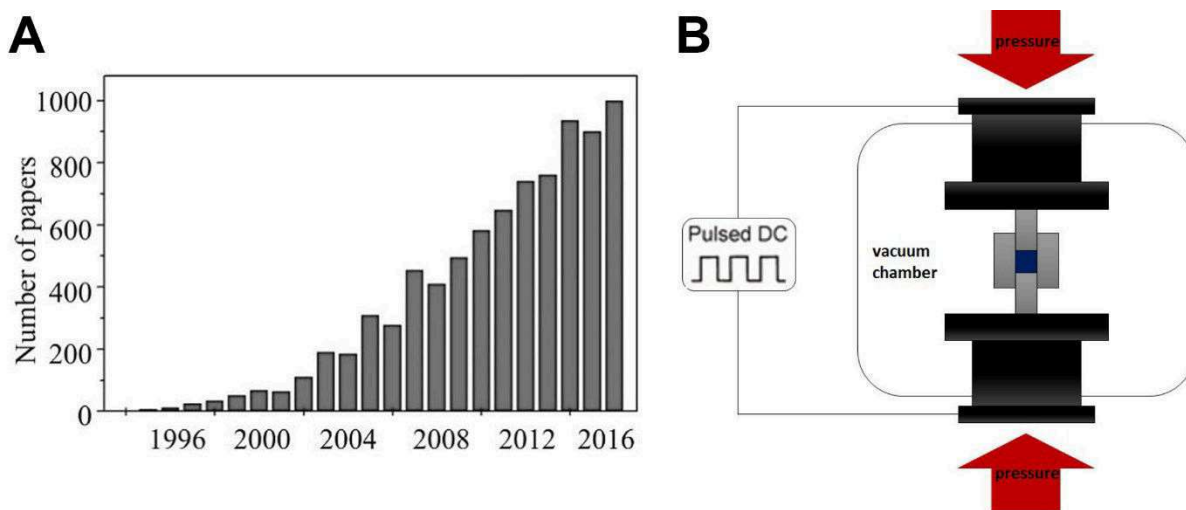


Figure 1.2. (A) Histogram of published papers using the term “spark-plasma sintering”, adapted from Yamanoglu and SCOPUS.^[20] (B) Scheme of a FAST process, the vacuum chamber can be filled with inert gas.

At the same time, the need of conductive pressing tools and the necessity of contacting the green body to the power circuit limits the amount of pressure that can be applied and in addition the achievable maximum temperature. Special qualities of graphite allow the application of pressures up to 230 MPa, though usual values range in the Area of 50-100 MPa, while temperatures up to 2400°C are possible. In general, non-conductive parts can be used, but electrical contacting has to be guaranteed somehow through the pressing tools, either by

conductive dies or conducting pistons and sample material. In addition, conductive foil has to be used to isolate the green body from the pressing tool, to avoid side reaction and, if graphite is used as material for the pressing tools, the sintering process has to be carried out under vacuum or inert gas atmosphere.

Chapter 1.1.1 Mechanisms of field activated sintering

During FAST processes, a large variety of parameters can be adjusted, and each plays a distinct role in the sintering process. This flexibility allows a wide range of applications and possibility for adjustments to even more complex processes, like reaction steps directly followed by sintering steps. Furthermore, it leads to a much more complex system and makes the investigation of the influence of single parameters very difficult. Detailed descriptions and evaluation of the exact influence of single parameters can be found in reviews by Garay^[23], Munir et al.^[24], Raj et al.^[25], Rivoirard^[26], Psyk et al.^[27], Batygin et al.^[28], Castro et al.^[28], Guillon et al.^[30], and Biesuz et al.^[10,31] and are presented in parts in the following paragraphs, focusing on mechanical, thermal and electrical effects, before describing a rough model of the involved densification mechanism.

Chapter 1.1.1.1 Mechanical Effects

The application of pressure is one of the most dominating factors for densification processes. It acts as an additional driving force by introducing additional pathways like particle sliding, improving the densification significantly. The influence of applied external pressure was widely underestimated, and extensive investigations have been carried out nearly exclusively on high-pressure systems.^[32] In general, it can be stated that the obtained maximum density rises with increasing applied pressure. Additionally, the sintering temperature needed to obtain sufficiently dense material can be significantly reduced, and grain-growth is limited under external pressure. Figure 1.3 shows the results of such studies, adapted from Anselmi-Tamburini et al.^[33,34], and Munir et al.^[35], which give more detailed investigation results.

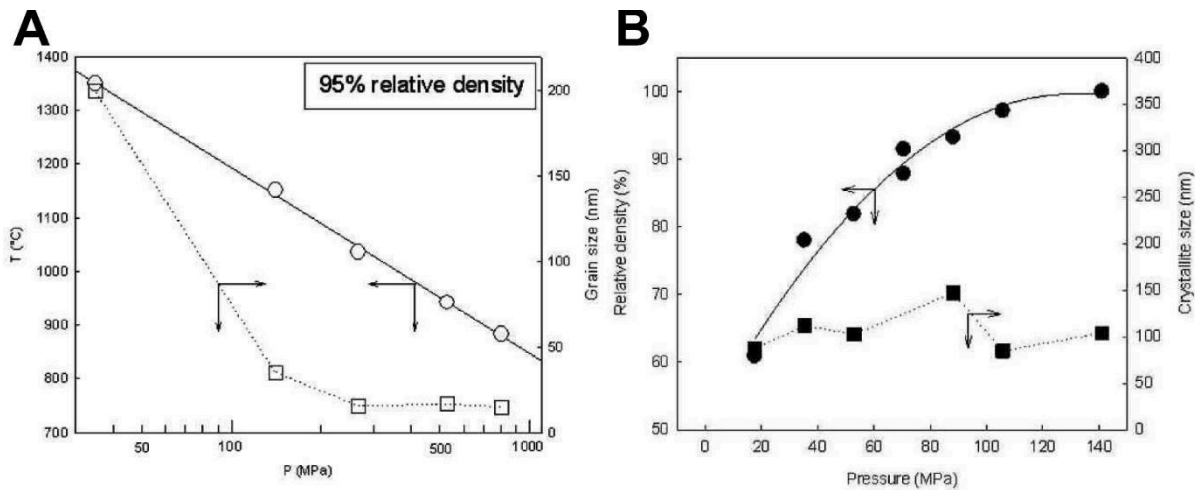


Figure 1.3. Comparison of the influence of pressure assisted (squares) and pressure less (circles) sintering, shown by temperature T needed to obtain a relative density of 95% (A) of ZrO_2 and the influence on relative density in relation to observed particle grain-growth (B). Adapted from Anselmi-Tamburini et al.^[33] and Munir et al.^[35]

A rather unusual approach to use plastic deformation creatively is the so-called deformable-punch SPS, developed by Mueche.^[36] Mueche et al. showed, that slight deformation of the pressing tools during FAST processing induces a transversal deformation in the sample, inhibiting grain-growth very efficiently.

Chapter 1.1.1.2 Thermal Effects

Thermal effects are the second main factor in sintering processes, where huge influences can be identified, e.g., activating diffusion, viscous flow and the formation of intrinsic defects in sintered samples. For FAST, the main thermal factor is the so-called Joule heating. Joule heating due to current flow can be easily singled out as the main cause for sample heating during FAST. Besides Joule heating, inductive heating and dielectric heating can be assumed as additional heating factors, while other effects, like plasma heating, can be excluded. Detailed descriptions of the single factors and the underlying physics can be found in Grasso et al.^[31] Since the main-heating source is caused by an electric current, a certain resistivity of the sample and/or pressing tool material is necessary to obtain high heating rates. Studies show that a large part of heat dissipation takes place in the graphite die and punches.^[37] Generally, this leads to a very direct and uniform sample heating, especially compared to conventional sintering methods, and enables very high heating rates without large temperature gradients through the sample. Especially for conductive samples, uniform and fast heating can be achieved. Nonetheless, remarkably uniform heating can be achieved for non-conductive samples as well, shown in Figure 1.4 adapted by Anselmi-Tamburini et al.^[33,34] The main reason is assumed to be, that the major part of the dissipated Joule heat is generated in the graphite punches and dies

anyway. Kieback et al showed that only 10% of electric heating occur within the sample volume of conductive samples.^[37] Further studies showed, that the temperature distribution can be even further improved with optimized experimental conditions, e.g., geometry of die and punches.^[38] This leads to the conclusion, that the actual specimen temperature might be underestimated in most cases. Additionally, high heating rates inhibit the grain-growth of particles in the sintered green body. While the temperature does not show large gradients over the sample, small points of contact and “necks” for current flow can lead to local overheating due to areas of high resistivity. This leads to the formation of observable “necks” between powder particles and melted areas on the particles.^[39,40]

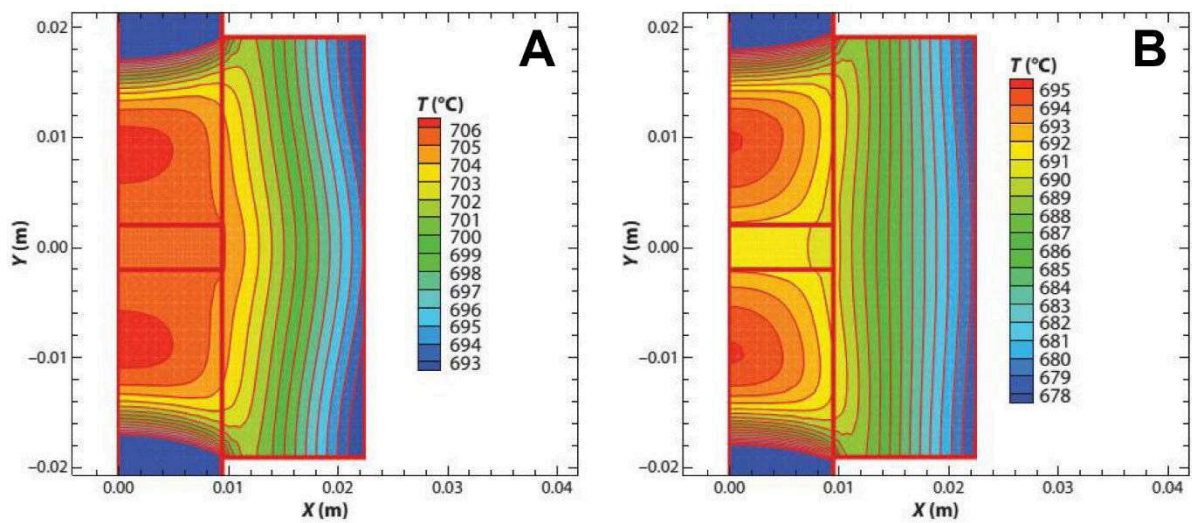


Figure 1.4. Example of heat-distribution in (A) a non-conducting sample of Al_2O_3 and (B) a Cu sample, applying 100 A and 40 kN as adapted from Garay^[23]

The exact determination of single thermal effects proved to be difficult, especially considering that most observable effects are co-dependent on multiple factors and most of the time variations in one parameter leads to multiple changes. Even though simulations of single influences, e.g. temperature gradients and temperature distributions, have been carried out and models for temperature evolution during FAST have been proposed, more research needs to be done on this field, especially since exact experimental measurements of single factors pose a high degree of difficulty.^[41-44]

Chapter 1.1.1.3 Electrical Effects

Since Joule heating is the main cause of heating within FAST, distinguishing between thermal effects and effects caused explicitly by the applied current is complicated. It is well known that Joule heating thermally activates diffusion and vitrification, but singling out pure electric

contributions poses a challenge. Since the formation of necks can be observed during many FAST applications, the presence of a spark plasma discharge was under discussion. The occurrence of spark plasma could never be observed and even if it seems like a plausible mechanism, nowadays is disproven in big parts by current studies. [17-19]

Another controversial factor is the role of pulsed current vs. direct current. Early patents largely emphasized the pulsing of current, but more recent investigations show that it has only a small influence on the FAST process and densification. As shown by Cen et al. [45] and Kieback et al. [37] pulsed current shows no effect on Mo-Si, Copper and steel systems, while Munir and Friedman et al. [24,46] showed that the current direction has no influence on interfacial reactions in Ag-Zn multilayers. In addition, measurements of Anselmi-Tamburini et al. [34] showed that the pulse train of some commercially available SPS systems is in fact not a square wave, and most pulses do not reach zero current. This means that most of the applied power is delivered as a direct current, no matter the programmed pulsing and basically makes detailed investigations impossible. Newly developed methods on the other hand, like Flash Spark Plasma Sintering – described in more detail in a later chapter – make use of pulsed current in a way to avoid large electric fields, while applying large chunks of thermal energy to the system. This allows the conclusion that most electric effects in FAST are tightly linked to the heating process and are therefore very hard to distinguish from thermal effects. Some of the discussed effects in this context are linked to the described neck-formation during FAST. The intensification of the local electric field at neck regions combined with the rapid release of surface enthalpies and additional space charge resistance might promote the overheating in these areas but are still under discussion. One idea, constantly being in the center of discussion about FAST, is the perturbation of defect chemistry in electric fields by inducing additional mechanisms like electromigration, electroplasticity and electrochemical reductions. It can be confirmed that FAST processed materials show enhanced defect chemistry, but the exact effects are still under discussion. [25,47,48]

Chapter 1.1.1.4 Densification Mechanism

Generally speaking, densification describes a process leading to the minimization of porosity within a powder compact. The porosity can be divided into two classes: interparticle porosity and intraparticle porosity. Intraparticle porosity describes the porosity within single particles, consisting of many not perfectly dense agglomerated crystallites, while interparticle porosity describes the porosity between these agglomerates. Densification mechanism can be split into three broad classes: sintering, particle and crystallite rearrangement and plastic deformation.

Sintering refers to the process of surface area reduction, firmly linked with a reduction of surface energy. The rearrangement of particles and crystallites within the powder compact is linked to, and reduces, the sample porosity. Most of the time it is driven by thermal and mechanical effects, like thermally enhanced particle diffusion and applied external pressure. Similarly, plastic deformation describes the material transport and deformation of the particles themselves once no other pathways are available and can be driven by pressure, thermal effects or current, shown in a simplified way in Figure 1.6 A.^[23] It can be divided into vaporization and solidification of material, diffusion along particle surfaces and diffusion between grain-boundaries or volume diffusion between particles in direct contact with each other. An exemplary distinction is shown in Figure 1.6 B.^[49]

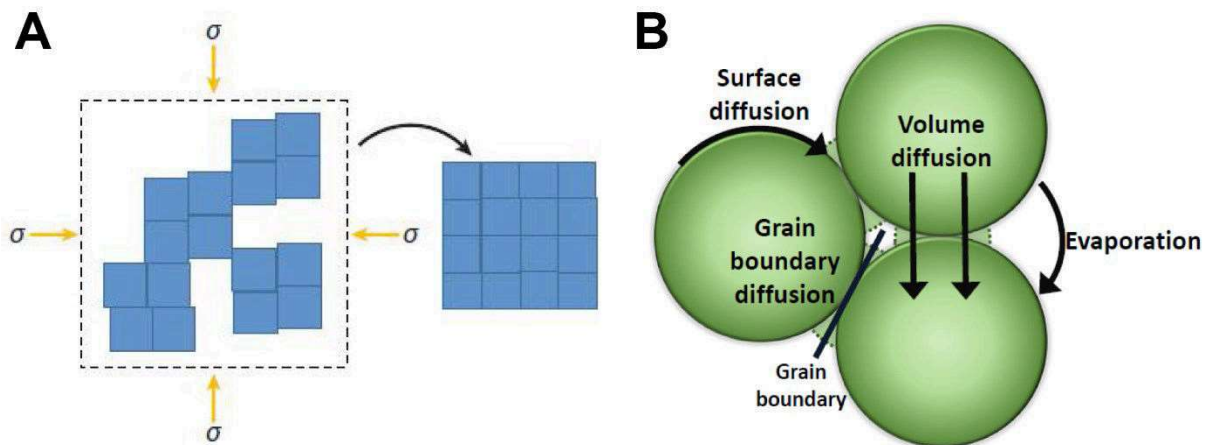


Figure 1.5. (A) Schematic of particle rearrangement, adapted from Garay.^[23] (B) Examples for material transport pathways between particles.

While diffusion on the surface in form of evaporation and solidification between particles mainly leads to particle coarsening, volume diffusion and grain boundary diffusion mainly lead to densification of the powder compact. Once the applied pressure exceeds the compressive yield of the sintered material, plastic deformation takes place, and the material is instantaneous and irreversibly densified. Many experiments and simulations were carried out in order to analyze single influences. And even if promising results were achieved, like the successful application of the master sintering curve to FAST, strong interactions between the single factors, especially with the addition of an electric current, make final conclusions very difficult.^[50-53]

In FAST, the effects and mechanisms described above take place just like in regular sintering processes, mainly due to high temperatures and applied pressure. Additional effects, caused specifically by the applied current, are percolation effects of current in porous powders, the

Peltier effect between sample and punches, electrochemical interface reactions and electromigration. More detailed descriptions can be found in book chapters and publications by Munir et al.^[54], Anselmi-Tamburini et al.^[55], Kieback et al.^[56], and Grasso et al.^[57]

Percolation means that the current flows always along the path of lowest resistance. Since powder compacts are usually far from being homogeneous and uniformly dense, current flow pathways in FAST follow a complex network along particle surfaces, as shown in Figure 1.7. A direct consequence is the overheating and local melting at points of high resistance within the material, mainly due to small contact areas. Within these hot-spots, the local temperature can exceed the average temperature of the powder compact by far and leads to significantly different microstructural mechanisms. Densification happens much faster along the current pathways compared to the surrounding areas and usually increases the conductivity within these networks, basically forming a kind of fingerprint of the fast process.

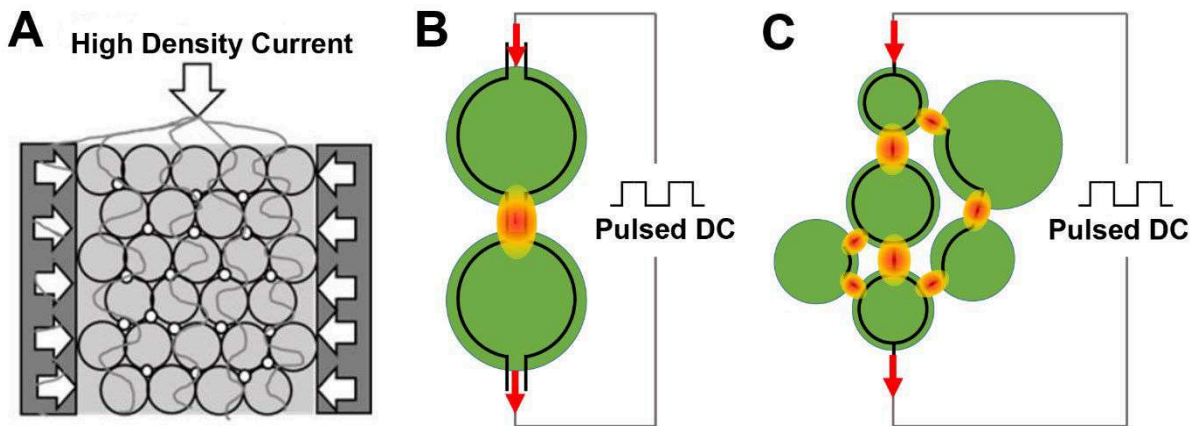


Figure 1.6. (A) Current flow through powder sample during FAST, adapted from Wachowicz.^[58] (B+C) Current pathways along lowest resistance between powder particles, leading to neck formation.^[59]

The Peltier effect is described by an electric current flowing through a material interface, causing a heat flow which is proportional to the current and the different of the so-called Peltier coefficients of both materials. The Peltier coefficient characterizes the amount of heat electrons carry within specific materials, and gains increasing importance with decreasing conductivity. Conductive materials show values near zero while it can reach up to 10% of the overall heating power in semiconductors. Contrary to Joule heating, the Peltier effect depends on the current direction and on the exact type of charge carriers, e.g., electrons as charge carriers lead to anode-heating whereas holes lead to anode cooling.^[44]

Lastly, electromigration describes preferential diffusion direction due to electron scattering on lattice atoms and is directly caused by a flowing current. This effect is very difficult to observe,

since it cannot be easily distinguished from similar effects and mainly enhances the mass transport within the powder compact. In FAST, even though high electric currents are applied, the achieved current densities are relatively low due to the die and plunge diameters. The direct dependence of electromigration on the current density makes it even harder to observe and quantify it for FAST. Nevertheless, its influence and presence are beyond dispute.

In addition, mechanisms like breakage of oxide layers on metals, also called surface oxide debonding, and mechanisms like surface cleaning of particles and surface debonding caused by micro-discharges could be observed in FAST processes by Groza et al.^[60] and Anderson et al.^[61], and even if first modeling approaches have been carried out by Wu et al.^[62] and Mainière et al.^[63], they are still subject to investigations.

Chapter 1.1.2 Application of field activated sintering

Applications of field activated sintering are mostly limited to the laboratory scale, due to technical restrictions in pressing tool size and shapes of obtained materials, almost exclusively producing thin discs of relatively small diameters. Theoretically, heating rates of up to thousand degree per minute can be achieved by FAST, but large heating rates pose a great challenge for the upscaling of processes. The same heating rates on larger scales are impossible to attain using the same current conditions, and changes in the current normally go hand in hand with changes in the reaction conditions and thus, obtained properties. In Addition, most reported FAST applications utilize some sort of milling as mean to prepare precursor materials. Upscaling of these milling processes poses significant challenges in terms of time, quantity and contaminations. All this complicates the transfer of FAST processes to a larger than laboratory scale and limits currently industrial application. The main focus and interest of FAST research lies in deformation, densification and coarsening of materials while synthetic applications are scarce and not widespread. Therefore, FAST research can be divided roughly in these three topics: deformation, densification and coarsening, and synthesis as show in Figure 1.8, adapted from Guillon et al.^[64]. In the following chapters, some selected examples for deformation and densification/coarsening will be presented together, while selected examples for synthesis application will be presented separately. More general overviews are presented by Guillon et al.^[64], in addition to book chapters by Olevsky et al.^[65] and Cavaliere.^[66]

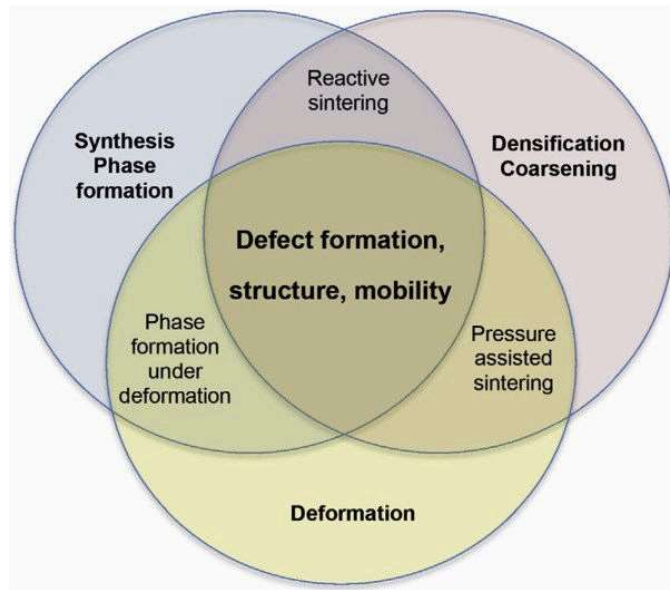


Figure 1.7. Schematic representation of fields of interest relevant for research of FAST synthesis and processing. Adapted from Guillon et al.^[64]

Chapter 1.1.2.1 Deformation, densification and coarsening

The main application of FAST lies in the field of densification and coarsening of material, while deformation of material is of high interest in related, current-supported applications like Flash Sintering. Since FAST allows preservation of the nanostructure of materials over the sintering process, its use for applications where specific nanostructures enhances the suitability of solid bodies highly interesting, like the field of thermoelectrics.^[14,30,35,67,68] In addition, FAST is of high interest for very specific applications, like fuel cell densification and preparation of ceramic reactor materials for nuclear chemistry, as described by Cologna^[69] and Kundu et al.^[70] Another example is the reliable production of so-called MAX-phases,^[71] a huge class of materials with over 150 compositions and interesting properties for many applications due to their layered structure and being a “bridge” between ceramics and metallic. Hereby, FAST plays a very important role in obtaining the right densities and material structures. The sintering of metallic alloys is another obvious field for interesting applications.

From steel to nickel, titanium or aluminum alloys, FAST gives access to very interesting nanostructured materials, which are inaccessible otherwise.^[72] Khan et al. showed that sintering of high-energy ball milled Mg-10 weight percent Al alloy retains its nanostructure and makes higher densities achievable, while corrosion behavior and hardness improved significantly.^[73] Nguyen et al. found similar results for the FAST treatment of ball milled cobalt powders.^[74] Yoshida et al. found for the TaO_{2.5}-doped SnO₂, that the direct current conductivity decreases

with higher densities, achieved at higher temperature and increase with faster heating rates and shorter holding times.^[75] Mo et al combined sol-gel process to obtain educt material for FAST to fabricate carbon nanotube reinforced aluminum with high hardness and fracture toughness,^[76] while Kang et al. developed a FAST process to obtain ultrafine lamellar structures in Ti-6Al-4V alloys.^[77] Ratzker et al. were able to synthesize fully dense and transparent Er₂O₃ ceramics with oxygen vacancies at relatively low temperatures.^[78] This shows that, while exact effect influences are not completely investigated, FAST allows access to a broad range of materials with improved mechanical and especially physical properties compared to conventional sintering techniques and are of high interest for mechanistic investigations. An overview of FAST and metallic systems can be found from Weston et al.^[79], while Khosghadam-Pireyousefan et al.^[80] give a good overview over Ceramic application and Wachowicz^[58] gives a more tool-oriented look.

Chapter 1.1.2.2 Synthesis and phase control

The application of FAST for direct material synthesis poses new challenges and difficulties compared to simple densification. Besides the stability of the single compounds towards overheating, the FAST atmosphere and pressing tool material, throughout mixing and phase stability of used materials in electric fields need to be considered.^[64] Besides obtaining material with more optimized structures, the field of thermoelectrics is one of the few examples where FAST was used in a way to combine synthesis and sintering to obtain directly usable bulk material. Ceretti et al. used this method for the so-called Magnéli-phases WO_{3-x} and Nb_{8-x}W_{9+x}O₄₇ and was able to identify an increase in defects of the called shear-planes, a typical defect motive for Magnéli-phases.^[81,82] Similarly Joos et al were able to synthesize magnéli-phase V₆O₁₁ while Portenhault et al focused on titanium oxides.^[83,84] Recknagel et al on the other hand were able to synthesize highly dense, homogenous, nanocrystalline skutterudites from ball-milled metal powders.^[85] In-depth studies, like the synthesis-development of of dense yttrium aluminum boride for thermoelectric application by Son et al, show the complexity of FAST synthesis.^[86] At the same time it show the huge potential of this method.

Other examples for FAST as mean for direct synthesis is the direct synthesis of inorganic solid-state batteries by Ihrig et al.^[87] Here, the direct synthesis and densification of composite anodes for lithium batteries was possible at much lower temperatures than with comparable methods. By this method, decomposition and the formation of secondary phases could be completely avoided, again showing the potential of FAST.

The scarce use of FAST as mean for direct synthesis was one of the main motivations for this theses and further examples of FAST synthesis are shown in detail in Chapter 2-5.

Chapter 1.1.3 Advanced field activated sintering methods

The spark in scientific interest in FAST as a mean to obtain unusual material with special properties, lead to various modifications of the FAST process, ranging from relatively simple approaches exchanging parts of the sintering tools by different, nonconductive material like boron nitride or more fundamentally different approaches. The related method of Flash Sintering and two prominent modifications are presented in the following chapters. An overview about FAST variations and closely related methods can be found in Biesuz et al.^[10]

Chapter 1.1.3.1 Flash Sintering

Originally discovered by Cologna, Raj et al. at the University of Colorado^[88], Flash Sintering poses an attractive alternative to FAST. Contrary to FAST, heating is applied externally while a high electric field is applied to a ceramic green body. Once a material dependent temperature is reached, the sample becomes sufficiently conductive to enable current flow. This sudden onset of current is usually accompanied by luminescence and rapid densification within seconds. With these observations, three process stages can be identified for Flash Sintering. First, the non-conductive sample heats up without Joule heating. Secondly, flash transition takes place, where the sample-conductivity increases abruptly and densification takes place once the so-called flash temperature is reached, an onset power triggering a thermal runaway of the Joule effect (the higher the material conductivity the lower the flash temperature). Finally, when the system reaches equilibrium and all parameters stabilize, heat dissipation by radiation from the sinter body counterbalances the electric power dissipation. And even if first applications by Yu et al.^[89] were successful, recent insight in flash sintering showed that additionally athermal effects play a non-neglectable role, strongly dependent on the used material. All this shows some of the main limitations of Flash Sintering. Usually, pre-heating is necessary and the current flows usually along preferential pathways, leading to inhomogeneities within the sample. Nevertheless, the near-complete dissipation of the heating power by the sample makes Flash Sintering a very energy-efficient process and fueled the development of large-scale applications from the UK company Lucideon. Just like for FAST, the exact involved mechanisms are still under debate and topic of many scientific investigations. More detailed descriptions of the mechanistic state of the art can be found by Biesuz et al.^[10,57], Yu et al.^[89] and Bram et al.^[90]

Chapter 1.1.3.2 Flash Spark Plasma Sintering

A combination of FAST and FS was first presented by Grasso et al.^[91,92] and requires very specific tool design or pressing tools from different materials, like boron nitride as used by Goronski et al.^[93] The sample has to be preheated before the onset of current flow to enable the flash effect. Rapid heating can be achieved by very short pulses of direct current, which delivers extremely high heating power in brief time periods. At the same time, the maximum power of the FAST device has to be limited to avoid sample melting. To improve the densification, well-defined mechanical loads can be applied. Holding the power at maximum for several seconds starts the rapid densification with occurring temperature gradients up to several hundred degree Kelvin. Flash spark plasma sintering (FSPS) is limited to materials which show a “flash temperature” but opens the path to apply various ultra-rapid densification processes to FAST, like “electrodischarge sintering” and “electroresistance sintering”. Examples and a more in-depth description of this process can be found in Grasso et al.^[92] and Bram et al.^[90]

Chapter 1.1.3.3 Pressureless Spark Plasma Sintering

A relatively novel method for SPS application is the so called “pressureless spark plasma sintering” (PSPS). Pressureless sintering is a well-known sintering process but application to FAST poses the additional challenge of necessary electric contacting to achieve a current flow and thereby heating. Bradbury and Olevsky solved this problem by using a T-shaped punch instead of cylindrical ones.^[94] This enables a fixed sample volume between the punches with zero external pressure during sintering as shown by Giuntini et al.^[95] The conduction and resistance of the pressing tools is vital for this process which limits its application on tool material such as graphite. Alternatively, additional graphite pieces can be put in between the punches as spacer to avoid external pressure on the sample, as used by Bertolla et al.^[96] Examples of modified pressing tools are shown in Figure 1.9 as adapted from Yamanoglu.^[20]

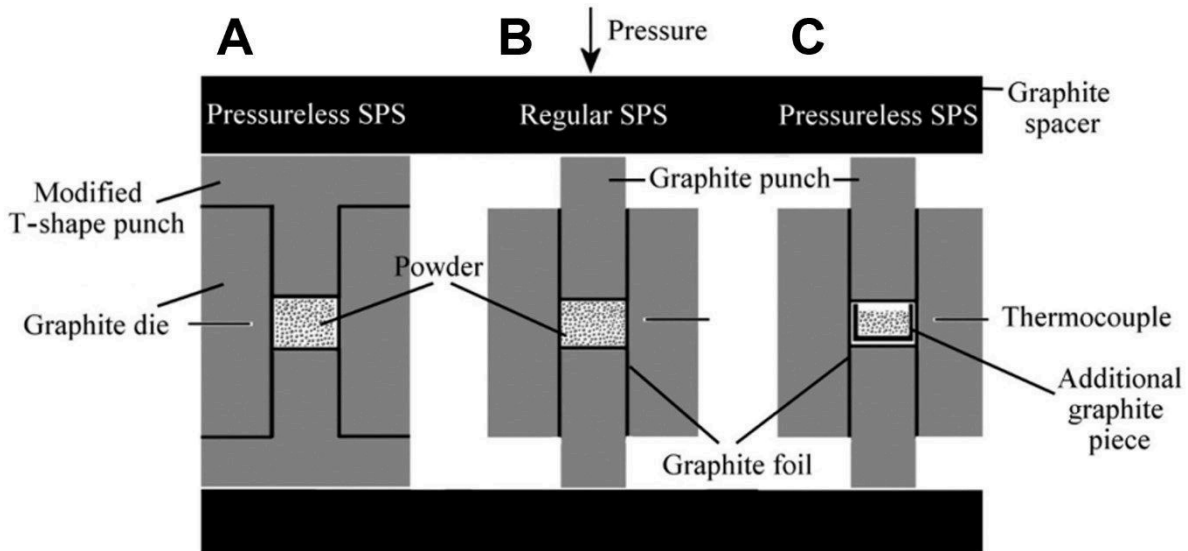


Figure 1.8. Alternative die designs for pressureless SPS using (A) T-shaped graphite punches or (C) additional graphite pieces to avoid external pressure in comparison to (B) regular SPS pressing tools. Adapted from Yamanoglu^[20]

This variation of FAST is mostly used in processes where the main interest lies in maintaining the structure of the sintered material, especially if porous alloys and materials are sintered. Indeed, by using this modified FAST, the gross particle morphology can be retained and only small areas where the material melted and formed necks between particles during FAST can be observed. For example, loosely packed aluminum powders could be sintered, retaining spherical morphology of the single particles,^[97] and only small melted areas at the place where the particles came into contact with each other could be observed in the processing of $Ti_5Al_{2.5}Fe$ alloy.^[98] Other examples where PPS was applied are SiC-C composites or hydroxyapatite microchannel structures, in both cases leading to special morphologies otherwise inaccessible.^[94] This makes pressureless SPS interesting in case the grain growth needs to be prevented further, the production of structures with controlled porosity, and further densification of already shaped powder compacts. Detailed examples can be found in a review by Yamanoglu.^[20]

References

- [1] C. B. Carter, M. G. Norton, *Ceramic Material Science and Engineering*, Springer, 2007
- [2] J.-C. Boch, P. Niepce, *Ceramic Materials*, ISTE, Newport Beach, USA, 2007
- [3] R. M. German, History of Sintering: empirical phase, *Powder Metall.*, 2013, 56, 117-123
- [4] H. W. Wollaston, On a method of rendering platina malleable, *J. Franklin Inst.*, 1829, 8, 226-233
- [5] J. Lux, Improved manufacture of electric incandescence lamp filaments from tungsten or molybdenum or an alloy thereof, GB190527002A, 1906
- [6] J. Lux, Improved manufacture of filaments of tungsten or molybdenum for electric incandescence lamps, GB190527002B, 1906
- [7] G. F. Taylor, Apparatus for making hard metal compositions, US1896854, 1933
- [8] J. G. Chaffee, Method and apparatus for heating dielectric materials, US2147689A, 1937
- [9] G. Weintraub, H. Rush, Improvements in and relating to the Treatment of Refractory Materials and Apparatus therefor, GB191220348A, 1912
- [10] M. Biesuz, S. Grasso, V. M. Sglavo, What's new in ceramic sintering? A short report on the latest trends and future prospects, *Curr. Opin. Solid. St. M.*, 2020, 24(5), 100868
- [11] W. D. Jones, *Fundamental Principles of Powder Metallurgy*, Edward Arnold, London, 1960
- [12] C. G. Goetzel, *Treatise on Powder Metallurgy: Technology of Metal Powders and Their Products*, Interscience Publisher, 1946, 1
- [13] P. C. Angelo, and R. Subramanian, *Powder Metallurgy: Science, Technology and Applications*, PHI Learning Pvt., 2008
- [14] R. Orru, R. Licheri, A. M. Locci, A. Cincotti, G. Cao, Consolidation/synthesis of materials by electric current activated/assisted sintering, *Mater. Sci. Eng. R Rep.*, 2009, 63(4-6), 127-287
- [15] U. Anselmi-Tamburini, J. R. Groza, Critical assessment: electric field/current application - a revolution in materials processing/sintering?, *Mater. Sci. Technol.*, 2017, 33, 1855-1862
- [16] S. Grasso, Y. Sakka, G. Maizza, Electric current activated/assisted sintering (ECAS): a review of patents 1906-2008, *Sci. Technol. Adv. Mater.*, 2009, 10, 053001

- [17] D. M. Hulbert, A. Anders, D. V. Dudina, J. Andersson, D. Jiang, C. Unuvar, U. Anselmi-Tamburini, A. K. Mukherjee, *J. Appl. Phys.*, 2008, *104*, 033305/1
- [18] D. M. Hulbert, A. Anders, J. Andersson, E. J. Lavernia, A. K. Mukherjee, *Scr. Mater.* 2009, *60*, 835
- [19] J. Trapp, A. Semenov, O. Eberhardt, M. Nöthe, T. Wallmersperger, and B. Kieback, Fundamental principles of spark plasma sintering of metals: part II - about the existence or non-existence of the 'spark plasma effect', *Powder Metall.*, 2020, *63(5)*, 312-328
- [20] R. Yamanoglu, Theory and Technology of Sintering, Thermal and Thermochemical Treatment – Pressureless Spark Plasma Sintering: A perspective from conventional sintering to accelerated sintering without pressure, *Powder Metall. Met. Ceram.*, 2019, *57*, 513-525
- [21] J. Hennicke, H. U. Kassel, *CFI/Berichte DKG*, 2004, *81*, 11
- [22] J. R. Groza, A. Zavaliangos, Sintering activation by external electrical field, *Mater. Sci. and Eng. A*, 2000, 171-177
- [23] J. E. Garay, Current-Activated, Pressure-Assisted Densification of Materials, *Annu. Rev. Mater. Res.*, 2010, *40(1)*, 445-468
- [24] Z. A. Munir, D.V. Quach, M. Ohyanagi, Electric Current Activation of Sintering: A Review of the Pulsed Electric Current Sintering Process. Journal of the American Ceramic Society, *J. Am. Ceram. Soc.*, 2011, *94(1)*, 1–19
- [25] R. Raj, M. Cologna, J.S.C. Francis, Influence of Externally Imposed and Internally Generated Electrical Fields on Grain Growth, Diffusional Creep, Sintering and Related Phenomena in Ceramics, *J. Am. Ceram. Soc.*, 2011, *94(7)*, 1941–1965
- [26] S. Rivoirard, High Steady Magnetic Field Processing of Functional Magnetic Materials, *JOM*, 2013, *65(7)*, 901–909
- [27] V. Psyk, D. Risch, B.L. Kinsey, A.E. Tekkaya, M. Kleiner, Electromagnetic forming— A review, *J. Mater. Proc. Technol.*, 2011, *211*, 787–829
- [28] Y.V. Batygin, S.F. Golovashchenko, A.V. Gnatov, Electromagnetic forming — A review, *J. Mater. Proc. Tech.*, 2013, *213*, 444–452
- [29] R.H.R. Castro, K. van Benthem (Eds.), Sintering: Mechanisms of Convention, *Nanodensification and Field Assisted Processes*, Springer, 2013
- [30] O. Guillon, J. Gonzalez-Julian, B. Dargatz, T. Kessel, G. Schierning, J. Räthel, and M. Herrmann, Field-Assisted Sintering Technology/Spark Plasma Sintering: Mechanism, Materials, and Technology Developments, *Adv. Eng. Mater.*, 2014, *16*, 830-849

- [31] M. Biesuz, T. Saunders, D. Ke, M. J. Reece, C. Hu, and S. Grasso, A review of electromagnetic processing of materials (EPM): heating, sintering, joining and forming, *J. Mater. Sci. Technol.*, 2021, *69*, 239-272
- [32] R. M. German, Sintering Theory and Practice. Wiley, New York, 1996
- [33] U. Anselmi-Tamburini, J. E. Garay, Z. Munir, A. Tacca, F. Maglia, and G. Spinolo, Spark plasma sintering and characterization of bulk nanostructured fully stabilized zirconia: Part I. Densification studies, *J. Mater. R.*, 2004, *19(11)*, 3255–3262
- [34] U. Anselmi-Tamburini, S. Gennari, J. E. Garay, and Z. A. Munir, Fundamental investigations on the spark plasma sintering/synthesis process: II. Modeling of current and temperature distributions, *Mater. Sci. Eng. A*, 2005, *394*, 132–38
- [35] Z. A. Munir, U. Anselmi-Tamburini, M. Ohyanagi, The effect of electric field and pressure on the synthesis and consolidation of materials: A review of the spark plasma sintering method, *J. Mater. Sci.*, 2006, *41*, 763-777
- [36] D. N. F. Muche, J. W. Drazin, J. Mardily, S. Dey, R. H. R. Castro, Colossal grain boundary strengthening in ultrafine nanocrystalline oxides, *Mater. Lett.*, 2014, *97*, 2405-2408
- [37] J. Trapp, and B. Kieback, Fundamental principles of spark plasma sintering of metals: part I – Joule heating controlled by the evolution of powder resistivity and local current densities, *Powder Metall.*, 2020, *63(5)*, 297-306
- [38] S. Munoz, U. Anselmi-Tamburini, Parametric investigation of temperature distribution in field activated sintering apparatus, *Int. J. Adv. Manuf. Technol.*, 2013, *65*, 127–140
- [39] J. Guyon, A. Hazotte, J. P. Monchoux, and E. Bouzy, Effect of powder state on spark plasma sintering of TiAl alloys, *Intermetallics*, 2013, *34*, 94–100
- [40] Z. Trzaska, A. Couret, J. P. Monchoux, Spark plasma sintering mechanisms at the necks between TiAl powder particles, *Acta. Mater.*, 2016, *118*, 100–108
- [41] A. Zavaliangos, J. Zhang, M. Krammer, and J. R. Groza, Temperature evolution during field activated sintering, *Mater. Sci. Eng. A*, 2004, *379(1–2)*, 218-228
- [42] C. Manière, A. Pavia, L. Durand, G. Chevallier, K. Afanga, and C. Estournès, Finite-element modeling of the electro-thermal contacts in the spark plasma sintering process, *J. Eur. Ceram.*, 2016, *36(3)*, 741-748
- [43] Y. Yang, T. D. Oyediji, P. Kühn, B.-X. Xu, Investigation on temperature-gradient-driven effects in unconventional sintering via non-isothermal phase-field simulation, *Scr. Mater.*, 2020, *186*, 152-157

- [44] A. S. Tukmakova, K. L. Samusevich, A. V. Asach, and A. V. Novotelnova, The Impact of Peltier Effect on the Temperature Field During Spark Plasma Sintering of Thermoelectric Materials, *Journal of Elec. Materi.*, 2019, 48, 1812–1817
- [45] D.-J Chen, and M. J. Mayo, Rapid Rate Sintering of Nanocrystalline ZrO_2 –3 mol% Y_2O_3 , *J. Am. Ceram.*, 1996, 79(4), 906–912
- [46] J.R Friedman, J.E Garay, U Anselmi-Tamburini, and Z.A Munir, Modified interfacial reactions in Ag–Zn multilayers under the influence of high DC currents, *Intermetallics*, 2004, 12(6), 589-597
- [47] C. Schmerbauch, J. Gonzalez-Julian, R. Röder, C. Ronning, and O. Guillon, Flash Sintering of Nanocrystalline Zinc Oxide and its Influence on Microstructure and Defect Formation, *J Am Ceram Soc.*, 2014, 97(6), 1728–1735
- [48] G. S. Rohrer, M. Affatigato, M. Backhaus, R. K. Bordia, H. M. Chan, S. Curtarolo, A. Demkov, J. N. Eckstein, K. T. Faber, J. E. Garay, Y. Gogotsi, L. Huang, L. E. Jones, S. V. Kalinin, R. J. Lad, C. G. Levi, J. Levy, J. P. Maria, L. Mattos, A. Navrotsky, N. Orlovskaya, C. Pantano, J. F. Stebbins, T. S. Sudarshan, T. Tani, and K. Scott Weil, Challenges in ceramic science: A report from the workshop on emerging research areas in ceramic science, *J. Am. Ceram. Soc.*, 2012, 95, 3699–3712
- [49] M. Tokita, Trends in Advanced SPS Spark Plasma Sintering Systems and Technology, *J. Soc. Powder Technol. Japan*, 1993, 30(11), 790–804
- [50] O. Guillon, and J. Langer, Master sintering curve applied to the Field-Assisted Sintering Technique, *J. Mater. Sci.*, 2010, 45, 5191–5195
- [51] L.P. Bulat, A.V. Novotelnova, A.S. Tukmakova, D. E. Yerezhep, V. B. Osvenskii, A. I. Sorokin, V. P. Panchenko, L. V. Bochkov, and S. Ašmontas, Simulation of SPS Process for Fabrication of Thermoelectric Materials with Predicted Properties, *Journal of Elec. Materi.*, 2018, 47, 1589–1594
- [52] A. Tukmakova, A. Novotelnova, K. Samusevich, A. Usenko, D. Moskovskikh, A. Smirnov, E. Mirofyanchenko, T. Takagi, H. Miki, and V. Khovaylo, Simulation of Field Assisted Sintering of Silicon Germanium Alloys, *Materials*, 2019, 12(4), 570
- [53] A. S. Tukmakova, K. L. Samusevich, A. V. Novotelnova, I. L. Tkhorzhevskiy, and E. S. Makarova, Simulation of Thermoelectric Materials Densification during Spark Plasma Sintering with the Example of Ge–Si, *Semiconductors*, 2019, 53, 772–774
- [54] Z. A. Munir, D. V. Quach, and M. Ohyanagi, Sintering: Mechanisms of Convention Nanodensification and Field Assisted Processes, *Springer*, Berlin/Heidelberg, 2012

- [55] U. Anselmi-Tamburini, G. Spinolo, F. Maglia, I. Tredici, T. B. Holland, and A. K. Mukherjee, *Sintering: Mechanisms of Convention Nanodensification and Field Assisted Processes*, Springer, Berlin/Heidelberg, 2012
- [56] J. Trapp , A. Semenov , M. Nöthe , T. Wallmersperger, and B. Kieback, Fundamental principles of spark plasma sintering of metals: part III – densification by plasticity and creep deformation, *Powder Metall.*, 2020, *63(5)*, 329-337
- [57] M. Biesuz, T. Saunders, D. Ke, M. J. Reece, C. Hu, and S. Grasso, A review of electromagnetic processing of materials (EPM): heating, sintering, joining and forming, *J. Mater. Res.*, 2021, *69*, 239-272
- [58] J. Wachowicz, Spark Plasma Sintering – new technology for obtaining tool materials, *Annals of Warsaw University of Life Sciences SGGW Forestry and Wood Technology*, 2020, *109*, 64-69
- [59] M. Suárez, A. Fernández, J.L. Menéndez, R. Torrecillas, H. U. Kessel, J. Hennicke, R. Kirchner, and T. Kessel, Challenges and Opportunities for Spark Plasma Sintering: A Key Technology for a New Generation of Materials, *J. Sinter. Appl.*, 2013, 319
- [60] J. R. Groza, and A. Zavaliangos, Sintering activation by external electrical field, *Mater. Sci. Eng.*, 2000, *A287*, 171–177
- [61] K.R. Anderson, J.R. Groza, M. Fendorf, and C.J. Echer, Surface oxide debonding in field assisted powder sintering, *Mater. Sci. Eng.*, 1999, *A270*, 278–282
- [62] M. Wu, Y. Yang, G. Yang, K. Huang, and D. Yin, Direct evidence for surface cleaning mechanism during field-activated sintering, *J. Alloys Compd.*, 2019, *784*, 975-979
- [63] O. Guillon, C. Elsässer, O. Gutfleisch, J. Janek, S. Korte-Kerzel, D. Raabe, C. A. Volkert, Manipulation of matter by electric and magnetic fields: Toward novel synthesis and processing routes of inorganic materials, *Mater. Today* 2018, *21*, 527- 536.
- [64] C. Manière, A. Pavia, L. Durand, G. Chevallier, K. Afanga, C. Estournès, Finite-element modeling of the electro-thermal contacts in the spark plasma sintering process, *J. Eur. Ceram.*, 2016, *36*, 741-748
- [65] E. Olevsky, D. Dudina, *Field-assisted sintering: science and applications*, Cham: Springer, 2018.
- [66] P. Cavaliere, *Spark plasma sintering of materials: advances in processing and applications*, Cham: Springer, 2019
- [67] H. Bakhshi, R. Sarraf-Mamoory, A. Yourdkhani, A. A. AbdelNabi, and Y. Mozharivskyj, Highly dense $\text{Sr}_{0.95}\text{Sm}_{0.0125}\text{Dy}_{0.0125-0.025}\text{Ti}_{0.90}\text{Nb}_{0.10}\text{O}_3 \pm \delta/\text{ZrO}_2$ composite

- preparation directly through spark plasma sintering and its thermoelectric properties, *Dalton Trans.*, 2020, 49, 17-22
- [68] C. van der Rest, V. Dupont, J.-P. Erauw, and P. J. Jacques, On the reactive sintering of Heusler Fe₂VAl-based thermoelectric compounds, *Intermetallics*, 2020, 125, 106890
- [69] M. Cologna, 2020. Use of Field Assisted Sintering for Innovation in Nuclear Ceramics Manufacturing.
- [70] A. Kundi, A. Sittiho, I. Charit, B. Jaques, and C. Jiang, Development of Fe-9Cr Alloy via High-Energy Ball Milling and Spark Plasma Sintering, *JOM*, 2019, 71(8), 2846-2855
- [71] J. Gonzales-Julian, Processing of MAX phases: From synthesis to applications, *J. Am. Ceram. Soc.*, 2021, 104, 659–690
- [72] K. Zarebski, P. Putyra, and D. Mierzwunski, Porosity and Microstructure Iron-Based Graded Materials Sintered by Spark Plasma Sintering and the Conventional Method, *Metals*, 2019, 9, 264
- [73] M. U. F. Khan, A. Patil, J. Christudasjustus, T. Borkar, and R.K. Gupta, Spark plasma sintering of a high-energy ball milled Mg-10wt% Al alloy, *J. Magnes. Alloy.*, 2020, 8, 319-328
- [74] V. M. Nguyen, R. Khanna, Y. Konyukhov, T. H. Nguyen, I. Burmistrov, V. Levina, I. Golov, and G. Karunakaran, Spark Plasma Sintering of Cobalt Powders in Conjunction with High Energy Mechanical Treatment and Nanomodification, *Processes*, 2020, 8, 627
- [75] H. Yoshida, K. Morita, B.-N. Kim, and K. Soga, Low temperature spark plasma sintering of tin oxide doped with tantalum oxide, In addition, metallic alloys are of interest as model systems for mechanistic investigation, *J. Caram. Soc. JAPAN*, 2016, 124(9), 932-937
- [76] C. B. Mo, S. I. Cha, K. T. Kim, K. H. Lee, S. H. Hong, Fabrication of carbon nanotube reinforced alumina matrix nanocomposite by sol-gel process, *Mater. Sci. Eng. A*, 2005, 395, 124-128
- [77] L. M. Kang, Y. J. Cai, X. C. Luo, Z. J. Li, X. B. Liu, Z. Wang, Y. Y. Li, and C. Yang, Bimorphic microstructure in Ti-6Al-4V alloy manipulated by spark plasma sintering and in-situ press forging, In addition, metallic alloys are of interest as model systems for mechanistic investigation, *Scr. Mater*, 2021, 193, 43-48

- [78] B. Ratzker, A. Wagner, S. Kalabukhov, and N. Frage, Transparent Er₂O₃ ceramics fabricated by high-pressure spark plasma sintering, *J. Eur. Ceram. Soc.*, 2020, 40, 4700-47003
- [79] N. S. Weston, B. Thomas & M. Jackson, Processing metal powders via field assisted sintering technology (FAST): a critical review, *Mater. Sci. and Technol.*, 2019, 35(11), 1306-1328
- [80] M. Khosghadam-Pireyousefan, A. Mohammadzadeh, A. Heidarzadeh, D. Brabazon, Fundamentals of Spark Plasma Sintering for Materials, Ceramic, and Polymer Matrix Composite Production, *Encyclopedia of Materials: Composites*, 2021
- [81] G. Cerretti, B. Balke, G. Kieslich, and W. Tremel, Towards Higher zT in Early Transition Metal Oxides: Optimizing the Charge Carrier Concentration of the WO₃-xCompounds, *Materials Today*, 2018, 5(4), 10240-10248
- [82] G. Cerretti, M. Schrade, X. Song, B. Balke, I. Lieberwirth, and W. Tremel, Thermal Stability and Enhanced Thermoelectric Properties of the Tetragonal Tungsten Bronzes Nb_{8-x}W_{9+x}O₄₇ (0 < x < 5), *J. Mater. Chem. A*, 2017, 5, 9768-9774
- [83] M. Joos, G. Cerretti, I. Veremchuk, P. Hofmann, H. Frerichs, D.H. Anjum, T. Reich, I. Lieberwirth, M. Panthöfer, W.G. Zeier, and W. Tremel, Spark Plasma Sintering (SPS)-Assisted Synthesis and Thermoelectric Characterization of Magnéli Phase V₆O₁₁, *Inorg. Chem.*, 2018, 57, 1259-1268
- [84] D. Portehault, V. Maneeratana, C. Candolfi, N. Oeschler, I. Veremchuk, Y. Grin, C. Sanchez, and M. Antonietti, Facile General Route toward Tunable Magnéli Nanostructures and Their Use As Thermoelectric Metal Oxide/Carbon Nanocomposites, *ACS Nano*, 2011, 5(11), 9052–9061
- [85] C. Recknagel, N. Reinfried, P. Höhn, W. Schnelle, H. Rosner, Yu Grin, and A. Leithe-Jasper, Application of spark plasma sintering to the fabrication of binary and ternary skutterudites, *Sci. Technol. Adv. Mater.*, 2007, 8, 357–363
- [86] H.-W. Son, D. Berthebaud, K. Yubuta, A. Yoshikawa, T. Shishido, K. Suzuta, and T. Mori, New Synthesis Route for Complex Borides; Rapid Synthesis of Thermoelectric Yttrium Aluminoboride via Liquid-Phase Assisted Reactive Spark Plasma Sintering, *Sci. Rep.*, 2020, 10, 8914
- [87] M. Ihrig, M. Finsterbusch, C.-L. Tsai, A. M. Laptev, C.-h. Tu, M. Bram, Y. J. Sohn, R. Ye, S. Sevinc, S.-k.Lin, D. Fattakhova-Rohlfing, and O. Guillon, Low temperature

- sintering of fully inorganic all-solid-state batteries – Impact of interfaces on full cell performance, *J. Power Sources*, 2021, 482, 228905
- [88] M. Cologna, B. Rashova, R. Raj, Flash Sintering of Nanograin Zirconia in <5 s at 850°C, *J. Am. Ceram. Soc.*, 2010, 93, 3556
- [89] M. Yu, S. Grasso, R. Mckinnon, T. Saunders, M. J. Reece, Review of flash sintering: materials, mechanisms and modelling, *Adv. Appl. Ceram.*, 2017, 116, 24
- [90] M. Bram, A.M. Laptev, T.P. Mishra, K. Nur, M. Kindelmann, M. Ihrig, J.G. Pereira da Silva, R. Steinert, H.P. Buchkremer, A. Litnovsky, F. Klein, J. Gonzalez-Julian, and O. Guillon, Application of Electric Current-Assisted Sintering Techniques for the Processing of Advanced Materials, *Adv. Eng. Mater.*, 2020, 22, 2000051
- [91] S. Grasso, T. Saunders, H. Porwal, O. Cedillos-Barraza, D. D. Jayaseelan, W. E. Lee, M. J. Reece, Review of flash sintering: materials, mechanisms and modelling, *J. Am. Ceram. Soc.*, 2014, 97, 2405
- [92] S. Grasso, T. Saunders, H. Porwal, B. Milson, A. Tudball, M. J. Reece, Flash Spark Plasma Sintering (FSPS) of α and β SiC, *J. Am. Ceram. Soc.*, 2016, 99, 1534
- [93] C. Gorynski, U. Anselmi-Tamburini, and M. Winterer, Controlling current flow in sintering: A facile method coupling flash with spark plasma sintering, *Rev. Sci. Instruments.*, 2020, 91, 015112
- [94] W. L. Bradbury, and E. A. Olevsky, Production of SiC–C composites by free-pressureless spark plasma sintering (FPSPS), *Scr. Mater.*, 2010, 63(1), 77–80
- [95] D. Giuntini, X. Wei, A. L. Maximenko, L. Wei, A. M. Ilyina, and E. A. Olevsky, Initial stage of free pressureless spark-plasma sintering of vanadium carbide: Determination of surface diffusion parameters, *Int. J. Refract. Met. Hard Mater.*, 2013, 41, 501–506
- [96] L. Bertolla, I. Dlouhý, P. Tatarko, A. Viani, A. Mahajan, Z. Chlup, M. Reece, and A.R. Boccaccini, Pressureless spark plasma–sintered Bioglass® 45S5 with enhanced mechanical properties and stress–induced new phase formation, *J. Eur. Ceram. Soc.*, 2017, 37(7), 2727–2736
- [97] D. V. Dudina, B. B. Bokhonov, and A. K. Mukherjee, Formation of aluminum particles with shell morphology during pressureless spark plasma sintering of Fe–Al mixtures: current-related or Kirkendall effect?, *Materials*, 2016, 9(5), 375
- [98] R. Yamanoglu, N. Gulsoy, E. A. Olevsky, and H. O. Gulsoy, Production of porous Ti5Al2.5Fe alloy via pressureless spark plasma sintering, *J. Alloys Compd.*, 2016, 680, 654–658

The contents of the following chapter are taken and partially adapted from *Adv. Funct. Mater.* **2020**, 30, 1909051.

Authorship contributions

Category 1

Conception and design of study:

[REDACTED]

Acquisition of data:

- [REDACTED] – preparation of samples.
- [REDACTED] – PXRD measurements.
- [REDACTED] – acquisition of ADT data and HR-TEM images.
- [REDACTED] – Laser microscope and SEM images.
- [REDACTED] – measurement of ^{19}F solid-state NMR.
- [REDACTED] – acquisition of UV/Vis-data.
- [REDACTED] – acquisition of photocatalytic data.
- [REDACTED] – acquisition of XPS data.

Analysis and/or interpretation of data:

- [REDACTED] – PXRD refinement.
- [REDACTED] – unit cell analysis and structure solution via ADT and PXRD data.
- [REDACTED] – analysis of ^{19}F solid-state NMR.
- [REDACTED] – interpretation of XPS data.

Category 2

Drafting the manuscript:

[REDACTED]

Revising the manuscript critically for important intellectual content:

Category 3

Approval of the version of the manuscript to be published:

Figure 2.1: prepared by
Figure 2.2: prepared by
Figure 2.3: prepared by
Figure 2.4: prepared by
Figure 2.5: prepared by
Figure 2.6: prepared by
Figure 2.7: prepared by
Figure 2.8: prepared by

**Chapter 2 | Solid State Fluorination on
the Minute Scale:
Synthesis of $\text{WO}_{3-x}\text{F}_x$ with
Photocatalytic Activity**

Chapter 2.1 Motivation

“Energy efficiency, sustainability, and economic viability are becoming increasingly important for materials manufacturing in industry. Microwave methods^[1,2] allow rapid materials processing with improved energy efficiency and reduced equipment costs. Similarly, spark plasma sintering (SPS) has become a state-of-the-art method,^[3,4] where a uniaxial force and a pulsed electric field (dc current) allow a high speed consolidation of polycrystalline powders.^[9,10] The detailed mechanism of SPS reactions is still far from being understood,^[3,4] but the primary effect of the current in the sintering process is likely to be Joule heating. Other non-thermal effects may contribute to the solid-state reaction kinetics. This may alter the nature of the final product.^[4,5,6,7,8] Although SPS is an important form-giving process, its application for the synthesis of new materials is still in its infancy.^[11,12,13]

In the past, a variety of fluorination techniques have been devised for fluoride “doping” or to synthesize oxyfluorides. Many of them requires fluorine gas, reactive fluorides, or hydrogen fluoride as toxic and corrosive fluorine sources that require special equipment and handling techniques.^[14,15,16] A synthesis of $\text{WO}_{3-x}\text{F}_x$ by heating WO_3 with HF under extreme conditions in sealed gold ampoules has been reported.^[17] High-temperature approaches using binary fluorides (like MF_2 or MF_3 ($M = \text{alkaline-earth or lanthanide metal}$)) have limitations because of the stability of the starting compounds compared to the intended products.^[18] Therefore, alternate fluorination routes have been developed for obtaining oxyfluorides.^[19-24]

Fluorination using a powder of the fluorinated polymers as a source of fluorine in a reductive fluorination process relies on their solid form, chemical stability at room temperature and their relatively low decomposition temperature compared with most inorganic compounds.^[21,22,23,24] This allows to perform a reductive fluorination of oxides easily and safely. The convenience and usability of this method for the synthesis of superconducting $\text{WO}_{3-x}\text{F}_x$ has already been demonstrated.^[22] $\text{WO}_{3-x}\text{F}_x$ has been synthesized with different fluorine contents, but photocatalytic activity similar as for the related Magneli phases^[25] has not been reported. We report a new SPS approach on a minute scale for the rapid fluorination of WO_3 with polytetrafluorethylene (PTFE) to the oxy-fluorides $\text{WO}_{3-x}\text{F}_x$ with high photocatalytic activity in copious amounts. These solid-state reactions were complete several minutes and lead, depending on the ratio of the starting compounds, to the formation of oxyfluorides $\text{WO}_{3-x}\text{F}_x$ ($0 < x < 0.6$) with colors ranging from light green to blue as the fluorine content increased. This systematic color change during fluorination reaction is the same as that generally observed in tungsten bronzes and indicates mixed-valency of the tungsten atoms through charge carriers

introduced into the system by chemical reduction. The reaction is diffusion controlled as seen from the presence of two phases in *ex situ* X-ray powder diffraction, in automated diffraction analysis (ADT) and by the shift of the reaction front from the periphery to the core of the tungsten oxide grains in transmission electron microscopy (TEM). This indicates that fluorine diffuses into the WO_3 particles prepared by ball milling. At an intermediate stage, a non-completely reacted WO_3 core is surrounded by a $\text{WO}_{3-x}\text{F}_x$ shell. At 450°C , the reaction proceeds *via* monoclinic and orthorhombic intermediates which have not been reported before. At 550°C , the reaction product for $x = 0.10$ contains an orthorhombic main phase and a cubic side phase (15%). For $x = 0.3-0.4$ the cubic phase is the majority phase with minor (5%) contribution of the orthorhombic phase. The cubic phase exhibits F atom disorder as demonstrated by ^{19}F magic angle spinning nuclear magnetic resonance (MAS-NMR) experiments.^[26,27]

X-ray photoelectron spectroscopy (XPS) revealed that SPS-prepared $\text{WO}_{3-x}\text{F}_x$ contained mixed-valent $\text{W}^{6+}/\text{W}^{5+}$. $\text{WO}_{3-x}\text{F}_x$ shows photocatalytic activity, whereas conventionally prepared $\text{WO}_{3-x}\text{F}_x$ is photocatalytically inactive. The conceptual advancement of this new synthetic approach toward functional nanomaterials lies in the combination of the fluorination with fluorinated polymers and spark plasma sintering (SPS), typically used in ceramics and alloys fields to sinter while limiting grain growth. SPS, reported for incorporating carbon into sol-gel-derived microstructured oxide matrixes,^[28,29] is used for the first time for the fast one-pot synthesis of oxyfluorides. It yields large monoliths of metal oxyfluoride nanopowders. The photocatalytic activity is strongly enhanced through the SPS processing. This suggests that new photocatalytic compounds based on cheap, air-stable, and environmentally benign elements might be discovered by SPS processing from polymer scrap.^[30]

Chapter 2.2 Results and Discussion

Chapter 2.2.1 SPS Synthesis and Chemical Analysis

$\text{WO}_{3-x}\text{F}_x$ was synthesized using SPS (Figure 2.1A). Prior to the reaction, the components WO_3 and PTFE were mixed for 30 x 10 min with 10 min intermissions at 740 rpm in a planetary ball mill using 8 g of grinding balls (ZrO_2 , 1 mm diameter) and approx. 10 mL of ethanol as dispersion medium. No reaction occurred during ball milling as judged by powder X-ray diffraction and ^{19}F -MAS NMR. In a second, pyrometer-controlled heating step the reactant mixture was SPS treated using the temperature profile shown in Figure 2.1B. After preparation, the products typically contained phase mixtures with densities $\geq 90\%$ of the calculated theoretical density. In the first steps, the samples were heated to 400°C , 450°C , 500°C , 550°C ,

and 600°C, and the reactions were quenched immediately after reaching the set-point temperatures. Higher temperatures did not accelerate the reaction, because unreacted PTFE decomposition products are lost, which leads to incomplete reaction. Similarly, high pressures lead to losses of PTFE decomposition products. Therefore, a relatively low pressure (19 MPa) was chosen for the synthesis. Above $\approx 750^\circ\text{C}$, F-containing products were lost, and the formation of reduced tungsten oxides was observed. Thus, the sintering time was varied between 2 and 6 min at 550° and at 600°C. The main reaction came to completion during this short heating segment.

The reaction of WO_3 with polytetrafluoroethylene (PTFE) is assumed to occur at the gas-solid interface, since PTFE starts to decompose slowly at 360°C.^[31] Thermal analysis showed the thermal decomposition to be complete above 400°C, the main decomposition products under vacuum conditions being the C_2F_4 monomer.^[32,33] In the SPS experiments, C_2F_4 resulting from the thermal decomposition of the fluorinated polymers will diffuse through the grain boundaries of the WO_3 sample at the reaction temperature of 550°C. Indications for this behavior is the need of ball-milling for high degrees of fluorination and the presence of flake-like particles at high PTFE: WO_3 ratios in the ball-mill (Figure 7.1.1). If the mixing by ball-milling is insufficient, PTFE-remains can be observed and lower degrees of fluorination in the product material are observed. In addition, a thin white deposition of PTFE on the (cold) outside of the pressing tools on top can be observed after SPS-reaction. However, the actual fluorination mechanism is not fully clear because (i) the state of matter of C_2F_4 under the reaction conditions (19 MPa, 550°C) is not clear, (ii) follow-up reactions of C_2F_4 may form fluorocarbon oligomers depending on reaction temperature and pressure. Increasing the applied pressure to 50 MPa after 4 min at 550°C and performing a second heating step for 3 min at 700°C allowed to further increase the fluorine content up to $x \approx 0.6$.

A conventional synthesis of $\text{WO}_{3-x}\text{F}_x$ was carried out as control experimentals using the same ball-milled precursor mixtures in evacuated quartz tubes that were sintered at 550 °C for 36 h. The reaction was performed with approximately 500 mg of mixture in quartz tubes having a volume of approx. 35 cm³.

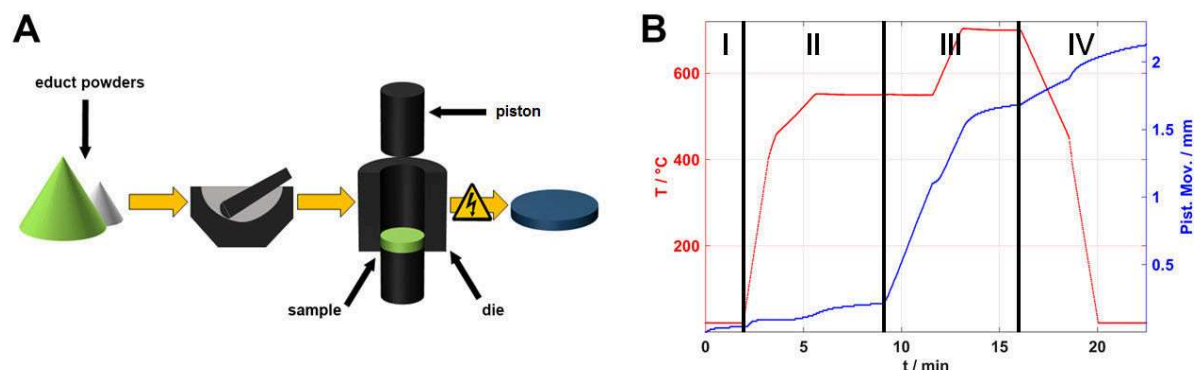


Figure 2.1. (A) Illustration of the synthesis procedure. Different from the conventional approach, reaction and consolidation take place simultaneously. Precursor materials: WO_3 and PTFE. (B) Temperature profile (red) and piston movement/densification (blue) during the SPS process. Capital letters indicate different segments of the process: I Evacuation of reaction chamber and first compression, II start of reaction by heating to 550°C and dwelling for 4 min, III increase of pressure at 550°C from 19 MPa to 50 MPa and second heating step at 700°C , IV sample cooling.

Chapter 2.2.2 Phase Analysis

The phase compositions of all samples were determined by powder X-ray diffraction (PXRD) and TEM. The fluorine content of phase pure samples based on PXRD was determined electrochemically with a F^- -ion selective electrode (for details see experimental section). The nominal and true F/W ratios are compiled in Table 2.1. Compositions determined by potentiometry will be used in the sequel. The true fluorine content increases with increasing nominal fluorine content in $\text{WO}_{3-x}\text{F}_x$, although not in a linear fashion. An excess of fluorinated polymer is needed to achieve high fluorine contents in $\text{WO}_{3-x}\text{F}_x$. The subsequent heat-treatment in air to remove carbon residues does not lead to observable changes in present phase compositions.

Table 2.1. Calculated F/W ratios of orthorhombic and cubic $\text{WO}_{3-x}\text{F}_x$, determined potentiometrically with a F^- -sensitive electrode. X_{nom} describes the F excess in the starting material, while X_{true} describes the ratios as determined by F^- -selective potentiometric measurements.

Method	$V/Z / \text{\AA}$	X_{nom}	X_{true}	$E_{\text{gap}} / \text{eV}$
SPS + 700°C	55.85	1.5	0.60	3.51
SPS	53.25	0.15	0.10	3.31
Conventional ampoule reaction	55.48	1.0	0.42	3.37
Conventional ampoule reaction	53.35	0.1	0.08	3.20

The SPS synthesis of $\text{WO}_{3-x}\text{F}_x$ yielded significantly higher degrees of fluorination than conventional methods using the same ball-milled precursor mixture, because heating to $T > 550^\circ\text{C}$ in quartz ampoules led to loss of fluorine or even the formation of reduced tungsten oxides.^[22,23,24] In SPS, the increase of the reaction temperature to 600°C still led to an increase of the fluorine content (indicated by an increase of the lattice parameter of the cubic unit $\text{WO}_{3-x}\text{F}_x$ cell for large PTFE excess), while samples dwelled at 600°C for more than 10 minutes showed a lower fluorine content (Figure 7.1.2). Optimization of the reaction protocol led to the temperature program shown Figure 7.1B. After a first reaction step at 550°C , fast heating and short dwelling at 700°C for 3 minutes allowed the synthesis of highly fluorinated samples (up to $x = 0.6$) while only negligible amounts of WO_2 were formed as a side phase (phase purity $> 98\%$). Increasing the annealing temperature and time resulted in additional side reactions of PTFE and decomposition products with graphite or C-containing decomposition products of PTFE. This led to a contamination of $\text{WO}_{3-x}\text{F}_x$ with several, non-identified phases. This maximum fluorine content of $\text{WO}_{3-x}\text{F}_x$ is significantly higher than that obtained in conventional reactions in quartz ampoules,^[22] and comparable to that of reactions with HF under high pressure ($x = 0.43$ in 48% aqueous HF, and $x = 0.66$ with anhydrous HF)^[17] However, reductive fluorination in SPS reactions was much faster (5-9 minutes vs. 24 h), and it can be upscaled easily to the kg range with appropriate dies.^[4] In addition, it is much easier, cheaper and safer to carry out than reactions under high pressure with HF in gold ampoules.

X-ray diffraction (XRD) patterns of $\text{WO}_{3-x}\text{F}_x$ for different values of x (Figure 2.2A and B) showed that the crystal structure of $\text{WO}_{3-x}\text{F}_x$ depends on the fluorine content x . The XRD patterns of $\text{WO}_{3-x}\text{F}_x$ for $x = 0.10$ and $x = 0.6$ could be indexed based on orthorhombic (space group: $Pb\bar{c}n$) and cubic (space group: $Pm\bar{3}m$) unit cells, respectively (*vide infra*). Crystallographic details and essential results of the Rietveld refinements^[34,35] for SPS-prepared $\text{WO}_{3-x}\text{F}_x$ for $x = 0.10$ and $x = 0.60$ (refined compositions $\text{WO}_{2.90}\text{F}_{0.10}$ and $\text{WO}_{2.40}\text{F}_{0.60}$) are listed in Table 2.2 and 2.3 (conventionally prepared $\text{WO}_{2.92}\text{F}_{0.08}$ and $\text{WO}_{2.58}\text{F}_{0.42}$ in Figure 7.1.3). A cubic $\text{WO}_{3-x}\text{F}_x$ phase with high fluorine content (0.17 - 0.66) has been reported before.^[17,22] Since the crystal structure of orthorhombic $\text{WO}_{2.9}\text{F}_{0.1}$ was unknown, it was determined using a combination of ADT and PXRD (*vide infra*).

Analysis of the unit cell volume per number of tungsten atoms in the unit cell (obtained by Rietveld refinement) are in agreement with the fluorine content determined by fluoride ion selective potentiometry assuming Vegard-behavior^[36] of the fluorine substituted samples. It is difficult to determine the accurate content of lattice F and O by electron and X-Ray diffraction.

Table 2.2. Dynamical refinement of WO_{2.58}F_{0.42} and WO_{2.90}F_{0.10} against ADT data.

	WO _{2.58} F _{0.42}	WO _{2.90} F _{0.10}			
Crystal data					
Chemical formula	WO _{2.58} F _{0.42}	WO _{2.90} F _{0.10}			
Crystal system, space group	cubic, <i>Pm-3m</i>	orthorhombic, <i>Pbcn</i>			
a (Å), b (Å), c (Å), V(Å ³)	3.8143(11), 55.49(3)	7.3435(15), 7.7253(15), 7.4228(12), 421.10(14)			
Z	1	8			
Calculated density (g.cm ⁻³)	6.98	7.32			
Data collection					
Radiation type	electrons, 300 kV	electrons, 300 kV			
Wavelength (Å)	0.01969	0.01969			
Precession angle (deg.)	1.0	1.0			
¹ Projected crystal dimensions (nm ²)	50x40	π*100 ²			
Average crystal thickness (refined, nm)	20.8	30.4	20.8	25.3	
Resolution (Å)	0.625	0.714			
Tilt step (deg.)	1	1			
No of frames	84	91	88	119	121
Completeness (%)	100	72	63	42	71
No. of used reflections (obs/all)	975/1057	3403/4715	2752/4375	2338/5613	4361/6122
Dynamical structure refinement					
g _{max} , S _g ^{max} (matrix), R _{Sg} , N _{or}	1.8, 0.02, 0.8, 96	1.6, 0.01, 0.6, 96			
R1, wR(F) (obs/all)	7.73/8.87, 9.19/9.26	12.72/18.02, 14.13/14.27			
Goodness of fit (obs)	5.32	5.55			
No. of refined parameters ²	7+84	28+419			
twinning fraction		0.47	0.49	0.49	0.67

¹ The projected crystal dimension for WO_{2.90}F_{0.10} was bigger than the area illuminated by the beam (diameter of 200 nm).

Table 2.3. Atomic positions (fractional units) of the WO_{2.90}F_{0.10} structure refined against XRPD and ADT data.

Site	Rietveld refinement			Distance d	Dynamical refinement		
	x	y	z		x	y	z
W1	-0.246	0.216	-0.490	0.01151	-0.247	0.216	-0.490
O1 ^a	-0.002	0.214	0.034	0.03692	0.000	0.212	0.030
O2 ^a	-0.287	0.990	-0.497	0.05553	-0.291	0.996	-0.499
O3 ^a	-0.218	0.255	-0.246	0.08223	-0.212	0.247	-0.248

^a Superposition of O/F in the ratio determined by potentiometry.

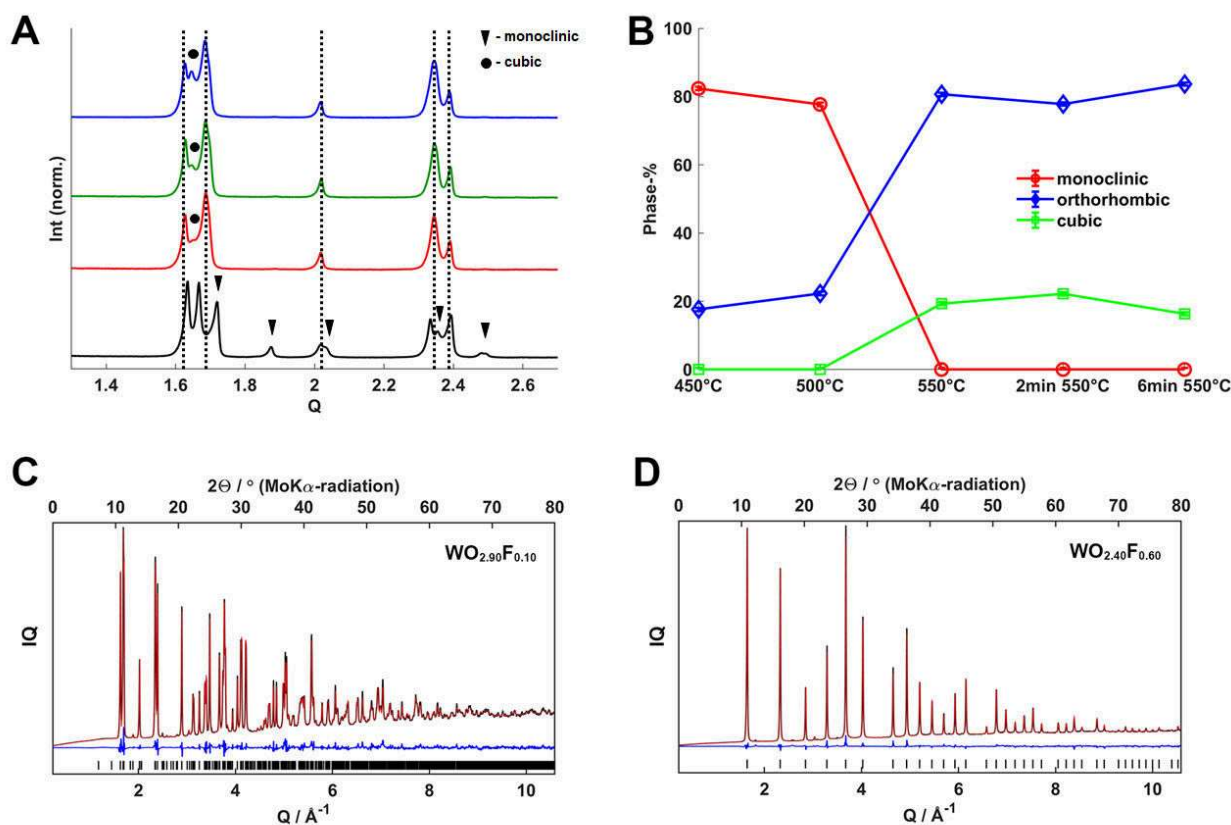


Figure 2.2. (A) X-ray powder diffractograms of samples obtained by quenching the SPS reaction (F:W ratio of the starting material ~ 0.15) at 500°C (black line) and 550°C (red line) with immediate cooling after heating, after 2 minutes at 550°C (green line) and after 6 minutes at 550°C (blue line, completed reaction). Dotted lines indicate reflections of the orthorhombic phase. Circles indicate growing reflections belonging of the cubic phase, triangles indicate vanishing reflections of monoclinic tungsten trioxide. An increase of the fluorine content leads to a larger unit cell and causes the shift of the reflections. (B) Analysis of the phase composition of the obtained samples at several stages of the reaction showing the gradual formation of orthorhombic and cubic $WO_{3-x}F_x$. (C, D) Rietveld refinements of SPS prepared $WO_{2.90}F_{0.10}$ and $WO_{2.40}F_{0.60}$ using X-ray powder data. A and B: $WO_{2.90}F_{0.10}$ (orthorhombic) and $WO_{2.40}F_{0.60}$ (cubic) prepared by SPS processing ($R_{wp} = 3.75\%/3.27\%$, $gof = 2.02/1.54$). Intensity weighted with Q-value.

Chapter 2.2.3 Structure determination of $WO_{2.90}F_{0.10}$ and $WO_{2.40}F_{0.60}$ by ADT

Neither structural solution nor refinement with the reported indexing^[22] was possible for synthesized $WO_{2.90}F_{0.10}$. Electron diffraction has the advantage that single crystal diffraction data may be obtained from nanometer-sized regions. It is also sensitive to superlattice reflections arising from weak, short-range effects. Using non-oriented diffraction patterns with a tomographic scan of the reciprocal space, ADT provides almost complete and pseudo-kinematic reflection intensities from a single nanocrystal and allowed unraveling the tilt

structures of $\text{WO}_{3-x}\text{F}_x$. ADT data was collected from the same “single crystal” (50-200 nm in diameter) in both, static and precession electron diffraction (PED) mode with a probe size of 200 nm in diameter within a tilting range from -60° to $+60^\circ$ resp. -45° to $+45^\circ$ using tilt steps of 1° . Lattice parameters were extracted from the non-precession data (Table 2.2), the precession data were used for structure determination. For $\text{WO}_{2.90}\text{F}_{0.10}$, 12 NED data sets were analyzed (Table 7.1.1). The unit cell could be identified as orthorhombic with three different cell parameters (Table 7.1.1), two being similar, but with distinguishably different size, better detectable in powder XRD (Table 2.2). The calculated average values of these parameters could be used to index the PXRD data. A full symmetry determination from the systematic absences in the ADT data was not possible due to two main problems: (i) The presence of very small (<20 nm) and just slightly differently oriented domains (mosaicity), as confirmed by HRTEM images (Figure 2.8, *vide infra*) and/or domains which are 90° rotated against each other with respect to the c axis (twin structure). (ii) With a density of ~ 7.3 g cm^{-3} and a projected particle diameter between 50 and 200 nm, the expected dynamical effects are relatively large.

These two problems ensure just that the presence of the reflections ($hk0$: $h + k = 2n$; $h0l$: $h + l = 2n$; $0kl$: $k + l = 2n$) are related only to the crystal structure and exclude any face or body centering. Indexing and analysis of powder XRD data led to the space group $Pbcn$ (No. 60; systematic absences $0kl$: $k = 2n + 1$; $h0l$: $l = 2n + 1$; $hk0$: $h + k = 2n + 1$).

An *ab-initio* structure model from powder XRD data was derived with the software EXPO. Possible crystal structures were checked by a rigid body structure refinement with WO_6 octahedra using the TOPAS software package. The atomic parameters were refined from full profile fits of PXRD data using TOPAS Academic 6.0 by applying the fundamental parameter approach.^[34,35]

The refined structure (ReO_3 related, with tilted WO_6 octahedra, derived from the cubic ReO_3 aristotype structure, Figure 2.3A, B) was used as a starting model for a dynamical refinement^[37,38] based on four datasets by applying for each dataset a twinning matrix of (010; -100; 001). Three of four twin fraction parameters converged to approx. 50% (Table 2.1), whereas one twin fraction converged to approx. 33%. This is in line with problem 1 (*vide supra*). Nevertheless, the consequential structure model based on a dynamical refinement confirmed the structure determination based on powder XRD data. It is supported by the small deviations in the atomic coordinates of both models (Table 2.3). All parameters and further information about the dynamical refinement are given in Table 2.3 Three representative zonal images showing different axis directions are presented in Figure 2.3C.

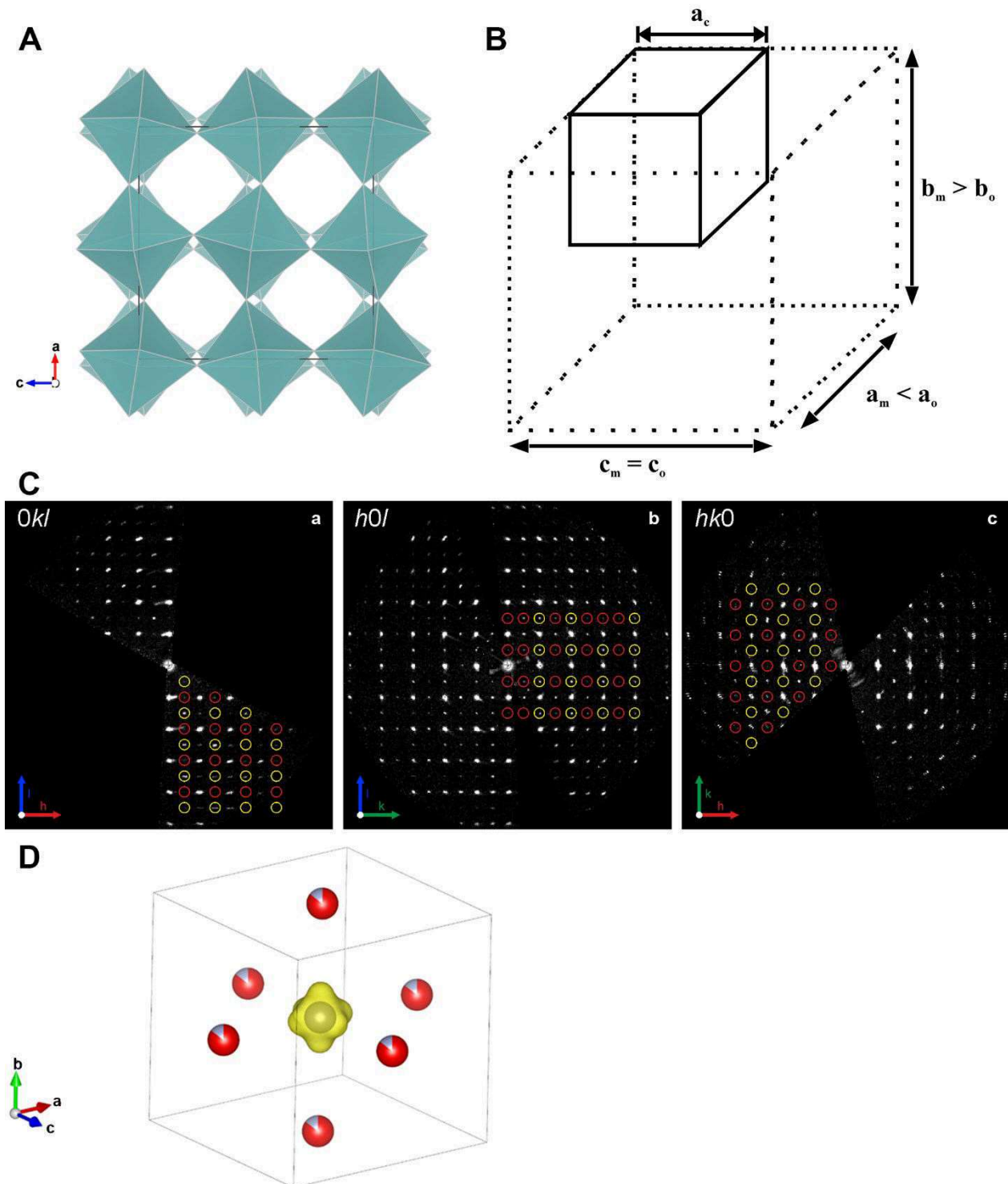


Figure 2.3. (A) View of the orthorhombic $\text{WO}_{3-x}\text{F}_x$ structure with tilted WO_6 octahedra along the b -axis. The tilt pattern corresponds to that of the tungsten oxide high-temperature ($Pbcn$) phase with the Glazer nomenclature $a^0 b^+ c^-$ (where $a < c < b$). (B) Relation of the monoclinic, orthorhombic and cubic $\text{WO}_{3-x}\text{F}_x$ lattices. (C) Reconstruction of zonal extinctions from ADT measurements. From left to right: a - $0kl$, b - $h0l$, c - $hk0$. Exemplary reconstructed crystallographic zonal patterns from ADT measurements. Bragg reflections in yellow and red circles are forbidden due to the extinctions derived from space group $Pbcn$. The presence of the yellow marked Bragg reflections could be explained by twinning. (D) Probability density function (in yellow) of the non-harmonic

The structure of the cubic phase ($\text{WO}_{2.40}\text{F}_{0.60}$) was solved with Superflip^[37,38,39] and refined dynamically based on ADT data (R-value of 8.5%). For an anisotropic (harmonic) refinement of the displacement parameters of tungsten, a significant spatial scattering density distribution could be observed in the difference Fourier synthesis. Only an inharmonic functional description of the anisotropic displacement parameters (ADPs) improved the dynamical refinement significantly (R value of 7.5%), possible due to a Jahn-Teller distortion.^[40] The density distribution (Figure 2.3D) of tungsten's non-harmonic ADP was interpreted by a superposition of different tungsten sites. For a further refinement the tungsten site W1 was shared with one additional atom W1', where the sum of the occupancies of W1 and W1' was fixed to one. The refinement converged, even with isotropic ADP for the tungsten sites, to a R-value of 7.5%.

Chapter 2.2.3.1 Crystal structures of $\text{WO}_{2.90}\text{F}_{0.10}$

The crystal structure of $\text{WO}_{2.90}\text{F}_{0.10}$ can be described as a $\text{WO}_{3-x}\text{F}_x$ tilt structure with $\text{W}(\text{O}/\text{F})_6$ octahedra tilted along the b-axis. The tilt pattern corresponds to that of the tungsten oxide high-temperature (*Pbcn*) phase with the Glazer nomenclature $a^0 b^+ c^-$ (where $a < c < b$) for perovskites.^[41-46] The relations between the unit cells of monoclinic and cubic WO_3 (space groups $P2_1/n$ and $Pm\bar{3}m$) and orthorhombic $\text{WO}_{3-x}\text{F}_x$ (space group *Pcnb*) are sketched schematically in Figure 2.3A. Apart from small variations of their length, the cell vectors are related according to $a_m \approx a_o \approx \frac{1}{2} a_c$; $b_m \approx c_o \approx \frac{1}{2} a_c$; $c_m \approx b_o \approx \frac{1}{2} a_c$.

Chapter 2.2.4 Local structure of $\text{WO}_{2.92}\text{F}_{0.08}$ (conventional synthesis), $\text{WO}_{2.9}\text{F}_{0.1}$ (SPS-prepared), $\text{WO}_{2.58}\text{F}_{0.42}$ (conventional synthesis), and $\text{WO}_{2.40}\text{F}_{0.60}$ (SPS-prepared) by ^{19}F MAS-NMR spectroscopy

ReO_3 -type WO_3 (where the W atoms are in octahedral and the O atoms in linear coordination) was subjected to fluorination as described above. The outcome are the oxyfluorides $\text{WO}_{2.92}\text{F}_{0.08}$ (conv.), $\text{WO}_{2.9}\text{F}_{0.1}$ (SPS) and $\text{WO}_{2.58}\text{F}_{0.42}$ (conv.), $\text{WO}_{2.40}\text{F}_{0.60}$ (SPS) (Figure 2.4B). Depending on the degree of fluorination, a W atom can be coordinated statistically by five O atoms (maximum six), one or two fluorine atoms (more F neighbors are possible, but statistically not feasible, minimum zero F neighbors) or a vacancy. The ^{19}F MAS NMR spectra of $\text{WO}_{3-x}\text{F}_x$ recorded at 25 kHz MAS display three (orthorhombic) to four (cubic) resonances. The spectra are discussed in terms of resonance frequency and full width at half height (fwhh) (Table 2.4

and Figure 2.4 and 7.1.4, Supporting Information). The resonance frequency (peak position) provides information about the fluorine environment. The line width (fwhh) is a measure for the uniformity of the local field, resp. for the local order. Higher disorder at a particular crystallographic site contributes to broader resonances (fwhh increases).

For octahedral complexes of the form $\{WX_{6-n}F_n\}$ the substituent effects in solution follow an addition relationship expressed by the equation^[47]

$$\delta_F = \delta_F^0 + pC + qT$$

where δ_F^0 represents the chemical shift for WF_6^{2-} , p and q are the numbers of substituents in *cis* and *trans* positions relative to the observed F nucleus, and C and T are shift increments for the *cis* and *trans* substitution, derived from the data for a series of compounds $WX_{6-n}F_n^{2-}$. The base value for δ_F^0 is +165, which corresponds to the chemical shift for WF_6 . The electronegativity of the elements building the crystal lattice plays an important role for the electron density around fluorine (with the highest electronegativity according to the Pauling/Hoffmann scales^[48,49]) and the ^{19}F chemical shift as well. The difference in electronegativity between W and F is 1.62, which places the W-F bond at the borderline between polar covalent and ionic bonding. According to the same notation the W-O bond is a polar covalent bond (the difference is 1.08) because oxygen is less electronegative than fluorine. Thus, the presence of more oxygen in the surroundings of fluorine (in the WO_3 crystal lattice) would increase the electron density around fluorine and shift the ^{19}F chemical shift to higher fields. At the same conditions the presence of more fluorine in such an environment would lead to less shielding of a fluorine atom and induce a low field shift of its resonance.

The ^{19}F spectra and the corresponding deconvolution of the SPS-prepared (orthorhombic $WO_{2.90}F_{0.10}$ – Figure 2.4A) and conventionally synthesized ($WO_{2.92}F_{0.08}$ – Figure 2.4B) and those of the SPS-prepared (cubic $WO_{2.40}F_{0.60}$ – Figure 2.4C) and conventionally synthesized ($WO_{2.58}F_{0.42}$ – Figure 2.4D) structures are presented in Figure 2.4. The shifts and the fwhh of the deconvoluted signals are summarized in Table 2.4.

Three fluorine resonances are detected for the orthorhombic structures at ~ -105 ppm, -112 ppm and -139 ppm. We attribute the signals at -105 ppm (SPS) and -106 ppm (conventional) with comparable fwhh of ~ 4100 Hz to the FW_2O_{10} environment. The resonances at ~ -112 ppm in both orthorhombic structures are probably related with the FW_2O_9F environment (fwhh of ~ 1400 Hz). Additionally, signals (fwhh of 1800 and 9400 Hz in both cases) are observed at -138 ppm and -139.6 ppm. They are assumed to be associated with environments around the detected fluorine containing more than one other fluorine atom.

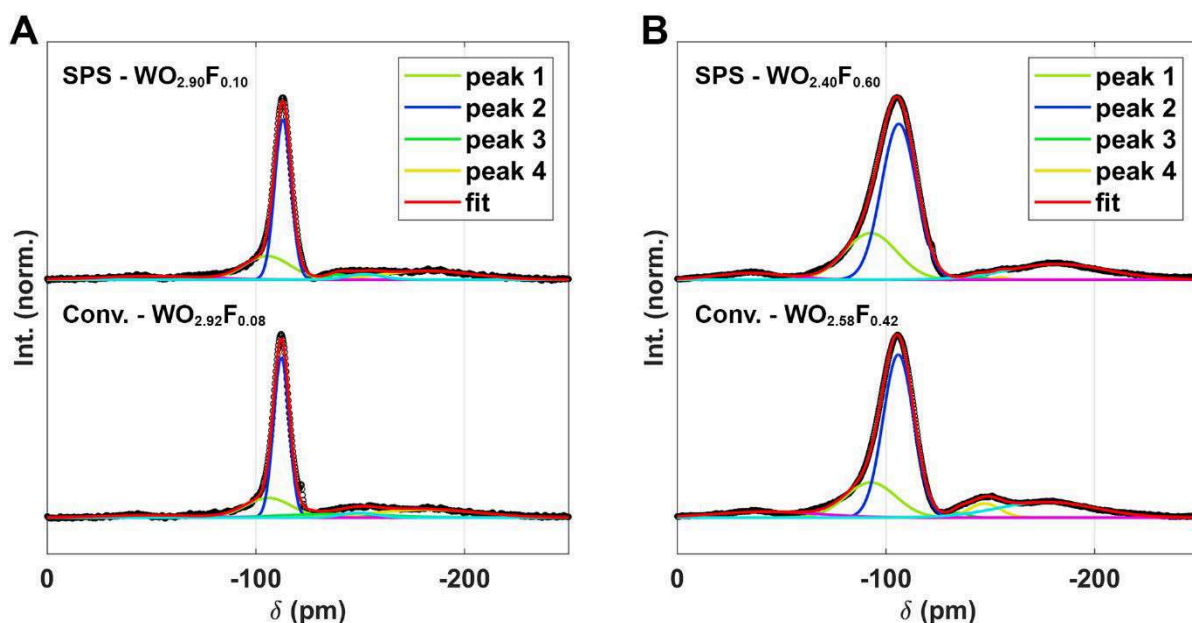


Figure 2.4. ^{19}F MAS-NMR spectra of orthorhombic $\text{WO}_{2.90}\text{F}_{0.10}$ (A) and cubic $\text{WO}_{2.58}\text{F}_{0.42}/\text{WO}_{2.40}\text{F}_{0.60}$ (B). In each figure the top spectrum is derived from a SPS-prepared sample, while the spectrum at the bottom was obtained from a conventionally prepared sample of comparable composition. The non-fitted peak areas at -180 ppm and -50 ppm belong to spinning side bands

Table 4. Assignment of the ^{19}F MAS-NMR signals for orthorhombic and cubic $\text{WO}_{3-x}\text{F}_x$.

SPS/ orthorhombic (Figure 2.4A)	Peak 1	Peak 2	Peak 3	Peak 4
Peak position / ppm	-105.4	-113.0	-139.6.0	
FWHM / kHz	4.2	1.5	4.9	
Relative peak area	29 %	69 %	3 %	
Conv./ orthorhombic (Figure 2.4A)				
Peak position / ppm	-106.0	112.2	138.0	
FWHM / kHz	4.1	1.4	9.4	
Relative peak area	24 %	66 %	10 %	
SPS/ cubic (Figure 2.4B)				
Peak position / ppm	-92.7	-106.2	-144.3	-154.8
FWHM / kHz	4.7	3.2	1.5	1.2
Relative peak area	31 %	69 %	1 %	1 %
Conv./ cubic (Figure 2.4B)				
Peak position / ppm	-92.8	-106.0	-135.5	-147.3
FWHM / kHz	4.5	2.8	1.5	2.8
Relative peak area	24 %	69 %	1 %	6 %

This would explain the significant inhomogeneous broadening observed in the ^{19}F spectrum also related with different possible orientations of the fluorine atoms. The conventional

synthesis (duration: 36 h) leads to an equilibrium structure with a random ligand distribution around the W atoms, whereas the SPS preparation (duration: a few minutes) favors a trapping of non-equilibrium states and local ordering effects. The smaller fwhh observed for the SPS-prepared samples is assumed to arise from the fast reaction at the surface of the WO₃ particle grains.

The spectra of the cubic structures exhibit four signals. The resonances at ~ -92.7 ppm (FW₂O₁₀) and -106 ppm (FW₂O₉F) are well defined in both, conventionally synthesized and SPS-prepared samples. The fwhh are comparable in both cases, but they are slightly broadened for the SPS-prepared samples with 200 to 400 Hz. The other low intensity resonances in both cases cover a range of -135 ppm to -154 ppm. They are probably associated with higher fluorine environments at the contact border between WO₃ and PTFE. The fwhh vary between 1200 Hz to 2800 Hz. A calculated degree of fluorination for the cubic samples ($x = 0.45$ and 0.60) corresponds statistically to 1.5 fluorine atoms in two interconnected octahedra. This matches the relative area of the second peak for both cubic samples at $\approx 50\%$. For higher amounts of fluorine in the cubic structures, the SPS reaction leads to a higher local fluorine content while the conventional reactions leads to a slightly more uniform product (the fwhh for the SPS reaction are broader for both). These assignments are supported by the calculated ¹⁹F δ_{iso} values of F atom environments in NbO₂F ($-62, -53, -43$ and -30 ppm)^[27] and TaO₂F ($-84, -73, -62$ and -46 ppm).^[27]

A SEM image of the polished pellet surface (Figure 2.5A) shows the formation of a dense product with a macroscopic uniform elemental distribution over the pellet cross-section which confirms the presence of just one single phase product as shown via diffraction. Both, TEM and SEM, images reveal the grains to be randomly oriented, without pronounced morphology and with a large size distribution, most likely due to ball-milling treatment of the starting materials. Furthermore, TEM-analysis reveals a far less pronounced grain growth during SPS synthesis compared to conventional synthesis (Figure 7.1.5) and more uniform grains after SPS. The observed porosity is most likely caused by the evaporation of decomposed PTFE as less thoroughly mixing leads to larger cavities and observable remains of PTFE (Figure 7.1.1B).

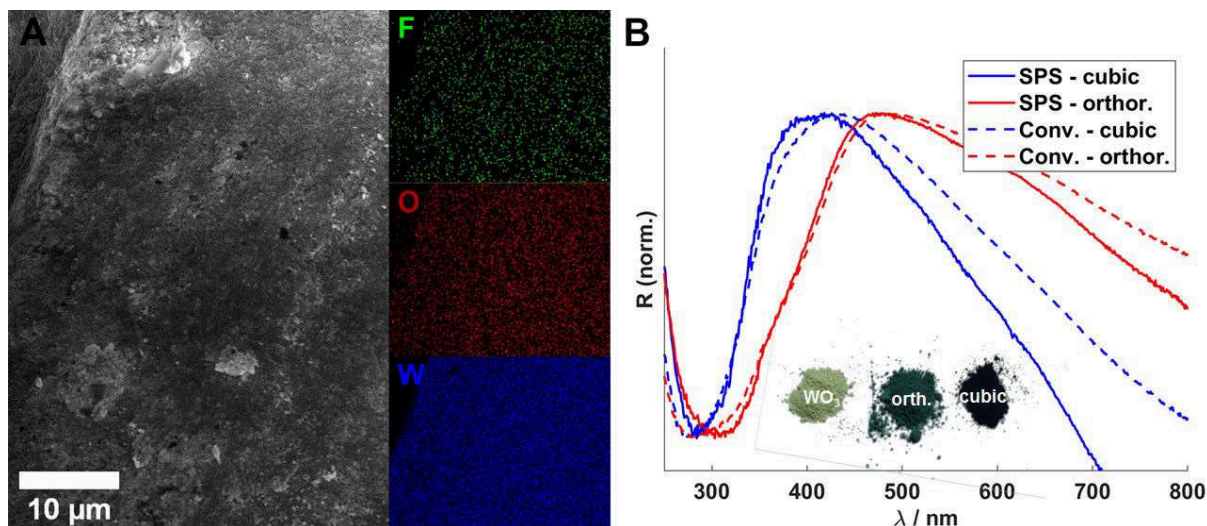


Figure 2.5. (A) SEM-EDX image of a cross-section of a SPS-pellet of cubic $\text{WO}_{2.4}\text{F}_{0.6}$. Observable cavities are caused by evaporated decomposed PTFE. (B) Diffuse reflectance UVVIS spectra of cubic and orthorhombic conventionally prepared $\text{WO}_{3-x}\text{F}_x$ (blue - $\text{WO}_{2.58}\text{F}_{0.42}$, red - $\text{WO}_{2.92}\text{F}_{0.08}$, dotted lines) and by SPS-prepared (blue - $\text{WO}_{2.40}\text{F}_{0.60}$, red - $\text{WO}_{2.90}\text{F}_{0.10}$, solid lines).

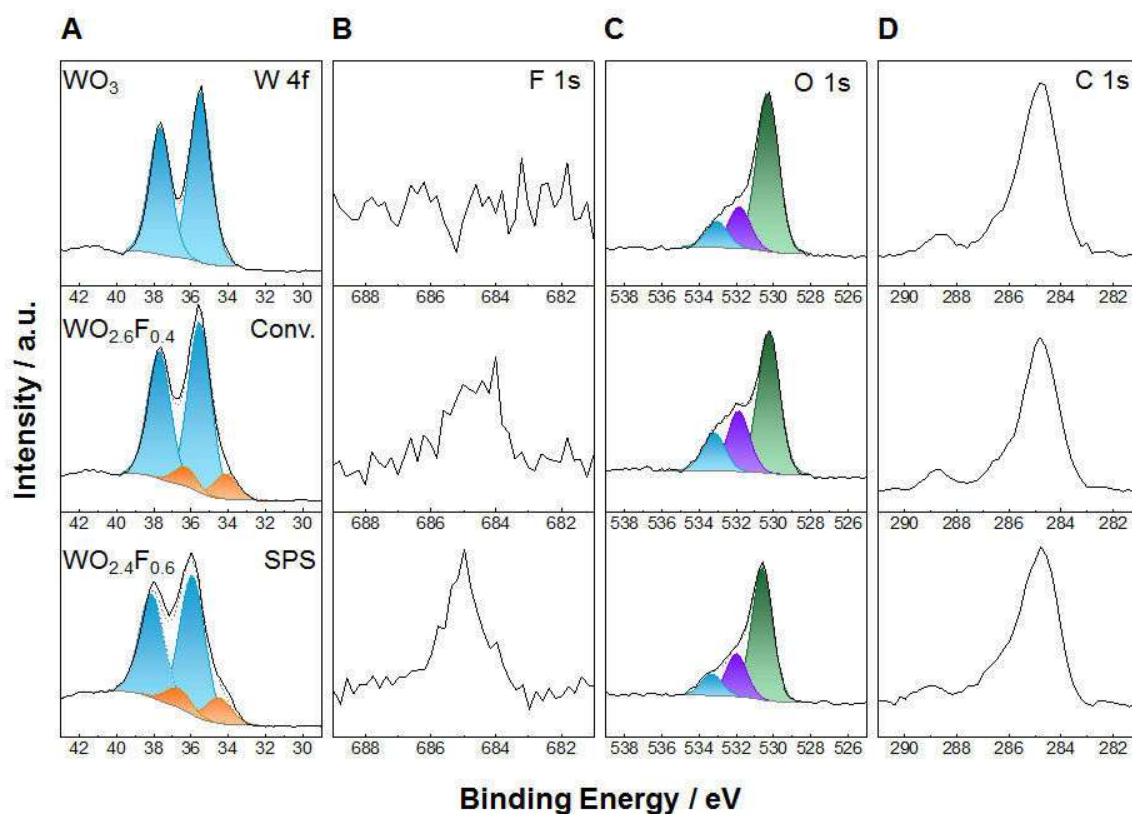


Figure 2.6. XPS sub-spectra of W 4f (A), F 1s (B), O 1s (C) and C 1s (D) of reference WO_3 (top) cubic $\text{WO}_{3-x}\text{F}_x$ prepared conventionally (middle) and by SPS (bottom). All spectra were calibrated by the C 1s signal and fitted considering the spin-orbit splits for each element.

Chapter 2.2.5 Electronic structure and composition of cubic $\text{WO}_{3-x}\text{F}_x$ by XPS spectroscopy

Figure 2.6A-D show the W 4f, F 1s, O 1s and C 1s regions of the XPS spectra of cubic $\text{WO}_{3-x}\text{F}_x$ synthesized by SPS and conventionally, before carbon removal, together with the spectra of a ball-milled and SPS treated WO_3 (99+%, ChemPur). The peaks centered at 36 and 38 eV (Figure 2.6A) are assigned to the W 4f 7/2 and W 4f 5/2 orbitals, respectively. They are characteristic for the oxidation state +6 for WO_3 and $\text{WO}_{3-x}\text{F}_x$. The spectra of cubic $\text{WO}_{3-x}\text{F}_x$ show significant shoulders at 34 and 36 eV, which indicate the presence of W^{5+} . The distinct shoulder in the W 4f region and the stronger signal in the F 1s region of SPS-prepared $\text{WO}_{2.4}\text{F}_{0.6}$ confirm the presence of fluorine and $\text{W}^{6+}/\text{W}^{5+}$ as expected for a higher degree of fluorination. The XPS spectra of the F 1s core electrons (Figure 2.6B) show a single, weak signal centered at 684-685 eV, originating from W–F bonds on the surface of the tungsten oxyfluoride samples. The O 1s regions (Figure 2.6C) show three signals at approx. 530, 532 and 533 eV, which can be assigned to lattice oxide, surface hydroxide groups and adsorbed water. Since these samples were not heated in air after synthesis, the C 1s region shows a strong signal, indicating the presence of carbon from Teflon remnants and additional surface-bound carbonate. The XPS overview spectrum and the spectra after heating in air in Figures 7.1.6 and 7.1.7 confirm the complete removal of carbon and the presence of W, O, and F together with adsorbed water species.

Chapter 2.3 Photocatalytic properties

The optical band gaps were derived from the equation: $(F(R) h\nu)^n = B(E-E_g)$, where $F(R)$ is the Kubelka–Munk function, $h\nu$ the photon energy, B a constant, and n is 2 or 1/2 for direct or indirect transitions, respectively.^[50] Energy gaps (E_g) of 3.2 and 3.5 eV were derived by extrapolating the linear region of $(Ah\nu)^{1/2}$ to $h\nu = 0$.

As shown in Figure 2.5B (vide supra), orthorhombic and cubic $\text{WO}_{3-x}\text{F}_x$ exhibit an intense absorption between 470 and 600 nm, suggesting that the light absorption for photocatalysis mainly derives from the visible part of the spectrum. The absorption edge is blue-shifted compared to the tungsten bronze $\text{W}_{18}\text{O}_{49}$.^[51]

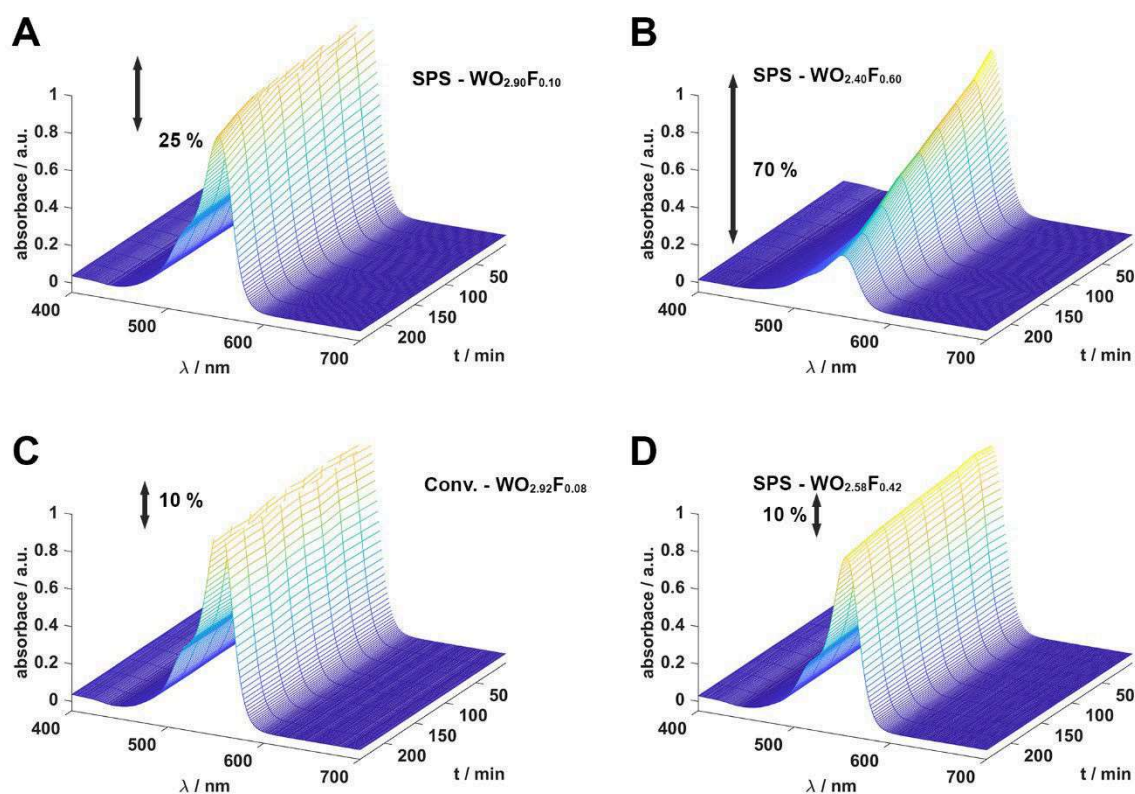


Figure 2.7. UV-vis spectra showing the photocatalytic degradation of RhB in aqueous solution for $\text{WO}_{2.92}\text{F}_{0.08}$ / $\text{WO}_{2.90}\text{F}_{0.10}$ (A, C) and $\text{WO}_{2.58}\text{F}_{0.42}$ / $\text{WO}_{2.40}\text{F}_{0.60}$ (D, B). Data in the upper row (A, B) was obtained by the SPS compound, while (C, D) were prepared by conventional solid state chemistry. Rate constants (Figure 7.1.10): $\text{WO}_{2.90}\text{F}_{0.10}$ - $-0.29 \mu\text{M}/\text{min}$; $\text{WO}_{2.40}\text{F}_{0.60}$ - $-0.59 \mu\text{M}/\text{min}$; $\text{WO}_{2.92}\text{F}_{0.08}$ - $-0.03 \mu\text{M}/\text{min}$; $\text{WO}_{2.58}\text{F}_{0.42}$ - $-0.09 \mu\text{M}/\text{min}$.

To understand the relationship between the tungsten oxyfluoride composition and its photocatalytic performance, the activity of SPS- and conventionally prepared samples was evaluated by the photocatalytic decomposition of the model substrate Rhodamin B (RhB) in aqueous solution under visible light (blue light LED, 18 W). The temporal evolution of UV-vis absorption spectra of RhB solution in the presence of $\text{WO}_{2.92}\text{F}_{0.08}$ and $\text{WO}_{2.58}\text{F}_{0.42}$ prepared by conventional solid state chemistry, (A, B) and $\text{WO}_{2.90}\text{F}_{0.10}$ and $\text{WO}_{2.40}\text{F}_{0.60}$ prepared by SPS (C, D) under blue light irradiation is displayed in Figures 2.7A-D and Figure 7.1.11, where the decrease of the absorption at 554 nm with exposure time is related to the concentration of RhB in solution. Figure 2.7 shows that only 10% of RhB are degraded by both, $\text{WO}_{2.92}\text{F}_{0.08}$ and $\text{WO}_{2.58}\text{F}_{0.42}$ (prepared conventionally), while 25% and 70% are degraded by $\text{WO}_{2.90}\text{F}_{0.10}$ and $\text{WO}_{2.40}\text{F}_{0.60}$ (prepared by SPS). The linear plots of (c_0/c) versus irradiation time (t) suggest a pseudo-first order kinetics. The rate constants are given in Figure 7.1.7. The photocatalytic activities of SPS-prepared $\text{WO}_{2.90}\text{F}_{0.10}$ and $\text{WO}_{2.40}\text{F}_{0.60}$ are much higher than those of samples prepared by conventional reactions. The activities of $\text{WO}_{2.92}\text{F}_{0.08}$ and $\text{WO}_{2.58}\text{F}_{0.42}$ (prepared

conventionally) and $\text{WO}_{2.90}\text{F}_{0.10}$ and $\text{WO}_{2.40}\text{F}_{0.60}$ (prepared by SPS) are dictated by the dye adsorption, the light absorption for electron–hole generation, and electron–hole separation. Therefore, we investigated the effect of RhB adsorption on $\text{WO}_{2.92}\text{F}_{0.08}$ / $\text{WO}_{2.90}\text{F}_{0.10}$ and $\text{WO}_{2.58}\text{F}_{0.42}$ / $\text{WO}_{2.40}\text{F}_{0.60}$. Aliquots of the respective oxyfluorides were added to 5 mL of RhB solution (0.2 mmol L^{-1}), and the solutions were stirred in the dark for 240 min to reach the adsorption–desorption equilibrium. The intensity of the RhB absorption band in the presence of $\text{WO}_{2.92}\text{F}_{0.08}$ / $\text{WO}_{2.90}\text{F}_{0.10}$ and $\text{WO}_{2.58}\text{F}_{0.42}$ / $\text{WO}_{2.40}\text{F}_{0.60}$ decreases with increasing adsorption time under dark condition (Figure 7.1.9). Figure 7.1.9 shows that $\sim 2\%$ (for $\text{WO}_{2.90}\text{F}_{0.10}$) and 10% (for $\text{WO}_{2.40}\text{F}_{0.60}$) of RhB were removed within 3 h in the dark, i.e. $\text{WO}_{2.90}\text{F}_{0.10}$ and $\text{WO}_{2.40}\text{F}_{0.60}$ have a low dye adsorption capacity. While the BET surface areas of the samples (approx. $10\text{--}12 \text{ m}^2\text{g}^{-1}$) are comparable, an increase in the fluorine content results in a much darker color and higher conductivity. The visible light absorption of $\text{WO}_{3-x}\text{F}_x$ may be associated with electronic transitions from (i) the valence band to (localized) polaron states, (ii) from polaron states to the conduction band or (iii) by electron hopping between W^{5+} and W^{6+} sites.^[52,53] The much higher photocatalytic activity of the SPS-prepared samples ($\text{WO}_{2.90}\text{F}_{0.10}$ and $\text{WO}_{2.40}\text{F}_{0.60}$) is attributed to the smaller domain size (Figure 7.1.5), the lower degree of ordering, the higher number of defect sites at the domain surfaces (Figure 2.8) and to the presence of F surface sites (lower adsorption due to the lower polarizability of F).

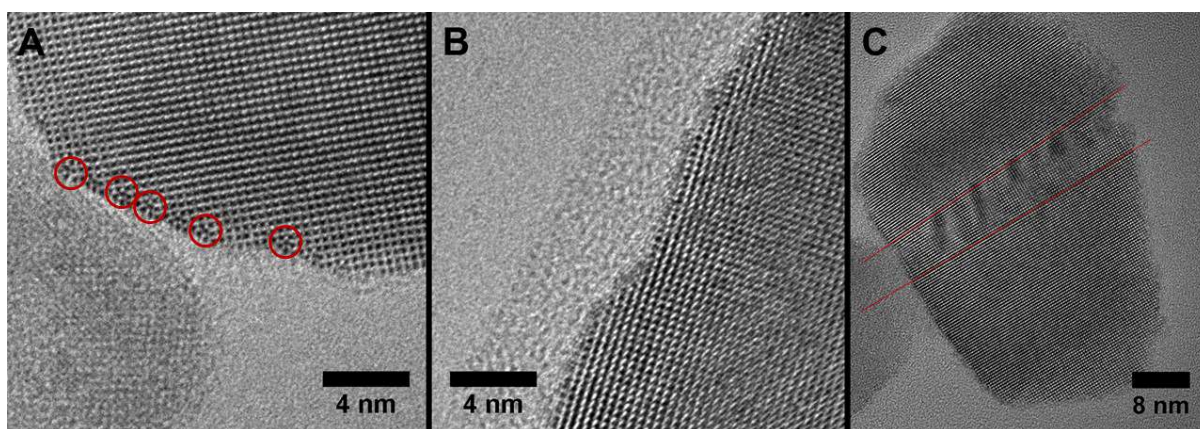


Figure 2.8. (A–C) TEM (HRTEM) images acquired with underfocus (black atom contrast) of a SPS-prepared (A) and conventionally prepared (B) samples of cubic $\text{WO}_{2.40}\text{F}_{0.60}$. The ReO_3 -type structure can easily be seen. The HRTEM images also show the lower ordering at the particle surface for the SPS-prepared sample in comparison with a conventional sample. (C) HRTEM image of an SPS-prepared particle with twin boundaries.

Chapter 2.4 Summary

We have shown that reactions using SPS allow the *high-speed* solid state fluorination of WO_3 using poly(tetrafluoroethylene) (PTFE) in large quantities. The degree of fluorination is very

high and comparable to that achieved with hydrofluoric acid under hydrothermal conditions in sealed gold ampoules. The reactions times could be reduced by more than 2 orders of magnitude from 2 days to a few minutes and do not require toxic and caustic chemicals. The structure and composition of the resulting tungsten oxyfluorides, $\text{WO}_{2.90}\text{F}_{0.10}$ and $\text{WO}_{2.40}\text{F}_{0.60}$, was determined by a combination of F^- -potentiometry, X-ray powder diffraction, automated electron diffraction tomography (ADT), ^{19}F MAS-NMR, XPS, HRTEM, and SEM/EDX. The rapid SPS transformations presumably involve F^- anion transport in the applied electric field. The fast SPS reaction leads to the formation of non-equilibrium micro- and surface structures with different levels of metastability. Thus, the SPS-derived oxyfluorides $\text{WO}_{3-x}\text{F}_x$ yield - different from the bulk phases obtained by conventional high-temperature reactions - monoliths of metal oxide fluoride nanoparticles with trap states associated with surface defects that lead to high photocatalytic activity. The high potential of this new synthetic SPS approach is that (i) mixed-valent tungsten oxide fluorides $\text{WO}_{3-x}\text{F}_x$ ($0 < x < 0.60$) are obtained within minutes, without toxic chemicals and in copious amounts and, (ii) the degree of fluorination is increased. (iii) Importantly, the chemical reactivity of the SPS-derived oxyfluorides $\text{WO}_{3-x}\text{F}_x$ differs significantly from that of products obtained by conventional solid state reaction. This study is a proof of concept for the development of cheap and functionally efficient materials from PTFE polymer. It even allows a reutilization of PTFE polymer scrap for the synthesis of valuable tungsten oxyfluorides through SPS processing.

Chapter 2.5 Experimental details

Synthesis. Tungsten trioxide (99+%, Chempur) and poly(tetrafluoroethylene) (PTFE, Sigma-Aldrich, 1 μm powder) were weighed in their respective molar ratios, ball-milled (Fritsch Pulverisette) for 5 h in ethanol and dried by centrifugation and drying overnight at 70°C in a drying chamber. The preparation is illustrated in Figure 2.1A (*vide supra*). WO_3 and PTFE were used in stoichiometric amounts as precursors for both conventional and SPS synthesis. SPS yielded dense pellets of products $\text{WO}_{3-x}\text{F}_x$ in a single step according to the representative reaction $4\text{WO}_3 + (\text{C}_2\text{F}_4)_n = 4\text{WO}_{3-n}\text{F}_n + 2n\text{CO}_2$.

For SPS preparation, samples containing ≈ 2.5 g of the powder mixtures were enclosed with graphite foil and placed in graphite dies. The dies were put subsequently into an SPS HP D 25 (FCT-systems) and heated up to 550°C with 50°C/min and kept at this temperature for 6 min ($p = 19$ MPa). To achieve a higher densification, an additional heating step at 700°C was added to the reaction process ($p = 50$ MPa). All samples were annealed for additional 3 h at 400°C in air

to remove remnants of carbon resulting from the decomposition of PTFE. Reference samples for conventional high temperature reactions were prepared by placing powder mixtures (≈ 500 mg) in evacuated quartz ampules and heating for 36 h at 550°C .^[22]

X-Ray Powder Diffraction Analysis. Samples for X-Ray diffraction were prepared on polyvinylacetate foil. Diffractograms were obtained using a STOE Stadi P powder diffractometer, equipped with a Mythen 1k detector using $\text{MoK}\alpha_1$ radiation. The sample was measured in transmission in 0.015° steps (continuous scan, 150 s°) covering a 2θ range from 1.5° to 73.4° . Rietveld refinement^[34] was performed with Topas Academic V6 using the fundamental parameters approach.^[35] The structures of the crystalline phases were determined by ADT.

High-resolution synchrotron powder diffraction data were collected at beamline 11-BM at the Advanced Photon Source (APS), Argonne National Laboratory using a wavelength of $\lambda = 0.41385$ nm. Data were fit using TOPAS Academic V6 program suite, using the fundamental parameter approach.^[35]

Scanning Electron Microscopy (SEM). Field-emission scanning electron microscopy was performed on a NOVA Nano-SEM with an attached Oxford Inca X-ray system for chemical analysis. The obtained SPS pellets were cut and polished to obtain cross-sectional pieces. Secondary and backscattered electron images were collected with acceleration voltages of 5 keV and 15 or 20 keV for EDX mapping, respectively.

X-ray photoelectron spectroscopy (XPS). Measurements were carried out using a PHI5000 Versa Probe II with an Al anode. The probed surface area was $100 \mu\text{m} \times 1400 \mu\text{m}$ (i.e., X-ray spot size), and an X-ray power of 100 W was used. The pass energy of the analyzer was set to 23.5 eV for detailed spectra and to 187.9 eV for survey scans. All spectra were charge corrected to a binding energy of 284.8 eV for the C 1s line corresponding to adventitious aliphatic carbon. Measurements were evaluated using the CasaXPS software.

Transmission Electron Microscopy (TEM). Powdered samples were prepared by placing one drop ($10 \mu\text{L}$) of a diluted NP solution in ethanol (0.1 mg mL^{-1}) on a carbon-coated copper grid and by letting it dry at room temperature for transmission electron microscopy (TEM), High-resolution TEM (HRTEM), electron dispersive X-ray spectroscopy (EDXS) and automated electron diffraction tomography (ADT) investigations. TEM, HRTEM, EDX and ADT measurements were carried out with a FEI TECNAI F30 S-TWIN transmission electron microscope equipped with a field emission gun and working at 300 kV. TEM images and nano electron diffraction (NED) patterns were taken with a CCD camera (16-bit 4.096×4.096 pixel

GATAN ULTRASCAN4000) and acquired by Gatan Digital Micrograph software. Scanning transmission electron microscopy (STEM) images were collected by a FISCHIONE high-angular annular dark field (HAADF) detector and acquired by Emispec ES Vision software.

Automated Electron Diffraction Tomography (ADT). Three-dimensional electron diffraction data were collected using an automated acquisition module developed for FEI microscopes.^[54] For high tilt experiments all acquisitions were performed with a FISCHIONE tomography holder. A condenser aperture of 10 μm and mild illumination settings (gun lens 8, spot size 6) were used in order to produce a semi-parallel beam of 200 nm in diameter on the sample (115 $\text{e}^-/\text{nm}^2\text{s}$). Crystal position tracking was performed in microprobe STEM mode and NED patterns were acquired sequentially in steps of 1.0° . Tilt series were collected within a total tilt range up to 120° resp. 90° , occasionally limited by overlapping of surrounding crystals or grid edges. ADT data were collected with electron beam precession (precession electron diffraction, PED).^[55] PED was used in order to improve reflection intensity integration quality.^[56] PED was performed using a Digistar unit developed by NanoMEGAS SPRL. The precession angle was kept at 1.0° . The eADT software package was used for three-dimensional electron diffraction data processing.^[57] *Ab initio* structure solution was performed assuming the kinematic approximation $I \approx |F_{\text{hkl}}|^2$. Scattering factors for electrons were taken from Doyle and Turner.^[58] The data were processed using the software packages PETS^[59] and JANA2006^[60] for dynamical refinement.^[36] The relevant information on the crystal structure determination by ADT is compiled in Table 2.1.

Brunauer/Emmett/Teller (BET) sorption. BET measurements were conducted using the gas adsorption setup Autosorb-6B from Quantachrome with nitrogen as analysis gas. The temperature during the measurements was 77 K. Data evaluations were conducted with the software Quantachrome ASiQWin 3.0.

UV–Vis Spectroscopy. Ultraviolet–visible (UV–vis) reflectance spectra ranging from 200 to 800 nm were collected on a Cary 5G UV–vis–NIR spectrophotometer using an Ulbricht sphere. BaSO_4 was used as white standard. The samples were measured by mixing a few mg of powder with BaSO_4 and pressing the mixture into a pellet.

Nuclear Magnetic Resonance (NMR) Spectroscopy. *Solid state NMR spectroscopy.* All solid-state NMR experiments were recorded on a Bruker Avance 400 DSX spectrometer at ^{19}F frequency of 376.25 MHz. A two-channel commercial Bruker 2.5 mm probe head at spinning speeds of 25 kHz was used for the ^{19}F direct excitation measurements. No changes in the spectra

are expected at slightly elevated temperatures, so no temperature correction for the frictional heating due to the sample rotation has been performed. All spectra are background corrected.

Fluorine-ion selective electrode measurements. F⁻-ion selective potentiometric measurements were carried out using an F⁻-ion-selective electrode and a Titrando 907, both from Metrom. 15-30 mg of the sample powders were dissolved in 25 mL 1.2 M NaOH solution and then neutralized with 1.2 M HCl solution. The solution then was transferred into 100 mL volumetric flasks and filled with TISAB IV (Bernd Kraft) solution. 40 mL of each mixture were used to determine the fluorine content by comparison of the measured potential with an external standard calibration. Standard solutions with the concentrations 0.2 mmol/L, 0.40 mmol/L, 1.0 mmol/L and 2.50 mmol/L were obtained by diluting a 0.1 mol/L NaF standard solution. The standard was prepared by dissolving 95 mg NaF (99,0% pa, Fluka) in 50 mL of deionized water.

Photocatalytic Activity of WO_{3-x}F_x. WO_{3-x}F_x particles (SPS- and conventionally prepared) were suspended in distilled water (1 mg/mL), and their photocatalytic activity was explored against the model substance Rhodamine B (RhB). Freshly prepared aqueous dispersions of WO_{3-x}F_x nanoparticles (1 mg/mL) were mixed with the model compound RhB (0.1 mg/mL) and irradiated using 6 light-emitting diodes from Osram OSOLON[®] SSL 80 with peak emission at 451 nm (deep blue) driven by constant current 350 mA in series connection.. The experiments were carried at room temperature as follows: The mixture was exposed for 4 h to the LEDs after equilibration time of 30 min. A 400 µL aliquot was taken every 30 min, centrifuged and 60 µL of the clear solution were diluted with 940 µL distilled water. The UV-Vis spectrum was recorded using a Cary 5G UV-Vis-NIR spectrophotometer (Varian Inc., Palo Alto, CA, USA). As control, a solution of RhB (0.1 mg/mL) and WO_{3-x}F_x nanoparticles (1 mg/mL) was treated in the dark under otherwise identical experimental conditions. The calculations (C/C₀) were performed considering a wavelength value of 554 nm - the maximum of the RhB UV-Vis spectral band.”

References

- [1] D. M. P. Mingos, D. R. Baghurst, *Chem. Soc. Rev.* 1991, 20, 1-47
- [2] H. J. Kitchen, S. R. Vallance, J. L. Kennedy, N. Tapia-Ruiz, L. Carassiti, A. Harrison, A. G. Whittaker, T. D. Drysdale, S. W. Kingman, D. H. Gregory, *Chem. Rev.* **2014**, 114, 1170–1206
- [3] O. Guillon, C. Elsässer, O. Gutfleisch, J. Janek, S. Korte-Kerzel, D. Raabe, C. A. Volkert, *Mater. Today* 2018, 21, 527- 536.

- [4] O. Guillon, J. Gonzales-Julian, B. Dargartz, T. Kessel, G. Schierning, J. Räthel, M. Herrmann, C. Sässer, O. Gutfleisch, J. Janek, S. Korte-Kerzel, D. Raabe, C. A. Volkert, *Adv. Eng. Mater.* **2014**, *16*, 830-849.
- [5] R. Orru, R. Licheri, A. M. Locci, A. Cincotti, G. Cao, *Mater. Sci. Eng. R* **2009**, *63*, 127-287.
- [6] Z. A. Munir, U. Anselmi-Tamburini, M. Ohyanagi, *J. Mater. Sci.* **2006**, *41*, 763-777.
- [7] H. Yoshida, K. Morita, K. Soga, *J. Ceram. Soc. Jpn.* **2016**, *124*, 932-937.
- [8] M. Joos, G. Cerretti, I. Veremchuk, P. Hofmann, H. Frerichs, D. H. Anjum, T. Reich, I. Lieberwirth, M. Panthöfer, W. G. Zeier, W. Tremel, *Inorg. Chem.* **2018**, *57*, 1257-1268.
- [9] J. R. Friedman, J. E. Garay, U. Anselmi-Tamburini, Z. A. Munir, *Intermetallics* **2004**, *12*, 589-597.
- [10] W. Chen, U. Anselmi-Tamburini, J. E. Garay, J. R. Groza, Z. A. Munir, *Mater. Sci. Eng. A* **2005**, *394*, 132-138.
- [11] C. Recknagel, N. Reinfried, P. Höhn, W. Schnelle, H. Rosner, Y. Grin, A. Leithe-Jasper, *Sci. Techn. Adv. Mat.* **2007**, *8*, 357-363.
- [12] M. Beekman, M. Baitinger, H. Borrmann, W. Schnelle, K. Meier, G. S. Nolas, Y. Grin, *J. Am. Chem. Soc.* **2009**, *131*, 9642-9643.
- [13] D. Portehault, V. Maneeratana, C. Candolfi, N. Oeschler, I. Veremchuk, Y. Grin, C. Sanchez, M. Antonietti, *ACS Nano* **2011**, *5*, 9052-9061.
- [14] P. R. Slater, J. P. Hodges, M. G. Francesconi, P. P. Edwards, C. Greaves, I. Gameson, M. Slaski, *Physica C* **1995**, *253*, 16-22.
- [15] S. Rüdiger, E. Kemnitz, *Dalton Trans.* **2008**, 1117-1127.
- [16] Functionalized inorganic fluorides: synthesis, characterization and properties of nanostructured solids (Tressaud, A., ed.), John Wiley & Sons, Ltd, 2010.
- [17] W. Sleight, *Inorg. Chem.* **1969**, *8*, 1764-1767.
- [18] Y. Kamihara, T. Watanabe, M. Hirano, H. Hosono, *J. Am. Chem. Soc.* **2008**, *130*, 3296-3297.
- [19] P. R. Slater, *J. Fluorine Chem.* **2002**, *117*, 43-45.
- [20] F. J. Berry, X. Ren, R. Heap, P. R. Slater, M. F. Thomas, *Solid State Commun.* **2005**, *134*, 621-624.
- [21] Y. Kobayashi, M. Tian, M. Eguchi, T. E. Mallouk, *J. Am. Chem. Soc.* **2009**, *131*, 9849-9855.
- [22] D. Hirai, E. Climent-Pascual, R. J. Cava, *Phys. Rev. B* **2011**, *84*, 17451.

- [23] S. E. Dutton, D. Hirai, R. J. Cava, *Mat. Res. Bull.*, **2012**, *47*, 714-718.
- [24] D. Hirai, O. Sawai, T. Nunoura, Z. Hiroi, *J. Fluorine Chem.*, **2018**, *209*, 43-48.
- [25] D. Spetter, M. N. Tahir, J. Hilgert, I. Khan, A. Qurashi, H. Lu, T. Weidner, W. Tremel, *ACS Sustainable Chem. Eng.* **2018**, *6*, 12641–12649.
- [26] L.-S. Du, F. Wang, C. P. Grey, *J. Solid State Chem.* **1998**, *140*, 285-294.
- [27] J. Dabachi, M. Body, C. Galven, F. Boucher, C. Legein, *Inorg. Chem.* **2017**, *56*, 5219–5232.
- [28] C. B. Mo, S. I. Cha, K. T. Kim, K. H. Lee, S. H. Hong, *Mater. Sci. Eng. A* **2005**, *395*, 124–128.
- [29] M. N. Tahir, B. Oschmann, D. Buchholz, X. Dou, I. Lieberwirth, M. Panthöfer, W. Tremel, R. Zentel, S. Passerini, *Adv. Energ. Mater.* **2016**, *6*, 150148928
- [30] H. Zhang, Y. Li, Y. Wang, P. Liu, H. Yang, X. Yao, T. An, B. J. Wood, H. Zhao, *J. Mater. Chem. A* **2013**, *1*, 6563-6571.
- [31] S. L. Madorsky, S. Straus, D. Thompson, L. Williams, *J. Polym. Sci.* **1949**, *4*, 639-664.
- [32] B. B. Baker, D. J. Kasprzak, *Polym. Degrad. Stabil.* **1993**, *42*, 181-188.
- [33] E. E. Lewis. M. A. Taylor, *J. Am. Chem. Soc.* **1947**, *69*, 1968-1970.
- [34] H. M. Rietveld, *J. Appl. Crystallogr.* **1969**, *2*, 65–71.
- [35] J. J. Coelho, *J. Appl. Crystallogr.* **2018**, *51*, 210–218.
- [36] I. Vegard, *Z. Phys.*, **1921**, *5*, 17-26.
- [37] L. Palatinus, D. Jacob, P. Cuvillier, M. Klementová, W. Sinkler, L. D. Marks, *Acta Crystallogr. Sect. A Found Crystallogr.* **2013**, *69*, 171–188.
- [38] L. Palatinus, V. Petricek, C. A. Correa, *Acta Crystallogr., Sect. A: Found. Crystallogr.* **2015**, *71*, 235-7244.
- [39] L. Palatinus, G. Chapuis, *J. Applied Crystallogr.* **2007**, *40*, 786–790.
- [40] R. A. Wheeler, M. H. Whangbo, T. Hughbanks, R. Hoffmann, J. K. Burdett, T. A. Albright, *J. Am. Chem. Soc.*, **1986**, *108*, 2222-2236.
- [41] A. M. Glazer, *Acta Crystallogr., Sect. B: Struct. Sci.* **1972**, *28*, 3384-3392.
- [42] A. M. Glazer, *Acta Crystallogr., Sect. A: Found. Crystallogr.* **1997**, *31*, 756-762.
- [43] P. M. Woodward, *Acta Cryst. B Struct. Sci.*, **1997**, *53*, 44-66.
- [44] P. M. Woodward, *Acta Cryst. B Struct. Sci.* **1997**, *53*, 44-66.
- [45] D. I. Woodward, I. M. Reaney, *Acta Cryst. B Struct. Sci.* **2005**, *61*, 387–399.
- [46] R. H. Mitchell, M. D. Welche, A. R. Chakhmouradian, *Mineral. Mag.* **2017**, *8*, 411–461.

- [47] M. Biswal, M. Body, C. Legein, A. Sadoc, F. Boucher, *J. Solid State Chem.* **2013**, *207*, 208–217.
- [48] L. Pauling, The Nature of the Chemical Bond. IV. *J. Am. Chem. Soc.*, **1932**, *54*, 3570–3582.
- [49] M. Rahm, T. Zeng, R. Hoffmann, *J. Am. Chem. Soc.*, **2019**, *141*, 342–351.
- [50] A. Yella, M. N. Tahir, S. Meuer, R. Zentel, R. Berger, M. Panthöfer, W. Tremel, *J. Am. Chem. Soc.* **2009**, *131*, 17566–17575.
- [51] G. Kortüm, *Reflectance Spectroscopy*, Springer 1969.
- [52] J. A. Duffy, *Bonding, Energy Levels and Bands in Inorganic Solids*, Longman, 1990.
- [53] G. Kieslich, G. Cerretti, I. Veremchuk, R. P. Hermann, M. Panthöfer, J. Grin, W. Tremel, *Phys. Stat. Solidi A* **2016**, *213*, 808–823.
- [54] E. Mugnaioli, T. Gorelik, U. Kolb, U. *Ultramicroscopy* **2009**, *109*, 758–765.
- [55] U. Kolb, T. Gorelik, C. Kübel, M. T. Otten, D. Hubert, *Ultramicroscopy* **2007**, *107*, 507–513.
- [56] R. Vincent, P. A. Midgley, *Ultramicroscopy* **1994**, *53*, 271–282.
- [57] U. Kolb, E. Mugnaioli, T. E. Gorelik, *Cryst. Res. Technol* **2011**, *46*, 542–554
- [58] P. A. Doyle, P. S. Turner, *Acta Crystallogr. Sect. A* **1968**, *24*, 390–397.
- [59] L. Palatinus, *PETS-Program for Analysis of Electron Diffraction Data*; Institute of Physics, Prague, 2011.
- [60] V. Petříček, M. Dušek, L. Palatinus, *Z. Kristallogr.* **2014**, *229*, 345–352.

The contents of the following chapter are taken and partially adapted from *Adv. Funct. Mater.* **2021**, *accepted to be published*.

Authorship contributions

Category 1

Conception and design of study:

[REDACTED]

Acquisition of data:

[REDACTED] preparation of samples.
[REDACTED] – PXRD measurements.
[REDACTED] – acquisition of neutron diffraction data.
[REDACTED] – HR-CS-GFMAS measurements.

[REDACTED] HR-TEM and SEM images.
[REDACTED] – measurement of ^{19}F solid-state NMR.
[REDACTED] acquisition of UV/Vis-data.
[REDACTED] – acquisition of oxygen evolution data.
[REDACTED] – acquisition of XPS data.
[REDACTED] – acquisition of pH-dependent ζ -potential data.

Analysis and/or interpretation of data:

[REDACTED] – PXRD refinement.
[REDACTED] – PDF analysis and interpretation (neutron diffraction).
[REDACTED] – HR-TEM and SEM analysis.
[REDACTED] – analysis of ^{19}F solid-state NMR.
[REDACTED] – interpretation of oxygen evolution data.
[REDACTED] – interpretation of HR-CS-GFMAS, ζ -potential data and XPS data.

Category 2

Drafting the manuscript:



Revising the manuscript critically for important intellectual content:



Category 3

Approval of the version of the manuscript to be published:



Figure 3.1: prepared by

Figure 3.2: prepared by

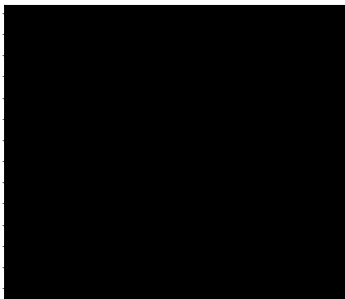
Figure 3.3: prepared by

Figure 3.4: prepared by

Figure 3.5: prepared by

Figure 3.6: prepared by

Figure 3.7: prepared by



**Chapter 3 | A Generalized Method for
High-Speed Fluorination of
Metal Oxides by Spark
Plasma Sintering Yields
 $\text{Ta}_3\text{O}_7\text{F}$ and TaO_2F with High
Photocatalytic Activity for
Oxygen Evolution from
Water**

Chapter 3.1 Motivation

“The search for clean, low-cost, and renewable energy sources is one important challenge of modern industrial societies.^[1] Hydrogen generated by photochemistry has been identified as a promising energy carrier with high energy density and zero CO₂ emission while being environmentally clean.^[2,3] To set up a light-driven and hydrogen based economy an exploration of new materials for eco-friendly, economically viable, stable, and efficient photocatalysts is needed.^[4] Noble metals like platinum, iridium, and ruthenium are efficient catalysts for the electrolysis of water, but their scarcity and high-costs limit large-scale technological use.^[5] The development of cheap and active catalysts with long-term stability for the hydrogen or oxygen evolution reaction (HER, OER) in standard electrolytes is an important goal.

Among the established and efficient photocatalysts for water splitting (hydrogen evolution (HER) and oxygen evolution (OER) systems) are TiO₂ and metal-TiO₂ heterostructures,^[6,7] α -Fe₂O₃,^[8,9] CoO,^[10] BiVO₄,^[11] layered niobates,^[12] perovskites,^[3] layered metal chalcogenides,^[13] metal nitrides^[14] and oxynitrides.^[15,16] Recently, metal-free polymeric carbon nitride photocatalysts (e.g. g-C₃N₄)^[17] became accessible.

While HER photocatalysts containing precious metals (Pd, Pt) or earth abundant 3d transition metal oxides (e.g. TiO₂,^[6,7] Fe₂O₃,^[8,9] CoO,^[10] spinels^[18] or nitrides^[14,17] and oxynitrides of the group 5 metals^[19,20] have been in the scientific focus since many years, oxyfluorides of the 4d or 5d transition metals^[21-28] received less attention, although they show good stability against photo- or chemical corrosion, are non-toxic, and have suitable band gaps.^[29,30] It has been proposed that the proton acidity in the oxide/hydroxide semiconductors Nb₃O₇(OH)^[31] can promote the adsorption of water, CO₂, or organic molecules.^[32] Nb₃O₇(OH)^[31] or Nb₃O₇F^[29,30] have been reported as photocatalysts for dye degradation and dye-sensitized solar cells, but the photocatalytic properties of Nb₃O₇(OH)^[32] and the related niobium or tantalum oxyfluorides towards water splitting reactions are still unexplored.^[29,30]

The use of oxyfluorides like Nb₃O₇F^[21-28] or TaO₂F^[22,24,26,28,33] for photocatalysis is hampered by synthetic and processing difficulties.^[34] Their chemical synthesis requires fluorine gas, reactive fluorides, or hydrogen fluoride as toxic and corrosive sources of fluorine that make special equipment and techniques for handling indispensable.^[26,33,35] The standard route to NbO₂F is based on the reaction of Nb₂O₅ with concentrated HF solution in water.^[26] Evaporation to dryness and heating at elevated temperatures leads to the formation of NbO₂F.^[21,26] The product composition depends on the sample history, and HF adduct

intermediates and mixed hydroxylated/fluorinated products $\text{Nb}_{1-x}\text{O}_{2-5x}(\text{OH},\text{F})_{1+5x}$ with OH defects and metal vacancies are formed.^[26] Efficient fluorination can be performed with HF only under extreme conditions in sealed gold ampoules.^[36] High-temperature reactions using binary fluorides as fluorinating agents have limitations due to the high stability of the starting compounds.^[35,36]

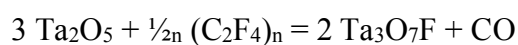
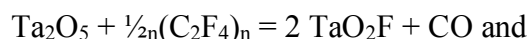
To address these weaknesses, alternative fluorination pathways^[37] to oxyfluorides have been pursued. We devised a new approach for the bulk synthesis of tantalum oxyfluorides from tantalum oxide and fluoropolymers (e.g. polytetrafluoroethylene (PTFE)) under mild conditions contrasting dramatically with conventional chemical approaches. Using Teflon scrap not meeting specifications during polymer processing as feedstock for fluorination is an elegant way of polymer waste disposal. The oxyfluorides $\text{Ta}_3\text{O}_7\text{F}$ and TaO_2F were prepared by spark plasma sintering (SPS),^[38,39] an energy efficient method enabling the densification of large samples by low electric current levels. SPS is typically used for fast industrial high-temperature processing ($> 1000^\circ\text{C}$) of ceramics and alloys.^[38,39] It is based on a modified hot-pressing process, where pulsed electric currents are passed directly through the pressing mould and the sample.^[38,39] This allows for rapid short heating and cooling, metastable products and also for short process cycles. The energy efficiency and processing speed make SPS meaningful for materials manufacturing in industry (responsible for $\sim 7\%$ of the primary energy and greenhouse gases in Germany) from an economic and environmental point of view.^[38]

Although SPS has opened up new options for sintering materials, applications in solid state synthesis are rare.^[40] Engineering nanoscale interfaces is a requisite for harnessing electrical transport within nanostructured materials, especially for photocatalytic applications. Reactions in electric fields affect the reaction kinetics by suppressing granular growth which alters the nature of the final product.^[38,39] The primary effect of current in sintering techniques is Joule heating, but other non-thermal effects may contribute to the solid state reaction kinetics as well. Therefore, SPS allows making metastable materials that cannot be obtained by conventional chemistry.^[41,42] Our approach relies on the chemical stability of fluorinated polymers at room temperature and their relatively low decomposition temperature compared to inorganic solids.^[43,44] $\text{Ta}_3\text{O}_7\text{F}$ and TaO_2F were synthesized in a “trash to treasure” approach by reacting Ta_2O_5 with PTFE under SPS conditions. The reactions were complete after a few minutes and led to the formation of $\text{Ta}_3\text{O}_7\text{F}$ and TaO_2F polycrystals with high photocatalytic activity, whereas the activity of the corresponding bulk phases (obtained after days by conventional solid state reactions) was low. The conceptual advance of this study is the evidence that the

microstructure and the metastability of the SPS reactions products affect - and strongly enhance - the materials properties. The practical advance of this new bottom-up approach lies in the combination of the versatility and scalability of SPS preparation for environmentally benign fluorination, the use of PTFE polymer scrap for waste removal and the fast and energy efficient synthesis of valuable photocatalysts.

Chapter 3.2 SPS reaction and chemical analysis.

Ta₃O₇F and TaO₂F were prepared as single-phase reaction products (Figure 3.1A, B) by SPS from Ta₂O₅ and PTFE according to



CO gas is released from the SPS press without carbothermal reduction below 750°C. In the first step, the starting materials PTFE and Ta₂O₅ were mixed in a planetary ball mill using ethanol as dispersion medium for 6 h prior to the reaction. In the subsequent, pyrometer-controlled step the reactants were heated using the temperature profile shown in Figure 3.1C. The products typically contained phase mixtures with densities of ~90% of the calculated theoretical density. Phase pure TaO₂F was obtained at 600°C. Ta₃O₇F could be synthesized with ~90% purity (side phase TaO₂F) at 600°C. SPS synthesis requires a small excess of fluorine for Ta₃O₇F (0.36 or 10% excess, calculated by fluorine in PTFE to tantalum in Ta₂O₅) and a large excess for TaO₂F (≥1.5 or 50% excess). For SPS reactions at temperatures ≥ 650°C Ta₃O₇F contained less TaO₂F contaminants, but still unreacted Ta₂O₅ (due to thermal loss of gaseous (C₂F₄)_n). Therefore, a relatively low pressure (19 MPa) was used for the synthesis, as high pressures lead to losses of PTFE decomposition products. For temperatures above 700°C subsequently less tantalum oxyfluoride was formed, likely due to thermal loss of gaseous (C₂F₄)_n before the reaction (SPS pressing tools are not closed and the reaction uses dynamic vacuum conditions) and slow thermal decomposition of oxyfluoride product. A table summarizing the phase distribution as a function of the SPS conditions is supplied in the supplementary information (Table 7.2.1). Single phase Ta₃O₇F could be prepared by conventional ampoule synthesis.

The reaction is assumed to proceed when PTFE undergoes thermolysis above 360°C.^[44] Thermal analysis showed the thermolysis to be complete above 400°. The C₂F₄ monomer is the main decomposition product at 400°C under vacuum conditions.^[44] The complete decomposition of PTFE was confirmed by the absence of PTFE signals in 19-F magic-angle-spinning solid state nuclear magnetic resonance spectroscopy experiments (19-F MAS-NMR).

Thus, excess PTFE is either completely carbonized or removed in form of volatile decomposition products from the product.

The reaction of Ta₂O₅ with polytetrafluoroethylene (PTFE) is likely to occur at the gas-solid interface. Under SPS conditions, monomeric C₂F₄ resulting from the thermal decomposition of PTFE in the carbon die diffuses into the Ta₂O₅ pellet. The fluorination mechanism cannot be analyzed in detail because (i) the state of C₂F₄ under the reaction conditions (19 MPa, 600°C) is unknown, and (ii) follow-up reactions of monomeric C₂F₄ may form carbon or fluorocarbons depending on the reaction temperature and pressure.

Chapter 3.2.1 Phase composition

Phase analysis of the samples was carried by X-ray powder diffraction and transmission electron microscopy. The experimental F/Ta ratios are 2:1 (for TaO₂F) and 1:2.5 (for Ta₃O₇F). The maximum fluorine content for TaO₂F is comparable to that obtained in conventional reactions at 650°C in quartz ampoules starting from Ta₂O₅ and PTFE (ratio 1.5:1 for TaO₂F and 1:3 for Ta₃O₇F).^[24,25,27,28] However, fluorination in SPS reactions are much faster (9 minutes compared to 12 h for TaO₂F and 36 h for Ta₃O₇F). The yields by SPS were 2 g after ~ 9 min (compared to 0.2 g of TaO₂F after 12 h and 0.8 g of Ta₃O₇F after ~ 36 h by conventional high temperature chemistry). The yields by SPS can easily be upscaled to the kg range with appropriate dies.^[38]

After cooling/quenching to room temperature, the cylindrical pellets were removed from the die and treated with SiC abrasive paper to clean the surface. The pellets were ground in a mortar, and the resulting powders were used for electron microscopy and physical characterization. Elemental analysis supports the SPS synthesis of Ta₃O₇F and TaO₂F. The total fluorine content in selected products was determined with a **high resolution-continuum source-graphite furnace molecular absorption spectrometer (HR-CS-GFMAS)**.

The X-ray diffraction (XRD) patterns of TaO₂F (ReO₃ structure type)^[22,26,33] and Ta₃O₇F (U₃O₈ structure type)^[21,23] (Figure 3.2A, B and Figure 7.2.1) could be indexed based on cubic (space group: *Pm* $\bar{3}$ *m*) and orthorhombic (space group: *Cmmm*) unit cells, respectively. Crystallographic details and essential results of the Rietveld refinements for Ta₃O₇F and TaO₂F are compiled in Table 7.2.2. The powder diffractograms of the SPS-prepared samples show strong anisotropic peak broadening (in comparison to those prepared by conventional chemistry). To achieve satisfactory Rietveld refinements strain parameters based on the Stephens broadening model^[45] were applied.

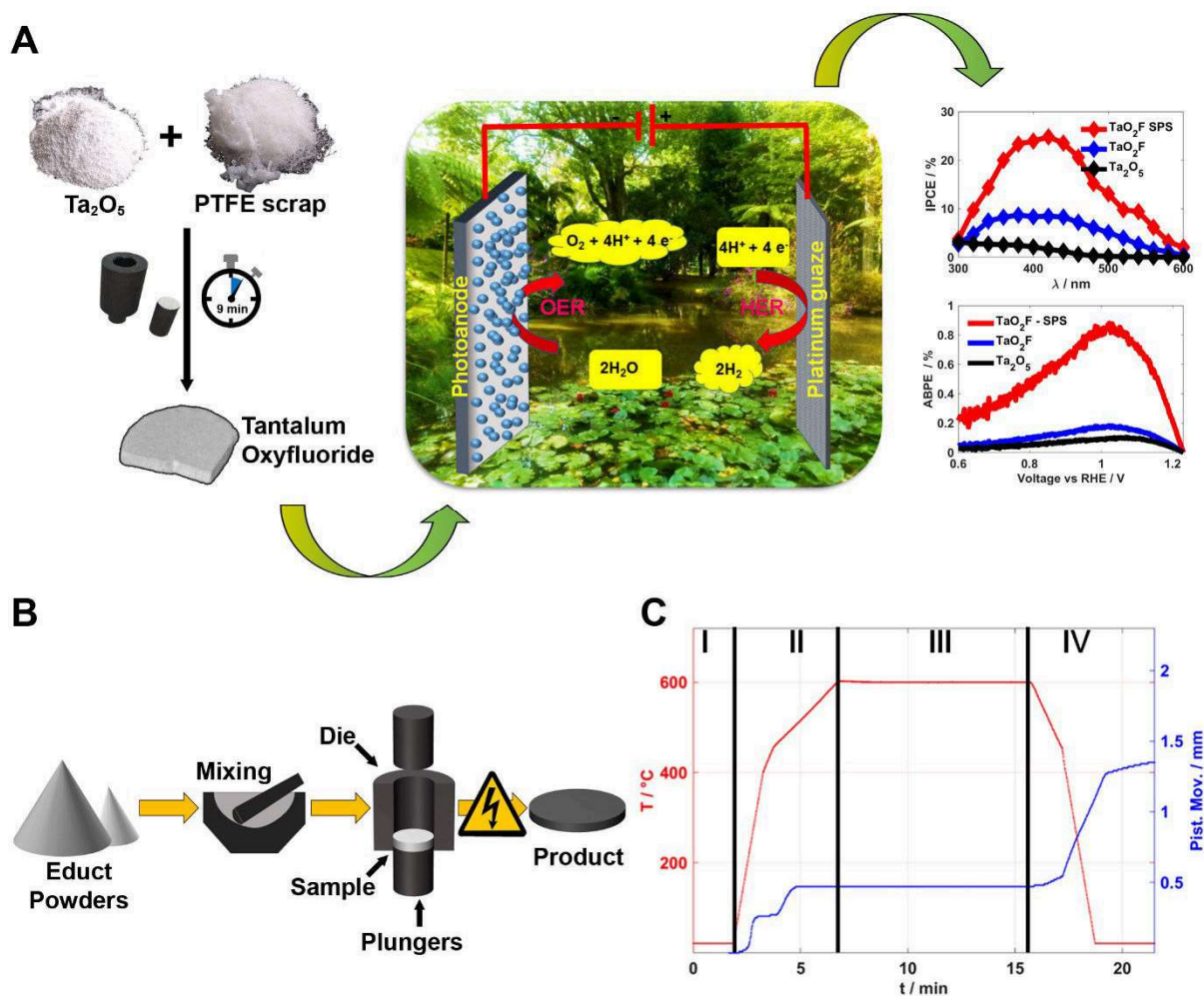


Figure 3.1. (A) General approach to convert Ta₂O₅ and Teflon scrap to tantalum oxyfluoride by SPS in minute intervals and enhanced photocatalytic properties compared to conventionally prepared tantalum oxyfluoride and a Ta₂O₅ reference, indicated by wavelength-dependent incident photon-to-current efficiency (IPCE, upper plot top right) and applied bias to photo-conversion (ABPE, lower plot top right). (B) Illustration of the SPS synthesis. Precursor materials are mixed by ball milling, placed in a graphite pressing tool (die and plungers) before transfer into an SPS press. (C) Temperature profile (red) and piston movement (blue) during the SPS process. Capital letters indicate different segments for the synthesis: I Evacuation of reaction chamber and first compression, II start of reaction by heating to 600°C with 50°C/min, III dwelling at 600°C for 9 min and IV sample cooling.

The samples obtained from both, SPS and conventional reactions are phase pure (with minor contamination of TaO₂F for Ta₃O₇F and *vice versa*). SPS synthesis prevents the formation of mixed hydroxylated/fluorinated products such as Nb₃O₇(OH) completely.^[31,32] It is difficult to determine the positions of oxygen and fluorine accurately from XRD data because the scattering contributions of the O and F atoms are almost indistinguishable. Therefore, the analytical F content was determined by HR-CS-GFMAS. This highly specific fluorine analysis is based on the molecular absorption after *in situ* formation of a diatomic molecule (e.g. “CaF” in the gas

phase) in a graphite furnace. Direct fluorine analysis was carried out with a slurry technique.^[48] Table 3.1 compares the expected fluorine to tantalum ratio (determined by the molecular formula and the phase composition derived from the Rietveld refinements) and by the S experimentally determined fluorine and tantalum concentrations (from HR-CS-GFMA) together with the fluorine to tantalum ratio. The expected fluorine content for both SPS prepared samples ($\mu\text{g kg}^{-1}$) is higher than the experimentally determined one. While the discrepancy for TaO_2F lies within the experimental error, the deviation for $\text{Ta}_3\text{O}_7\text{F}$ is higher. Possible reasons for this discrepancy could be incomplete sample digestion or the presence of vacancies (as shown by MAS NMR) or the presence of $-\text{OH}$ instead of fluorine in the structure. pH-dependent Zeta potential measurements show the presence of $-\text{OH}$ groups (Table 7.2.3), as confirmed by XPS spectroscopy (Figure 3.5).

Table 3.1. Experimental and theoretical fluorine concentration and degree of fluorination determined by HR-CS-GFMAS.

SPS Sample	Fluorine concentration via HR-CS-GFMAS ($\text{g kg}^{-1} \pm \text{sd}$)	Tantalum concentration via HR-CS-GFMAS (g kg^{-1})	Determined F:Ta ratio (expected values)
$\text{Ta}_3\text{O}_7\text{F}$ (87%) + TaO_2F (13%)	$28.4 \pm 3.2^*$	788 ± 14	$0.34 \pm 0.04:1$ (0.41:1)
TaO_2F (95%)	$69.5 \pm 4.8^*$	747 ± 29	$0.89 \pm 0.08:1$ (0.97:1)

*n = 4

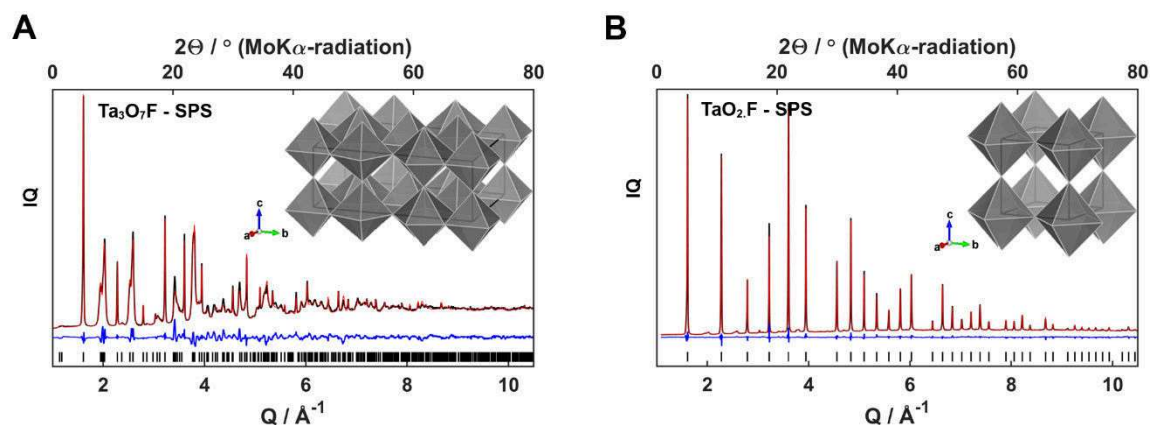


Figure 3.2. Structural characterization of SPS-prepared $\text{Ta}_3\text{O}_7\text{F}$ and TaO_2F by powder X-ray diffraction. (A) Rietveld refinement of SPS-prepared $\text{Ta}_3\text{O}_7\text{F}$ (red line) using X-ray powder data (88 % $\text{Ta}_3\text{O}_7\text{F}$, 12 % TaO_2F). (B) Rietveld refinement of SPS-prepared TaO_2F (red line) using X-ray powder data. Experimental data: crosses, calculated curve after refinement: continuous line. The tick marks correspond to the Bragg reflections of the cubic and orthorhombic structures. The continuous blue curve under the tick marks represents the difference between the experimental data and the calculated curve. The insets show a polyhedral representation of the crystal structures.

Chapter 3.2.2 Micro- and local structure of Ta₃O₇F and TaO₂F

(HR)TEM analysis confirmed Ta₃O₇F and TaO₂F (obtained by SPS at 600°C) to consist of crystallites in the size range of 10 to 50 nm, agglomerated and melted together to larger polycrystalline particles in a broad size range between ten and several hundreds of nm (Figure 3.3A, B). Samples obtained by conventional high temperature chemistry at 600°C (Figure 3.3C, D) were polycrystalline with larger particle sizes > 100 nm and with larger crystalline areas, rarely below 50 nm. N₂ sorption isotherms of SPS-prepared materials showed Brunauer-Emmett-Teller (BET) specific surface areas of 10.28 m² g⁻¹ (Ta₃O₇F) and 14.20 m² g⁻¹ (TaO₂F). In contrast, materials produced by conventional ampoule reactions exhibited smaller BET surface areas of 6.18 m² g⁻¹ (Ta₃O₇F) and 6.82 m² g⁻¹ (TaO₂F) which confirms the presence of more small particles (< 50 nm) and generally smaller polycrystallites for SPS-prepared samples. Particles prepared by SPS had rougher surfaces, while their conventional counterparts had sharp edges. The difference in particle size and BET surface is attributed to the much shorter reaction time (few minutes), a known consequence of SPS processing.^[38,39] Line defects and stepped surfaces with layer-like appearance were present for all samples (Figure 3.3 and Figure 7.2.2), but the SPS samples showed more and more irregular steps, smaller crystallites and more grain boundaries than their conventional counterparts, as confirmed by SEM (Figure 7.2.3). The surface area of SPS samples is approximately two times larger and the number of grain boundaries much higher.

The local structure of SPS-prepared Ta₃O₇F and TaO₂F was probed with total-scattering data *via* X-ray diffraction, collected at the Diamond beamline ID 15-1. The reduced structure function F(Q) and the pair distribution function (PDF) D(r) were extracted with the program *GUDRUN4*.^[46] We applied the reverse Monte Carlo (RMC) method to obtain structural models for the materials using the software *RMCprofile*.^[47] Figure 3.4B shows the F(Q) of the SPS-prepared TaO₂F and the corresponding best RMC fit using the structure of the crystalline phase as the initial model. The resulting model, displayed in Figure 3.4A, confirms the presence of local distortions and a very high amount of strain in SPS-prepared TaO₂F.

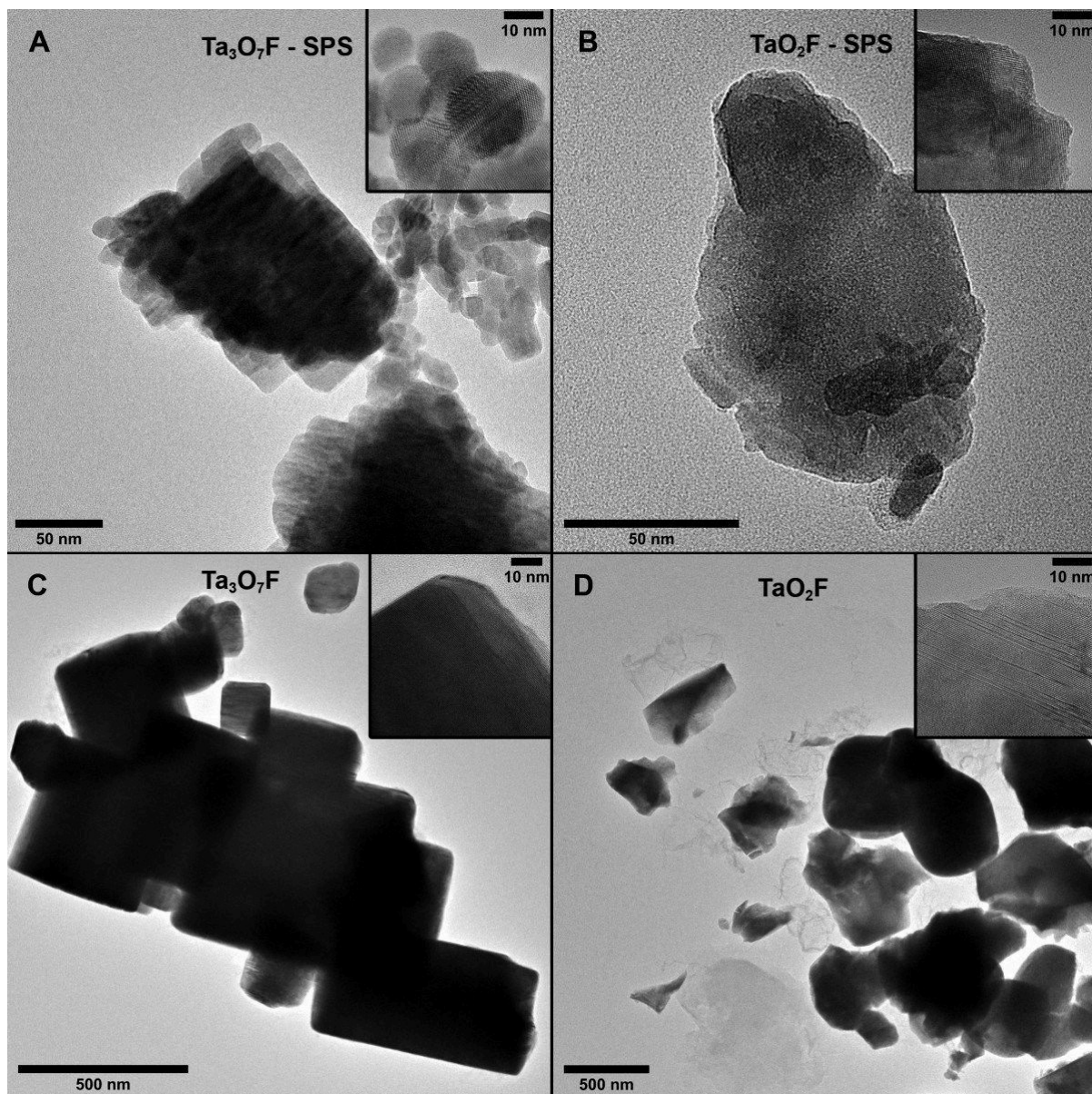


Figure 3.3. Microstructure of Ta₃O₇F and TaO₂F prepared by SPS and conventional solid state chemistry. (A, B) (HR)TEM images of Ta₃O₇F and TaO₂F prepared by SPS, (C, D) and conventional chemistry. Insets show a individual particles in high resolution.

Figure 3.4C shows the pair distribution function $D(r)$ calculated using the experimental total scattering data in comparison to the simulated PDF of crystalline TaO₂F. The peaks of the experimental PDF are much broader and less resolved, which further supports the presence of disorder and strain, *i.e.*, randomly tilted Ta(O/F)₆ octahedra lead to a broader bond distance distribution (Figure 3.4A, C). Furthermore, the PDF of the cubic phase shows significantly more disorder than the PDF of the orthorhombic phase (Figure 7.2.4). This illustrates that the SPS processing leads to local non-equilibrium configurations and therefore metastable structures. This is in agreement with the ¹⁹F-MAS NMR results, which show that close fluorine

contacts occur more often in SPS prepared than in conventionally prepared material and leads to a less equilibrated atom distribution (Table 7.2.5, Figure 7.2.8).^[26,33] All signals are very broad, which is an additional indicator of strong local disorder in SPS-prepared samples.

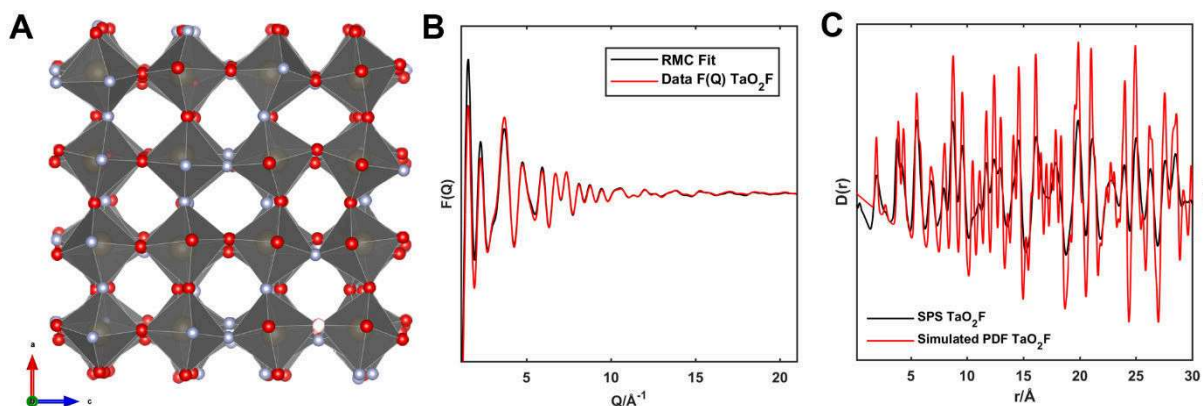


Figure 3.4. Local structure of SPS-prepared TaO₂F by total scattering. (A) Section of the reverse Monte Carlo (RMC) model of SPS prepared TaO₂F obtained from total-scattering data. (B) Reduced structure function $F(Q)$ and the corresponding RMC fit and (C) pair distribution function (PDF) $D(r)$ in comparison to the simulated PDF function of TaO₂F.

Chapter 3.2.3 Band structure, charge carrier concentration and charge transfer

The band gap energy (E_g) of a photocatalyst is essential for application in light-driven processes like photocatalytic water splitting reactions. The electronic structures of bulk Ta₃O₇F and TaO₂F, computed with the aid of density functional theory (DFT), are available through the materials genome project.^[49] As expected, the conduction bands of both compounds contain mostly Ta 5d contributions, while their valence bands are made up of Ta 6p, O 2p and F 2p contributions. The computed band gaps E_g are 2.22 eV for Ta₃O₇F and 2.05 eV for TaO₂F, compared to 3.83 eV for orthorhombic β -Ta₂O₅,^[50] a well-known wide band semiconductor.^[49] These values show that the differences in E_g between Ta₃O₇F, TaO₂F, and β -Ta₂O₅ are determined by the differences in chemical composition and crystal structure. The computed band gaps are significantly smaller than the experimental values of 4.03, 4.10, and 4.23 eV (for Ta₃O₇F, TaO₂F, and β -Ta₂O₅, Figure 7.2.5), which shows the well-known underestimation of the band gap by standard DFT.^[51]

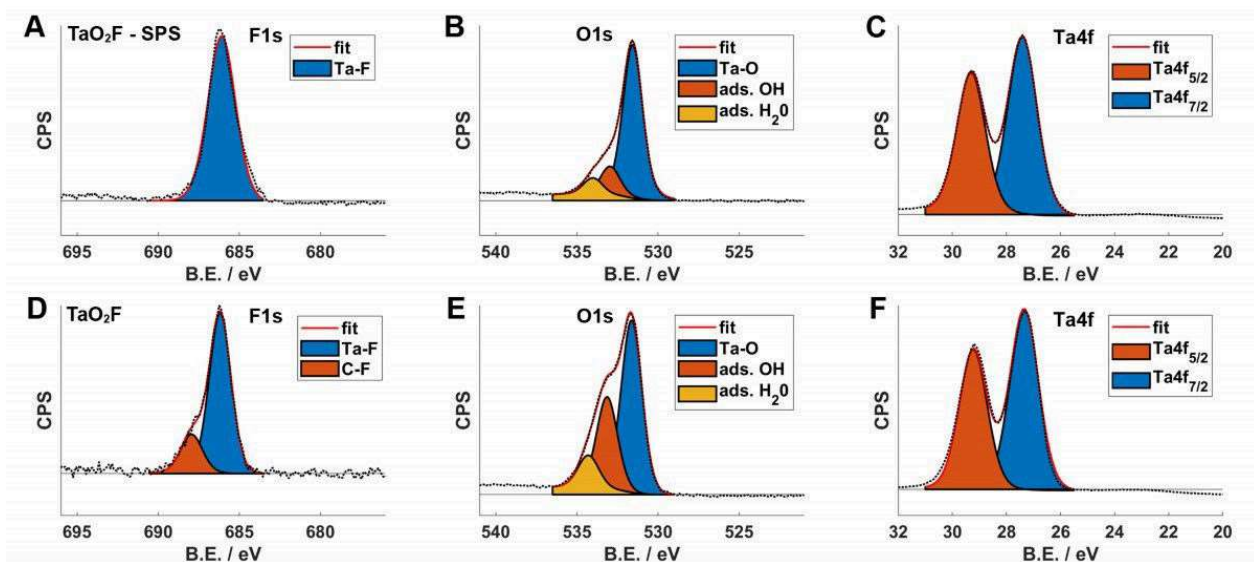


Figure 3.5. Electronic and surface structure of Ta_3O_7F and TaO_2F prepared by SPS and conventional solid state chemistry. (A-F) XPS spectra (with F, O, and Ta sub-spectra in (A,D), (B,E) and (C,F)) of TaO_2F , prepared by SPS (A-C) and conventional ampoule chemistry (D-F) with fitted signals for the respective environments.

Figure 3.5A-F show the F, O and Ta regions of the XPS spectra of TaO_2F synthesized by SPS (Figure 3.5A-C) and conventional ampoule chemistry (Figure 3.5D-F). The XPS survey spectra (Figure 7.2.6) confirm the presence of the elements Ta, O, and F. In Figure 3.5A and D, the signals centered at 27 and 29 eV are assigned to the Ta 4f $7/2$ and Ta 4f $5/2$ orbitals, respectively, revealing the oxidation state of 5+ for Ta in TaO_2F . The XPS spectra of the F 1s core electrons (Figure 3.5C and F) show a signal centered at 686 eV with a less intense additional signal at 688 eV, originating from Ta–F and C–F (remnants of PTFE in conventional ampoule chemistry) bonds on the surface of TaO_2F . The O 1s areas in Figure 3.5B and E show two signals at 531.5, 533 eV, which correspond to lattice O, surface hydroxyl groups and surface water, respectively. Conventionally prepared TaO_2F shows significantly less surface fluorine compared to the SPS-prepared TaO_2F (Table 7.2.4) (ratio F/O conventional = 1:10, ratio F/O SPS 1:5 to 1:3).

The optical properties of as-prepared Ta_3O_7F and TaO_2F (by SPS and conventional ampoule chemistry) and Ta_2O_5 were determined between 200 and 800 nm by optical UV-Vis spectroscopy (Figure 7.2.5F) and compared with the reported and measured optical band gaps for β - Ta_2O_5 . The spectra display absorption edges at \sim 300 nm, corresponding to estimated electronic energy band-gap values of 4.03 eV and 4.10 (4.09 and 4.08 eV) for Ta_3O_7F and TaO_2F prepared by SPS (conventional ampoule chemistry) while the determined band-value of β - Ta_2O_5 is 4.23 eV. The indirect band gaps were determined from the Kubelka-Munk function

(Figure 7.2.5) by plotting $(Fhv)^{1/2}$ as a function of photon energy ($h\nu$), where F is the normalized Kubelka–Munk function of the diffuse reflectance R (from panel A) (intercept at energy axis).^[52] SPS-prepared samples, and especially cubic TaO_2F compared to orthorhombic Ta_3O_7F , clearly show a higher absorption at 2-4 eV, which corresponds to the wavelengths of the light source used in our photoelectric measurements. In addition, the onset of the absorption edges and flat bands (Figure 7.2.5F) of Ta_3O_7F and TaO_2F are shifted to smaller wavelengths compared to β - Ta_2O_5 .

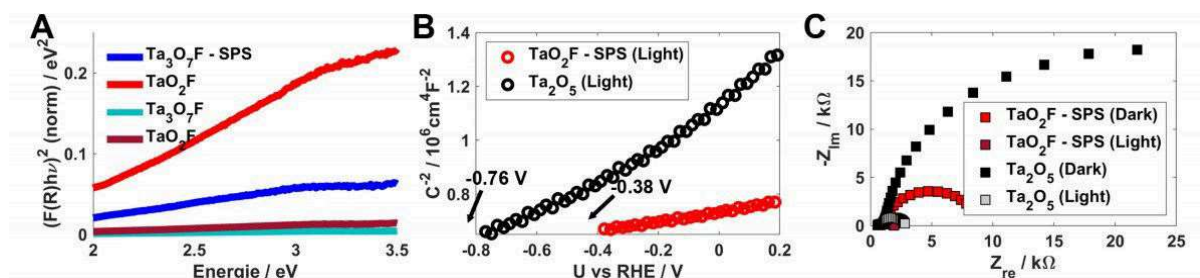


Figure 3.6. Band gap, band edge positions and charge carrier concentrations of Ta_3O_7F and TaO_2F prepared by SPS and conventional solid state chemistry. (A) Low energy region of Kubelka-Munk Plot of Ta_3O_7F (blue line) and TaO_2F (red line) prepared by SPS (solid lines) and conventional ampoule chemistry (dashed lines). (B) Mott-Schottky plot, and (C) EIS Nyquist plot spectra under illumination.

Surface states or the morphology of nanostructured materials can affect the band-edge positions.^[53] To obtain absolute band-edge positions with respect to water redox potentials we determined the flat-band potentials^[54,55] of SPS-prepared TaO_2F by plotting $1/C^2$ as a function of electrochemical potentials, where the capacitance C was obtained from impedance measurements (Figure 3.6B, C). The Mott-Schottky analysis was performed at 1000 Hz frequency. A significant difference in the flat band potentials between Ta_2O_5 and SPS-prepared TaO_2F was observed, the flat band positions (-0.38 V vs. RHE for TaO_2F -SPS) allowing for a lower water oxidation potential and enhanced photocurrent. This anodic shift for the flat band potential of the TaO_2F -SPS sample to less negative potential (-0.38 V) from more negative potential (-0.76 V, for Ta_2O_5) photoanodes shows the enhancement in the charge densities (charge carrier concentration). Lower energy is required to knock more electrons, thereby creating more holes for water oxidation.^[56-61]

Thus, the high PEC activity of SPS-prepared TaO_2F is associated with a lowering of the flat-band potential of TaO_2F nanocrystals by ~ 0.5 V. The shift of the flat band potentials as evident from the Mott-Schottky plots appears to be related to a reorientation of valence and conductance bands (the bandgap is slightly reduced) upon fluorine addition. New band positions are adopted

as confirmed from theoretical calculations of the optical band positions. The calculation method and optical band positions are provided as supplementary material (Table 7.2.6 and Figure 7.2.9). The positive slope of the Mott–Schottky plot indicates that TaO₂F is an n-type semiconductor (possibly related to an incomplete O/F substitution).

Chapter 3.3 Photoelectrochemical water splitting

Ta₃O₇F and TaO₂F synthesized by SPS and conventional ampoule chemistry showed water splitting activity under simulated 1-SUN light in photoelectrochemical cells. Figure 3.7 provides the PEC results in terms of photocurrent-voltage (*I-V*), stability curve and periodic chopped photocurrent-time (*I-t*) plots. Figure 3.7A shows the comparative *I-V* response obtained from linear sweep voltammetry (LSV) of Ta₂O₅, and the tantalum oxyfluorides, Ta₃O₇F and TaO₂F (prepared by SPS and conventional chemistry), under continuous irradiation with light. Ta₃O₇F and TaO₂F prepared by SPS showed a good photo-response behavior with large values of the photocurrent density, i.e. 0.31 mA cm⁻² and 0.72 mA cm⁻² at 1.23 V vs. RHE for Ta₃O₇F-SPS and TaO₂F-SPS, respectively. In contrast, Ta₃O₇F and TaO₂F, prepared by conventional ampoule chemistry, showed a lower photoresponse with a photocurrent density reaching only 0.17 mA cm⁻² and 0.13 mA cm⁻² 1.23 V vs. RHE (the minimum threshold voltage for water splitting). The Ta₂O₅ photoanode showed a very small photoresponse under simulated light at voltage 1.23 V vs. RHE, which is related to the UV part of the optical spectrum.

TaO₂F-SPS showed a higher photoresponse than Ta₃O₇F-SPS. The orbital overlap in the ReO₃-type structure with Ta-O(F)-Ta bond angles close to 180° [33, 62] facilitates charge transfer and charge carrier transport, thereby improving the photocatalytic activity. XPS (Figure 3.5, Figure 7.2.6, 7.2.7 and Table 7.2.4) shows that the overall F atom surface density in TaO₂F-SPS is higher than for Ta₃O₇F-SPS (in agreement with the composition). This improves the efficiency of photocurrent generation. Ta₂O₅, Ta₃O₇F, and TaO₂F photoanodes showed low dark currents (Figure 3.7B). Another striking effect of the tantalum oxyfluorides is the cathodic shift of the overpotential of the TaO₂F-SPS photoanode to a minimum value of ~0.55 V vs. RHE, which reached to saturation at 1.16 V vs. RHE. We achieved a maximum photocurrent density of 0.31 mAcm⁻² and 0.72 mAcm⁻² at 1.23 V vs. RHE for photoanodes with SPS-prepared Ta₃O₇F and TaO₂F, respectively. In contrast, Ta₃O₇F, TaO₂F and Ta₂O₅ prepared by conventional ampoule chemistry showed photocurrent values of 0.17 mAcm⁻², 0.13 mAcm⁻² and 0.12 mAcm⁻², respectively. The photocurrent for TaO₂F at 1.23 V vs. RHE enhanced by a factor of six compared to a Ta₂O₅ photoanode (0.12 mAcm⁻² at 1.23 V vs. RHE), the value being roughly

comparable with those of hematite ($\alpha\text{-Fe}_2\text{O}_3$, 0.45 mA cm^{-2}),^[63] pristine CoO_x ($\sim 0.7 \text{ mA cm}^{-2}$)^[64] or pristine BiVO_4 (1.2 mA cm^{-2} at 1.23 V vs. RHE) and pristine BiVO_4 photoanodes.^[11]

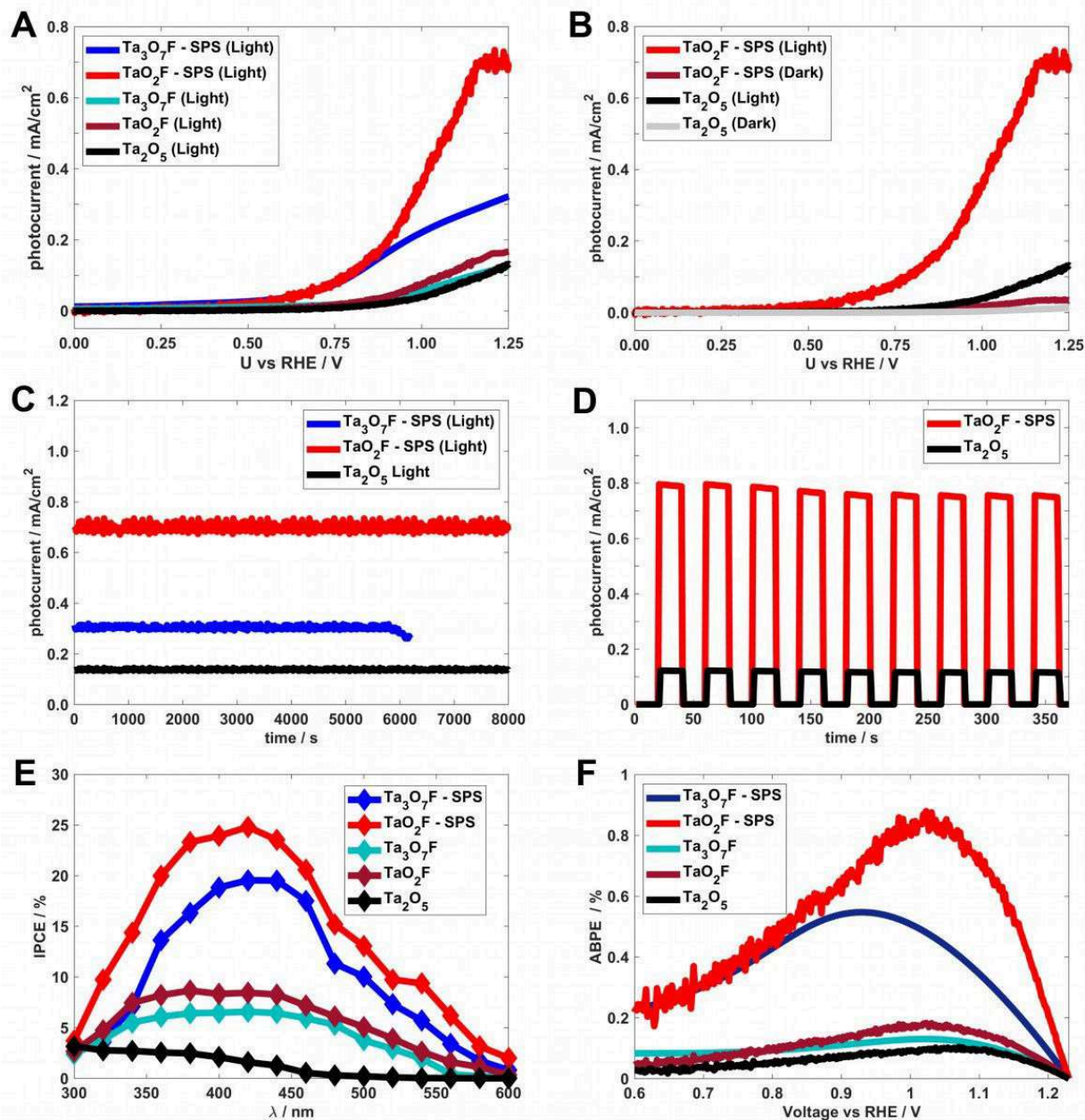


Figure 3.7. Photoelectrochemical (PEC) measurements for Ta_2O_5 and the tantalum oxyfluorides, prepared by SPS and conventional ampoules chemistry. (A, B) Linear sweep voltammograms under light and dark conditions, (C) I - t photostability curve under continuous luminescence at 1.23 V vs RHE, and (D) amperometric I - t curves at an applied potential of 1.23 V vs RHE with 20 s ON/OFF cycle. (E) Incident photon-to-current efficiencies, IPCE (%) and (F) applied bias to photo-conversion ABPE (%) for Ta_2O_5 , $\text{Ta}_3\text{O}_7\text{F}$ (SPS-prepared and conventional synthesis) and TaO_2F (SPS-prepared and conventional synthesis).

$\text{Ta}_3\text{O}_7\text{F}$ -SPS and TaO_2F -SPS photoanodes were stable for 2 hours under continuous light illumination Figure 3.7C, and TaO_2F showed a better photostability than $\text{Ta}_3\text{O}_7\text{F}$ indicating low

photo-charge recombination and high charge transfer efficiency. The better photostability of TaO₂F may be attributed to its crystal structure, because TaO₂F is the thermodynamically stable oxyfluoride, whereas Ta₃O₇F is an intermediate during TaO₂F formation. The photocurrent of SPS-prepared Ta₃O₇F started to decay and collapsed after ~1.5 h, which might be attributed to the recombination of photoexcitons. We also demonstrated the periodic photocurrent generation capacities of Ta₂O₅ and SPS-prepared TaO₂F photoanodes by applying transient irradiation at regular intervals of ~20 s. Figure 3.7D shows a consistent decrease and increase of the photocurrent under regular chopped light conditions. The periodic photoresponse was still stable after 10 cycles. To exclude any electrochemical contribution for water oxidation in this voltage range, we performed an electrochemical analysis (LSV) of freshly prepared photoanodes. Even at 2.00 V vs. RHE, no significant contribution from electrochemical response was detected (Figure 7.2.10).

Chapter 3.3.1 Photoconversion efficiency

The wavelength-dependent incident photon-to-current efficiency (IPCE) was calculated according to

$$IPCE (\%) = \frac{1240 \times I_{\text{photon}}}{\lambda \times P_{\text{incident light}}} \quad (1)$$

where, I_{photon} , λ and $P_{\text{incident light}}$ indicate the photocurrent (mA), the wavelength of the incident light (nm), and the incident irradiating power at the specific wavelength (mW). A Xe lamp fitted with band-pass monochromatic irradiation filters (central wavelengths: 400-600 nm with 20 nm in each pass) was used to measure the IPCE (%) dependence at each value. The monochromatic incident light was quantified by equation 1 and plotted as a function of wavelength at 1.23 V vs. RHE (Figure 3.7E). The % IPCE values for SPS-prepared Ta₃O₇F and TaO₂F are substantially higher than that for Ta₂O₅. Figure 3.7E shows that the Ta₂O₅ photoanode utilized only 3.1 % of the incident light compared to Ta₃O₇F and TaO₂F. The comparative % IPCE values (Table 3.2) show the highest photoconversion values for Ta₃O₇F-SPS and TaO₂F-SPS, i.e., tantalum oxyfluoride photoanodes exhibit a strongly enhanced light-absorbing and utilization capacity. Ta₃O₇F-SPS and TaO₂F-SPS showed photoconversion efficiencies of 19.4 % and 24.7 %, the highest values reported so far for such materials. Importantly, sufficient absorption occurs in the visible range of the solar spectrum (400 – 700 nm).

Table 3.2. Comparison of photochemical parameters and their effect on PEC performance of Ta₃O₇F and TaO₂F photoanodes

Photoanode	Photocurrent density at 1.23 V vs. RHE / mA cm ⁻²	IPCE (%) at □ nm	ABPE (%) values at potential (V vs. RHE)
Ta ₃ O ₇ F - SPS	0.33	19.4 % at 421 nm	0.55 % at 0.93 V
TaO ₂ F - SPS	0.72	24.7 % at 415 nm	0.86 % at 1.01 V
Ta ₃ O ₇ F	0.11	6.7 % at 374 nm	0.13 % at 1.04 V
TaO ₂ F	0.17	8.7 % at 384 nm	0.19 % at 1.01 V
Ta ₂ O ₅	0.13	3.1 % at 300 nm	0.102 % at 1.09 V

We transformed the I - V data (recorded by a 3-electrode system) to % applied bias to photo-conversion (% ABPE) efficiency according to [65,66]

$$ABPE (\%) = \frac{J_{ph} (1.23 - |V_{app}|)}{P_{light}} \times 100 \quad (2)$$

where, J_{ph} is the photocurrent density (mA cm⁻²), V_{app} is the applied potential vs. RHE, and P_{light} is the power density of illumination (100 mW cm⁻²). The results are shown in Figure 3.7F. The ABPE for the TaO₂F-SPS photoelectrode was up to 0.86 % at 1.01 V vs. RHE, which is about eight times higher than the corresponding value for a Ta₂O₅ electrode and higher than, or comparable to the values for hematite (0.24 %) [57] and pristine BiVO₄ (~1 %) [11]. Similarly, a SPS-prepared Ta₃O₇F photoelectrode also showed a good ABPE value of 0.55 % at 0.93 V vs. RHE. In contrast, Ta₃O₇F and TaO₂F prepared by conventional ampoule chemistry showed much lower ABPE values of 0.13 % and 0.19 %, respectively. These results show the importance of materials processing during synthesis for the light-induced characteristics of the material.

Chapter 3.3.2 Water splitting

Interfacial charge transfer, a critical factor to test the PEC efficiency of photocatalysts, was determined by electronic impedance spectroscopy (EIS) under simulated solar condition. Measurements were conducted by sweeping a DC voltage across the working electrode. Nyquist plots (real vs. imaginary) with representative impedance values for Ta₂O₅, Ta₃O₇F-SPS and TaO₂F-SPS are shown in Figure 3.7C. The impedance is indicative of interfacial phenomena operative near the electrode surface. As expected, the charge transfers kinetics in TaO₂F-SPS is more dominant compared to Ta₂O₅, which explains the lower resistance curve in

Figure 3.6C. The higher electrical conductivity is attributed to an increased exciton density generated by photons of lower energy.

Thus, F/O replacement appears to be a crucial factor for the enhanced photoelectrical efficiency of Ta_3O_7F and TaO_2F . It leads to a “band realignment” and leads (for TaO_2F) to structural changes that facilitate charge transfer and carrier separation. A reduced charge carrier recombination rate that enhances the photocatalytic activity has been reported in fluorine-doped oxides and attributed to the presence of additional energy levels and alternative pathways that enhance exciton life times.^[67-69]

Importantly, SPS preparation prevents the growth of large crystallites, generates a larger BET surface, more grain boundaries and thus more active surface sites. In addition, SPS reduces surface passivation due to surface O-H with increasing fluoride content. This is supported by the XPS results, which are compatible with the presence of surface F-atoms and defect formation while the Mott-Schottky analysis (Figure 3.6B, C) revealed a band repositioning of the bands for tantalum oxyfluorides.

Chapter 3.4 Summary

In summary, we demonstrated a very fast, energy saving and environmentally benign synthesis for tantalum oxyfluoride photocatalysts by SPS starting from PTFE scrap as solid, non-toxic and abundant source of fluorine. SPS processing reduces reaction times to the order of minutes rather than days, which reduce process times and the energy costs by several orders of magnitude. Local strain and atom disorder due to the SPS-processing makes TaO_2F an active photocatalysts with a ReO_3 -type F/O disordered substructure, which shows, even in the absence of co-catalysts, an excellent photocatalytic activity for oxygen evolution, reaching photoconversion efficiencies up to 24.7 % and applied bias to photoconversion values of 0.86 %. In contrast, conventionally prepared TaO_2F shows only moderate photoactivity. Similarly, SPS-prepared Ta_3O_7F exhibits unique electronic properties, endowing it with good electron transfer abilities for photocatalytic oxygen generation. In view of their low charge transfer resistance, the corresponding niobium oxyfluorides may have prospects in photoelectro- or electrochemistry as well. Microstructural changes due to non-equilibrated atom distributions, atom disorder, grain boundaries and thus more active surface sites are generally not considered in electronic structure calculations which are based on equilibrium structures. This study is a proof of concept for the rapid and energy saving production of valuable photocatalysts for water

splitting from plastic waste without using toxic or caustic chemicals. It opens new perspectives for the recycling of plastic waste and the search of stable photocatalysts by materials processing.

Chapter 3.5 Experimental Methods

Synthesis. Tantalum (V) oxide (99+%, Chempur) and poly(tetrafluoroethylene) (PTFE, Sigma-Aldrich, 1 μm powder) were weighed in their respective molar ratios, ball-milled (Fritsch Pulverisette) for 5 h in ethanol and dried after centrifugation overnight at 70°C in a drying chamber. Ta₂O₅ and PTFE were used in stoichiometric amounts for Ta₃O₇F and with excess PTFE for TaO₂F.

For SPS preparation of Ta₃O₇F and TaO₂F, samples containing ≈ 2 g of the powder mixtures were enclosed with graphite foil and placed in graphite dies. Afterwards, the dies were placed into an SPS HP D 25 (FCT-systems) and heated up to 600°C with 50°C/min at 19 MPa and kept at this temperature for 9 min. Reference samples for conventional high temperature reactions were prepared by placing powder mixtures in evacuated quartz ampules and heating for 12 h at 650°C to obtain TaO₂F (≈ 300 mg) and for 36 h at 650°C to obtain Ta₃O₇F (≈ 500 mg).

ζ -potential measurements. For ζ -potential measurements, 1 mg/mL suspensions of the powder samples were prepared in 0.1 M NaNO₃-solution and mixed for 1 h in an ultrasonic bath right before measurement. The different pH values were achieved by adding the necessary volumes of a 10 mM NaOH- or an 10 mM HNO₃-solution to the 0.1 M NaNO₃-solutions. Seven solutions with the following pH-values were prepared: 3.1, 4.1, 5.2, 6.8, 8.9, 9.8 and 11.1. Measurements were carried out on a Zetasizer Nano ZS from Malvern using a folded capillary ζ -cell at 25°C.

X-Ray powder diffraction analysis. Samples for X-Ray diffraction were prepared on polyvinylacetate-foil. Diffractograms were obtained using a STOE Stadi P, equipped with a Mythen 1k detector using MoK α_1 radiation. The sample was measured in transmission in 0.015° steps (continuous scan, 150 s/°) covering a 2 θ range from 1.5° to 43°. Rietveld refinement^[70] was performed with Topas Academic V6 using the fundamental parameters approach.^[71] Crystalline phases were identified according to the PDF-2 database (PDF-2, Release 2004, JCPDS – International Center for Diffraction Data, Newton Square (PA) US (2004)) using Bruker AXS.^[72]

Total scattering. Total scattering experiments of the SPS samples were performed at beamline ID 15-1 at the Diamond Light Source, UK, using an X-ray energy of 76.69 keV ($\lambda = 0.161669$ Å). A Perkin Elmer XRD 4343 CT and a PerkinElmer XRD 16611 CP 3 was used as a primary and secondary detector. The resulted 2D images were integrated by using the program

DAWNscience.^[73] The reduced structure function $F(Q)$ was calculated utilizing the *GuDrun4X* software.^[74] The analysis of the total scattering data were performed using the *RMCPProfile* software.^[75] The RMC simulations used configurations of 10x10x10 supercells of the corresponding initial phases (TaO₂F cubic and Ta₃O₇F orthorhombic). Calculations were performed using distant windows and soft bond valence summation (BVS) restraints to avoid chemical unreasonable solutions.^[14] Anion swapping of a random oxygen position with a random fluorine position was applied to achieve faster convergence of the model.

Brunauer/Emmett/Teller (BET) sorption. BET measurements were conducted using the gas adsorption setup Autosorb-6B from Quantachrome with nitrogen as analysis gas. The temperature during the measurements was 77 K. Data evaluation was conducted with the software Quantachrome ASiQWin 3.0.

Transmission electron microscopy (TEM). Powdered samples were prepared by placing one drop (10 μ L) of a diluted NP solution in ethanol (0.1 mg mL⁻¹) on a carbon-coated copper grid and by letting it dry at room temperature for transmission electron microscopy (TEM), high-resolution TEM (HRTEM), electron dispersive X-ray spectroscopy (EDXS). TEM, HRTEM and EDX measurements were carried out with a FEI TECNAI F30 S-TWIN transmission electron microscope equipped with a field emission gun and working at 300 kV. TEM images and nano electron diffraction (NED) patterns were taken with a CCD camera (16-bit 4.096 x 4.096 pixel GATAN ULTRASCAN4000) and acquired by Gatan Digital Micrograph software.

X-ray photoelectron spectroscopy (XPS). XPS measurements were carried out on an Axis Ultra *DLD* imaging photoelectron spectrometer. Measurements were carried out using the Hybrid mode with 10 mA and 15 kV at the Al anode. The analysis area was 700 μ m \times 300 μ m (i.e., X-ray spot size). Survey spectra were measured at a pass energy of 80 and elemental spectra at 20 pass energy of the analyzer. All spectra were charge corrected to a binding energy of 284.8 eV for the C 1s line corresponding to adventitious aliphatic carbon. Measurements were evaluated using the CasaXPS software.

UV–Vis spectroscopy. Ultraviolet–visible (UV–vis) reflectance spectra ranging from 200 to 800 nm were collected on a Cary 5G UV–vis–NIR spectrophotometer using an Ulbricht sphere. BaSO₄ was used as white standard. The samples were measured by mixing a few mg of powder with BaSO₄ and pressing the mixture into a pellet.

Nuclear magnetic resonance (NMR) spectroscopy. *Solid state NMR spectroscopy.* All solid-state NMR experiments were recorded on a Bruker Avance 400 DSX spectrometer at ¹⁹F frequency of 376.25 MHz. A two-channel commercial Bruker 2.5 mm probe head at spinning

speeds of 25 kHz was used for ^{19}F direct excitation measurements. No changes in the spectra are expected at slightly elevated temperatures, so no temperature correction for the frictional heating due to the sample rotation was performed. All spectra were background corrected.

Scanning electron microscopy (SEM). Field-emission scanning electron microscopy was performed on a NOVA Nano-SEM with an attached Oxford Inca X-ray system for chemical analysis. The obtained SPS pellets were cut and polished to obtain cross-sectional pieces. Secondary and backscattered electron images were collected with acceleration voltages of 5 keV and 15 or 20 keV for EDX mapping, respectively.

High resolution-continuum source-graphite furnace molecular absorption spectrometry. HR-CS-GFMAS. Fluorine analysis was conducted by means of a HR-CS-GFMAS System ContrAA 800 G from Analytik Jena (Jena, Germany). Three independent samples were prepared. About 0.1 g of sample was weighed in and 10 mL of a Triton X 100 solution (0.1% (w/v)) were added. The sample suspension was sonicated for 15 min within an ultrasonication bath; afterwards each sample was vortex-mixed for 5 min. Before analysis, the sample slurries were vortex mixed again for 30 sec. Subsequently, 10 μL of the sample slurry and 10 μL of a 4g L^{-1} $\text{Ca}(\text{NO}_3)_2 \times 4\text{H}_2\text{O}$ solution (dissolved in MilliQ water) (Ca as molecule forming agent) were injected into the graphite furnace of the system. The absorption wavelength was set to 606.440nm, and each sample was analyzed 4 times. Quantification was performed by external calibration with an aqueous fluoride standard (Certipur standard, Merck, Darmstadt, Germany).

Fabrication of photoanodes and PEC measurements. The photocatalytic water splitting was carried out in a three-electrode electrochemical cell, where Pt and saturated calomel electrode (SCE) acted as counter and reference electrodes. The working electrode was fabricated by drop casting as-synthesized $\text{Ta}_3\text{O}_7\text{F}$, TaO_2F and Ta_2O_5 powders on a fluorinated tin oxide (FTO) support.

In each photoelectrochemical reaction, 5 mg of the photocatalysts were suspended into a 1 mL equimolar mixture of ethanol/deionized (DI) water and sonicated at room temperature to obtain a uniformly dispersed mixture. Each solution was enriched with 5 μL of 0.5 % Nafion solution to increase the binding characteristics and the uniformity of the film on the ink-covered $1 \times 1\text{ cm}^2$ area of FTO. A 0.5 M Na_2SO_4 solution in DI water was used as electrolyte (pH 7.1) for the PEC measurements without any additional sacrificial agent.

All data was collected on an Autolab potentiostat supported by the NOVA software package and a simulated light source (Oriel Sol-AAA Newport). The intensity of the simulator is adjusted to one SUN after calibration with a silicon diode solar cell (Oriel-diode). A full light

spectrum is used in all PEC measurements to provide a reasonable comparison of the PEC performance of the Ta₃O₇F, TaO₂F and Ta₂O₅ photoanodes.”

References

- [1] M. J. Burke, J. J. Stephens, *Energy Res. Social Sci.* **2018**, *35*, 78–93.
- [2] H. B. Gray, *Nat. Chem.* **2009**, *1*, 7.
- [3] J. Suntivich, K. J. May, H. A. Gasteiger, J. B. Goodenough, Y. Shao-Horn, *Science* **2011**, *334*, 1383–1385.
- [4] I. Staffell, D. Scamman, A. V. Abad, P. Balcombe, P. E. Dodds, P. Ekins, N. Shahd, K. R. Warda, *Energy Environ. Sci.* **2019**, *12*, 463–491.
- [5] I. Roger, M. A. Shipman, M. D. Symes, *Nat. Rev. Chem.* **2017**, *1*, 0003.
- [6] J. Schneider, M. Matsuoka, J. Zhang, Y. Horiuchi, M. Anpo, D. W. Bahnemann, *Chem. Rev.* **2014**, *114*, 9919–9986.
- [7] F. E. Osterloh, *Chem. Soc. Rev.* **2011**, *42*, 2294–2320.
- [8] A. Kay, I. Cesar, M. Grätzel, *J. Am. Chem. Soc.* **2006**, *128*, 15714–15721.
- [9] O. Zandi, T. W. Hamann, *Nat. Chem.* **2016**, *8*, 778–783.
- [10] L. Liao, Q. Zhang, Z. Su, Z. Zhao, Y. Wang, Y. Li, X. Li, D. Wei, G. Feng, Q. Yu, X. Cai, J. Zhao, Z. Ren, H. Fang, F. Robles-Hernandez, S. Baldelli, J. Bao, *Nat. Nanotechnol.* **2014**, *9*, 69–73.
- [11] T. W. Kim, K.-S. Choi, *Science* **2014**, *343*, 990–994.
- [12] T. Oshima, O. Ishitani, K. Maeda, *Adv. Mater. Interfaces* **2014**, *1*, 1400131.
- [13] T. F. Jaramillo, K. P. Jorgensen, J. Bonde, J. H. Nielsen, S. Horch, I. Chorkendorff, *Science* **2007**, *317*, 100–102.
- [14] L. Yuliati, J. H. Yang, X. C. Wang, K. Maeda, T. Takata, M. Antonietti, K. Domen, *J. Mater. Chem.* **2010**, *20*, 4295–4298.
- [15] K. Maeda, K. Teramura, D. Lu, T. Takata, N. Saito, Y. Inoue, K. Domen, *Nature* **2006**, *44*, 295.
- [16] K. Maeda, D. Lu, K. Domen, *Angew. Chem. Int. Ed.* **2013**, *52*, 6488–6491.
- [17] X. C. Wang, K. Maeda, A. Thomas, K. Takanabe, G. Xin, J. M. Carlsson, K. Domen, M. Antonietti, *Nat. Mater.* **2009**, *8*, 76–80.
- [18] L. Reith, K. Lienau, C. A. Triana, S. Siol, G. R. Patzke, *ACS Omega* **2019**, *4*, 15444–15456.

- [19] T. Hisatomi, C. Katayama, Y. Moriya, T. Minegishi, M. Katayama, H. Nishiyama, T. Yamadad, K. Domen, *Energy Environ. Sci.* **2013**, *6*, 3595–3599.
- [20] C. Pan, T. Takata, M. Nakabayashi, T. Matsumoto, N. Shibata, Y. Ikuhara, K. Domen, *Angew. Chem., Int. Ed.* **2015**, *54*, 2955–2959.
- [21] S. Andersson, *Acta Chem. Scand.* **1964**, *18*, 2339-2344.
- [22] L. Jahnberg, S. Andersson, *Acta Chem. Scand.* **1967**, *21*, 615-619.
- [23] M. Vlasse, C. Morilliere, J.-P. Chaminade, M. Poucard, *Bull. Mineral.* **1975**, *98*, 325-330.
- [24] D. Hirai, E. Climent-Pascual, R. J. Cava, *Phys. Rev. B* **2011**, *84*, 17451.
- [25] S. E. Dutton, D. Hirai, R. J. Cava, *Mat. Res. Bull.* **2012**, *47*, 714-718.
- [26] J. Dabachi, M. Body, C. Galven, F. Boucher, C. Legein, *Inorg. Chem.* **2017**, *56*, 5219–5232.
- [27] D. Hirai, O. Sawai, T. Nunoura, Z. Hiro, *J. Fluorine Chem.* **2018**, *209*, 43-48.
- [28] M. A. Lange, Y. Krysiak, J. Hartmann, G. Dewald, G. Cerretti, M. N. Tahir, M. Panthöfer, B. Barton, T. Reich, W. G. Zeier, M. Mondeshki, U. Kolb, W. Tremel, *Adv. Funct. Mater.* **2020**, *30*, 1909051.
- [29] H. Zhang, Y. Li, Y. Wang, P. Liu, H. Yang, X. Yao, T. An, B. J. Wood, H. Zhao, **J. Mater. Chem. A** **2013**, *1*, 6563-6571.
- [30] J. Duan, G. Mou, S. Zhang, S. Wang, J. Guan, *J. Mater. Chem. A* **2015**, *3*, 14686-14695.
- [31] H. Zhang, H. Wang, P. Liu, S. L. Chou, J. Z. Wang, H. Liu, G. Wang, H. Zhao, *ACS Nano* **2016**, *10*, 507–514.
- [32] M. Mhadeh, V. Hoepfner, E. Larios, K. Liao, J. Jia, M. Jose-Yacaman, G. A. Ozin, *ChemSusChem* **2014**, *7*, 2104-2111.
- [33] C. R. Morelock, B. K. Greve, M. Cetinkol, K. W. Chapman, P. J. Chupas, A. P. Wilkinson, *Chem. Mater.* **2013**, *25*, 1900–1904.
- [34] A. D. Menard, J. F. Trant, *Nat. Chem.* **2020**, *12*, 17-25.
- [35] E. Kemnitz, J. Noack, *Dalton Trans.* **2015**, *44*, 19411-19431.
- [36] W. Sleight, *Inorg. Chem.* **1969**, *8*, 1764-1767.
- [37] Y. Kobayashi, M. Tian, M. Eguchi, T. E. Mallouk, *J. Am. Chem. Soc.* **2009**, *131*, 9849–9855.
- [38] O. Guillon, C. Elsässer, O. Gutfleisch, J. Janek, S. Korte-Kerzel, D. Raabe, C. A. Volkert, *Mater. Today* **2018**, *21*, 527- 536.

- [39] O. Guillon, J. Gonzales-Julian, B. Dargartz, T. Kessel, G. Schierning, J. Räthel, M. Herrmann, C. Säßer, O. Gutfleisch, J. Janek, S. Korte-Kerzel, D. Raabe, C. A. Volkert, *Adv. Eng. Mater.* **2014**, *16*, 830-849.
- [40] C. Recknagel, N. Reinfried, P. Höhn, W. Schnelle, H. Rosner, Y. Grin, A. Leithe-Jasper, *Sci. Techn. Adv. Mat.* **2007**, *8*, 357-363.
- [41] M. Beekman, M. Baitinger, H. Borrmann, W. Schnelle, K. Meier, G. S. Nolas, Y. Grin, *J. Am. Chem. Soc.* **2009**, *131*, 9642–9643.
- [42] D. Portehault, V. Maneeratana, C. Candolfi, N. Oeschler, I. Veremchuk, Y. Grin, C. Sanchez, M. Antonietti, *ACS Nano* **2011**, *5*, 9052-9061.
- [43] E. E. Lewis, M. A. Taylor, *J. Am. Chem. Soc.* **1947**, *69*, 1968-1970.
- [44] B. B. Baker, D. J. Kasprzak, *Polym. Degrad. Stabil.* **1993**, *42*, 181-188.
- [45] P. W. Stephens, *J. Appl. Cryst.* **1999**, *32*, 281-289.
- [46] S. E. McLain, D. T. Bowron, A. C. Hannon, A. K. Soper, ISIS Facility, Rutherford Appleton Laboratory, Chilton, Didcot, OXON, United Kingdom OX11 0QX
- [47] M. G. Tucker, D. A. Keen, M. T. Dove, A. L. Goodwin, Q. Hui, *J. Phys. Condens. Materie* **2007**, *19*, 335218.
- [48] N. Ozbe, S. Akman, *Food Anal. Methods* **2016**, *9*, 2925–2932.
- [49] A. Jain, S. P. Ong, G. Hautier, W. Chen, W. D. Richards, S. Dacek, S. Cholia, D. Gunter, D. Skinner, G. Ceder, K. Persson, *Appl. Phys. Lett. Mater.* **2013**, *1*, 011002.
- [50] R. Nashed, W. M. I. Hassan, Y. Ismail, N. K. Allam, *Phys. Chem. Chem. Phys.* **2013**, *15*, 1352-1357.
- [51] A. Morales-García, R. Valero, F. Illas, *J. Phys. Chem. C* **2017**, *121*, 18862–18866.
- [52] G. Kortüm, *Reflectance Spectroscopy*, Springer 1969.
- [53] S. M. Sze, M. K. Le, *Semiconductor Devices – Physics and Technology*, Wiley 2010
- [54] A. Hankin, F. E. Bedoya-Lora, J. C. Alexander, A. Regoutz, G. H. Kelsall, *J. Mater. Chem. A* **2019**, *7*, 26162–26176.
- [55] C. Lohaus, A. Klein, W. Jaegermann, *Nat. Commun.* **2018**, *9*, 4309.
- [56] Y. Zhu, J. Xu, H. Jiang, D. Niu, X. Zhang, and S. Hu, *CrytEngComm* 2018, *20*, 6430-6437.
- [57] S. W. LaGasse, P. Dhakras,, K. Watanabe, T. Taniguchi, and J. U. Lee *Adv. Mater.* **2019**, *31* (24), 1901392.
- [58] T. Xu, L. Zhang, H. Cheng, and Y. Zhu, *Appl. Catal. B – Environ.* **2011**, *101*, 382-387.

- [59] C. Liu, Y. Qui, F. Wang, Q. Liang, and Z. Chen, *Adv. Mater. Interfaces* **2017**, *4*, 1700681.
- [60] S. S. Kalanur, *Catalysts* **2019**, *9* (5), 456.
- [61] Z. Zhang, and P. Wang, *Energy Environ. Sci.* **2012**, *5*, 6506-6512.
- [62] K. Kamali, T. R. Ravindran, T. N. Sairam, *Vibr. Spectr.* **2014**, *71*, 12-17.
- [63] Gurudayal, S. Y. Chiam, M. H. Kumar, P. S. Bassi, H. L. Seng, J. Barber, L. H. Wong, *ACS Appl. Mater. Interfaces* **2014**, *6*, 5852–5859.
- [64] M. Favaro, J. Yang, S. Nappini, E. Magnano, F. M. Toma, E. J. Crumlin, J., Yano, I. D. Sharp, *J. Am. Chem. Soc.* **2017**, *139*, 8960–8970.
- [65] Y. Wan, S. K. Karuturi, C. Samundsett, J. Bullock, M. Hettick, D. Yan, J. Peng, P. R. Narangari, S. Mokkapati, H. H. Tan, C. Jagadish, A. Javey, A. Cueva, *ACS Energy Lett.* **2018**, *3*, 125–131.
- [66] T. Hisatomi, J. Kubota, K. Domen, *Chem. Soc. Rev.* **2014**, *43*, 7520–7535.
- [67] S. Y. Moon, E. H. Gwag, J. Y. Park, *Energy Technol.* **2018**, *6*, 459–469.
- [68] L. Liu, Z. Mei, Y. Hou, H. Liang, A. Azarov, V. Venkatachalapathy, A. Kuznetsov, X. Du, *Sci. Rep.* **2015**, *5*, 15516.
- [69] Y. Zhu, J. Xu, H. Jiang, D. Niu, X. Zhang, S. Hu, *CrystEngComm* **2018**, *20*, 6430-6437.
- [70] H. Rietveld, *J. Appl. Crystallogr.* **1969**, *2*, 65–71.
- [71] A. A. Coelho, *J. Appl. Crystallogr.* **2018**, *51*, 210–218.
- [72] EVA 10.0 Rev. 1, Bruker AXS, Madison, WI/USA, 2003.
- [73] J. Filik, A. W. Ashton, P. C. Y. Chang, P. A. Chater, S. J. Day, M. Drakopoulos, M. W. Gerring, M. L. Hart, O. V. Magdysyuk, S. Michalik, A. Smith, C. C. Tang, N. J. Terrill, M. T. Wharmby, H. Wilhelm, *J. Appl. Cryst.* **2017**, *50*, 959-966.
- [74] S. E. McLain, D. T. Bowron, A. C. Hannon, A. K. Soper, ISIS Facility, Rutherford Appleton Laboratory, Chilton, Didcot, OXON, United Kingdom OX11 0QX
- [75] M. G. Tucker, D. A. Keen, M. T. Dove, A. L. Goodwin, Q. Hui, *J. Phys. Condens. Materie* **2007**, *19*, 335218.
- [76] S. T. Norberg, M. G. Tucker, S. Hull, *J. Appl. Cryst.* **2009**, *42*, 179-184.

The contents of the following chapter are taken and partially adapted from *Dalton Transaction*. 2021, accepted to be published..

Authorship contributions

Category 1

Conception and design of study:

[REDACTED]

Acquisition of data:

[REDACTED] preparation of samples.
[REDACTED] – PXRD measurements.
[REDACTED] – HR-CS-GFMAS
[REDACTED] – TEM images
[REDACTED] HR-TEM and SEM images.
[REDACTED] – measurement of ^{19}F solid-state NMR.
[REDACTED] acquisition of UV/Vis-data.
[REDACTED] – acquisition of oxygen evolution data.
[REDACTED] – acquisition of XPS data.

Analysis and/or interpretation of data:

[REDACTED] – PXRD refinement.
[REDACTED] HR-TEM and SEM analysis.
[REDACTED] – analysis of ^{19}F solid-state NMR.
[REDACTED] interpretation of oxygen evolution data.
[REDACTED] interpretation of HR-CS-GFMAS, ζ -potential data and XPS data.

Category 2

Drafting the manuscript:

[REDACTED]

Revising the manuscript critically for important intellectual content:



Category 3

Approval of the version of the manuscript to be published:



Figure 4.1: prepared by

Figure 4.2: prepared by

Figure 4.3: prepared by

Figure 4.4: prepared by

Figure 4.5: prepared by

Figure 4.6: prepared by



**Chapter 4 | Photocatalysts for water
splitting from plastic scrap:
Ultrafast spark plasma
synthesis of NbO₂F and
Nb₃O₇F by solid state
fluorination of Nb₂O₅**

Chapter 4.1 Motivation

“Sustainability, energy efficiency, and economic viability have become increasingly important for materials manufacturing in industry. The political course set for the reduction of greenhouse gases is offset by the fact that still 7% of the primary energy in Germany is used for industrial high-temperature processing ($> 1000^{\circ}\text{C}$) of metals and ceramics. Spark Plasma Sintering (SPS) (or Field Assisted Sintering Technology, FAST) might allow to overcome this problem which allows manufacturing of materials with unprecedented functionalities (nanostructured, composite or gradient materials) easily and at reduced costs. It is based on a modified hot-pressing process where the electric current passes directly through the pressing tool and the sample.^[1,2] An electric current allows for very rapid heating and cooling and very short process cycles. Reactions in electric fields affect the reaction kinetics by suppressing granular growth and may alter the nature of the final product.^[2,3-6] Although the mechanism of SPS reactions is still not well understood, the primary effect of current in sintering techniques is likely to be Joule heating, but other non-thermal effects may contribute to the solid state reaction kinetics as well. SPS allows making metastable materials with compositions and properties that cannot be obtained by conventional solid state chemistry. Although it has opened up new options for sintering materials,^[7,8] applications in solid state synthesis are still rare.^[9-11]

We have applied SPS for the synthesis of niobium oxyfluorides. The starting compounds, niobium oxides and fluoropolymers are chemically very unreactive and inert. Teflon waste falls off during processing, especially after sintering or as polymer scrap that does not meet specifications and cannot be used in its intended applications. Many fluoroplastics can be reused as they are thermoplasts and processes are being developed to convert scrap PTFE to usable feedstocks.^[12]

An elegant solution for waste recycling is to use fluoropolymers as starting compounds for fluorination reactions. Most of these reactions require fluorine gas, reactive fluorides, or hydrogen fluoride as toxic and corrosive sources of fluorine that need special equipment and sophisticated techniques for handling.^[13-15] The standard route to NbO_2F uses a concentrated aqueous HF solution that reacts with Nb_2O_5 , followed by slow evaporation to dryness and heating of the reaction products at elevated temperatures and different durations.^[16-27] The product composition depends on the sample history. HF adduct intermediates and mixed hydroxylated/fluorinated products $\text{Nb}_{1-x}\text{O}_{2-5x}(\text{OH},\text{F})_{1+5x}$ with OH defects and metal vacancies have been reported.^[28] Efficient fluorination has been carried out with HF under extreme conditions in sealed gold ampoules.^[29]

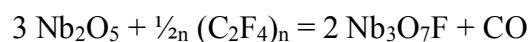
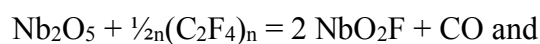
High-temperature approaches starting from binary fluorides (like MF_2 or MF_3 (M = alkaline-earth or lanthanide metal) have limitations because of the high stability of the starting compounds.^[30] Therefore, alternative fluorination routes have been pursued^[31,32] for making oxyfluorides.^[33,34,35] Small-scale fluorinations can be carried out using microwave chemistry.^[36,37] We report a very rapid fluorination of the very inert and unreactive niobium oxide Nb_2O_5 using SPS. Reductive fluorination of oxides starting from fluorinated polymers using conventional ampoule chemistry has been reported before.^[33-35,37,38] It benefits from the chemical stability of fluorinated polymers at room temperature and their relatively low decomposition temperature compared to inorganic solids. NbO_2F and $\text{Nb}_3\text{O}_7\text{F}$ were synthesized by reacting Nb_2O_5 with PTFE under SPS conditions. The reactions were complete after only ~ 6 minutes and led, depending on the ratio of the starting compounds, to the formation of the oxyfluorides NbO_2F , which is not accessible in conventional ampoule reactions, and $\text{Nb}_3\text{O}_7\text{F}$ in gram amounts, independent of the PTFE provider. The fluorination reaction appears to be controlled by solid state diffusion of the PTFE decomposition products. The cubic NbO_2F phase exhibits F atom disorder as demonstrated by ^{19}F magic angle spinning nuclear magnetic resonance (MAS-NMR) experiments.^[4,40]

The conceptual advancement of the SPS synthesis lies in the combination of the fluorination with fluorinated polymers and SPS. SPS is typically used for the consolidation of ceramics and alloys, while “reactive SPS” is only rarely used in a “one-pot” approach for a fast and energy or cost-efficient synthesis of functional solids from molecular precursors.^[3,11,42] The SPS reaction yields monoliths of NbO_2F and $\text{Nb}_3\text{O}_7\text{F}$ with high photocatalytic activity in water splitting reactions. This indicates that new photocatalytic compounds based on cheap, air-stable, and environmentally benign elements^[43] may be discovered by SPS processing of plastic scrap.

Chapter 4.2 Results and Discussion

Chapter 4.2.1 SPS Reaction and Chemical Analysis

NbO₂F and Nb₃O₇F were synthesized by reactive SPS from Nb₂O₅ and PTFE with minor impurities (Figure 4.1) according to



In the first step for NbO₂F, the starting materials PTFE and Nb₂O₅ were mixed in a planetary ball mill with ethanol as dispersion medium for 5 h prior to the reaction. For Nb₃O₇F the precursors were used directly without prior preparation. In a subsequent, pyrometer-controlled step the reactants were heated using the temperature profile shown in Figure 4.1 with 600°C as dwelling temperature for NbO₂F and 900°C for Nb₃O₇F. The products typically contained phase mixtures with densities > 95% of the calculated theoretical density.

The reaction of Nb₂O₅ with polytetrafluoroethylene (PTFE) is assumed to occur at the gas-solid interface, because PTFE is known to thermolyze slowly above 360°C.^[44] Thermolysis is complete above 400°C (as shown by thermal analysis). The main decomposition product under vacuum conditions is the C₂F₄ monomer.^[44,45] In the reactive SPS experiments volatile C₂F₄ resulting from the thermal decomposition of the fluorinated polymers in the carbon die diffuses into the Nb₂O₅ pellet during the reaction. The actual fluorination mechanism is not known in detail because (i) the phase of C₂F₄ under the reaction conditions (19-50 MPa, 600/900°C) can only be estimated and (ii) follow-up reactions of C₂F₄ may form other fluorocarbons depending on reaction temperature and pressure, especially since gaseous C₂F₄ can leave the reaction volume before it reacts with the oxide. In case of SPS, which uses a dynamic vacuum, it is then lost for further reaction.

Chapter 4.2.2 Phase analysis

Phase analysis of the samples was carried by X-ray powder diffraction and transmission electron microscopy. A large excess of fluorinated polymer ($x_{\text{cub}} \geq 1.5$) is required to achieve high fluorine contents in NbO₂F and Nb₃O₇F ($x_{\text{orth}} \geq 1$), where x describes the calculated F:Nb ratio in the educt mixtures to obtain cubic NbO₂F (x_{cub}) and orthorhombic Nb₃O₇F (x_{orth}). Compared to the synthesis for tungsten and tantalum oxyfluorides, phase pure NbO₂F could only be obtained by SPS processing, with very minor impurities (~1%), while conventionally prepared samples showed 10-15% of side phases (see Table S1).^[34,35,38,39] In addition, reductive

fluorination in reactive SPS are orders of magnitude faster (9 minutes vs. 24 h), and the yields can be upscaled to the kg range with an appropriate die.^[2]

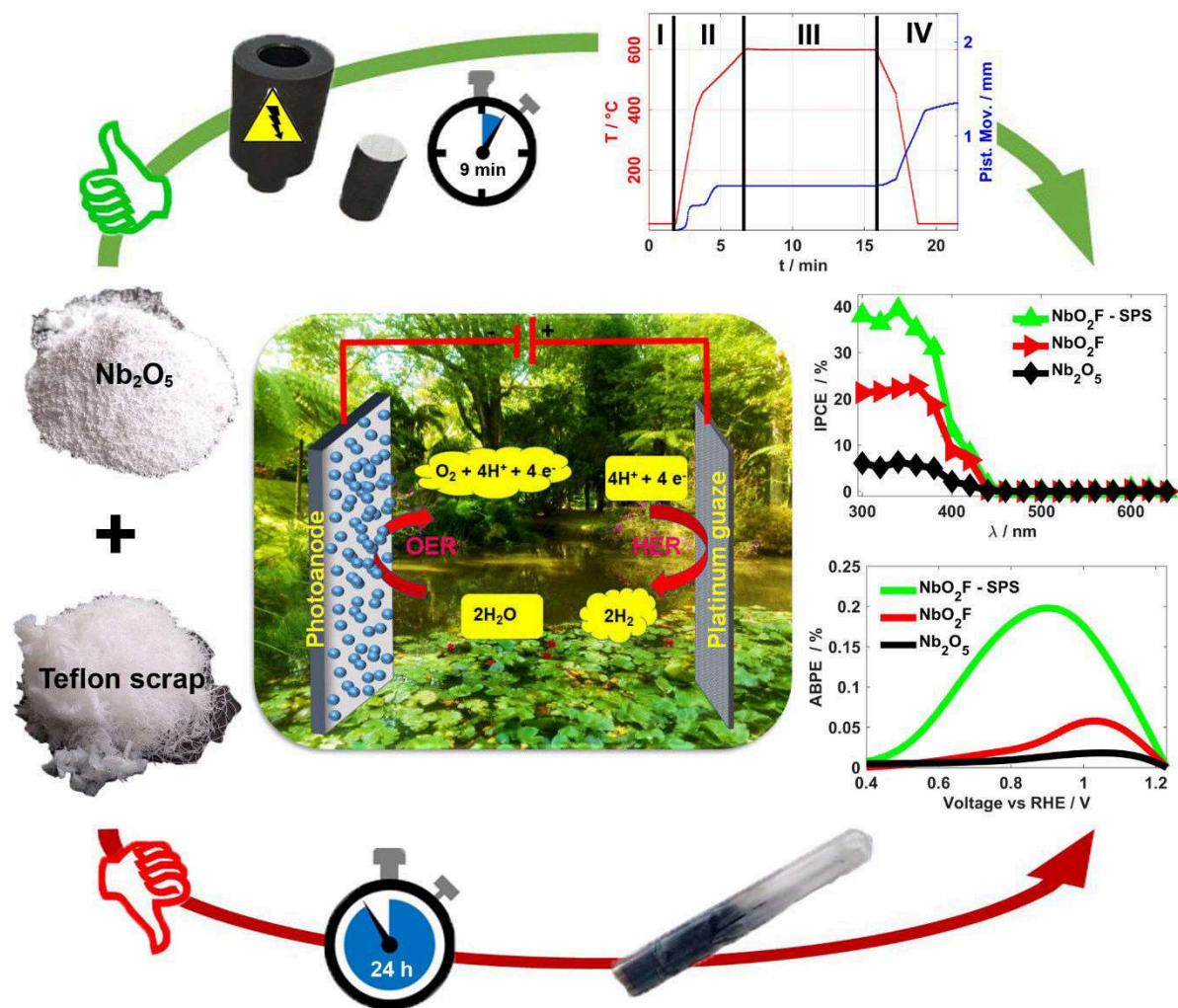


Figure 4.1. General approach to convert Nb_2O_5 and Teflon scrap to niobium oxyfluoride photocatalysts by SPS (top) and conventional synthesis (bottom) and effect of the synthesis on photocatalytic properties. Results for SPS processing are shown in green, for conventional ampule chemistry in red. A temperature profile of the SPS program is shown on the top right (red) including the absolute piston movement/densification (blue) during the SPS process of NbO_2F . Capital letters indicate different segments of the process: **I** Evacuation of reaction chamber and first compression, **II** start of reaction by heating to 600°C with 50°C/min, **III** dwelling at 600°C for 9 min from and **IV** sample cooling. For $\text{Nb}_3\text{O}_7\text{F}$ heating was carried out up to 900°C. All other parameters remained unchanged.

The cooled cylindrical pellets were removed from the die, treated with SiC abrasive paper to clean the surface, and finally crushed with a mortar. The obtained powders were used for electron microscopy and physical characterization. The X-ray diffraction (XRD) patterns of NbO_2F and $\text{Nb}_3\text{O}_7\text{F}$ (Figure 4.2A and B and Figure 7.3.2A and B) could be indexed based on cubic (space group: $Pm\bar{3}m$) and orthorhombic (space group: $Cmmm$) unit cells, respectively.

Crystallographic details and essential results of the Rietveld refinements for NbO_2F and $\text{Nb}_3\text{O}_7\text{F}$ are compiled in Table 7.31. NbO_2F obtained from reactive SPS and $\text{Nb}_3\text{O}_7\text{F}$ via conventional solid-state synthesis is nearly phase pure, with only minor impurities of $\text{Nb}_3\text{O}_7\text{F}$ (~1%). NbO_2F obtained by conventional solid-state reaction contains larger impurities of $\text{Nb}_3\text{O}_7\text{F}$, and $\text{Nb}_3\text{O}_7\text{F}$ was obtained with minor impurities of NbO_2F (~2%) from reactive SPS and phase pure by conventional solid-state reaction. The powder diffractograms of the samples show significant anisotropic peak broadening which is even more pronounced in the samples prepared by reactive SPS. To achieve satisfactory Rietveld refinements, strain parameters based on the Stephens broadening model were applied.^[46]

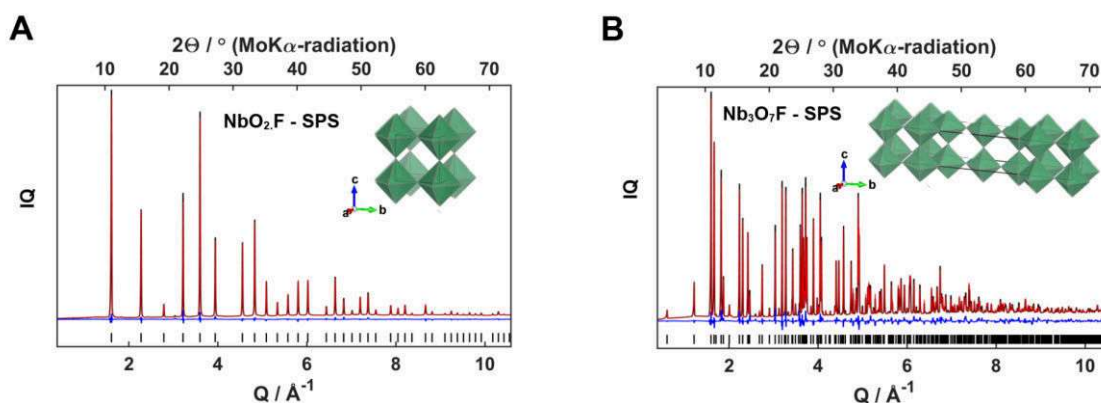


Figure 4.2. (A) Rietveld refinement of SPS-prepared NbO_2F (red line) using X-ray powder data. (B) Rietveld refinement of SPS-prepared $\text{Nb}_3\text{O}_7\text{F}$ (red line) using X-ray powder data. Experimental data are indicated by black crosses, the calculated curve obtained after the refinement is indicated by a continuous line. The continuous blue curve above the tick marks indicates the differential curve between calculation (red) and experimental data (black). The tick marks correspond to the reflexes of the main compounds, cubic NbO_2F (A) and orthorhombic $\text{Nb}_3\text{O}_7\text{F}$ (B). The insets show polyhedral representations of the structures.

Although the reactive SPS approach prevents the formation of mixed hydroxylated/fluorinated products $\text{Nb}_{1-x}\text{O}_{2-5x}(\text{OH},\text{F})_{1+5x}$ with OH defects and metal vacancies (encountered in the HF preparation), it is difficult to determine the positions of oxygen and fluorine accurately from the XRD data because the scattering contributions of O and F are virtually indistinguishable. Thus, the F content was determined by elemental analysis with a high resolution-continuum source-graphite furnace molecular absorption spectrometer (HR-CS-GRMAS). The results are compiled in Table 4.1 and, within the scope of experimental error, support the results of the phase analysis.

Table 4.1. Experimental and theoretical fluorine concentration (pure phases) and degree of fluorination for niobium oxyfluoride samples from SPS and conventional synthesis as determined by HR-CS-GFMAS.

SPS Sample	Fluorine conc. <i>via</i> HR-CS-GFMAS (g kg ⁻¹ ± sd)	Niobium conc. <i>via</i> HR-CS-GFMAS (g kg ⁻¹ ± sd)	F:Nb ratio	Theor. F:Nb
Nb ₃ O ₇ F - SPS (≥99%)	44 ± 11*	547 ± 13*	0.39 ± 0.06 :1	1:3
NbO ₂ F - SPS (≥99%)	125 ± 9*	648 ± 18*	0.95±0.07:1	1:1

*n = 3

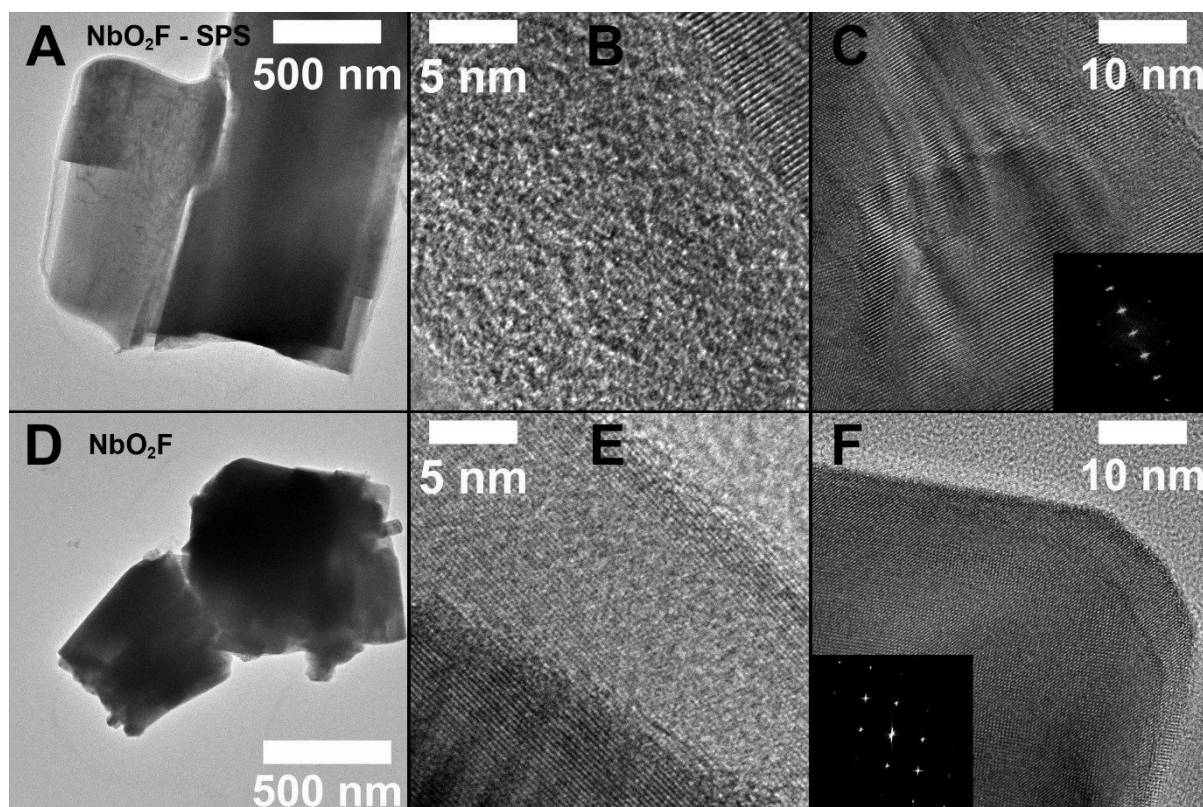


Figure 4.3. (A-C) (HR)TEM images of NbO₂F prepared by SPS, (D-F) and conventional chemistry. (A, D) show representative particles, which consist in both cases of several smaller crystallites. (B, E) show a zoom on the edges of the layered-like built particles. For the SPS product, the outer layer is thicker and less crystallized compared to the product obtained from of the conventional synthesis. (C, F) show magnified crystalline area. The SPS product shows less ordering and characteristics of twinning, because the Fourier transformations (insets) are more diffuse and the intensities are elongated along one axis.

Chapter 4.2.3 Micro and local structure of NbO₂F and Nb₃O₇F

TEM analysis shows that the oxyfluorides consist of agglomerated particles with diameters in the 20 nm -1 μm range (Figure 7.3.3). The NbO₂F samples have a much smaller size distribution, while samples of Nb₃O₇F contain more particles with sizes in the μm range (Figure 7.3.3). Reactive SPS synthesis leads to slightly smaller particle sizes, in particular for NbO₂F

(Figure 7.3.3A, C). This can easily be rationalized from the ball-milling treatment prior to the SPS synthesis of NbO_2F , while commercially available Nb_2O_5 was used as starting material for $\text{Nb}_3\text{O}_7\text{F}$. The niobium oxyfluoride particles consist of thin “plate-like” blocks, which is more pronounced in samples prepared by SPS (Figure 4.3A, 7.3.3A). Typically, the particles are surrounded by a layer which is thicker (10-25 nm vs. < 10 nm) and amorphous for SPS-prepared samples, while there are clear indications of crystallinity for conventionally prepared samples (Figure 4.3B, E and 7.3.2B,E). Crystalline areas of SPS-prepared samples show features that hint to disorder in the crystal structure, thereby confirming the higher strain values and preferred orientation derived from the Rietveld refinements and appearing in the Fourier transformations of their TEM images (insets of Figure 3C, F and Figure S2C, F).

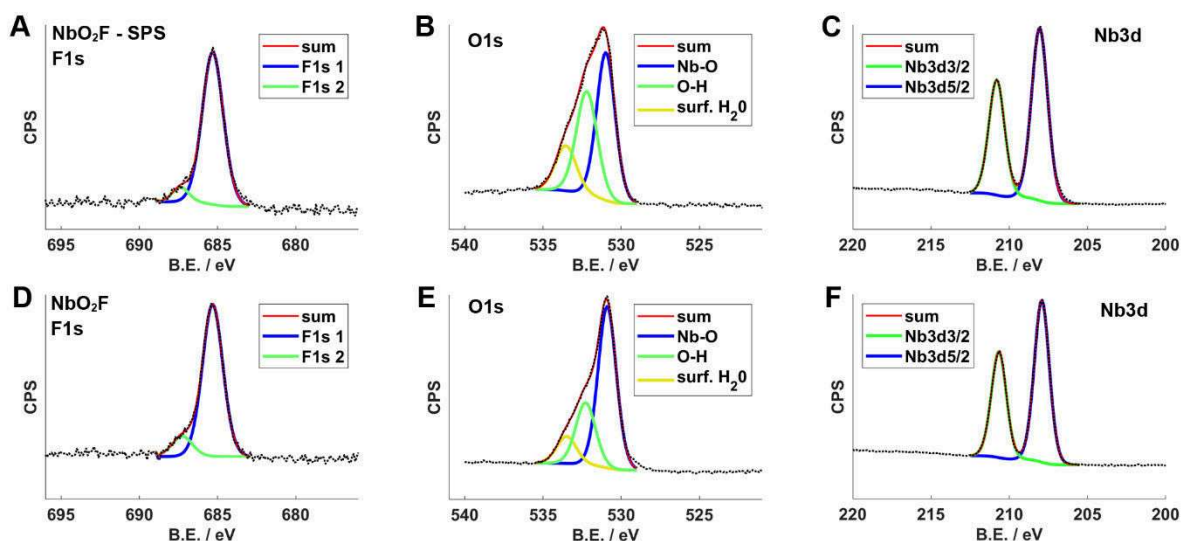


Figure 4.4. (A-F) XPS spectra (with F, O, and Nb sub-spectra in (A,D), (B,E) and (C,F)) of NbO_2F , prepared by SPS (A-C) and conventional ampoule chemistry (D-F) with fitted signals for the respective environments.

XPS spectra were recorded out to investigate the surface layer of the niobium oxyfluorides. Survey spectra are shown in Figure 7.3.4. XPS (surface analysis) show much higher fluorine contents on the surface for SPS- compared to conventionally prepared samples. In addition, more niobium is present on the particle surface for SPS-prepared material. As a consequence, SPS-prepared samples show a much higher F:O ratio on the surface than their conventional counterparts (1:4 for NbO_2F and 1:6 for $\text{Nb}_3\text{O}_7\text{F}$ compared to 1:6 and 1:8 for conventionally prepared samples). In essence, for conventionally prepared NbO_2F and $\text{Nb}_3\text{O}_7\text{F}$ a larger amount of fluorine atoms is located in the bulk and less niobium is exposed at the surface. This supports the assumption that the SPS synthesis – different from conventional high temperature synthesis - freezes the product before an equilibrium and even distribution of the atoms can be achieved.

We assume that the elemental surface distribution and the higher strain and defect density are responsible for the enhanced oxygen evolution activity, although the exact pathway of the water splitting reaction is unclear. The fluorine signal (Figure 4.4A, D) shows two peaks. The main peak can be attributed to fluorine bound directly to bulk Nb atoms, the smaller signal to fluorine atoms either bound to carbon atoms or to niobium with neighboring –OH groups within the amorphous surface layer of the particles or with adjacent vacancies. The Nb 3d region (Figure 4.4C, E) shows the expected two signals for Nb 3d_{3/2} and 3d_{5/2} with an area ratio of 2:3. Three signals appear in the oxygen region which can be attributed to oxide, hydroxide oxygen or oxygen species linked to defect sites and adsorbed surface water. Analysis of the spectra by deconvolution of the element signals shows a much larger second O peak for SPS-prepared NbO₂F (compared to conventionally prepared NbO₂F), while an opposite trends was observed for Nb₃O₇F (Figure 7.3.5). SPS-prepared samples show less surface H₂O and -OH than conventionally prepared ones, resulting in less surface deactivation.^[38] We assume this signal to be associated with oxide species in “distorted” coordination or adjacent to vacancy sites. To further analyze the local environment we recorded ¹⁹F solid state NMR spectra at three different magic angle spinning speeds (MAS) to determine the ¹⁹F isotropic shifts and distinguish spinning side band from fluorine signals. The spectra measured at 29 kHz MAS were analyzed by deconvolution in terms of chemical shift related with the electronic environment of fluorine and full width at half height (fwhm) related with the local order. The ¹⁹F ssNMR spectra of the conventionally and SPS-prepared NbO₂F and Nb₃O₇F samples reveal three types of signals after deconvolution: One main resonance in the range between -50 and -60 ppm and two less intense peaks ranging from -26 to -33 ppm and -72 to -85 ppm. All signals are associated with bridging F atoms with shifts depending on the number of F/O atoms connecting adjacent octahedra in the structure.^[41] All resonances are inhomogeneously broadened (fwhm from 2 to 6 kHz) which corresponds to a broad distribution of environments (i.e., low local order with broader peaks) and therefore low local order for the SPS-prepared samples. The low field shifts correspond to one other fluorine atom in the environment of the bridging fluorine atoms. The signal at -50 to -60 ppm corresponds to 3-4 fluorine atoms and the high field shifted signal to more than five fluorine atoms in the vicinity of a bridging one.^[41] The presence of vacancies of the type F-Nb-□ as well as the terminal F atoms cannot be confirmed unambiguously as the expected chemical shift ranges at ~ 50 ppm and -130 ppm overlap with spinning sidebands from the main resonance for all cases and spinning speeds. For the SPS-prepared materials these areas are slightly more pronounced. This supports the results

of the TEM and XPS studies that no equilibrium distribution of F atoms and a higher degree of disorder exists as a result of SPS processing.

Chapter 4.3 Band Gap and Photoelectrochemical Water Splitting

The band gap energy (E_g) of a semiconductor photocatalyst is essential for applications in light-driven processes. E_g values were derived from diffuse reflectance spectra (Figure 4.5A) with the Kubelka-Munk function by plotting $(Fh\nu)^{1/2}$ as a function of photon energy ($h\nu$), where F is the normalized Kubelka–Munk function of the diffuse reflectance R (Figure 7.3.6).^[47] The band gaps for SPS-prepared NbO_2F and $\text{Nb}_3\text{O}_7\text{F}$ are 3.29 eV and 3.39 eV, whereas the respective values for conventionally prepared NbO_2F and $\text{Nb}_3\text{O}_7\text{F}$ are slightly larger (3.36 eV and 3.54 eV). The absorption range of the SPS-prepared materials extends as a broad shoulder in the visible region, especially that for NbO_2F . Surface states or the morphology of nanostructured materials can affect the band-edge positions significantly.^[48] In order to determine the effect of the preparation method and fluorination on the flat band potential shift, a Mott-Schottky analysis was performed under 1 Sun light (Figure 4.5B). The positive slope of the Mott-Schottky plot indicates a n-type behavior. Moreover, a significant shift in the flat band potentials between Nb_2O_5 (-0.61 V vs. RHE) and SPS-prepared NbO_2F (-0.39 V vs. RHE) is observed. This anodic shift of flat band potential after fluorination signifies the enhancement in the charge densities (charge carrier concentration). The shift of flat band potentials derived from the Mott-Schottky plots also relates the reorientation of valence and conductance bands (bandgap slightly reduced) upon fluorination (Figure 7.3.6). We have also calculated the theoretical optical conduction band (E_{CB}) and valence band (E_{VB}) positions using empirical equations (Supplementary Information). The derived band gap values are shown in Figure 7.3.8 and are compiled in Table 7.3.5.

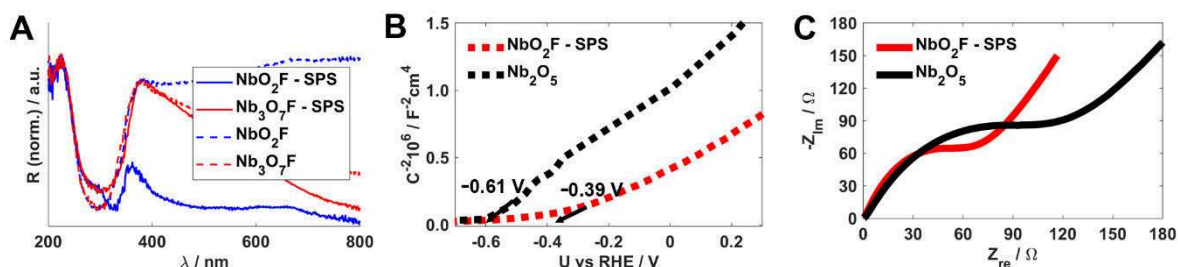


Figure 4.5. (A) UV-Vis diffuse reflectance spectra of $\text{Nb}_3\text{O}_7\text{F}$ (blue line) and NbO_2F (red line) prepared by SPS (solid lines) and conventional ampoule chemistry (dashed lines). (B) Mott-Schottky plot, and (C) EIS Nyquist plot spectra under illumination.

Electronic impedance spectroscopy (EIS) under simulated solar condition was used to study the interfacial charge transfer (Figure 4.5C). Measurements were conducted by sweeping a DC voltage across the working electrode. The data is represented in terms of Nyquist plots. The comparative analysis of Nyquist plots radii shows that SPS-prepared NbO₂F has a lower radius (lower interfacial resistance) than Nb₂O₅, which indicates the better charge transfer kinetics for the photoanode of the SPS-prepared material.

Chapter 4.3.1 Photoelectrochemical water splitting mechanism

The performance of materials in PEC water splitting is proportional to the generation of electron-hole pairs in the conduction and valence bands of semiconductors. These pairs are highly mobile and induce chemical reactions leading to water splitting at the interface of the semiconductor. A major drawback of the excited states is their quick recombination. Therefore, most of the energy is dissipated as heat.^[48,49] Upon fluorination, the rate of recombination can be reduced by “inserting” additional energy levels which provide alternative pathways for excitons to enhance their life time.^[50,51,52,53,54] Photoanodes prepared from NbO₂F, Nb₃O₇F and pristine Nb₂O₅ synthesized by SPS and conventional ampule chemistry were tested for their PEC water oxidation performance under simulated 1-SUN light in three-electrode PEC cell. The linear sweep voltammetry (LSV) results are shown in Figure 4.6A. The NbO₂F and Nb₃O₇F photoanodes prepared by SPS showed higher photocurrent densities (0.92 and 0.58 mA cm⁻² @ 1.23 V vs. RHE) with lower onset potential compared to photoanodes prepared by conventional ampule chemistry and pristine Nb₂O₅ (i.e., 0.45, 0.36 and 0.13 mA cm⁻² @ 1.23 V vs. RHE, respectively). The LSV plots indicate a strong correlation between the photocurrent density and preparation method. The results from water oxidation are summarized in Table 4.2. Table 4.2 and Figure 4.6A show that pristine Nb₂O₅ photoanodes have the lowest photocurrent density of 0.13 mA cm⁻² @ 1.23 V vs. RHE, which agrees well with the flat band potential positions indicated by the Mott Schottky plot (Figure 4.6A and B). In comparison, the niobium oxyfluorides, in particular the SPS-prepared samples, generated higher photocurrent densities, i.e., 0.92 mA cm⁻² @ 1.23 V vs. RHE for SPS-prepared NbO₂F (~ 7 times higher than that for pristine Nb₂O₅). The SPS-prepared Nb₃O₇F photoanode showed a photocurrent density of 0.58 mA cm⁻² @ 1.23 V vs. RHE. Additionally, the transient photocurrent density analysis in Figure 4.6C demonstrates a periodic recovery of the photocurrent density upon cyclic illumination and de-illumination. The photoanodes were stable for several cycles under intermittent chopped

light conditions. All samples show a constant photocurrent density level even after 1000 s of continuous illumination at 1.23 V vs. RHE (Figure 4.6D). The higher values for the SPS-prepared samples can be explained by the non-equilibrium nature of the SPS prepared materials due to the short reaction time for solid state reactions, which leaves the material after the reaction “shock-frozen” in a more disordered state. This is confirmed by the presence of more crystallite-interfaces, the higher disorder in the crystal structure and the higher fluorine content on the particle surface as determined by HR-TEM, SEM, PXRD refinement, MAS F-NMR and XPS measurements.

Chapter 4.3.2 Photoconversion Efficiency

The wavelength-dependent incident photon-to-current efficiency (IPCE) was calculated according to

$$IPCE (\%) = \frac{1240 \times I_{photon}}{\lambda \times P_{incident\ light}}$$

where, I_{photon} , λ and $P_{incident\ light}$ indicate the photocurrent (mA), the wavelength of the incident light (nm), and the incident irradiating power at the specific wavelength (mW).

A Xe lamp fitted with band-pass monochromatic irradiation filters (central wavelengths: 400-600 nm with 20 nm in each pass) was used to measure the IPCE (%) dependence at each value. The monochromatic incident light was quantified by equation 1 and plotted as a function of wavelength (λ) at 1.23 V vs. RHE (Figure 4.6E). The % IPCE analysis showed higher sustainability values for SPS-prepared NbO₂F and Nb₃O₇F (39.33% and 25.96 %, respectively) than for pristine Nb₂O₅ (6.14%). NbO₂F and Nb₃O₇F prepared by conventional ampoule chemistry showed photon-to-current efficiencies of 22.29% and 16.74% (Figure 4.6F). The maximum absorption occurs in the range of 300-450 nm. The % IPCE data for all samples are compiled in Table 4.2.

We transformed the I - V data (recorded by a 3-electrode system) to % applied bias to photo-conversion (% ABPE) efficiency according to

$$ABPE (\%) = \frac{J_{ph}(1.23 - |V_{app}|)}{P_{light}} \times 100 \quad (2)$$

where, J_{ph} is the photocurrent density (mA cm⁻²), V_{app} is the applied potential vs. RHE, and P_{light} is the power density of illumination (100 mW cm⁻²).

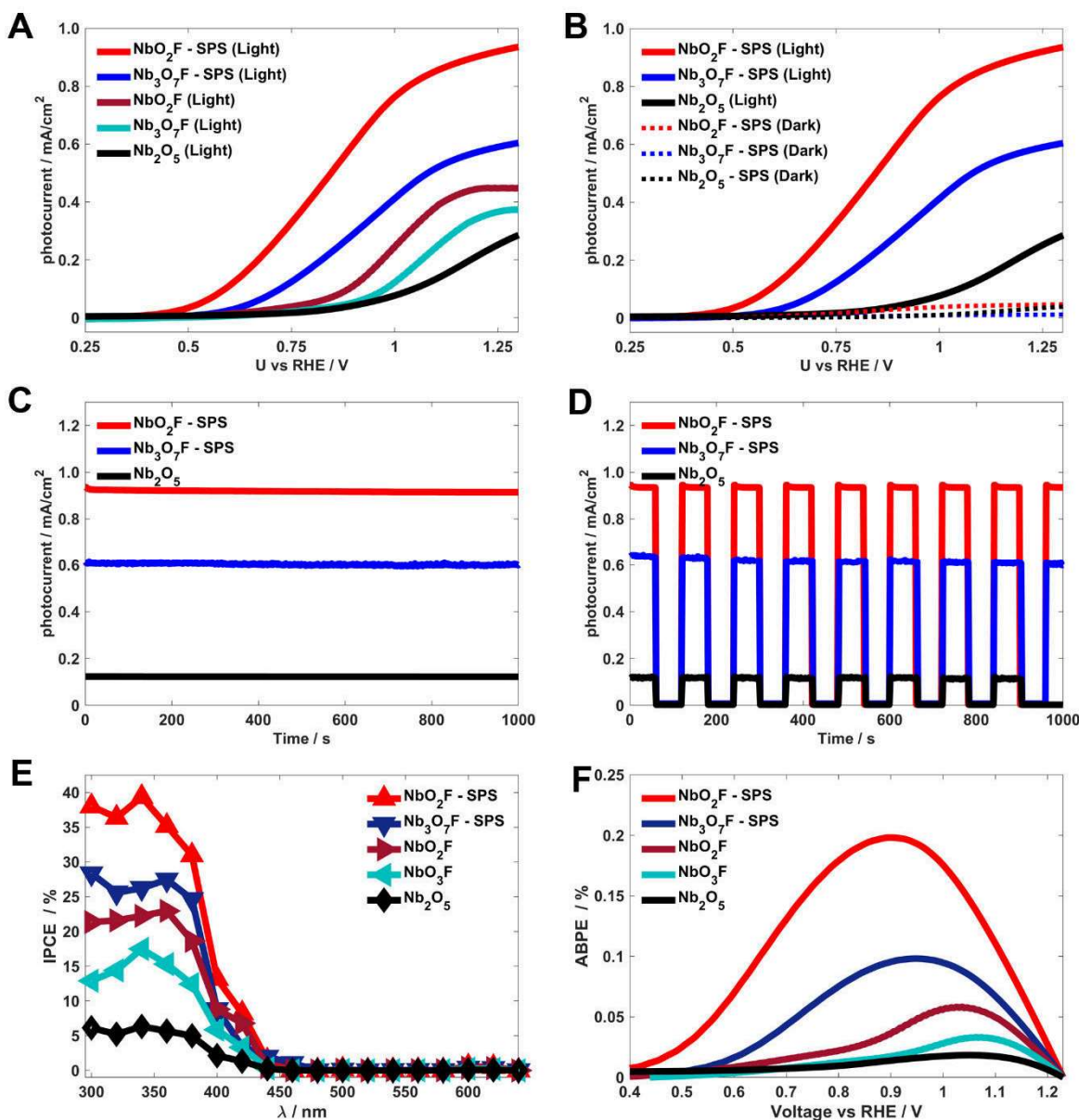


Figure 4.6. Photoelectrochemical (PEC) measurements for Nb₂O₅ and the niobium oxyfluorides NbO₂F and Nb₃O₇F, prepared by SPS and conventional ampoule chemistry (A, B) Linear sweep voltammograms under light and dark conditions, (C) *I-t* photostability curve under continuous luminescence at 1.23 V vs RHE, and (D) amperometric *I-t* curves at an applied potential of 1.23 V vs RHE with 20 s ON/OFF cycle. (E) Incident photon-to-current efficiencies, IPCE (%) and (F) applied bias to photo-conversion ABPE (%) for Nb₂O₅, Nb₃O₇F (SPS-prepared and conventional synthesis) and NbO₂F (SPS-prepared and conventional synthesis).

The results are plotted in Figure 4.6E. SPS-prepared NbO₂F shows the highest value for % ABPE (*i.e.*, 0.198% @ 0.89 V vs. RHE), about one order of magnitude higher than the corresponding value for pristine Nb₂O₅ and 3.4 times higher than for NbO₂F prepared by conventional ampoule chemistry. Similarly, SPS-prepared Nb₃O₇F photoelectrodes showed a higher % ABPE value (0.098 % @ 0.90 V vs. RHE) than Nb₃O₇F photoelectrodes prepared by

conventional ampoule chemistry. These results underline the effect of materials processing for the light-induced characteristics of the photoelectrode materials and especially the prospect of SPS in enhancing these properties.

Table 4.2. Results from water oxidation measurements

Sample	Onset potential (V) vs. RHE	Photocurrent density (mAcm ⁻²) @ 1.23 V _{RHE}	% ABPE @ V _{RHE}	% IPCE
NbO ₂ F-SPS	~ 0.61	0.02	0.198 % @ 0.89 V _{RHE}	39.33
Nb ₃ O ₇ F-SPS	~ 0.51	0.58	0.098 % @ 0.90 V _{RHE}	25.96
NbO ₂ F	~ 0.94	0.45	0.059 % @ 1.03 V _{RHE}	22.29
Nb ₃ O ₇ F	~ 0.85	0.36	0.032 % @ 1.06 V _{RHE}	16.74
Nb ₂ O ₅	~ 1.05	0.13	0.019 % @ 1.08 V _{RHE}	06.14

Chapter 4.4 Summary

We demonstrated a very fast chemical and environmentally benign fluorination route to niobium oxyfluoride photocatalysts by SPS processing using Teflon scrap as non-toxic, solid, unreactive and highly abundant source of fluorine and without any caustic chemicals. Reactive SPS reduces the energy costs for preparation by several orders of magnitude, because the reaction and processing times could be decreased to a few minutes rather than days. The local structure due to SPS processing (e.g., strain and atom disorder) makes NbO₂F (with ReO₃-type structure) a very active photocatalysts with F/O disorder. It shows, even in the absence of co-catalysts, an excellent photocatalytic activity for oxygen evolution. The photoconversion efficiencies reached 39 % and applied bias to photoconversion values of 0.2 %. In contrast, NbO₂F prepared by conventional high temperature chemistry shows only a moderate photoactivity. SPS-prepared Nb₃O₇F exhibits unique electronic properties as well, leading to promising electron transfer abilities for photocatalytic oxygen generation. The pronounced change of the materials properties due to structural metastability resulting from SPS processing poses new challenges for computational chemistry to analyze, understand and predict the underlying factors which are not captured in the crystal structures of equilibrium compounds. Variations of the microstructures due to atom disorder, grain boundary effects and thus active surface sites are typically not taken into account in electronic band structure calculations. The results of study pose new challenges to theory development like Materials Genome Initiative (MGI) that strives to accelerate materials deployment through complementary efforts in theory, computation, and experiment.^[55] In summary, this study is a proof of concept for the rapid and energy-saving production of valuable photocatalysts for water splitting from plastic waste. It

opens new perspectives for the recycling of plastic waste and the search of stable photocatalysts by materials processing.

Chapter 4.5 Experimental methods

Synthesis. Niobium (V) oxide (99+%, Chempur) and poly(tetrafluoroethylene) (PTFE, Sigma-Aldrich, 1 μm powder) were weighed in their respective molar ratios, ball-milled (Fritsch Pulverisette) for 5 h in ethanol and dried after centrifugation overnight at 70°C in a drying chamber. Nb_2O_5 and PTFE were used in stoichiometric amounts for $\text{Nb}_3\text{O}_7\text{F}$ and with excess PTFE for NbO_2F . Samples prepared with PTFE from Acros and fluorochem led to the same products.

For the SPS preparation of $\text{Nb}_3\text{O}_7\text{F}$ and NbO_2F , samples containing ≈ 2 g of the powder mixtures were enclosed with graphite foil and placed in graphite dies. Afterwards, the dies were placed into an SPS HP D 25 (FCT-systems) and heated up to 600°C with 50°C/min at 19 MPa and kept at this temperature for 9 min. Reference samples for conventional high temperature reactions were prepared by placing powder mixtures in evacuated quartz ampules and heating for 12 h at 650°C to obtain NbO_2F (≈ 300 mg) and for 36 h at 650°C to obtain $\text{Nb}_3\text{O}_7\text{F}$ (≈ 500 mg).

X-Ray powder diffraction analysis. Samples for X-Ray diffraction were prepared on polyvinylacetate-foil. Diffractograms were obtained using a STOE Stadi P, equipped with a Mythen 1k detector using $\text{MoK}\alpha_1$ radiation. The sample was measured in transmission in 0.015° steps (continuous scan, 150 s/°) covering a 2θ range from 1.5° to 43°. Rietveld refinement^[56] was performed with Topas Academic V6 using the fundamental parameters approach^[57] Crystalline phases were identified according to the PDF-2 database (PDF-2, Release 2004, JCPDS – International Center for Diffraction Data, Newton Square (PA) US (2004)) using Bruker AXS.^[58]

Brunauer/Emmett/Teller (BET) sorption. BET measurements were conducted using the gas adsorption setup Autosorb-6B from Quantachrome with nitrogen as analysis gas. The temperature during the measurements was 77 K. Data evaluation was conducted with the software Quantachrome ASiQWin 3.0.

Transmission electron microscopy (TEM). Powdered samples were prepared by placing one drop (10 μL) of a diluted NP solution in ethanol (0.1 mg mL^{-1}) on a carbon-coated copper grid and by letting it dry at room temperature for transmission electron microscopy (TEM), high-resolution TEM (HRTEM), electron dispersive X-ray spectroscopy (EDXS). TEM, HRTEM

and EDX measurements were carried out with a FEI TECNAI F30 S-TWIN transmission electron microscope equipped with a field emission gun and working at 300 kV. TEM images and nano electron diffraction (NED) patterns were taken with a CCD camera (16-bit 4.096 x 4.096 pixel GATAN ULTRASCAN4000) and acquired by Gatan Digital Micrograph software.

X-ray photoelectron spectroscopy (XPS). XPS measurements were carried out on an Axis Ultra *DLD* imaging photoelectron spectrometer. Measurements were carried out using the Hybrid mode with 10 mA and 15 kV at the Al anode. The analysis area was 700 μm \times 300 μm (i.e., X-ray spot size). Survey spectra were measured at a pass energy of 80 and elemental spectra at 20 pass energy of the analyzer. All spectra were charge corrected to a binding energy of 284.8 eV for the C 1s line corresponding to adventitious aliphatic carbon. Measurements were evaluated using the CasaXPS software.

UV–Vis spectroscopy. Ultraviolet–visible (UV–vis) reflectance spectra ranging from 200 to 800 nm were collected on a Cary 5G UV–vis–NIR spectrophotometer using an Ulbricht sphere. BaSO₄ was used as white standard. The samples were measured by mixing a few mg of powder with BaSO₄ and pressing the mixture into a pellet.

Nuclear magnetic resonance (NMR) spectroscopy. Solid state NMR spectroscopy. All solid-state NMR experiments were recorded on a Bruker Avance 400 DSX spectrometer at ¹⁹F frequency of 376.25 MHz. A two-channel commercial Bruker 2.5 mm probe head at spinning speeds of 25 kHz was used for ¹⁹F direct excitation measurements. No changes in the spectra are expected at slightly elevated temperatures, so no temperature correction for the frictional heating due to the sample rotation was performed. All spectra were background corrected.

Scanning electron microscopy (SEM). Field-emission scanning electron microscopy was performed on a NOVA Nano-SEM with an attached Oxford Inca X-ray system for chemical analysis. The obtained SPS pellets were cut and polished to obtain cross-sectional pieces. Secondary and backscattered electron images were collected with acceleration voltages of 5 keV and 15 or 20 keV for EDX mapping, respectively.

High resolution-continuum source-graphite furnace molecular absorption spectrometry.

HR-CS-GFMAS. Fluorine analysis was conducted by means of a HR-CS-GFMAS System ContrAA 800 G from Analytik Jena (Jena, Germany). Three independent samples were prepared. About 0.1 g of sample was weighed in and 10 mL of a Triton X 100 solution (0.1% (*w/v*)) were added. The sample suspension was sonicated for 15 min within an ultrasonication bath; afterwards each sample was vortex-mixed for 5 min. Before analysis, the sample slurries were vortex mixed again for 30 sec. Subsequently, 10 μL of the sample slurry and 10 μL of a

4g L⁻¹ Ca(NO₃)₂ x 4H₂O solution (dissolved in MilliQ water) (Ca as molecule forming agent) were injected into the graphite furnace of the system. The absorption wavelength was set to 606.440nm, and each sample was analyzed 4 times. Quantification was performed by external calibration with an aqueous fluoride standard (Certipur standard, Merck, Darmstadt, Germany).

Fabrication of photoanodes and PEC measurements. The photocatalytic water splitting was carried out in a three-electrode electrochemical cell, where Pt and saturated calomel electrode (SCE) acted as counter and reference electrodes. The working electrode was fabricated by drop casting as-synthesized Nb₃O₇F, NbO₂F and Nb₂O₅ powders on a fluorinated tin oxide (FTO) support.

In each photoelectrochemical reaction, 5 mg of the photocatalysts were suspended into a 1 mL equimolar mixture of ethanol/deionized (DI) water and sonicated at room temperature to obtain a uniformly dispersed mixture. Each solution was enriched with 5 μL of 0.5 % Nafion solution to increase the binding characteristics and the uniformity of the film on the ink-covered 1x1 cm² area of FTO. A 0.5 M Na₂SO₄ solution in DI water was used as electrolyte (pH 7.1) for the PEC measurements without any additional sacrificial agent.

All data was collected on an Autolab potentiostat supported by the NOVA software and simulated light source (Oriel Sol-AAA Newport). The intensity of the simulator is adjusted to one SUN after calibration with a silicon diode solar cell (Oriel-diode). A full light spectrum is used in all PEC measurements to provide a reasonable comparison of the PEC performance of the Nb₃O₇F, NbO₂F and Nb₂O₅ photoanodes.“

References

- [1] O. Guillon, C. Elsässer, O. Gutfleisch, J. Janek, S. Korte-Kerzel, D. Raabe, and C. A. Volkert, *Mater. Today* 2018, 21, 527- 536
- [2] O. Guillon, J. Gonzalez-Julian, B. Dargatz, T. Kessel, G. Schierning, J. Rathel, and M. Herrmann, *Adv. Eng. Mater.* 2014, **16**, 830-849.
- [3] Z. A. Munir, U. Anselmi-Tamburini, and M. Ohyanagi, *J. Mater. Sci.* 2006, **41**, 763-777.
- [4] R. Orru, R. Licheri, A. M. Locci, A. Cincotti, and G. Cao, *Mater. Sci. Eng. R* 2009, **63**, 127-287.
- [5] H. Yoshida, K. Morita, B.-N. Kim, K. Soga, *J. Ceram. Soc. Jpn.* 2016, **124**, 932-937
- [6] M. Joos, G. Cerretti, I. Veremchuk, P. Hofmann, H. Frerichs, D. H. Anjum, T. Reich, I. Lieberwirth, M. Panthöfer, W. G. Zeier, and W. Tremel, V₆O₁₁. *Inorg. Chem.* 2018, **57**, 1259–1268.

- [7] J. R. Friedman, J. E. Garay, U. Anselmi-Tamburini, and Z.A. Munir, *Intermetallics* 2004, **12**, 589-597.
- [8] W. Chen, U. Anselmi-Tamburini, J.E. Garay, J. R. Groza, and Z. A. Munir, *Mater. Sci. Eng. A* 2005, **394**, 132-138.
- [9] C. Recknagel, N. Reinfried, P. Höhn, W. Schnelle, H. Rosner, Yu. Grin, A. Leithe-Jasper, *Sci. Techn. Adv. Mat.* 2007, **8**, 357-363.
- [10] M. Beekman, M. Baitinger, H. Borrmann, W. Schnelle, K. Meier, G. S. Nolas, and Y. Grin, *J. Am. Chem. Soc.* 2009, **131**, 9642–9643.
- [11] D. Portehault, V. Maneeratana, C. Candolfi, N. Oeschler, I. Veremchuk, Y. Grin, C. Sanchez, and M. Antonietti, *ACS Nano* 2011, **5**, 9052-9061
- [12] A. Lakshmanan, *Sintering Techniques of Materials*, chapter 9. Intechopen, 2015.
- [13] P. R. Slater, J. P. Hodges, M.G. Francesconi, P. P. Edwards, C. Greaves, I. Gameson, and M. Slaski, *Physica* 1995, **C253**, 16-22.
- [14] S. Rüdiger and E. Kemnitz, *Dalton Trans.* **2008**, 1117–1127.
- [15] *Functionalized inorganic fluorides: synthesis, characterization and properties of nanostructured solids* (A. Tressaud, ed.), John Wiley & Sons, Ltd, 2010.
- [16] S. Andersson and A. Aström, *Acta Chem. Scand.* 1965, **19**, 2136–2138.
- [17] L. Jahnberg and S. Andresson, *Acta Chem. Scand.* 1967, **21**, 615–619.
- [18] L. Permér and M. Lundberg, *J. Solid State Chem.* 1989, **81**, 21–29.
- [19] C. Bohnke, J. L. Fourquet, N. Randrianantoandro, T. Brousse, and O. Crosnier, *J. Solid State Electrochem.* 2001, **5**, 1–7.
- [20] J. Köhler, A. Simon, L. van Wüllen, S. Cordier, T. Roisnel, M. Poulain, and M. Somer, *Z. Anorg. Allg. Chem.* 2002, **628**, 2683–2690.
- [21] H. Mizoguchi, M. Orita, M. Hirano, S. Fujitsu, T. Takeuchi, and H. Hosono, *Appl. Phys. Lett.* 2002, **80**, 4732–4734.
- [22] F. J. Brink, R. L. Withers, and L. Noren, *J. Solid State Chem.* 2002, **166**, 73–80.
- [23] J. Z. Tao and A. W. Sleight, *J. Solid State Chem.* 2003, **173**, 45–48.
- [24] T. Murase, H. Irie, and K. Hashimoto, *J. Phys. Chem. B* 2005, **109**, 13420–13423.
- [25] M. Cetinkol, A. P. Wilkinson, C. Lind, W. A. Bassett, and C.-S. Zha, *J. Phys. Chem. Solids* 2007, **68**, 611–616.
- [26] S. Sawhill and E. Savrun, *Ceram. Int.* 2012, **38**, 1981–1989.
- [27] C. R. Morelock, B. K. Greve, M. Cetinkol, K. W. Chapman, P. J. Chupas, and A. P. Wilkinson, *Chem. Mater.* 2013, **25**, 1900–1904.

- [28] A. P. Wilkinson, R. E. Josefsberg, L. C. Gallington, C. R. Morelock, and C. M. Monaco, *J. Solid State Chem.* 2014, **213**, 38–42.
- [29] W. Sleight, *Inorg. Chem.* 1969, **8**, 1764-1767.
- [30] Y. Kamihara, T. Watanabe, M. Hirano, and H. Hosono. *J. Am. Chem. Soc.* 2008, **130**, 3296- 3297.
- [31] P. R. Slater, *J. Fluorine Chem.* 2002, **117**, 43–45.
- [32] F. J. Berry, X. Ren, R. Heap, P.R. Slater, and M. F. Thomas, *Solid State Commun.* 2005, **134**, 621–624.
- [33] Y. Kobayashi, M. Tian, M. Eguchi, and T. E. Mallouk, *J. Am. Chem. Soc.* 2009, **131**, 9849–9855.
- [34] D. Hirai, E. Climent-Pascual, and R. J. Cava, *Phys. Rev. B* 2011, **84**, 174519
- [35] S. E. Dutton, D. Hirai, and R. J. Cava, *Mat. Res. Bull.* 2012, **47**, 714-718.
- [36] G. W. Bluck, N. B. Carter, S. C. Smith, and M. D. Turnbull, *J. Fluorine Chem.* 2004, **125**, 1873-1877.
- [37] H. J. Kitchen, S. R. Vallance, J. L. Kennedy, N. Tapia-Ruiz, L. Carassiti, A. Harrison, A. G. Whittaker, T. D. Drysdale, S. W. Kingman, and D. H. Gregory, *Chem. Rev.* 2014, **114**, 1170–1206.
- [38] M. A. Lange, Y. Krysiak, J. Hartmann, G. Dewald, G. Cerretti, M. N. Tahir, M. Panthöfer, B. Barton, T. Reich, W. G. Zeier, M. Mondeshki, U. Kolb, and W. Tremel, *Adv. Funct. Mater* 2020, **30**, 1909051.
- [39] D. Hirai, O. Sawai, T. Nunoura, and Z. Hiroi. *J. Fluorine Chem.* 2018, **209**, 43-48.
- [40] L.-S. Du, F. Wang, and C. P. Grey, *J. Solid State Chem.* 1998, **140**, 285-294.
- [41] J. Dabachi, M. Body, C. Galven, F. Boucher, and C. Legein, *Inorg. Chem.* 2017, **56**, 5219–5232.
- [42] M. N. Tahir, B. Oschmann, D. Buchholz, X. Dou, L. Wu, I. Lieberwirth, W. Tremel, S. Passerini, and R. Zentel, *Adv. Energ. Mater.* 2016, **6**, 1501489.
- [43] H. Zhang, Y. Li, Y. Wang, P. Liu, H. Yang, X. Yao, T. An, B. J. Woode, and H. Zhao, *J. Mater. Chem. A* 2013, **1**, 6563-6571.
- [44] B. B. Baker and D. J. Kasprzak, *Polym. Degrad. Stabil.* 1993, **42**, 181-188.
- [45] E. E. Lewis and M. A. Naylor, *J. Am. Chem. Soc.* 1947, **69**, 1968-1970.
- [46] P. W. Stephens, *J. Appl. Cryst.* 1999, **32**, 281-289.

- [47] S. E. McLain, D. T. Bowron, A. C. Hannon, and A. K. Soper, A Computer program developed for analysis of neutron diffraction data. ISIS Facility, Rutherford Appleton Laboratory, Chilton, Didcot, OXON, United Kingdom OX11 0QX
- [48] S. M. Sze and M. K. Le, *MSemiconductor Devices – Physics and Technology*, Wiley 2010
- [49] A. Hankin, F. E. Bedoya-Lora, J. C. Alexander, A. Regoutz, and G. H. Kelsall, *J. Mater. Chem. A* 2019, **7**, 26162–26176.
- [50] C. Lohaus, A. Klein, and W. Jaegermann, *Nat. Commun.* 2018, **9**, 4309.
- [51] J. C. Yu, Y. Ho, and J. Zhang, *Chem. Mater.* 2002, **14**, 3808-3816.
- [52] S. Y. Moon, E. H. Gwag, and J. Y. Park, *Energy Technol.* 2018, **6**, 459 – 469
- [53] L. Liu, Z. Mei, Y. Hou, H. Liang, A. Azarov, V. Venkatachalapathy, A. J. Kuznetsov, and X. Du, *Sci. Rep.* 2015, **5**, 15516.
- [54] Y. Zhu, J. Hu, D. Niu, X. Zhang, and S. Hu, *CrystEngComm* 2018, **20**, 6430-6437.
- [55] J. J. de Pablo, N. E. Jackson, M.A. Webb, L.-Q. Chen, J. E. Moore, D. Morgan, R. Jacobs, T. Pollock, D. G. Schlom, E. S. Toberer, J. Analytis, I. Dabo, D. M. DeLongchamp, G. A. Fiete, G. M. Grason, G. Hautier, Y. Mo, K. Rajan, E. J. Reed, E. Rodriguez, V. Stevanovic, J. Suntivich, K. Thornton, and J.-C. Zhao, *npj Comput Mater* 2019, **5**, 41. <https://doi.org/10.1038/s41524-019-0173-4>
- [56] H. Rietveld, *J. Appl. Crystallogr.* 1969, **2**, 65–71.
- [57] A. A. Coelho, *J. Appl. Crystallogr.* 2018, **51**, 210–218.
- [58] EVA 10.0 Rev. 1, Bruker AXS, Madison, WI/USA, 2003.

The contents of the following chapter are taken and partially adapted from *Adv. Funct. Mater.*, 2021, to be submitted.

Authorship contributions

Category 1

Conception and design of study:

[REDACTED]

Acquisition of data:

- [REDACTED] – preparation of samples.
- [REDACTED] – PXRD measurements.
- [REDACTED] XPS measurements.
- [REDACTED] HR-TEM and SEM images.
- [REDACTED] acquisition of UV/Vis-data.
- [REDACTED] – acquisition of neutron diffraction data.

Analysis and/or interpretation of data:

- [REDACTED] – PXRD and neutron diffraction refinement.
- [REDACTED] – HR-TEM and SEM analysis.
- [REDACTED] – Band-gap/UV-Vis analysis
- [REDACTED] – interpretation of XPS data.

Category 2

Drafting the manuscript:

[REDACTED]

Revising the manuscript critically for important intellectual content:

[REDACTED]

Category 3

Approval of the version of the manuscript to be published:



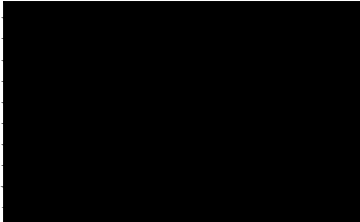
Figure 5.1: prepared by

Figure 5.2: prepared by

Figure 5.3: prepared by

Figure 5.4: prepared by

Figure 5.5: prepared by



Chapter 5 | Rapid Topochemical Nitridation of Ta₂O₅ with Vacancy-Assisted N³⁻/O²⁻- Exchange

Chapter 5.1 Motivation

“Transition metal oxides are in the focus of solid state science for almost a century because they form the material basis of solid state synthesis, solid state physics and technology, energy science or catalysis.^[1] Meanwhile, metal nitrides^[2] or compounds with multiple anions beyond the pure oxide ion (such as oxysulfides or oxyhalides) offer a new and extended materials platform from which new functionality may arise.^[3–5] In particular, transition-metal oxynitrides are emerging as a potent and promising class of materials, because their physical, chemical, and functional properties can be tailored by adjusting the oxygen-to-nitrogen ratio.^[6] This leads to potentially useful optical, electrical, magnetic, mechanical and photocatalytic properties.^[7–13]

Different from oxides, which exhibit a well-known structural chemistry and reactivity, the structures of mixed anion compounds are more complex and less explored, with much to learn. This becomes apparent immediately from the structure of oxynitrides, where the metal cations have more than a single anion neighbor. The different properties of the anionic constituents like charge, radius, electronegativity, or polarizability add more dimensions to the crystal chemistry, electronic structure and properties that are not available with the binary counterparts.

Even TaON, the simplest oxynitride of tantalum, exists in several modifications. β -TaON is the most stable polymorph.^[14] It is bright yellow (optical band gap of ~ 2.6 eV) in its thermodynamically equilibrated form, but can also be obtained in a green color, possibly due to more Ta-N bonds. It crystallizes in the monoclinic baddeleyite-type structure also reported for ZrO₂.^[15] The synthesis conditions play a key role for the formation of defects and strain in β -TaON, which in turn influence the photocatalytic properties.^[16] A metastable polymorph is the orange-colored (optical band gap of ~ 2.15 eV) γ -TaON adopting a VO₂(B) type-structure.^[17] Both, β - and γ -TaON, have an ordered distribution of oxygen and nitrogen atoms.^[18] δ -TaON, prepared by reacting gaseous NH₃ with amorphous Ta₂O₅, crystallizes in the anatase structure-type.^[19] Computational methods have been used to verify and predict structures of TaON with notable success,^[20–22] and allowed to reject an α -TaON polymorph, that was reported erroneously.^[23] Pressures $> \sim 31$ GPa were predicted to induce a phase transformation from β -TaON (7 coordination of Ta) to a cotunnite-type structure (9 coordination of Ta), which could be verified experimentally.^[24] The transformation of metastable red δ -TaON (anatase-type) with ordered anion structure to β -TaON is kinetically controlled.^[19]

Oxynitrides are prepared by annealing the corresponding oxides at elevated temperatures under a flow of gaseous ammonia or from Chlorides under inert gas conditions with liquid ammonia.¹⁵ These reactions with a toxic and corrosive reactant need special equipment and sophisticated techniques for handling. Ta₂O₅ reacts with gaseous ammonia at 700-900°C with reaction times of several hours to days.^[25,26] The exchange of oxide against nitride anions in ammonolysis reactions is characterized by transport lengths of 1 to 10 μm. This is crucial because diffusion coefficients in the solid state are in the order of 10⁻¹⁶ to 10⁻¹² cm² s⁻¹.^[27] Even in the presence of gaseous NH₃ the reaction is slow, because the rate-limiting step comprises diffusion of atoms or ions through crystalline reactant, product and possible intermediate phases. This requires days of high temperature treatment, consuming large amounts of energy and favoring thermodynamic reaction control. Refractory metal oxides are particularly difficult to react, and important aspects of the chemistry are lost by the use of high reaction temperatures and long reaction times.^[28,29] Thin films of TaO_xN_y prepared by reactive magnetron sputtering^[30] are nanostructured with small structural units < 10 Å having only nearest-neighbor order and a composition changing gradually from TaN to δ-TaON and Ta₂O₅ for increasing oxygen content. Annealed thin films contain a mixture of crystalline TaN, β-TaON, and Ta₂O₅.

We devised an alternative and very fast approach to TaON by Spark Plasma Sintering (SPS) or Field-Assisted Sintering Technology (FAST), a technique that is used typically for a high speed consolidation of powders with a direct electric current passing through the sample.^[31,32] The application of SPS/FAST as a synthetic tool, in particular the role of the electric field, is still far from being understood.^[33,34] Even though the term “SPS” is more frequently used, the existence of the “spark plasma” could not be confirmed so far.^[35,36] Hence the term field assisted sintering is more precise and will be used in the following. FAST has opened up new options for sintering materials,^[37,38] but applications in solid state synthesis are still rare.^[33,34,39-43]

Different from standard ammonolysis routes to TaON,^[26,44] FAST synthesis uses Ta₂O₅ and Mg₃N₂ as stable solid precursors, which are inexpensive and commercially available. The FAST reaction leads to a topotactic replacement of N³⁻ for O²⁻ within the anion sublattice, thereby maintaining a defect Ta₂O₅ structure of the starting compound with a partially ordered O/N distribution as shown by neutron diffraction. This metastable “ε-TaO_xN_y” undergoes a transformation to β-TaON upon annealing at 800°C. Control reactions of Ta₂O₅ and Mg₃N₂ using conventional high-temperature ampoule chemistry revealed the formation of single phase β-TaON within 48 h. “ε-TaON” has two direct band gaps of 2.6 – 3.0 and 4.0 eV.

Chapter 5.2 Synthesis

Crystalline “ ϵ -TaO_xN_y” was prepared by nitridation of Ta₂O₅ with solid Mg₃N₂ *via* FAST synthesis. A comparison with conventional high temperature chemistry was made by carrying out the reaction in standard quartz glass ampoules and allowed a systematic test of the reaction variables temperature, heating rate, dwell time, and reactant ratio. The FAST synthesis is illustrated in Figure 5.2 a) and a representative temperature program and corresponding piston movement are shown in Figure 5.2 b). Figure 5.2 c) shows digital photographs of the Ta₂O₅ starting compound and products from the FAST reaction of Ta₂O₅ with Mg₃N₂ at different temperatures and holding times.

Ta₂O₅ exists in several low-temperature polymorphs (L-Ta₂O₅),^[45–48] whose structures are controversial. Ball milled commercial Ta₂O₅ crystallizes in the so-called 11-f.u.-Ta₂O₅ structure which contains 11 formula units per unit cell⁴⁵ and will be referred to as L11-Ta₂O₅ in the following. FAST treatment of white L11-Ta₂O₅ powder (space group *Pmm2*) leaves the starting compound unchanged (Figure 5.2 c) iii). FAST reaction of Ta₂O₅ with (sand-colored) Mg₃N₂ in a 1:1 ration leads to characteristic color changes depending on temperature and holding time. MgO (and Mg(OH)₂) that was formed according to $\text{Ta}_2\text{O}_5 + \text{Mg}_3\text{N}_2 = 2 \text{TaON} + 3 \text{MgO}$ and traces of unreacted Mg₃N₂ could be removed after the reaction by washing with dilute HCl. The formation of MgO (according to the Pearson hardness of the Mg and Ta) appears to be the thermodynamic driving force of the reaction. Higher temperatures and longer holding times led to the formation of darker powders (ϵ -TaO_xN_y), due to the increase in incorporated Nitrogen, and subsequently grey/black powders, due to the formation of various phases containing tantalum, oxygen, nitrogen, and magnesium (TaO₂, TaON, Mg₄Ta₂O₉, MgTa₂O₆, Ta₃N₅, Ta₄N₅).

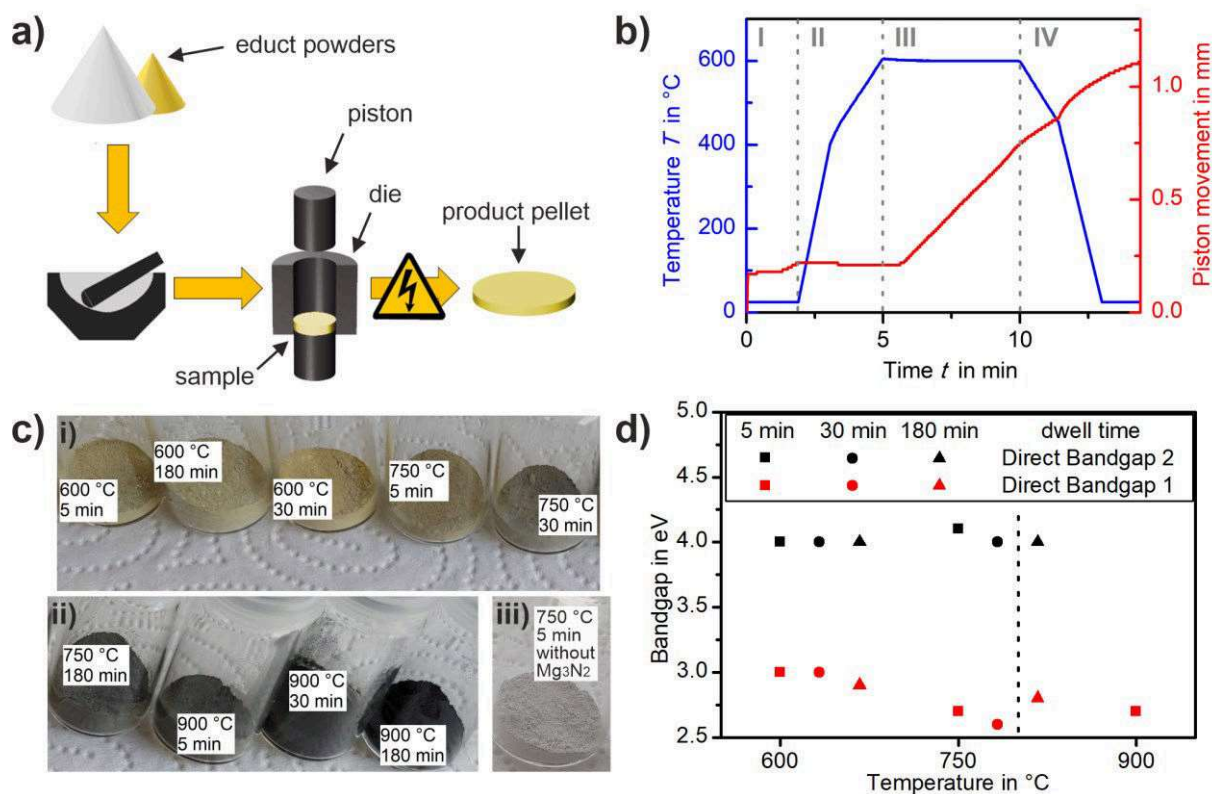


Figure 5.2. **a)** Scheme of the FAST synthesis procedure. **b)** Temperature profile (blue) and piston movement/densification (red) during the FAST process. Capital letters indicate different segments of the process: **I** Evacuation of reaction chamber and first compression, **II** start of reaction by heating to 600 $^{\circ}\text{C}$, **III** Dwelling for 5 min at 600 $^{\circ}\text{C}$ and increase of pressure from 19 MPa to 52 MPa, **IV** sample cooling. **c)** Digital images of the products after the FAST synthesis. **i) - ii)** Are products of the FAST reaction of Ta_2O_5 and Mg_3N_2 (1:1) after FAST treatment at different reaction temperatures and after different processing times. **i)** Samples where the powder XRD almost only showed the L11- Ta_2O_5 phase. The color change can be attributed to the $\text{N}^{3-}/\text{O}^{2-}$ exchange. **ii)** Samples with larger amounts of different magnesium tantalum oxide phases. **iii)** Pure Ta_2O_5 after FAST processing without Mg_3N_2 . **d)** Optical bandgaps of the products after different FAST treatments. The dashed line marks the stability border of the L11- Ta_2O_5 phase. Optical bandgaps for samples with longer holding times of the FAST synthesis at 900 $^{\circ}\text{C}$ could not be determined reliably.

Chapter 5.3 Results and Discussion

Chapter 5.3.1 Diffraction Study

X-ray powder diffraction analysis of the starting compounds prior to the reaction showed that Ta_2O_5 adopts the 11-f.u. structure as proposed by Stephenson et al^[45] (Figure 7.4.1). Figure 5.3 a) and b) show the results of a Rietveld analysis of products after FAST treatment at 600 $^{\circ}\text{C}$ or 750 $^{\circ}\text{C}$ for 5 minutes and washing the samples with dilute HCl. Before the washing step magnesium oxide could be identified as side product, indicating an N/O exchange between Ta_2O_5 and Mg_3N_2 . Refinements from X-ray powder diffraction data of the cleaned reaction

products after FAST processing for 5 min in Figure 5.3 a) and b) show that the L11-Ta₂O₅ structure⁴⁵ provides a good structural description of the product obtained at 600°C and 750°C without any impurity phases that might cause the color change of the product. Details concerning the Rietveld refinements are given in Table 7.4.4. The quality of the fits demonstrates the correctness of the structural model, with assumed statistical distribution of O and N atoms on the O sites of the L11-Ta₂O₅ structure which cannot be distinguished only by PXRD. Slight differences in the quality parameters for the product of the reaction carried out at 750°C may be explained by increased strain or changes of the defect distribution caused by the FAST treatment or the N/O exchange. The formation of a new and metastable ε -TaO_xN_y polymorph was also supported by an elemental analysis, which revealed the fundamental presence of nitrogen after cleaning with dilute HCl, but the exact content is impossible to determine. Longer holding times at 750 °C or a FAST synthesis at higher temperature (900 °C) lead to the formation of magnesium tantalum oxides (Table 7.4.2).

In contrast, the reaction of Ta₂O₅ and Mg₃N₂ by conventional ampoule chemistry at 800°C for 48 h leads to the formation of β -TaON. Reactions carried out at 600 °C and 750 °C yielded mixtures of Ta₂O₅, TaON and TaO₂, while a reaction at 900 °C yielded different tantalum nitrides and magnesium tantalum oxides (Table 7.4.3). Further studies using conventional high temperature chemistry showed that by increasing the temperature to 800 °C and the Ta:N ratio to 1:1.2 phase pure β -TaON was formed after 48 h. Even without varying the atom positions and site occupancies the refinement immediately converged at $GOF/\chi^2 = 1.73$ and $R_{wp} = 3.46\%$ as shown in Figure 5.3 c) and revealed a phase purity of 97.5 % for β -TaON (with minor impurities of Ta₂O₅ (2%) and TaO₂ (0.5%)). Similar results were obtained after a holding time of 6 h indicating that shorter reaction times are possible. Adapting these conditions to the FAST synthesis (800 °C, 5 min, Ta:N ratio of 1:1.2) led to similar results as the FAST parameters discussed above (750 °C, 5 min, Ta:N ratio of 1:1).

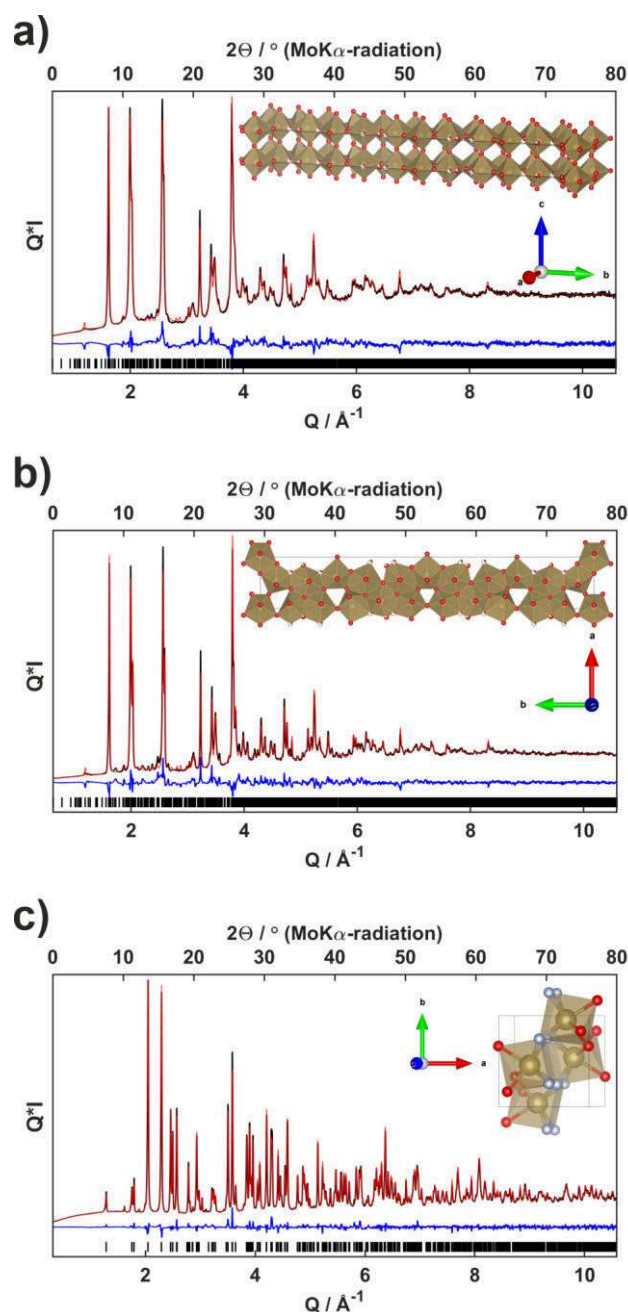


Figure 5.3. **a)** Rietveld refinement of product after FAST treatment at 600 °C for 5 min. L11-Ta₂O₅ type, $a = 3.893(2)$ Å, $b = 40.30(2)$ Å, $c = 6.211(4)$ Å, space group C2/m, $V = 974.4(9)$ Å³, $R_{wp} = 5.39\%$; GOF = 2.91, phase purity 100%. **b)** Product after FAST treatment at 750 °C for 5 min. L11-Ta₂O₅ type, $a = 3.8931(8)$ Å, $b = 40.31(1)$ Å, $c = 6.202(3)$ Å, space group C2/m, $V = 973.1(6)$ Å³, $R_{wp} = 6.69\%$; GOF = 3.32, phase purity 99%. **c)** Product after conventional synthesis at 800 °C for 48 h. β -TaON, $a = 4.9677(1)$ Å, $b = 5.0373(7)$ Å, $c = 5.1881(6)$ Å, $\beta = 99.69(6)$ space group P2₁/c, $V = 127.97(5)$ Å³, $R_{wp} = 3.46\%$; GOF = 1.73, phase purity 97.5% (impurities 2% Ta₂O₅ + 0.5% TaO₂). **a)-c)** Experimental powder pattern (black), Rietveld analysis (red), difference plots (blue). Tick marks show peak positions of L11-Ta₂O₅ and β -TaON structure, respectively. The insets show graphical representations of the corresponding structures. **a) + b)** L11-Ta₂O₅ type, **c)** β -TaON.

Chapter 5.3.2 Neutron diffraction analysis

Since oxygen and nitrogen are difficult to differentiate in X-ray diffraction, neutron data (thermal neutrons, $\lambda = 1.8691 \text{ \AA}$) were collected in at the T5 beam tube with the E9 detector of the Helholtz center Berlin. The O/N scattering contrast (neutron scattering lengths b are $b_{\text{Ta}} = 0.691 \text{ fm}$, $b_{\text{O}} = 0.581 \text{ fm}$, and $b_{\text{N}} = 0.936 \text{ fm}$) allows to differentiate between oxygen and nitrogen atoms. In addition, neutron diffraction is sensitive to small anion displacements because the scattering lengths of the heavy and light atoms are comparable. The sensitivity of powder neutron data to anion order in the L11-Ta₂O₅ structure depends on the magnitude of the accompanying lattice distortion that broadens or splits the diffraction peaks. The large lattice parameter of the 11-fold enlarged unit cell leads to a significant reflection overlap which complicates structure refinement against the neutron data. To compare and analyze the O/N ordering in obtained samples, the 11-f.u. structure was refined against good powder data of FAST treated Ta₂O₅ to obtain the exact atomic positions. These positions were fixed and used to refine the O/N occupancy using the obtained neutron data. B_{iso} -values for this refinement were fixed to cancel out possible influences ($B_{\text{iso}}(\text{N}) = 0.6$, $B_{\text{iso}}(\text{O}) = 0.4$, $B_{\text{iso}}(\text{Ta}) = 0.12$)^[49–53]. The results of these refinements are listed in Table 7.4.4. An exemplary structural representation is given in Figure 5.3 and comparisons between the single samples are shown in Figure 7.4.5 (Reference Ta₂O₅ and samples obtained at 600°C and 750°C). Both positional refined samples are in agreement with each other. As expected the degree of Nitridation rises from the 600°C sample at 22% to the 750°C sample with 24%. The Nitridation seems to take place on the height of the first and second third of the c-axis within the unit cell. Preferably oxygen in the Ta-plane gets substituted before oxygen around the edge-Ta is substituted. There seem to be two channel-like areas near the ends of the c-axis, which remain untouched. But in general, the Nitridation seems to take place mostly randomly without many clearly preferred position, which confirms the assumption that FAST is a very harsh method for synthesis and does not allow proper thermic equilibrium.

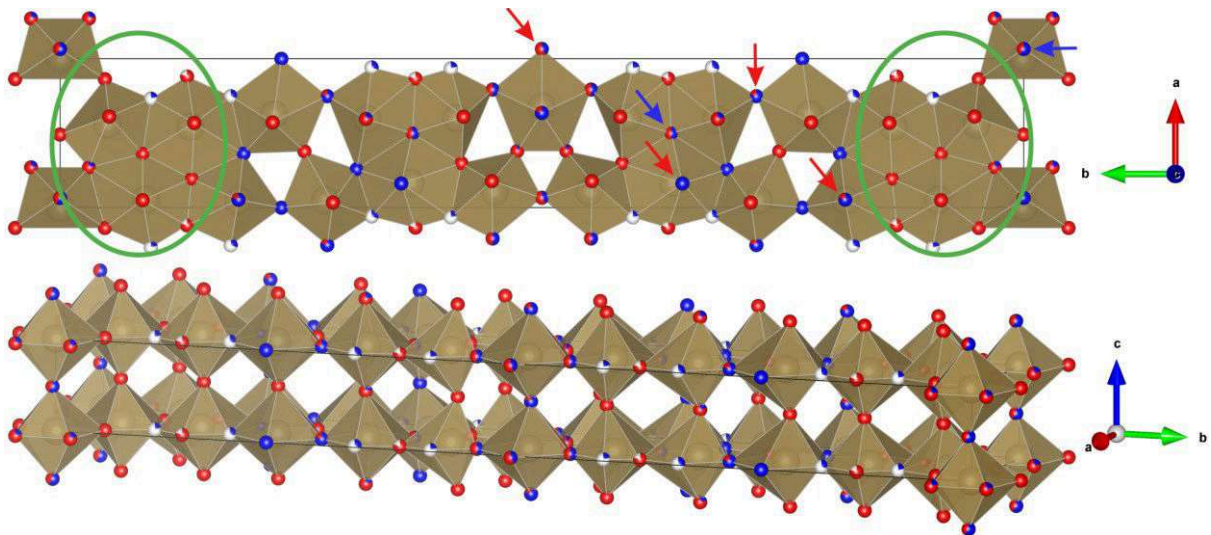


Figure 5.4. Graphical representation of the neutron diffraction results for the sample FAST treated at 750 °C for 5 min. The tantalum atoms are in the centers of the polyhedral. The anion positions are color coded corresponding to the type of occupancy: red: oxygen, blue: nitrogen, white: vacancy. The arrows indicate positions that are more occupied by oxygen (red) or nitrogen (blue) in the 600 °C sample. The green ellipse mark regions that almost exclusively dominated by oxygen.

Chapter 5.3.3 Electron microscopy

Representative scanning electron microscopy (SEM) images of FAST- and conventionally prepared ϵ -TaO_xN_y in Figure 7.4.6 show that the product morphology does not change significantly for the products of both routes. Figure 5.5 f) shows one exemplary SEM image of the FAST-prepared ϵ -TaO_xN_y. High resolution transmission electron microscopy (HRTEM) images of FAST-prepared ϵ -TaO_xN_y (750 °C, 5 min) and β -TaON prepared by conventional high temperature reaction of Ta₂O₅ and Mg₃N₂ at 800°C are shown in Figure 5.5 a)-e). The product of the FAST synthesis is shown in Figure 5.5 a)-c) and consists of larger crystal agglomerates. The distinct layers in Figure 5.5 c) are compatible with the “layer-like” structure as observed for L11-Ta₂O₅. An important feature here is the lamellar structural characteristic which originates from stacking faults and strain. This is supported by the strain parameter derived from the Rietveld refinements. Figure 5.5 d) and e) show different magnifications of the product prepared by conventional high temperature reaction. The contrast pattern Figure 5.5 e) originates from the small anion-anion distances and missing distinct Ta-planes in β -TaON as shown in the inset of Figure 5.3 c). Thus, the HRTEM images strongly support the proposed structural models.

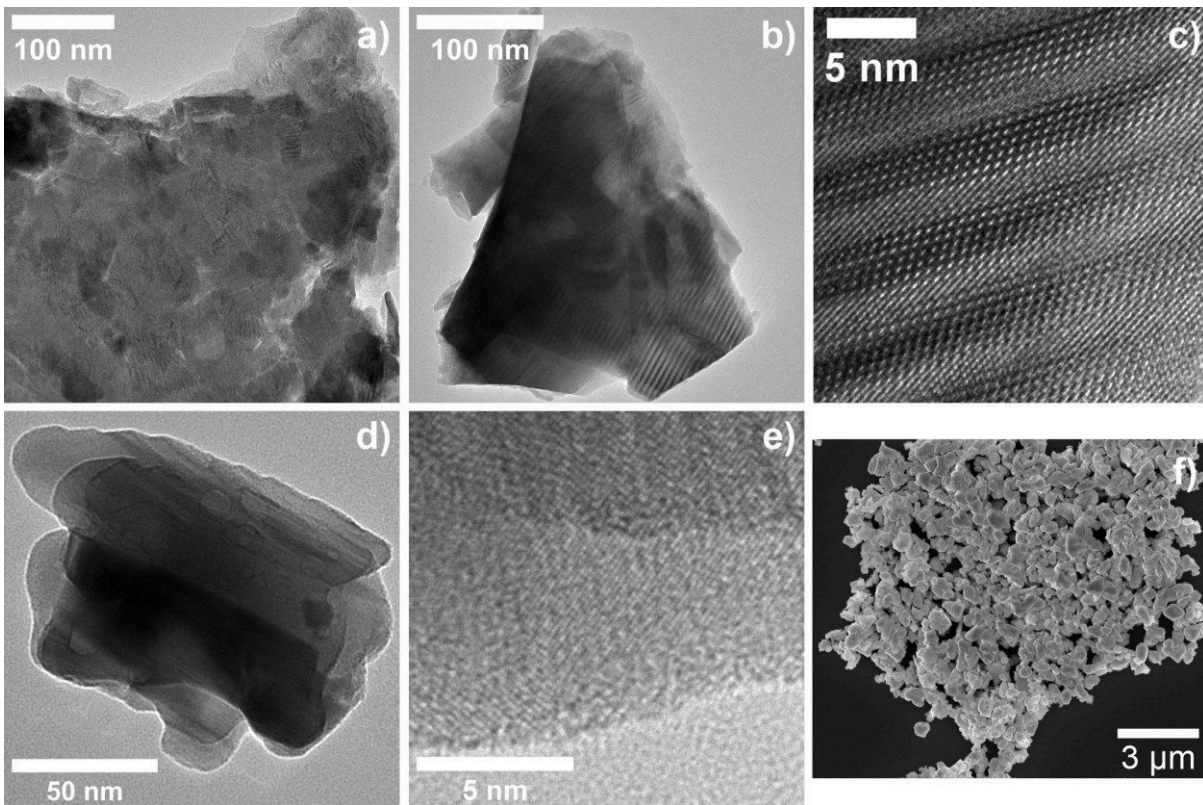


Figure 5.5. Representative TEM images of **a)-c)** FAST-prepared ϵ - TaO_xN_y ($T = 750\text{ }^\circ\text{C}$) and **d), e)** β - TaO_xN_y prepared via conventional high temperature reaction of Ta_2O_5 and Mg_3N_2 at $800\text{ }^\circ\text{C}$ for 48 h at different magnifications. **a) + b)** Overviews of typical crystallite agglomerates after the FAST synthesis. **c)** Magnification of a region with often observed lamellar contrast. **d)** Overview of a typical crystallite after the conventional synthesis. **e)** Magnification of the crystallite shown in **d)**. **f)** Representative SEM images of FAST-prepared ϵ - TaO_xN_y ($T = 750\text{ }^\circ\text{C}$).

The following conclusions can be drawn at this point. (i) None of the known (α -, β -, γ -, δ -) TaON polymorphs was formed by FAST processing, i.e., FAST offers unprecedented opportunities for the synthesis of new metastable phases. (ii) The synthesis uses solid powders as starting compounds and does not require sophisticated inert gas conditions, continuous gas flow or toxic chemicals.^[25,26] (iii) The synthesis can be carried out within a few minutes, whereas conventional reactions require hours or days and thus proceed almost 2 orders of magnitude slower. This saves not only time, but also energy on a large scale for temperature treatment. (iv) The solid precursor approach with Mg_3N_2 in conventional solid-state synthesis also enables the synthesis of the β -TaON polymorph and may be useful for the nitridation of metal oxides.

Chapter 5.3.4 UV/Vis diffuse reflectance spectroscopy

The optical band gaps of different FAST treated samples were determined by UV/Vis diffuse reflectance spectroscopy (Figure 5.2 d)). For temperatures below T_c (indicated by the vertical dashed line) the X-ray diffractograms are compatible with “ ϵ - TaO_xN_y ” adopting the L11- Ta_2O_5 structure. The FAST-treated samples ($600^\circ C \leq T_{anneal} \leq 750^\circ C$) show two direct bandgaps. One optical bandgap at ~ 4.0 eV matches the bandgap of untreated L11- Ta_2O_5 .^[54] The second optical bandgap of “ ϵ - TaO_xN_y ” decreases compared to L11- Ta_2O_5 , i.e., the transitions are red-shifted (from 3.0 eV to 2.6 eV) for longer holding times and higher temperatures. This can be attributed to a shift of the valence band maximum (VBM) due to N substitution. Changing the nitridation level of tantalum oxynitrides is an approach to tune the electronic properties due to the lower electronegativity of N compared to O.^[10] Similar observations were also reported by Bae et al.^[25] after nitridation of a different Ta_2O_5 polymorph *via* NH_3 treatment. Products prepared at temperatures $> 900^\circ C$ for longer holding times show impurities (Table 7.4.2), which makes the determination of the band gaps difficult. β -TaON reference samples synthesized from Ta_2O_5 and Mg_3N_2 *via* conventional solid-state synthesis show optical bandgaps of 2.5 eV^[55] and support the successful synthesis of β -TaON by all-solid-state synthesis.

Chapter 5.3.5 XPS analysis

Figure 5.6 compares the XPS spectra of different FAST-prepared and conventionally prepared TaO_xN_y (FAST treatment at 600 and 750°C, FAST at 750°C and annealed, conventional synthesis). Ta_2O_5 (ball-milled, FAST at 750 °C) was used as reference (black and grey curves). Peak broadening of the ball-milled samples is the main difference in the Ta 4d spectra due to a higher amount of surface hydroxide species (compared to FAST-treated and annealed samples). Figure 5.6 b) compares the Ta 4p and N 1s spectra, Figure 5.6 c) shows an analytical fit of the Ta 4p and N 1s spectra. The Ta 4p and N 1s spectra of the FAST-prepared samples are in good agreement with literature that uses high temperature annealing in NH_3 atmosphere.^[25] An accurate quantification is critical due to the overlap of the Ta 4p and the N 1s regions. However, the appearance of the $N^{\circ}1s$ peak in the ϵ - TaO_xN_y spectra after the FAST synthesis compared to the reference sample supports the assumed N^{3-}/O^{2-} exchange. The most intense $N^{\circ}1s$ peak is clearly shown by the β -TaON sample after conventional synthesis and indicates a higher nitrogen content compared to ϵ - TaO_xN_y or more nitrogen exposed at the surface.

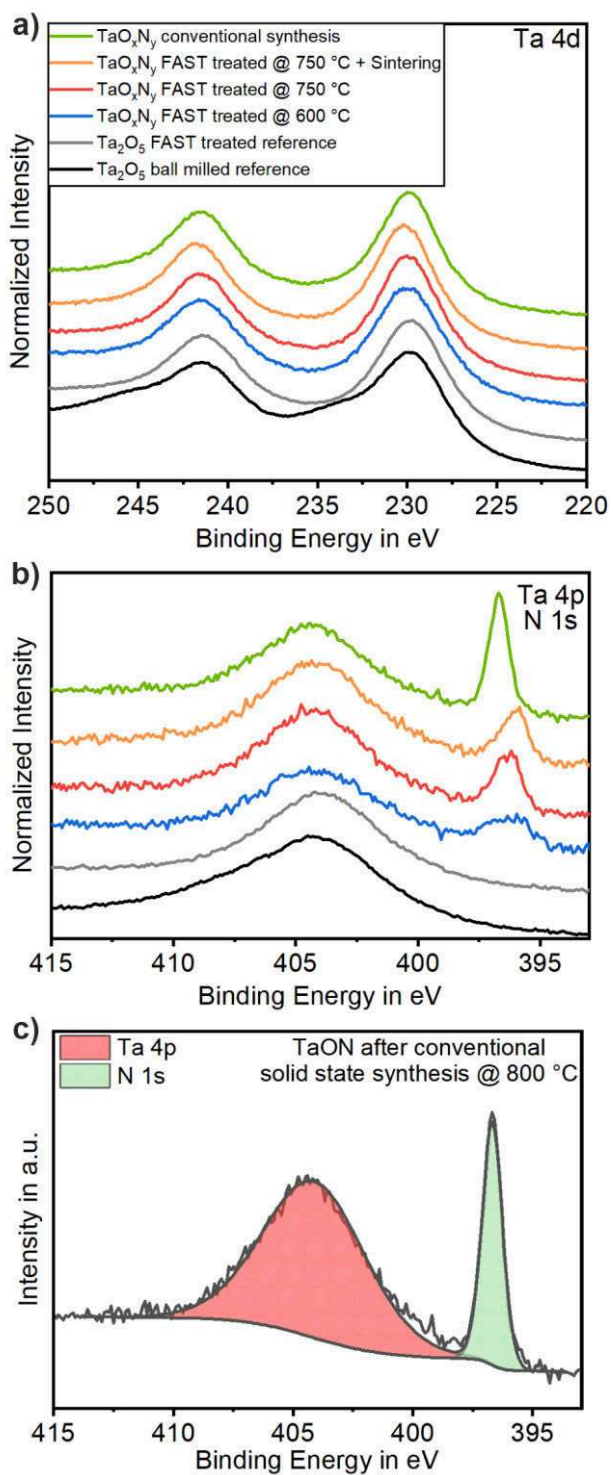


Figure 5.6. a)-c) XPS analysis of ϵ -TaO_xN_y prepared by FAST at 600 and 750°C, FAST at 750°C with subsequent annealing and β -TaON prepared by conventional synthesis. Reference: Ta₂O₅ (ball-milled + FAST). **a)** Ta 4d spectra. **b)** Ta 4p spectra. **c)** Representative fit of the Ta 4p and N 1s spectra for TaON obtained by conventional solid-state synthesis at 800 °C to determine the surface N-contents: ϵ -TaO_xN_y prepared by FAST at 600 (12.2%); at 750°C (15.6%); at 750°C and subsequent annealing at 750°C (13.8%), TaON conventionally prepared (23.9%).

Chapter 5.4 Conclusion

We have shown that reactions using FAST allow the *high-speed* nitridation of Ta₂O₅ from the solid precursors Ta₂O₅ and Mg₃N₂ in large quantities. The degree of nitridation is comparable to that achieved with gaseous NH₃ under high-temperature conditions. The reaction times could be reduced from multiple hours for reactions with gaseous NH₃ to a few minutes. These reactions do not require the use of toxic and caustic chemicals. The structure and composition of TaO_xN_y was determined by a combination of X-ray and neutron powder diffraction analysis. The rapid FAST transformation involves a topotactic N³⁻/O²⁻ anion exchange within the anion sublattice. Ion exchange is greatly accelerated by the applied electric field, thereby maintaining a metastable and so far undiscovered defect Ta₂O₅ structure with a partially ordered O/N distribution. Metastable “ε-TaO_xN_y” undergoes transformation to the thermodynamically stable β-TaON polymorph upon annealing at 800 °C. β-TaON could also be synthesized in 48 h by an all-solid-state synthesis using Mg₃N₂ as nitridation agent. “ε-TaON” has two direct band gaps of 2.6 – 3.0 and 4.0 eV. The conceptual advancement of this new synthetic approach for metal oxide nitrides lies in the combination of solid precursors and field assisted sintering technology for “one-pot” chemical synthesis (rather than simply sintering ceramics). FAST processing reduces reaction times by almost two orders of magnitude and is therefore a very energy-efficient green synthesis tool, in particular as the synthesis can be upscaled easily to the kg range. Field assisted sintering technology overcomes the limitations of traditional, diffusion-limited, solid-state synthesis, which allows no control of the reaction pathway and therefore no control over which intermediates are formed.^[28,56,57]

Chapter 5.5 Experimental Methods

Synthesis. Tantalum oxide (99,9 %, Chempur) was ball-milled in a Fritsch *Pulverisette 7* planetary ball mill for 3 hours in ethanol and dried by centrifugation and drying overnight at 70°C in a drying chamber. The resulting tantalum oxide and magnesium nitride (99,6 %, Alfa Aesar) were weighed in their respective molar ratios and thoroughly mixed in a quartz mortar. For FAST preparation, samples containing ≈ 2 g of the powder mixtures were enclosed with graphite foil and placed in graphite dies with a diameter of 20 mm. The dies were put subsequently into an SPS HP D 25 (FCT-systems), heated up to 600, 750 or 900 °C with 100 °C/min and kept at this temperature for 5, 30 or 180 min. During heating, a pressure of 19 MPa was applied which was increased to and kept at 50 MPa once the synthesis temperature was reached. The preparation method using FAST is illustrated in Figure 5.1 a)+b). Reference

samples for conventional high temperature reactions were prepared by placing powder mixtures (≈ 200 mg) in evacuated quartz ampules and annealing them for at 800 °C for 48 h. After the FAST treatment, all samples were manually grinded into powders, dispersed in dilute hydrochloric acid to remove Mg_2O and Mg_3N_2 residues and washed twice with water.

X-Ray Powder Diffraction Analysis. Samples for X-Ray diffraction were prepared on polyvinylacetate foil. Diffractograms were obtained using a STOE Stadi P powder diffractometer, equipped with a Mythen 1k detector using $MoK\alpha$ radiation. The sample was measured in transmission in 0.015° steps (continuous scan, 150 s/ $^\circ$) covering a 2θ range from 1.5° to 80° . Rietveld refinement¹ was performed with Topas Academic V6 using the fundamental parameters approach.²

Neutron Diffraction Analysis. Samples for neutron diffraction were measured at the T5 tube of the HZB beamline with the fine resolution powder diffractometer E9 (FIREPOD) at a wavelength of $1.7977(1)$ Å from Ge(511) over the range of $3^\circ \leq \Theta \leq 142^\circ$ with a resolution of 0.33° .

X-ray photoelectron spectroscopy (XPS). For XPS measurements, the powder was pressed at 4 tons for 1 min in a dry room. The XPS characterization, was conducted using an Axis Ultra DLD, Kratos, with a pass energy of 20 eV using a monochromatic Al $K\alpha$ source ($h\nu = 1486.6$ eV) at a 10 mA filament current and a 12 kV filament voltage source power. Additionally, a charge neutralizer was used for compensating the charging of the samples. To ensure reproducibility two or three spots were measured on each sample. The software CasaXPS was used to analyze the obtained spectra.

UV–Vis Spectroscopy. Ultraviolet–visible (UV–vis) reflectance spectra ranging from 200 to 800 nm were collected on a Cary 5G UV–vis–NIR spectrophotometer using an Ulbricht sphere. $BaSO_4$ was used as white standard. The samples were measured by distributing a small amount of powder on the $BaSO_4$ standard.

Transmission Electron Microscopy (TEM). Powdered samples for transmission electron microscopy (TEM) investigations were prepared by placing one drop (10 μ L) of a diluted NP solution in ethanol on a carbon-coated copper grid and letting it dry at room temperature. This procedure had to be repeated 3-5 times to achieve a sufficient covering. TEM and HRTEM, measurements were carried out with a FEI TECNAI F30 S-TWIN transmission electron microscope equipped with a field emission gun and working at 300 kV. TEM images were taken with a CCD camera (16-bit 4.096×4.096 pixel GATAN ULTRASCAN4000) and acquired by Gatan Digital Micrograph software.

Scanning Electron Microscopy (SEM). Field-emission scanning electron microscopy was performed on a NOVA Nano-SEM with an attached Oxford Inca X-ray system for chemical analysis. The obtained SPS pellets were cut and polished to obtain cross-sectional pieces. Secondary and backscattered electron images were collected with acceleration voltages of 5 keV and 15 or 20 keV for EDX mapping, respectively.

Elemental analysis. Nitrogen sensitive elemental analysis was performed on a „vario EL cube“ device by Elementar Analysensysteme GmbH.”

References

- [1] Goodenough, J. B. Perspective on Engineering Transition-Metal Oxides. *Chem. Mater.* **2014**, *26*, 820–829.
- [2] Sun, W.; Bartel, C. J.; Arca, E.; Bauers, S. R.; Matthews, B.; Orvañanos, B.; Chen, B.-R.; Toney, M. F.; Schelhas, L. T.; Tumas, W.; Tate, J.; Zakutayev, A.; Lany, S.; Holder, A. M.; Ceder, G. A map of the inorganic ternary metal nitrides. *Nat. Mater.* **2019**, *18*, 732–739.
- [3] Tremel, W.; Hoffmann, R. Square nets of main-group elements in solid-state materials. *J. Am. Chem. Soc.* **1987**, *109*, 124–140.
- [4] Kamihara, Y.; Watanabe, T.; Hirano, M.; Hosono, H. Iron-Based Layered Superconductor La[O_{1-x}F_x]FeAs (x = 0.05–0.12) with T_c = 26 K. *J. Am. Chem. Soc.* **2008**, *130*, 3296–3297.
- [5] Kageyama, H.; Hayashi, K.; Maeda, K.; Attfield, J. P.; Hiroi, Z.; Rondinelli, J. M.; Poeppelmeier, K. R. Expanding frontiers in materials chemistry and physics with multiple anions. *Nat. Commun.* **2018**, *9*, 772.
- [6] Lerch, M.; Janek, J.; Becker, K. D.; Berendts, S.; Boysen, H.; Bredow, T.; Dronskowski, R.; Ebbinghaus, S. G.; Kilo, M.; Lumey, M. W.; Martin, M.; Reimann, C.; Schweda, E.; Valov, I.; Wiemhöfer, H. D. Oxide nitrides: From oxides to solids with mobile nitrogen ions. *Prog. Solid State Chem.* **2009**, *37*, 81–131.
- [7] Kim, Y.-I.; Woodward, P. M.; Baba-Kishi, K. Z.; Tai, C. W. Characterization of the Structural, Optical, and Dielectric Properties of Oxynitride Perovskites AMO₂N (A = Ba, Sr, Ca; M = Ta, Nb). *Chem. Mater.* **2004**, *16*, 1267–1276.
- [8] Asahi, R.; Morikawa, T.; Ohwaki, T.; Aoki, K.; Taga, Y. Visible-light photocatalysis in nitrogen-doped titanium oxides. *Science (80-.)*. **2001**, *293*, 269–271.
- [9] Ebbinghaus, S. G.; Abicht, H.-P.; Dronskowski, R.; Müller, T.; Reller, A.;

- Weidenkaff, A. Perovskite-related oxynitrides – Recent developments in synthesis, characterisation and investigations of physical properties. *Prog. Solid State Chem.* **2009**, *37*, 173–205.
- [10] Jansen, M.; Letschert, H. P. Inorganic yellow-red pigments without toxic metals. *Nature* **2000**, *404*, 980–982.
- [11] Hosono, A.; Stoffel, R. P.; Masubuchi, Y.; Dronskowski, R.; Kikkawa, S. Melting Behavior of Alkaline-Earth Metal Carbodiimides and Their Thermochemistry from First-Principles. *Inorg. Chem.* **2019**, *58*, 8938–8942.
- [12] Maeda, K.; Teramura, K.; Saito, N.; Inoue, Y.; Kobayashi, H.; Domen, K. Overall water splitting using (oxy)nitride photocatalysts. *Pure Appl. Chem.* **2006**, *78*, 2267– 2276.
- [13] Hitoki, G.; Takata, T.; Kondo, J. N.; Hara, M.; Kobayashi, H.; Domen, K. An oxynitride, TaON, as an efficient water oxidation photocatalyst under visible light irradiation ($\lambda \leq 500$ nm). *Chem. Commun.* **2002**, *2*, 1698–1699.
- [14] Brauer, G.; Weidlein, J. R. Synthese und Eigenschaften des Tantaloxynitrids TaON. *Angew. Chemie* **1965**, *77*, 913–913.
- [15] Sasaki, Y.; Tokuyasu, Z.; Ono, Y.; Iwasaki, M.; Ito, S. Synthetic Conditions and Color Characteristics of Tantalum Oxynitride Prepared via Liquid-NH₃ Process. *Adv. Mater. Sci. Eng.* **2009**, *2009*, 1–4.
- [16] Rohloff, M.; Cosgun, S.; Massué, C.; Lunkenbein, T.; Senyshyn, A.; Lerch, M.; Fischer, A.; Behrens, M. The role of synthesis conditions for structural defects and lattice strain in β -TaON and their effect on photo- and photoelectrocatalysis. *Zeitschrift für Naturforsch. B* **2019**, *74*, 71–83.
- [17] Schilling, H.; Stork, A.; Irran, E.; Wolff, H.; Bredow, T.; Dronskowski, R.; Lerch, M. γ -TaON: A Metastable Polymorph of Tantalum Oxynitride. *Angew. Chemie Int. Ed.* **2007**, *46*, 2931–2934.
- [18] Armytage, D.; Fender, B. E. F. Anion ordering in NaON: a powder neutron-diffraction investigation. *Acta Crystallogr. Sect. B Struct. Crystallogr. Cryst. Chem.* **1974**, *30*, 809–812.
- [19] Lüdtke, T.; Schmidt, A.; Göbel, C.; Fischer, A.; Becker, N.; Reimann, C.; Bredow, T.; Dronskowski, R.; Lerch, M. Synthesis and Crystal Structure of δ -TaON, a Metastable Polymorph of Tantalum Oxide Nitride. *Inorg. Chem.* **2014**, *53*, 11691–11698.
- [20] Lumey, M.-W.; Dronskowski, R. The Electronic Structure of Tantalum Oxynitride and the Falsification of α -TaON. *Z. Anorg. Allg. Chem* **2003**, *629*, 2173–2179.

- [21] Lumey, M.-W.; Dronskowski, R. First-Principles Electronic Structure, Chemical Bonding, and High-Pressure Phase Prediction of the Oxynitrides of Vanadium, Niobium, and Tantalum. *Z. Anorg. Allg. Chem* **2005**, *631*, 887–893.
- [22] Lowther, J. E. Compressibility of highly coordinated metal oxynitrides: LDA calculations. *Phys. Rev. B* **2005**, *72*, 172105.
- [23] Buslaev, Y.; Safronov, M.; Pakhomov, V.; Glushkova, M.; Repko, V.; Ershova, M.; Zhukov, A.; Zhadanova, T. Single crystals and structure of tantalum oxynitride. *Izv. Akad. Nauk SSSR Neorg. Mater* **1969**, *5*, 45–48.
- [24] Woodhead, K.; Pascarelli, S.; Hector, A. L.; Briggs, R.; Alderman, N.; McMillan, P. F. High pressure polymorphism of β -TaON. *Dalt. Trans.* **2014**, *43*, 9647–9654.
- [25] Bae, S. T.; Shin, H.; Lee, S.; Kim, D. W.; Jung, H. S.; Hong, K. S. Visible-light photocatalytic activity of NH₃-heat-treated Ta₂O₅ to decompose rhodamine B in aqueous solution. *React. Kinet. Mech. Catal.* **2012**, *106*, 67–81.
- [26] Murase, T.; Irie, H.; Hashimoto, K. Visible Light Sensitive Photocatalysts, Nitrogen-Doped Ta₂O₅ Powders. *J. Phys. Chem. B* **2004**, *108*, 15803–15807.
- [27] Prot, D.; Monty, C. Self-diffusion in α -Al₂O₃ II. Oxygen diffusion in ‘undoped’ single crystals. *Philos. Mag. A Phys. Condens. Matter, Struct. Defects Mech. Prop.* **1996**, *73*, 899–917.
- [28] Fister, L.; Johnson, D. C. Controlling Solid-State Reaction Mechanisms Using Diffusion Length in Ultrathin-Film Superlattice Composites. *J. Am. Chem. Soc* **1992**, *114*, 4639.
- [29] Stein, A.; Keller, S. W.; Mallouk, T. E. Turning down the heat: Design and mechanism in solid-state synthesis. *Science (80-.)*. **1993**, *259*, 1558–1564.
- [30] Taviot-Guého, C.; Cellier, J.; Bousquet, A.; Tomasella, E. Multiphase Structure of Tantalum Oxynitride TaO_xN_y Thin Films Deposited by Reactive Magnetron Sputtering. *J. Phys. Chem. C* **2015**, *119*, 23559–23571.
- [31] Munir, Z. A.; Anselmi-Tamburini, U.; Ohyanagi, M. The effect of electric field and pressure on the synthesis and consolidation of materials: A review of the spark plasma sintering method. *J. Mater. Sci.* **2006**, *41*, 763–777.
- [32] Olevsky, E. A.; Dudina, D. V. *Field-Assisted Sintering*; Springer International Publishing: Cham, 2018.
- [33] Beekman, M.; Baitinger, M.; Borrmann, H.; Schnelle, W.; Meier, K.; Nolas, G. S.; Grin, Y. Preparation and crystal growth of Na₂₄Si₁₃₆. *J. Am. Chem. Soc.* **2009**, *131*,

9642–9643.

- [34] Portehault, D.; Maneeratana, V.; Candolfi, C.; Oeschler, N.; Veremchuk, I.; Grin, Y.; Sanchez, C.; Antonietti, M. Facile general route toward tunable magnéli nanostructures and their use as thermoelectric metal oxide/carbon nanocomposites. *ACS Nano* **2011**, *5*, 9052–9061.
- [35] Guillon, O.; Gonzalez-Julian, J.; Dargatz, B.; Kessel, T.; Schierning, G.; Räthel, J.; Herrmann, M. Field-assisted sintering technology/spark plasma sintering: Mechanisms, materials, and technology developments. *Adv. Eng. Mater.* **2014**, *16*, 830–849.
- [36] Suarez, M.; Fernandez, A.; Menendez, J. L.; Torrecillas, R.; U., H.; Hennicke, J.; Kirchner, R.; Kessel, T. Challenges and Opportunities for Spark Plasma Sintering: A Key Technology for a New Generation of Materials. In *Sintering Applications*; InTech, 2013; pp 319–342.
- [37] Friedman, J. R.; Garay, J. E.; Anselmi-Tamburini, U.; Munir, Z. A. Modified interfacial reactions in Ag-Zn multilayers under the influence of high DC currents. *Intermetallics* **2004**, *12*, 589–597.
- [38] Chen, W.; Anselmi-Tamburini, U.; Garay, J. E.; Groza, J. R.; Munir, Z. A. Fundamental investigations on the spark plasma sintering/synthesis process. *Mater. Sci. Eng. A* **2005**, *394*, 132–138.
- [39] Recknagel, C.; Reinfried, N.; Höhn, P.; Schnelle, W.; Rosner, H.; Grin, Y.; Leithe-Jasper, A. Application of spark plasma sintering to the fabrication of binary and ternary skutterudites. *Sci. Technol. Adv. Mater.* **2007**, *8*, 357–363.
- [40] Lange, M. A.; Krysiak, Y.; Hartmann, J.; Dewald, G.; Cerretti, G.; Tahir, M. N.; Panthöfer, M.; Barton, B.; Reich, T.; Zeier, W. G.; Mondeshki, M.; Kolb, U.; Tremel, W. Solid State Fluorination on the Minute Scale: Synthesis of $\text{WO}_{3-x}\text{F}_x$ with Photocatalytic Activity. *Adv. Funct. Mater.* **2020**, *30*, 1909051.
- [41] Ihrig, M.; Finsterbusch, M.; Tsai, C. L.; Laptev, A. M.; Tu, C. hao; Bram, M.; Sohn, Y. J.; Ye, R.; Sevinc, S.; Lin, S. kang; Fattakhova-Rohlfing, D.; Guillon, O. Low temperature sintering of fully inorganic all-solid-state batteries – Impact of interfaces on full cell performance. *J. Power Sources* **2021**, *482*, 228905.
- [42] Gil-González, E.; Perejón, A.; Sánchez-Jiménez, P. E.; Román-González, D.; Pérez-Maqueda, L. A. Control of experimental conditions in reaction flash-sintering of complex stoichiometry ceramics. *Ceram. Int.* **2020**, *46*, 29413–29420.

- [43] Son, H. W.; Berthebaud, D.; Yubuta, K.; Yoshikawa, A.; Shishido, T.; Suzuta, K.; Mori, T. New Synthesis Route for Complex Borides; Rapid Synthesis of Thermoelectric Yttrium Aluminoboride via Liquid-Phase Assisted Reactive Spark Plasma Sintering. *Sci. Rep.* **2020**, *10*, 1–16.
- [44] Mikita, R.; Aharen, T.; Yamamoto, T.; Takeiri, F.; Ya, T.; Yoshimune, W.; Fujita, K.; Yoshida, S.; Tanaka, K.; Batuk, D.; Abakumov, A. M.; Brown, C. M.; Kobayashi, Y.; Kageyama, H. Topochemical Nitridation with Anion Vacancy-Assisted N₃-/O₂-Exchange. *J. Am. Chem. Soc.* **2016**, *138*, 3211–3217.
- [45] Stephenson, N. C.; Roth, R. S. Structural systematics in the binary system Ta₂O₅–WO₃. V. The structure of the low-temperature form of tantalum oxide L-Ta₂O₅. *Acta Crystallogr. Sect. B Struct. Crystallogr. Cryst. Chem.* **1971**, *27*, 1037–1044.
- [46] Aleshina, L. A.; Loginova, S. V. Rietveld analysis of X-ray diffraction pattern from β-Ta₂O₅ oxide. *Crystallogr. Reports* **2002**, *47*, 415–419.
- [47] Fukumoto, A.; Miwa, K. Prediction of hexagonal structure by first-principles calculations. *Phys. Rev. B* **1997**, *55*, 11155–11160.
- [48] Lee, S.-H.; Kim, J.; Kim, S.-J.; Kim, S.; Park, G.-S. Hidden Structural Order in Orthorhombic Ta₂O₅. *Phys. Rev. Lett.* **2013**, *110*, 235502.
- [49] Brese, N. E.; O’Keeffe, M.; Rauch, P.; DiSalvo, F. J. Structure of Ta₃N₅ at 16 K by time-of-flight neutron diffraction. *Acta Crystallogr. Sect. C Cryst. Struct. Commun.* **1991**, *47*, 2291–2294.
- [50] Čapková, P.; Smrčok, L.; Šlma, V.; Valvoda, V.; Chalupa, B.; Etmayer, P. Thermal Vibrations in Substoichiometric Vanadium Nitrides. Dynamical Deformation Effect. *Phys. status solidi* **1987**, *143*, 471–476.
- [51] Kuzovnikov, M. A.; Antonov, V. E.; Ivanov, A. S.; Hansen, T.; Savvin, S.; Kulakov, V. I.; Tkacz, M.; Kolesnikov, A. I.; Gurev, V. M. Neutron scattering study of tantalum dihydride. *Phys. Rev. B* **2020**, *102*, 024113.
- [52] Henderson, S. J.; Hector, A. L. Structural and compositional variations in Ta₃N₅ produced by high-temperature ammonolysis of tantalum oxide. *J. Solid State Chem.* **2006**, *179*, 3518–3524.
- [53] Riekel, C.; Schöllhorn, R. A neutron diffraction study on the intercalation of ammonia into tantalum disulfide. *Mater. Res. Bull.* **1976**, *11*, 369–376.
- [54] Kim, J.-Y.; Magyari-Köpe, B.; Lee, K.-J.; Kim, H.-S.; Lee, S.-H.; Nishi, Y. Electronic structure and stability of low symmetry Ta₂O₅ polymorphs. *Phys. status solidi -*

Rapid Res. Lett. **2014**, *8*, 560–565.

- [55] Liu, Q. L.; Zhao, Z. Y.; Yi, J. H. Effects of crystal structure and composition on the photocatalytic performance of Ta-O-N functional materials. *Phys. Chem. Chem. Phys.* **2018**, *20*, 12005–12015.
- [56] Novet, T.; Johnson, D. C. New synthetic approach to extended solids: selective synthesis of iron silicides via the amorphous state. *J. Am. Chem. Soc.* **1991**, *113*, 3398–3403.
- [57] Fister, L.; Brown, R.; Johnson, D. C. Synthesis of $\text{Cu}_x\text{Mo}_6\text{Se}_8$ without Binary Compounds as Intermediates: A Study Using Superlattices to Kinetically Control a Solid-State Reaction. *J. Am. Chem. Soc.* **1994**, *116*, 629–633.

Chapter 6 | Conclusions

This work focused on the development, transfer and optimization of solid-state syntheses for field-activated sintering technique (FAST). The materials and syntheses selected for this purpose were chosen on account of their suitability as model systems in order to be able to develop process parameters that are as generally valid as possible. In addition, the fluorination of oxides with the aid of Teflon was chosen because it represents a little-used but experimentally simple modification variant. In addition, oxyfluorides are of interest for a wide range of applications. For this reason, analogous nitridation using magnesium nitride was also chosen in order to make the oxynitride class accessible via FAST, which also has a wide range of uses. Both classes of compounds are frequently used to improve oxides with already known good properties by simple modification for applications such as catalytic processes. Especially in the field of photocatalytic processes, such as photocatalytic hydrogen evolution, oxyfluorides like tantalum oxyfluoride, more complex oxyfluorides and oxynitrides are of particular interest.

Within the framework of this work, it was possible to develop process parameters for FAST that permit a general application of fluorination with the aid of Teflon to all the investigated oxides and is potentially applicable to other and especially more complex oxides. Here, the required reaction time could be drastically reduced from 24 h to 9 min. Furthermore, the application of FAST allowed a significant increase of the produced amount of product material, increasing the yield from a few hundred milligrams to several grams of material, which could be further increased with the right pressing tools. The obtained phase can be defined solely by the ratios of Teflon to metal oxide used in the educt mixture and the method of reactant mixing (ball milling, mixing in a vortexer, or simple mortaring).

In studying the products obtained from this FAST synthesis, a new, previously unknown, phase of tungsten oxyfluoride was identified and, using automated electron diffraction tomography as well as synchrotron data, its structure was solved. As the main influence of using FAST for synthesis compared to conventional synthesis in quartz ampoules, a large disorder in the obtained materials was found. This is manifested in larger and rougher particle surfaces clearly visible via electron microscopy - much smaller crystalline regions fused together to form larger particles - and lower long-range order of the product powders. The latter is particularly evident in data from nuclear magnetic resonance spectroscopy and analysis of neutron diffraction data and the associated pair distribution functions. Thus, FAST leads to "freezing" of the products in a metastable state before thermal equilibration is possible. Similarly, FAST was found to inhibit the overall crystal growth during synthesis, likely due to the much shorter reaction time.

All these factors could be confirmed for the investigated niobium, tantalum and tungsten oxyfluorides and cause a drastic improvement in the suitability of the obtained material for photocatalytic decomposition of Rhodamine B (tungsten oxyfluoride) or for photocatalytic hydrogen evolution (niobium and tantalum oxyfluoride). The performance of the materials obtained via FAST in these applications reaches the range of the currently best known compounds and is a proof of the potential of this method.

Another goal of this work was the investigation of nitridation, using magnesium nitride as a nitrogen analogue of fluorination using Teflon. Within the framework of a supervised master's thesis, the first positive preliminary tests were successfully led to a synthesis of tantalum oxynitride, which was used as a model compound. It is particularly interesting to note that the application of FAST to the synthesis initially only leads to the incorporation of nitrogen while maintaining the structure and only forming a superstructure before the corresponding oxynitride phase is formed. The nitrogen atoms are incorporated particularly in the center of the structure. This observation opens the potential to incorporate nitrogen into compounds while the structure is preserved, but requires further investigation using other oxide systems. Initial attempts in this direction yielded promising results.

In summary, the potential of FAST for synthesis could be demonstrated by the successful transfer of two synthesis processes. More precisely, the influence of this method on the micro- and macrostructure of materials could be shown in comparison to conventional synthesis methods. In particular, these differences lead to drastic changes in the suitability of the obtained products for photocatalytic processes, which further illustrates the potential of FAST.

Chapter 7 | Supplementary Information

The contents of the following chapter are taken and partially adapted from the supplementary information to *Adv. Funct. Mater.* **2020**, 30, 1909051.

Authorship contributions

Category 1

Conception and design of study:

[REDACTED]

Acquisition of data:

[REDACTED] preparation of samples.
[REDACTED] – PXRD measurements.
[REDACTED] acquisition of ADT and HR-TEM data.
[REDACTED] Laser microscope and SEM images.
[REDACTED] – measurement of ^{19}F solid-state NMR.
[REDACTED] acquisition of UV/Vis-data.
[REDACTED] acquisition of photocatalytic data.
[REDACTED] – acquisition of XPS data.

Analysis and/or interpretation of data:

[REDACTED] – unit cell analysis via ADT data.
[REDACTED] – PXRD refinement and phase evolution analysis.
[REDACTED] – analysis of ^{19}F solid-state NMR.
[REDACTED] interpretation of XPS data.

Category 2

Drafting the supplementary information:

[REDACTED]

Revising the supplementary information critically for important intellectual content:

[Redacted]

Figure 7.1.1: prepared by
Figure 7.1.2: prepared by
Figure 7.1.3: prepared by
Figure 7.1.4: prepared by
Figure 7.1.5: prepared by
Figure 7.1.6: prepared by
Figure 7.1.7: prepared by
Figure 7.1.8: prepared by
Figure 7.1.9: prepared by
Figure 7.1.10: prepared by
Figure 7.1.11: prepared by

[Redacted]

Chapter 7.1 Supplementary Information from Chapter 2

“

Table 7.1.1. Unit cell parameter values obtained by averaging the lattice parameters of 12 EDT data sets from different crystals of the same sample (SPS prepared $\text{WO}_{2.90}\text{F}_{0.10}$). Mean values and deviations are calculated neglecting crystal 6 due to complex twinning.

measured crystal	<i>a</i> - axis	<i>b</i> - axis	<i>c</i> - axis
crystal 1	7.330	7.371	7.714
crystal 2	7.360	7.390	7.712
crystal 3	7.364	7.412	7.725
crystal 4	7.352	7.397	7.717
crystal 5	7.439	7.480	7.678
crystal 6	7.361	7.456	7.717
crystal 7	7.347	7.397	7.726
crystal 8	7.381	7.433	7.720
crystal 9	7.355	7.433	7.711
crystal 10	7.363	7.438	7.693
crystal 11	7.356	7.455	7.735
crystal 12	7.373	7.428	7.751
mean + std. dev.	7.358 ± 0.013	7.419 ± 0.027	7.720 ± 0.014
powder refinement	7.400	7.462	7.720

Table 7.1.2. Fit parameter of the three orthorhombic (Figure 2.4A) and four cubic (Figure 2.4B) deconvoluted peaks from the F⁻ solid state MAS NMR of WO_{2.90}F_{0.08} (conventional synthesis)/WO_{2.90}F_{0.10} (SPS-prepared) and WO_{2.60}F_{0.40} (conventional synthesis)/ WO_{2.40}F_{0.60} (SPS-prepared).

SPS – orthorh. (Figure 7.1.6A)	Peak 1	Peak 2	Peak 3	Peak 4
Peak position / ppm	-136.0	-113.7	-109.0	
FWHM / ppm	26.0	3.9	12.2	
Relative peak area	65 %	24 %	11 %	
Conv. – orthorh. (Figure 7.1.6A)				
Peak position / ppm	-138.0	-112.4	-105.2	
FWHM / ppm	28.0	4.8	12.0	
Relative peak area	50 %	35 %	15 %	
SPS – cubic (Figure 7.1.6B)				
Peak position / ppm	-138.0	-108.5	-99.3	-94.7
FWHM / ppm	28.0	6.6	5.8	15.6
Relative peak area	39 %	43 %	5 %	13 %
Conv. – cubic (Figure 7.1.6B)				
Peak position / ppm	-146.0	-108.2	-102.4	94.6
FWHM / ppm	22.0	7.1	2.2	3.8
Relative peak area	32 %	48 %	8 %	13 %

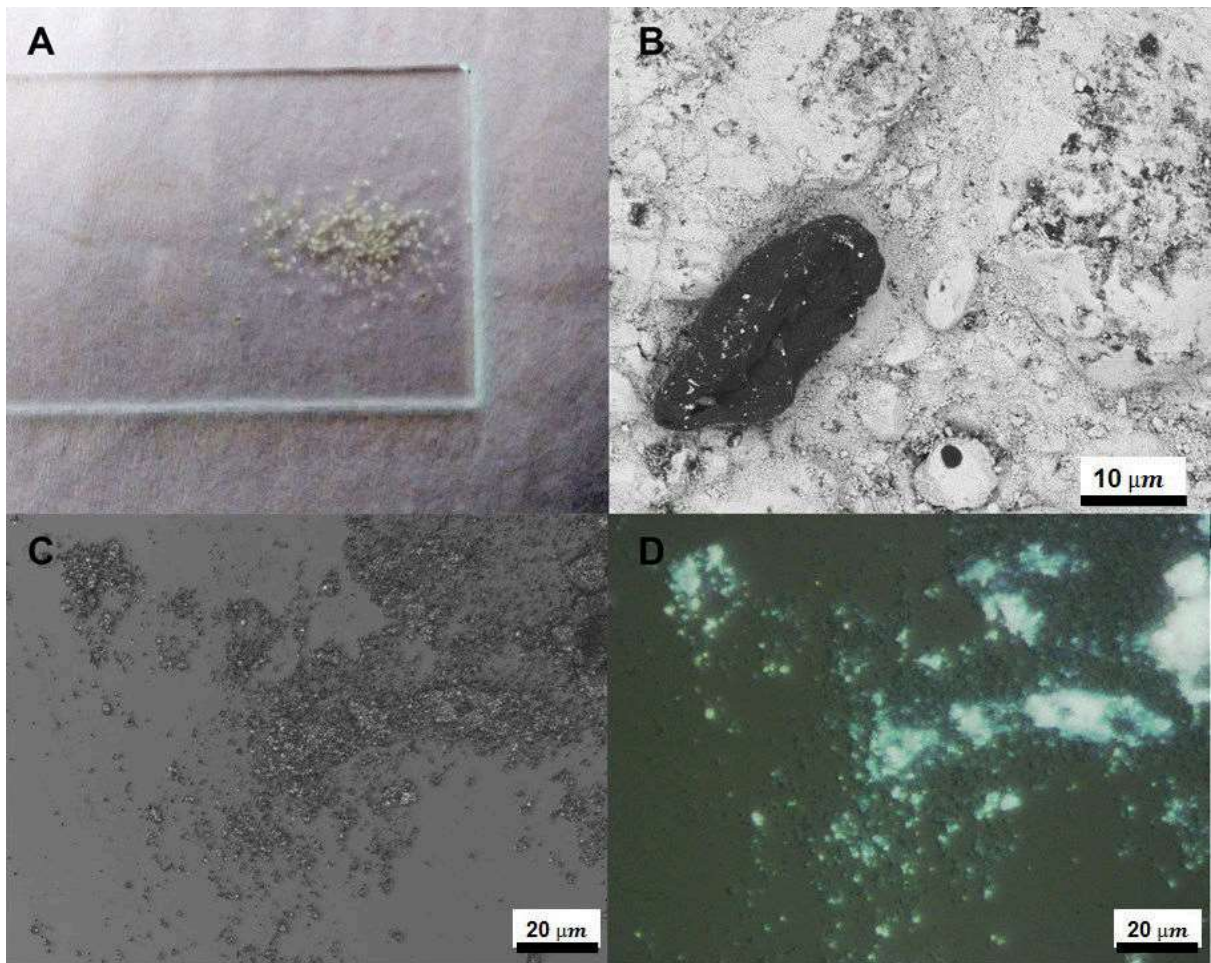


Figure 7.1.1. Observeable flakes after ball-milling of powder mixtures with high PTFE/ WO_3 ratios (**A+C+D**) and pellet cross-section of not ball-milled precursor mixture (**B**). The black particles in the SEM picture consists of PTFE-remains which form when the precursors are insufficiently mixed (eg no ball-milling), likely due to incomplete decomposition/reaction with WO_3 . These particle create/make up the present “pores” in reacted product-pellets.

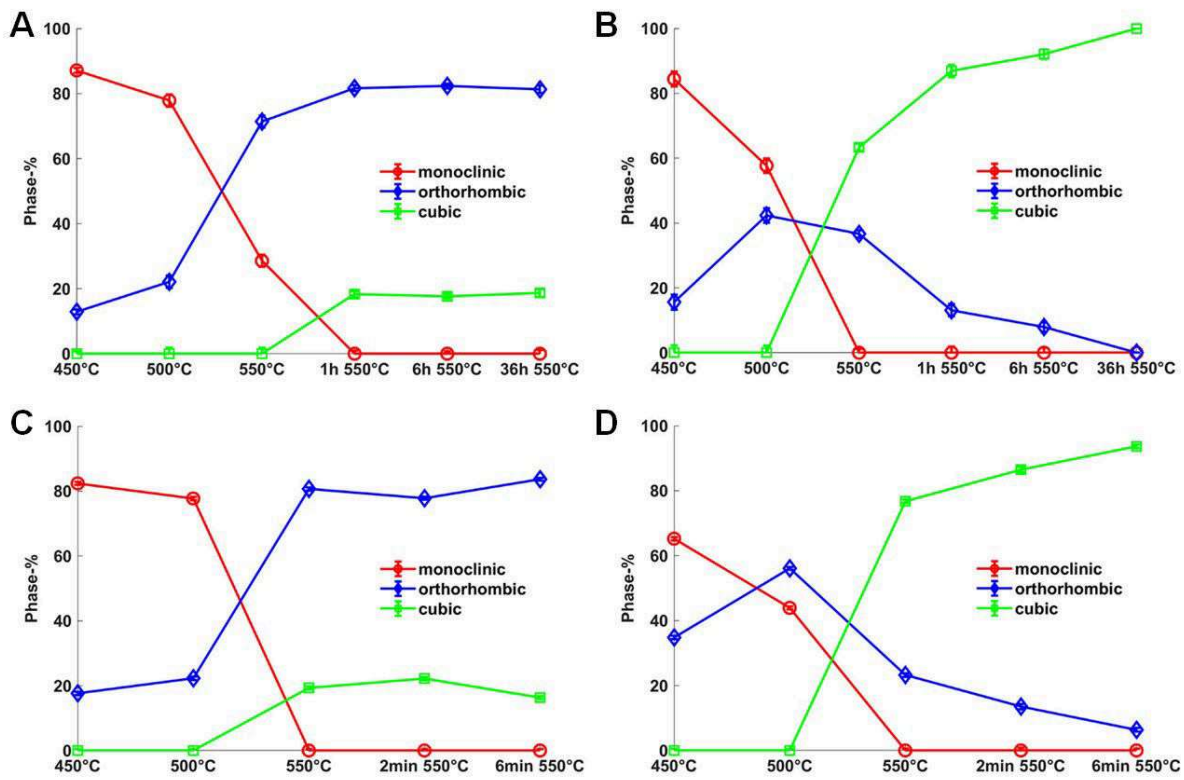


Figure 7.1.2. Evolution of $\text{WO}_{3-x}\text{F}_x$ monoclinic, orthorhombic and cubic phases during the SPS reaction for two different starting compositions $x = 0.15$ (A + C) and $x = 1.0$ (B + D). Analyses were carried out by stopping the reaction at the indicated points of the reaction on the x axis. The progress of the SPS reaction is shown in C+D and that of the conventional synthesis in A+B.

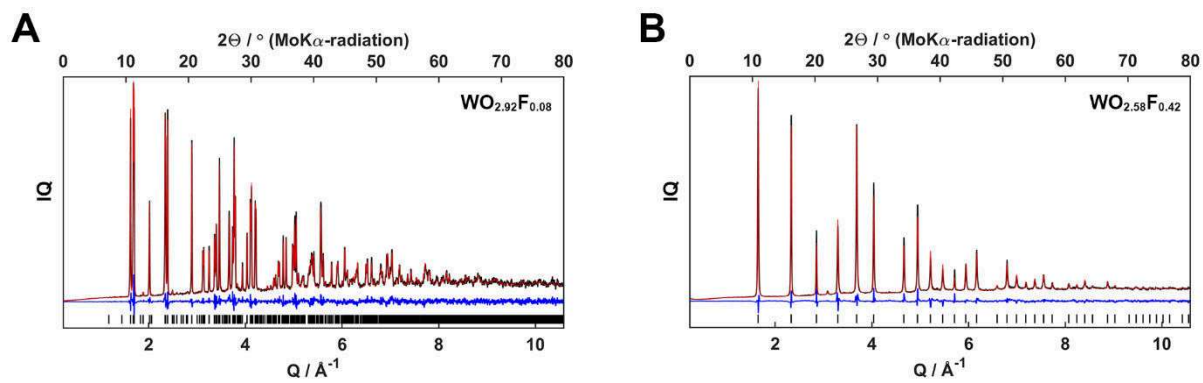


Figure 7.1.3. Rietveld Refinements of phase pure conventional sample $\text{WO}_{2.92}\text{F}_{0.08}$ (A) and $\text{WO}_{2.60}\text{F}_{0.40}$ (B). Intensities are weighted with q -values.

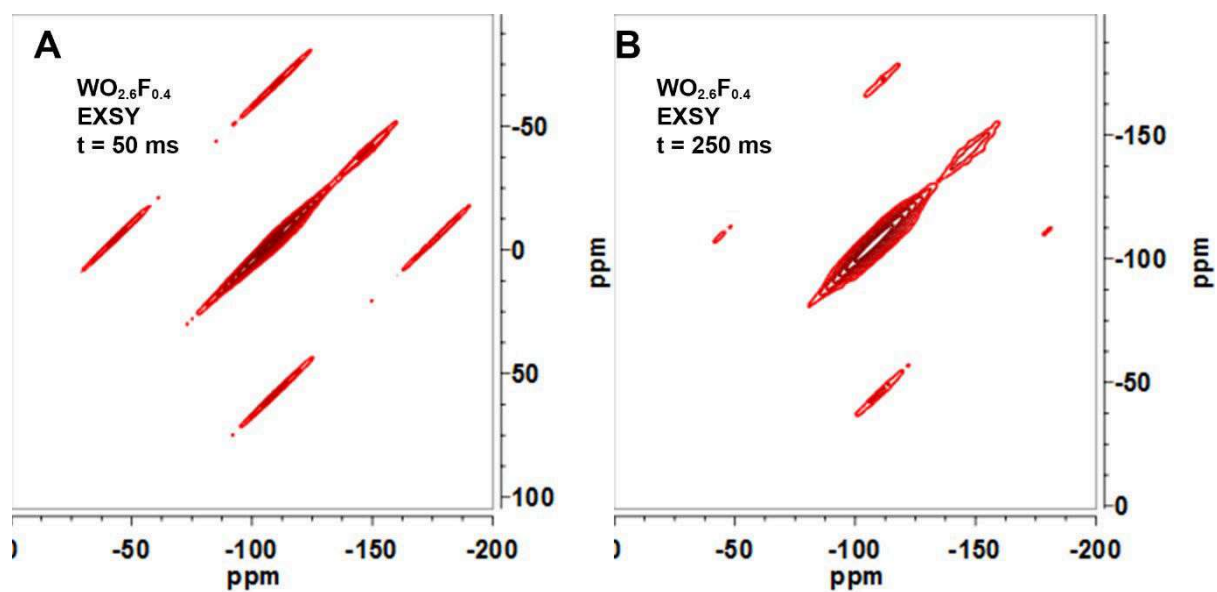


Figure 7.1.4. (A) ^{19}F EXSY solid state spectrum of cubic $\text{WO}_{2.6}\text{F}_{0.4}$ at $t_{\text{mix}} = 50$ ms. Three to four distinct fluorine environments were identified. Two to three between 100 and 120 ppm and one at 148 ppm. (B) ^{19}F EXSY solid state spectrum of cubic $\text{WO}_{2.6}\text{F}_{0.4}$ at $t_{\text{mix}} = 250$ ms. Three to four distinct fluorine environments were identified. All fluorine environments are independent due to the absence of cross correlation. Spinning side bands at 45 ppm and 180 ppm are correlated to the fluorine signal at approx. 110 ppm.

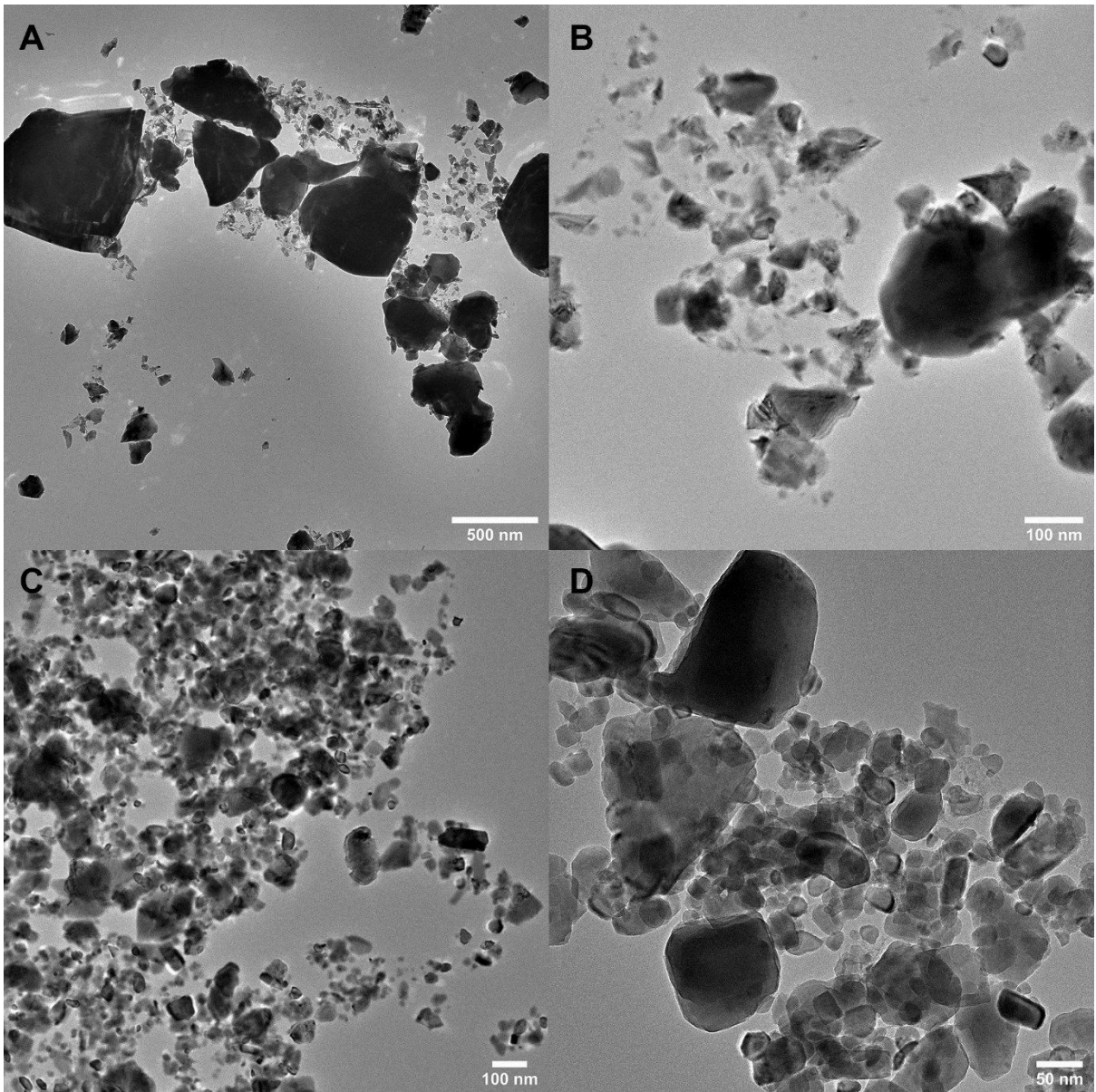


Figure 7.1.5. Overview TEM pictures for conventional synthesized $\text{WO}_{2.58}\text{F}_{0.42}$ (A + B) and $\text{WO}_{2.40}\text{F}_{0.60}$ (C + D) synthesized by SPS using the same preparation procedure by ball-milling. The observable grains in the SPS sample are much more uniform and smaller than in the conventional sample.

X-ray photoelectron spectroscopy (XPS). For additional XPS measurements of air heated samples, powders were pressed into indium foil and transferred into the XPS spectrometer (SPECS GmbH, Germany). When the pressure inside the vacuum chamber was below 5×10^{-8} mbar, the spectra were recorded using both non-monochromatized Al K α radiation (1486.6 eV) and Mg K α radiation (1253.6 eV) from the twin-anode X-ray source XR 50, which was operated at 10 kV and 10 mA. To measure a survey spectrum, the hemispherical energy analyzer PHOIBOS 100 was operated at constant analyzer pass energy $E_p = 50$ eV. High-resolution spectra of W 4f and 5p, and O 1s were recorded with ten sweeps, F 1s with 50 sweeps each at $E_p = 13$ eV.

CasaXPS (Casa Software Ltd., UK) was used for XPS data analysis. After subtraction of the X-ray satellites and calculation of the background according to Shirley, the individual spectral components of the W 4f and 5p, F 1s, and O 1s spectra were fitted using a product of a Gaussian function with a Lorentzian (GL(60)).

Results of XPS spectroscopy of air heated $\text{WO}_{3-x}\text{F}_x$ samples

Figure 7.1.5 and 7.1.6 show the F (A+D), O (B+E), and W (C+F) regions of the XPS spectra of $\text{WO}_{2.9}\text{O}_{0.1}$ (S5) and $\text{WO}_{2.55}\text{O}_{0.45}$ (S6) synthesized by SPS (A-C) and conventionally (D-F). The XPS overview spectrum (Figure 7.1.4) confirms the presence of the elements W, O, and F. Furthermore the absence of Carbon after air heating can be confirmed. In Figure 7.1.5/6 C and F, the peaks centered at 36 and 39 eV are assigned to the W 4f 7/2 and W 4f 5/2 orbitals, respectively, revealing the oxidation states of VI for $\text{WO}_{2.9}\text{F}_{0.1}$ and $\text{WO}_{2.55}\text{O}_{0.45}$. Independent of the synthesis method. No W(V) states could be clearly identified leading to the conclusion that the particle surface gets at least partially oxidized during air-heating. Fitting the W 4f orbitals leaves a small residue which could indicate a small amount W(V) states. The O 1s areas in Figure 7.1.5/6 B and E show two signals at 531 and 533 eV for conventional synthesized samples, which correspond to lattice O and surface hydroxyl groups. Compared to Figure 2.6, surface water was completely removed and for SPS synthesized samples, surface hydroxyl was removed too. The XPS spectra of the F 1s core electrons (Figure 2.6A and D) show a signal centered at 685 eV, originating from W–F bonds on the surface of the tungsten oxyfluoride samples. A second F 1s peak at 687 eV, only present in the spectrum of the oxyfluoride synthesized conventionally, is assigned to substitutional F atoms that occupy oxygen sites in the lattice with their associated W–O–H bonds.

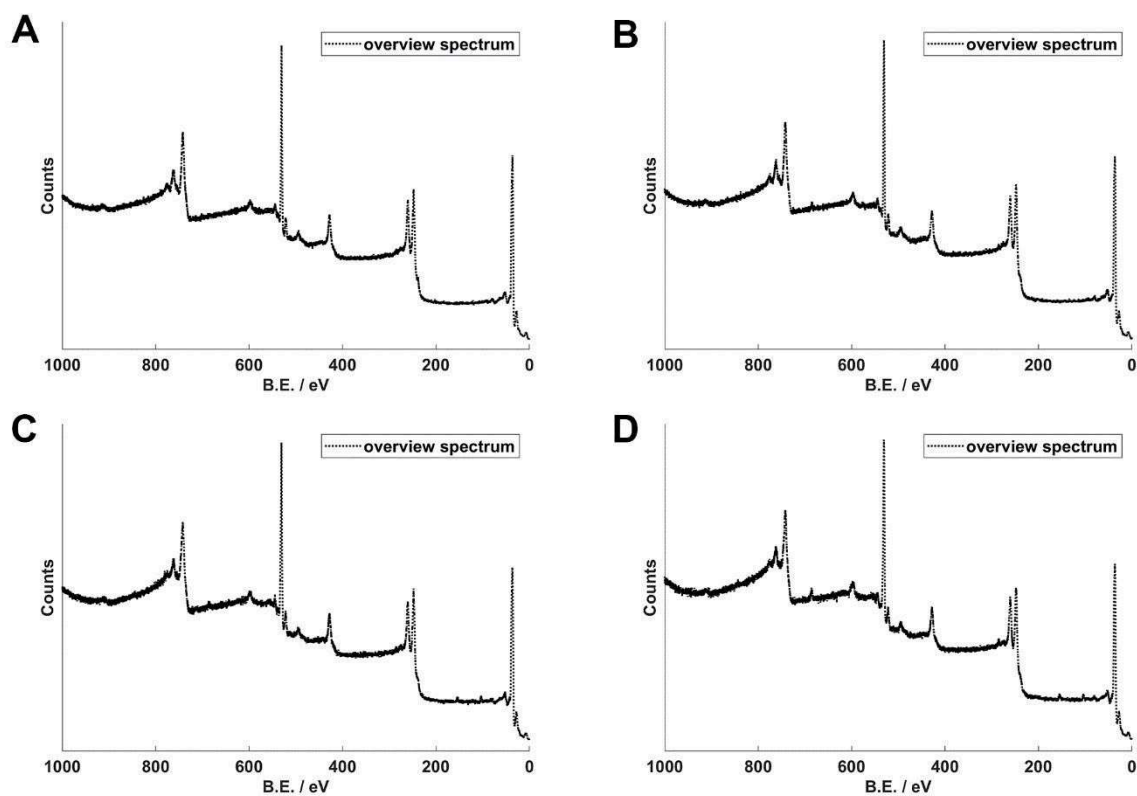


Figure 7.1.6. XPS overview spectra of conventional (C,D) and SPS (A,B) synthesized orthorhombic $WO_{2.90}O_{0.10}$ (A,C) and cubic $WO_{2.60}O_{0.40}$ (B,C).

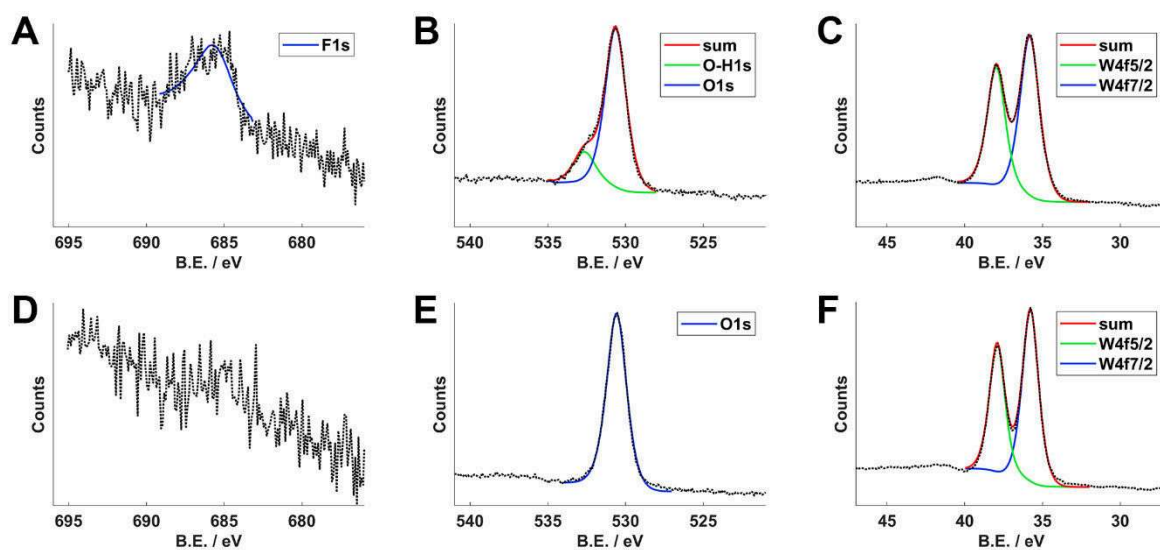


Figure 7.1.7. Fitted XPS spectra of conventionally (A-C) and SPS (D-F) prepared orthorhombic $\text{WO}_{2.90}\text{O}_{0.10}$. The F, O, and W sub-spectra are shown in (A,D), (B,E) and (C,F).

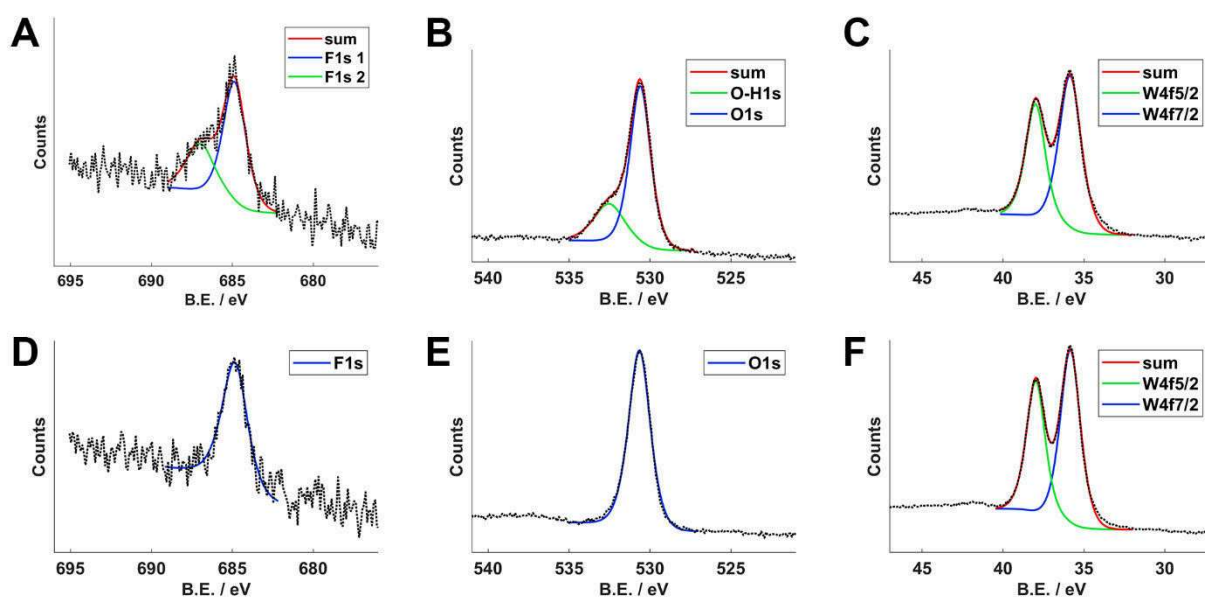


Figure 7.1.8. Fitted XPS spectra of conventionally (A-C) and SPS (D-F) prepared cubic $\text{WO}_{2.60}\text{O}_{0.40}$. The F, O, and W sub-spectra are shown in (A,D), (B,E) and (C,F).

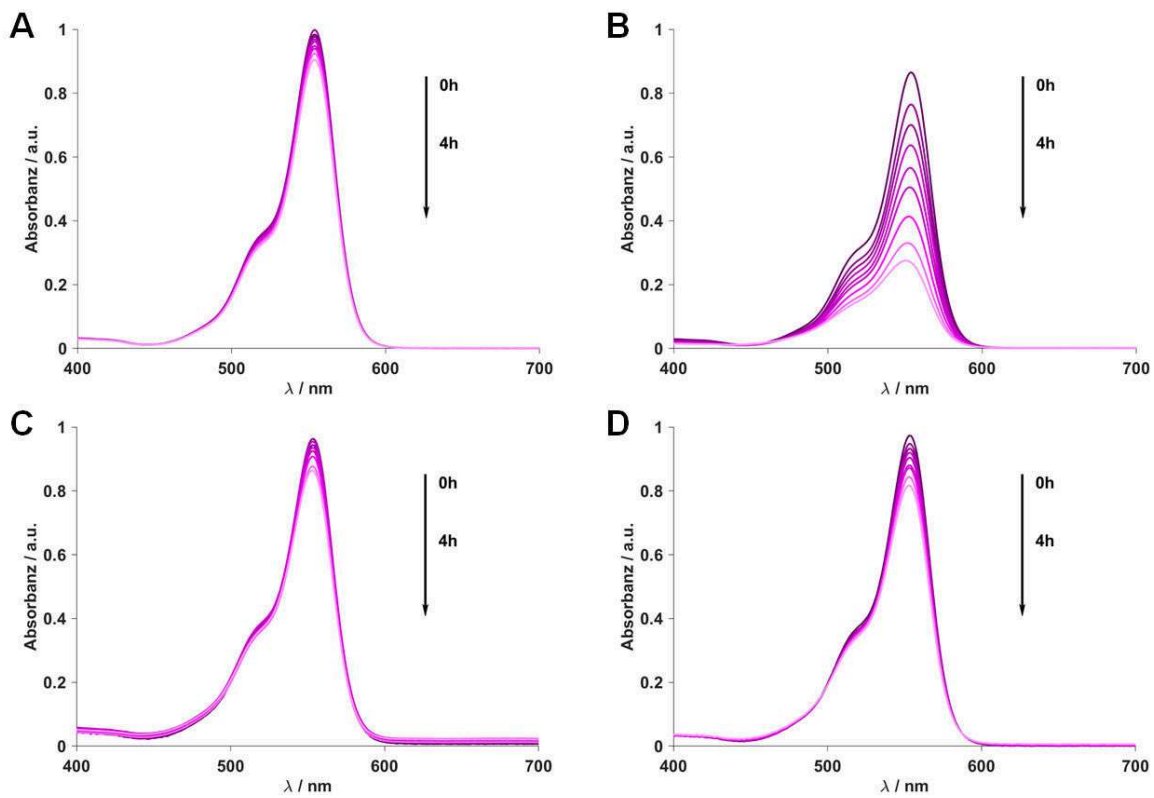


Figure 7.1.9. UV-vis spectra showing the photocatalytic degradation of RhB in aqueous solution for cubic (A + B) and orthorhombic (C + D) $\text{WO}_{3-x}\text{F}_x$ prepared by conventional solid state chemistry (A - $\text{WO}_{2.60}\text{F}_{0.40}$, C - $\text{WO}_{2.92}\text{F}_{0.82}$) and by SPS (B - $\text{WO}_{2.40}\text{F}_{0.60}$, D- $\text{WO}_{2.90}\text{F}_{0.10}$).

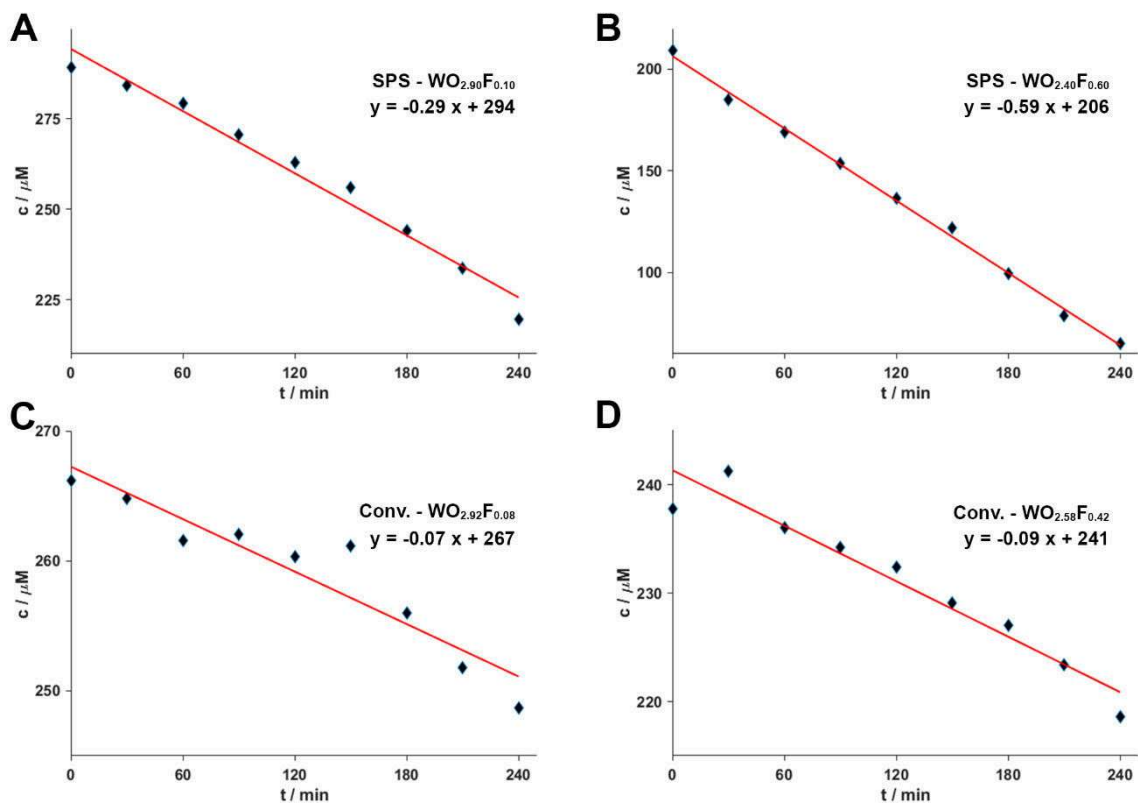


Figure 7.1.10. Plots showing the concentration development of RhB during photocatalytic degradation in aqueous solution for $\text{WO}_{2.55}\text{O}_{0.45}$ (**B + D**) and $\text{WO}_{2.9}\text{F}_{0.1}$ (**A + C**) prepared by conventional solid state chemistry (**C, D**) and by SPS (**A, B**).

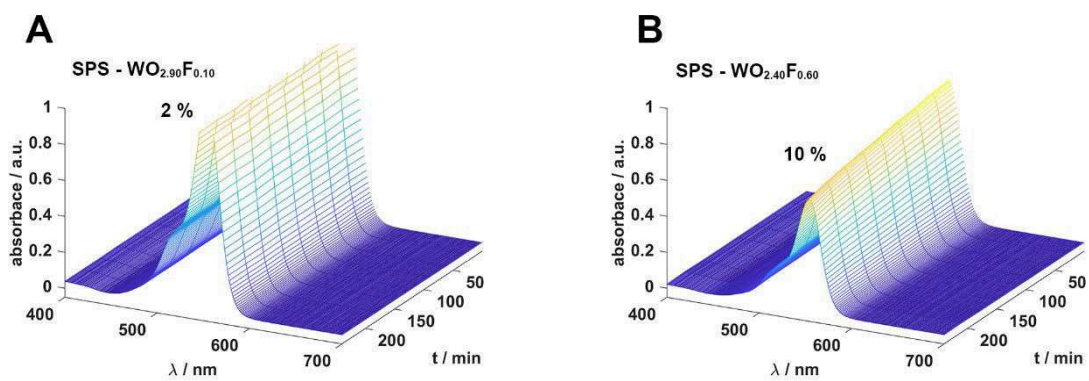


Figure 7.1.11. UV–vis spectra showing the photocatalytic degradation of RhB in aqueous solution under dark conditions for SPS prepared orthorhombic $\text{WO}_{2.90}\text{F}_{0.10}$ (**A**) and cubic $\text{WO}_{2.40}\text{F}_{0.60}$ (**B**).

«

The contents of the following chapter are taken and partially adapted from the supplementary information of *Adv. Funct. Mater.* **2021**, *accepted and to be published*.

Authorship contributions

Category 1

Conception and design of study:

[REDACTED]

Acquisition of data:

- [REDACTED] – preparation of samples.
- [REDACTED] – PXRD measurements.
- [REDACTED] – acquisition of neutron diffraction data.
- [REDACTED] – HR-TEM and SEM images.
- [REDACTED] – measurement of ^{19}F solid-state NMR.
- [REDACTED] – acquisition of UV/Vis-data.
- [REDACTED] – acquisition of XPS data.

Analysis and/or interpretation of data:

- [REDACTED] – PXRD refinement.
- [REDACTED] – PDF analysis and interpretation (neutron diffraction).
- [REDACTED] – HR-TEM and SEM analysis.
- [REDACTED] – analysis of ^{19}F solid-state NMR.
- [REDACTED] – interpretation of XPS data.
- [REDACTED] – analysis of UV/Vis.

Category 2

Drafting the supplementary information:

[REDACTED]

Revising the supplementary information critically for important intellectual content:

Category 3

Approval of the version of the supplementary information to be published:

Figure 7.2.1: prepared by
Figure 7.2.2: prepared by
Figure 7.2.3: prepared by
Figure 7.2.4: prepared by
Figure 7.2.5: prepared by
Figure 7.2.6: prepared by
Figure 7.2.7: prepared by
Figure 7.2.8: prepared by
Figure 7.2.8: prepared by
Figure 7.2.8: prepared by

Chapter 7.2 Supplementary Information from Chapter 3

«

Table 7.2.1. Effect of reaction parameters during SPS preparation on the phase distribution (50°C/min heating and dwelling at $T = 600^\circ\text{C}$ for $t = 9$ min and under a pressure of $p = 19$ MPa). Side phase are listed. No tantalum carbides were formed.

Educt mixture	T < 600°C	T > 650°C	T > 750°C	Grinding in mortar	t < 9 min	t >> 9 min	p > 19 MPa
Ta₃O₇F – (x = 1.0, vortexed)	Ta₂O₅	-	Ta₂O₅	-	Ta₂O₅ (none for t < 5 min)	Ta₂O₅	Ta₂O₅
Ta₂O₂F – (x = 1.2, ball-milled)	Ta₂O₅ > Ta₃O₇F	Ta₃O₇F	Ta₃O₇F	Ta₃O₇F	Ta₃O₇F	Ta₃O₇F	Ta₂O₅

Table 7.2.2. Results of Rietveld-Refinement of Ta₃O₇F and TaO₂F synthesized by SPS (Figure 3.2A and 2B) and by conventional chemistry (Figure 7.2.1). Because of large strain along long axis, conventional prepared Ta₃O₇F was taken as a reference for phase refinement, phase-purity was assumed.

Sample	unit cell parameters			gof	R _{wp}	Side phase	% side phase
	a	b	c				
Ta ₃ O ₇ F - SPS	6.457(5)	10.624(7)	3.904(1)	2.82	4.76	TaO ₂ F	12.9 ± 0.1 %
TaO ₂ F - SPS	3.8991(4)	-	-	1.64	4.55	TaO ₂ F	5.6 ± 0.1 %
Ta ₃ O ₇ F	6.481(4)	10.545(5)	3.910(1)	2.92	11.73	TaO ₂ F	0% assumed
TaO ₂ F	3.8990(2)	-	-	1.36	7.01	Ta ₃ O ₇ F	1.8 ± 0.2 %

ζ-potential measurements were carried out at different pH values in probe the presence of hydroxide at the particle surface.¹ Potential values are compiled in Table 7.2.3. Fluorination with Teflon leads to much values for the ζ-potential. The ζ-potential values increase from orthorhombic Ta₃O₇F to cubic TaO₂F, i.e., more hydroxide groups are present for Ta₃O₇F, the lower fluorinated phase. This is in agreement with larger deviations of the nominal fluorine contents. Still, the deviations of the ζ-potentials are not significant enough to enable conclusions concerning the effect of surface OH groups on the photoelectrocatalytic properties.

Table 7.2.3. pH-dependence of the ζ potentials of Ta₃O₇F and TaO₂F. All values are the average of three individual determinations at identical pH under identical conditions.

Sample	pH 3.1	pH 4.1	pH 5.2	pH 6.8	pH 8.9	pH 9.8	pH 11.1
Ta ₃ O ₇ F - SPS	-3.1	-13.3	-17.2	-20.8	-21.6	-22.6	-23.4
TaO ₂ F – SPS	1.6	-7.5	-9.1	-13.0	-17.9	-18.7	-25.6
Ta ₃ O ₇ F	-7.7	-11.5	-19.8	-22.1	-22.7	-23.7	-25.2
TaO ₂ F	-1.6	-3.5	-9.6	-14.2	-15.3	-17.6	-22.0
Ta ₂ O ₅	21.1	4.9	-17.8	-18.7	-20.1	-21.3	-22.4

Table 7.2.4. Summary of XPS determined elemental compositions and calculated F/O ratio on surface.

Sample	F 1s %	O 1s %	Ta 4f %	F : O ratio
Ta₃O₇F - SPS	12.6	67.0	20.4	4 : 20
Ta₃O₇F	10.8	71.8	17.4	3 : 20
TaO₂F - SPS	21.0	61.1	17.9	7 : 20
TaO₂F	8.5	76.6	14.9	2 : 20
Ta₂O₅	0.4	76.3	23.3	0.1 : 20

Table 7.2.5. Fit parameter of the four to five deconvoluted peaks from the F^- solid state MAS NMR of Ta_3O_7F (conventionally (bottom) and SPS-prepared (top), Figure 7.2.8E) and TaO_2F (conventionally (bottom) and SPS-prepared (top), Figure 7.2.8F), exemplary for the 28 and 29 kHz measurements.

Ta₃O₇F - SPS (Figure 7.2.6A)	Peak 1	Peak 2	Peak 3	Peak 4	Peak 5
Peak position / Hz	14.15	-13.88	-31.15	-42.32	-58.67
FWHM / Hz	5.57	4.04	3.08	3.41	2.45
Relative peak area	7.8 %	11.1 %	69.7 %	5.7 %	5.7 %

TaO₂F - SPS (Figure 7.2.6B)	Peak 1	Peak 2	Peak 3	Peak 4
Peak position / Hz	16.77	-19.78	-26.63	-51.90
FWHM / Hz	6.02	6.02	3.57	3.76
Relative peak area	10.4 %	12.6 %	69.3 %	7.7 %

Ta₃O₇F (Figure 7.2.6A)	Peak 1	Peak 2	Peak 3	Peak 4	Peak 5
Peak position / Hz	14.51	-14.31	-30.86	-42.36	-58.67
FWHM / Hz	6.02	4.51	3.11	2.55	2.21
Relative peak area	8.4 %	13.4 %	70.3 %	2.7 %	5.2 %

TaO₂F (Figure 7.2.6B)	Peak 1	Peak 2	Peak 3	Peak 4
Peak position / Hz	13.36	-19.27	-26.23	-51.52
FWHM / Hz	6.02	6.02	3.47	0.75
Relative peak area	8.7 %	13.3 %	77.1 %	0.9 %

MAS-NMR ^{19}F spectroscopy of TaO_2F and Ta_3O_7F . Under ambient conditions, TaO_2F crystallizes in a cubic ReO_3 -type average structure, with a disordered distribution of oxygen and fluorine atoms over the available anion sites. The local structure of TaO_2F prepared by fluorination of Ta_2O_5 with HF by aqueous solution synthesis has been shown to have O and F randomly distributed over the available anion sites which could be described by a $3 \times 3 \times 3$ supercell model containing $-Ta-O-Ta-O-Ta-F-$ chains along $\langle 1\ 0\ 0 \rangle$, with different Ta-O and

Ta–F distances and O/F off-axis displacements.² TaO₂F (and NbO₂F) prepared with HF from the corresponding oxides have been shown to contain hydroxyl defects and metal vacancies according to M_{1-x}□_xO_{2-5x}(OH,F)_{1+5x}.¹² Obtaining pure TaO₂F (and NbO₂F) from these samples by fully removing metal vacancies and hydroxide, while avoiding the formation of the oxide is difficult.³

The TaO₂F and Ta₃O₇F samples were analyzed with ¹⁹F solid state magic angle spinning (MAS) NMR spectroscopy. The ¹⁹F NMR spectra provide information about the fluorine environment (changes in the shielding / the chemical shift) and the local order (uniformity of the local field expressed / full width at half maximum (fwhm) of a signal). Clearly, higher order at a crystallographic site results in sharper ¹⁹F resonances. All ¹⁹F NMR spectra with the resp. deconvolution tables are presented in the Supporting Information Figure 7.2.8, Table 7.2.3. In order to determine the isotropic ¹⁹F chemical shifts we have recorded the ¹⁹F NMR spectra as a function of the spinning frequency. This approach results in frequency dependent shift of the spinning sidebands while the fluorine resonances remain unaffected.

The spectra of the cubic conventionally and SPS synthesized TaO₂F samples consist of one dominant resonance line at ca. -70 ppm and three weaker signals appearing in the shift ranges of ca 35.5 – 44.6 ppm, -51 - -52.6 ppm and -137 - -138 ppm. The dominant resonance at ca -70 ppm is assigned to the bridging fluorine in TaO₂F environment (the fluorine atom is bound to two tantalum atoms), which perfectly coincides with earlier published calculated and experimental data. The signals, which appears in the lowest field (35.5 – 44.6 ppm), are due to the F-Ta□ environment. This confirms the presence of cationic vacancies most probably arising from the substitution of the divalent O²⁻ with the monovalent F⁻.³ The signals at ca -51 ppm are related with the terminal fluorine atoms. Earlier reports show that the chemical shift of such fluorine can vary as a function of the compound in which they are as well as the local environment related with surroundings ligands. The most high field shifted resonance at ca. -137 ppm is related with an additional electron acceptor such as fluorine, i.e. TaOF₂ environment, as already revealed before.⁴ The ratios between the integrals in both cases are comparable: conventional synthesis – ca 40 ppm: -70 ppm: -51 ppm: -138 ppm = 9 : 13 : 77 : 1 and SPS synthesis 10 : 13 : 69 : 8. The only significant difference is observed in the case of the most high field shifted resonance at ca -137 - -138 ppm. Clearly, the SPS synthesis favors the occurrence of such environment esp. at the contact border of the Ta₂O₅ grains and PTFE. The conventional synthesis in an ampule takes significantly longer (typically over 24 hours vs

couples of minutes for SPS) and allows better homogenization resulting in compounds with poor TaOF₂ environment. The large full width at half maximum (fwhm) of all signals (in the range of 3.5 to 6 kHz) reveals pronounced local disorder related with a number of environments around a fluorine atom as well as different possible orientations.

We have investigated the orthorhombic conventionally and SPS synthesized Ta₃O₇F structures also applying ¹⁹F NMR spectroscopy. Contrary to the cubic TaO₂F samples, the ¹⁹F spectra of both orthorhombic Ta₃O₇F ones are characterized by five resonances with almost perfectly coinciding shifts and integrals – at ca. 37.6 – 38.6 ppm, ca -37 - -38 ppm, ca. -82 ppm, ca. -112.5 ppm and – 156 ppm. The ratios between the integrals are similar: 38 ppm : -38 ppm : -82 ppm : -112 ppm : -156 ppm = 8 : 11: 70 : 6 : 5 for the SPS and 8 : 13 : 70 : 3 : 5 for the conventional synthesis. It should also be noted that the fwhm of all resonances (2 to 6 kHz) is very comparable with the cubic samples. This means that local order remains on average independent on the kind of crystal lattice structure. Cationic vacancies are also present as revealed by the signals at ca 38 ppm. The shifts at ca -38 ppm and the most intense peak at -82 ppm relate with respectively the border fluorine atoms and those in TaO₂F environments. The resonance at -112.5 ppm even though shifted to lower field by 25 ppm relates with a second fluorine in the vicinity of the detected one, while the signals at -156 ppm reveal also fluorine environments with more than one fluorine atoms being present.

Summarizing, in both TaO₂F and Ta₃O₇F structures, cationic vacancies, border fluorine atoms as well as fluorine atoms with another fluorine in the environment of the detected one are present in addition to the dominant ¹⁹F signal related with -Ta-F-Ta- environment. Additionally, in the case of Ta₃O₇F a fluorine environment with more than one fluorine atoms in the vicinity of the detected one is revealed. All fluorine resonances are broadened inhomogeneously due to a distribution of environments and orientations. The local order is independent on the type of the crystal lattice. Better homogenization and longer reaction time are probably the reason for the significant reduction of TaO₂F environments for the conventionally synthesized cubic TaO₂F samples.

Calculation of theoretical optical band positions. The conduction band (E_{CB}) and valence band (E_{VB}) potentials of semiconductors can be calculated using the following empirical equations [5,6,7]

$$E_{CB} = \chi - E_e - 1/2 E_g$$

$$E_{VB} = E_{CB} + E_g$$

Where E_{VB} is the valence band potential and E_{CB} the conduction band potential. E_e is the energy of free electrons of the hydrogen scale (4.5 eV), E_g is the band gap of the respective semiconductor and χ stands for the absolute electronegativity of the atom semiconductor (geometric mean of the absolute electronegativity of the constituent atoms) and is calculated via the following equation

$$\chi = [\chi(A)^a \times \chi(B)^b \times \chi(C)^c]^{1/(a+b+c)}$$

a , b , c are the numbers of the respective elements A , B , C in the chemical formula of the semiconductor. By application of these formulas, the values listed in Table 7.2.4 were obtained. They are represented graphically in Figure 7.2.9.

Table 7.2.6. Calculated Band edge position values

Semiconductor	Absolute electronegativity (χ)	Energy of free electrons (hydrogen scale)	Band gap value (E_g)	Conduction band potential (E_{CB})	Valence band potential (E_{VB})
TaO ₂ F	6.34	4.5 eV	4.23	-0.28 eV	3.95 eV
Ta ₃ O ₇ F	7.02	4.5 eV	4.10	0.47 eV	4.57 eV
Ta ₂ O ₅	6.58	4.5 eV	4.03	0.06 eV	4.09 eV

Fluorination shifts the optical band positions. The conduction band of Ta₂O₅ overlaps with the potential for hydrogen generation. After fluorination, we achieve oxidation, as the conduction band is shifted and shows less overlap with the HER potential. Cui et al.⁷ observed a similar trend in tuning the conductance band by substitution of oxygen by nitrogen. Here, the HER potential of the sample still overlaps with the hydrogen evolution potential.

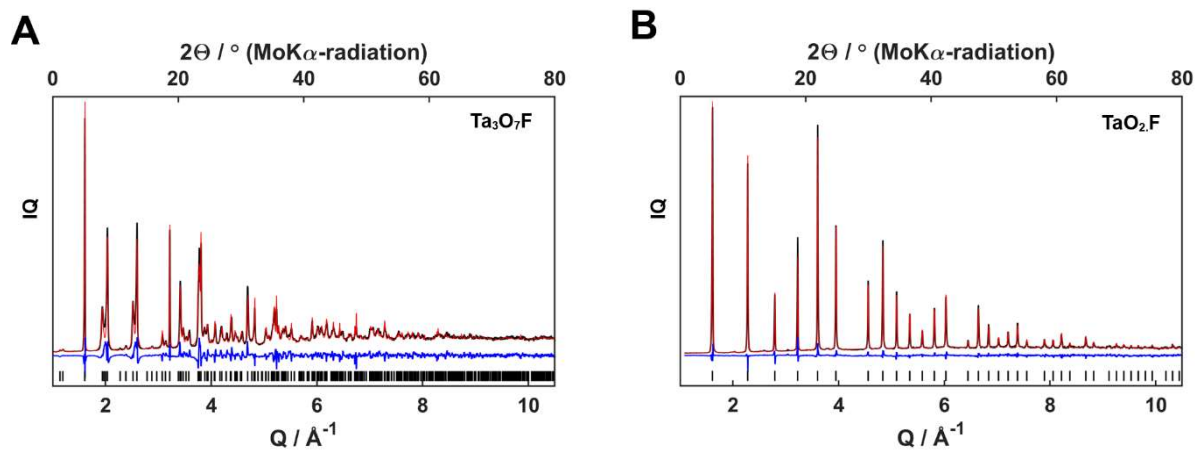


Figure 7.2.1. (A) Rietveld refinement of conventional prepared $\text{Ta}_3\text{O}_7\text{F}$ (red line) using X-ray powder data (88 % $\text{Ta}_3\text{O}_7\text{F}$, 12 % TaO_2F). (B) Rietveld refinement of conventional-prepared $\text{Ta}_3\text{O}_7\text{F}$ (red line) using X-ray powder data. Experimental data are indicated by crosses, the calculated curve obtained after the refinement is indicated with a continuous line. The tick marks correspond to the Bragg reflections of the cubic and orthorhombic structures. The continuous blue curve under the tick marks represents the difference between the experimental data and the calculated curve.

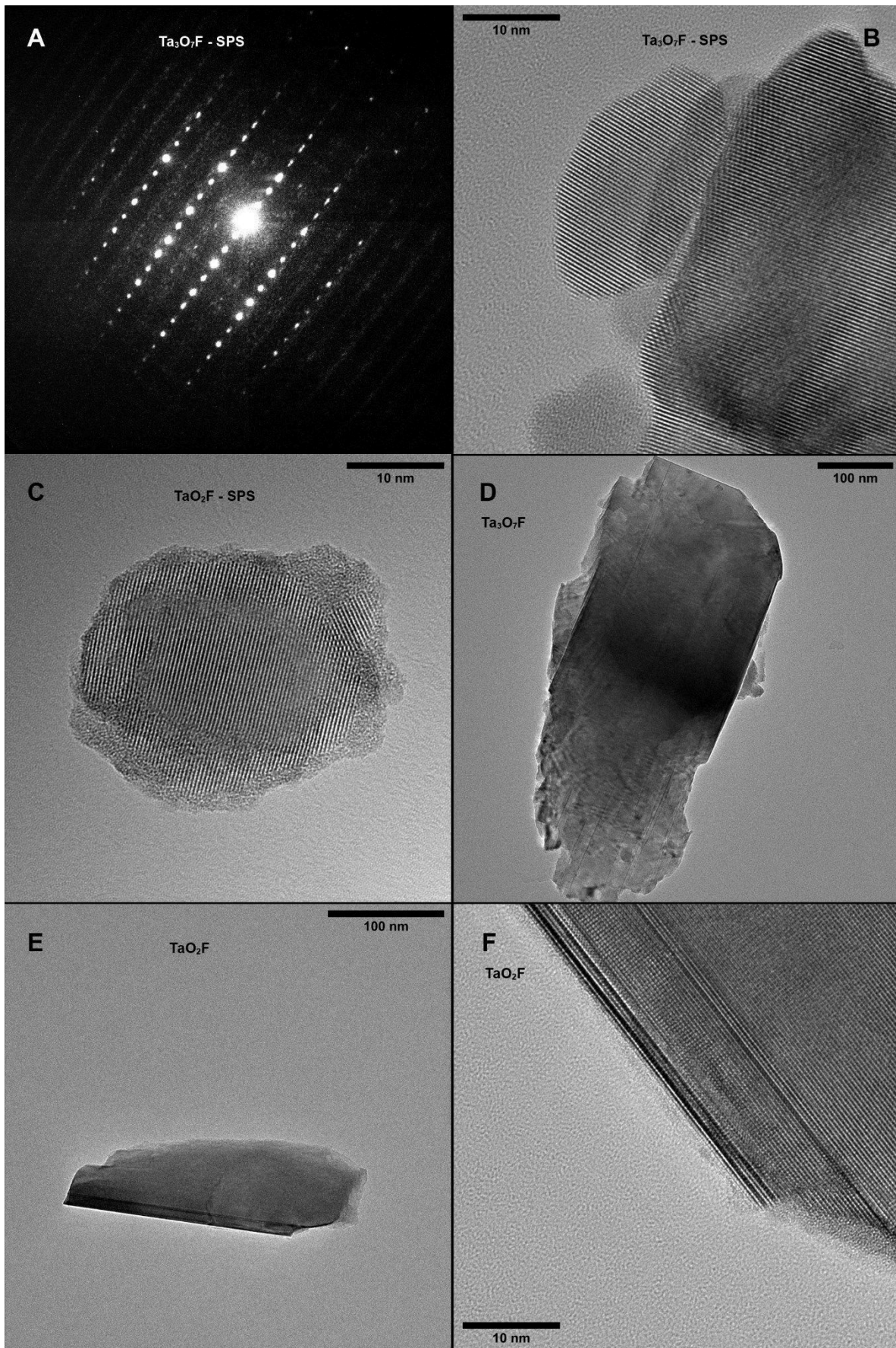


Figure 7.2.2. Diffraction image of Ta₃O₇F prepared by SPS (A). HR-TEM images of Ta₃O₇F and TaO₂F prepared

by SPS (B-C) and conventional ampoule chemistry (D-F) showing presence of line defects.

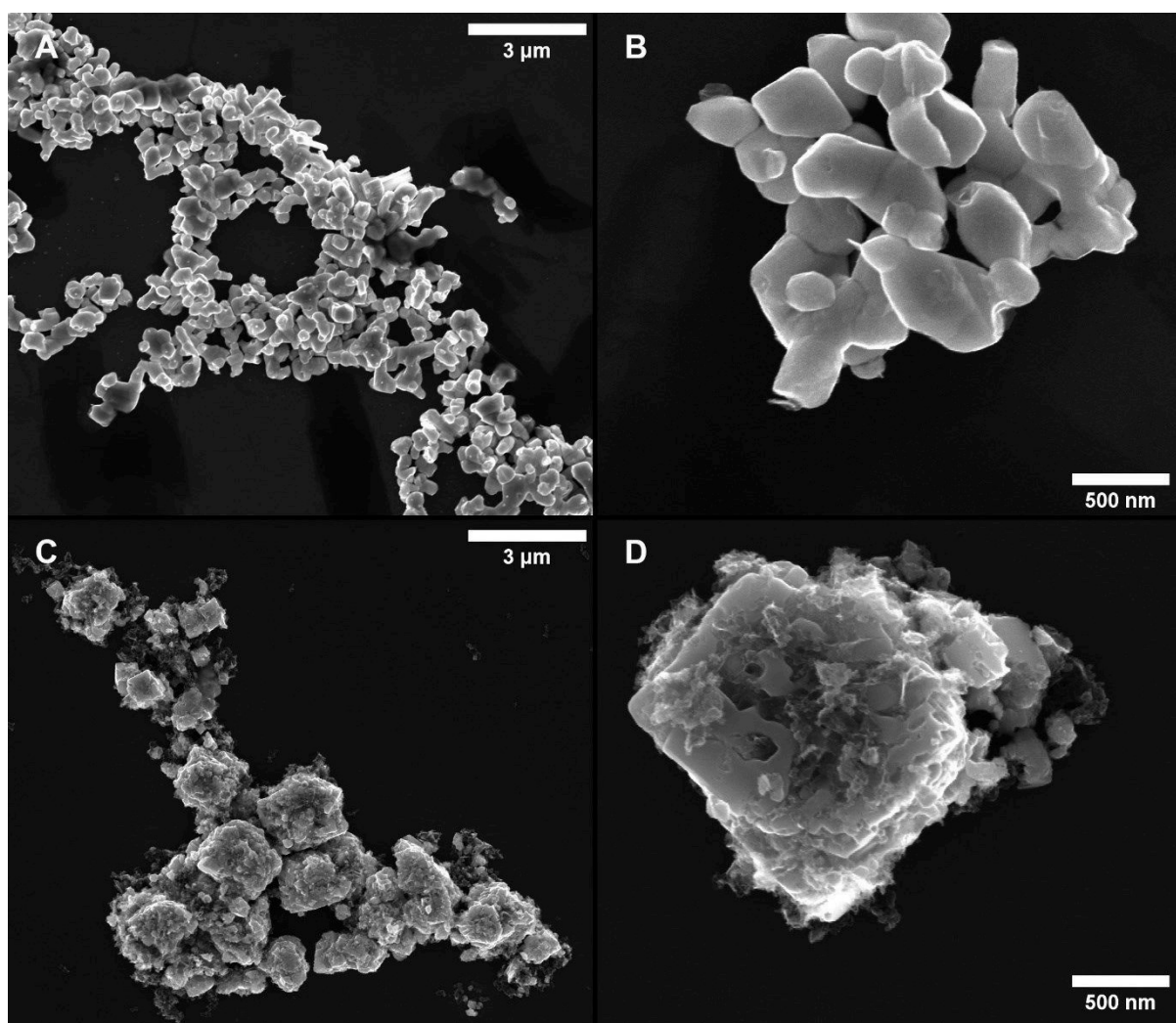


Figure 7.2.3. SEM images of Ta_3O_7F prepared by conventional synthesis (A+B) and SPS synthesis (C+D) showing the much rougher surface and less uniform areas in the material synthesized by field assistance.

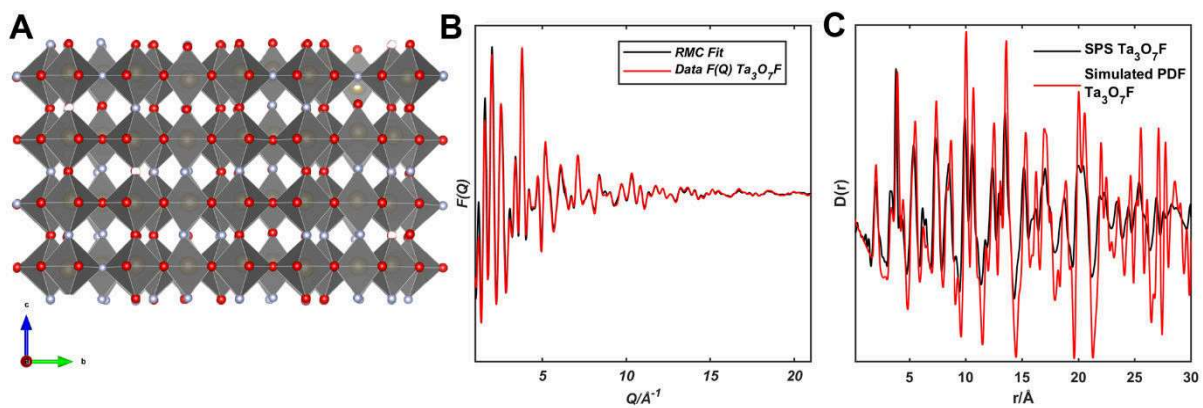


Figure 7.2.4. (A) Section of the reverse Monte Carlo (RMC) model of SPS prepared Ta₃O₇F obtained from total-scattering data. (B) Reduced structure function $F(Q)$ and the corresponding RMC fit and (C) pair distribution function (PDF) $D(r)$ in comparison to the simulated PDF function of TaO₂F.

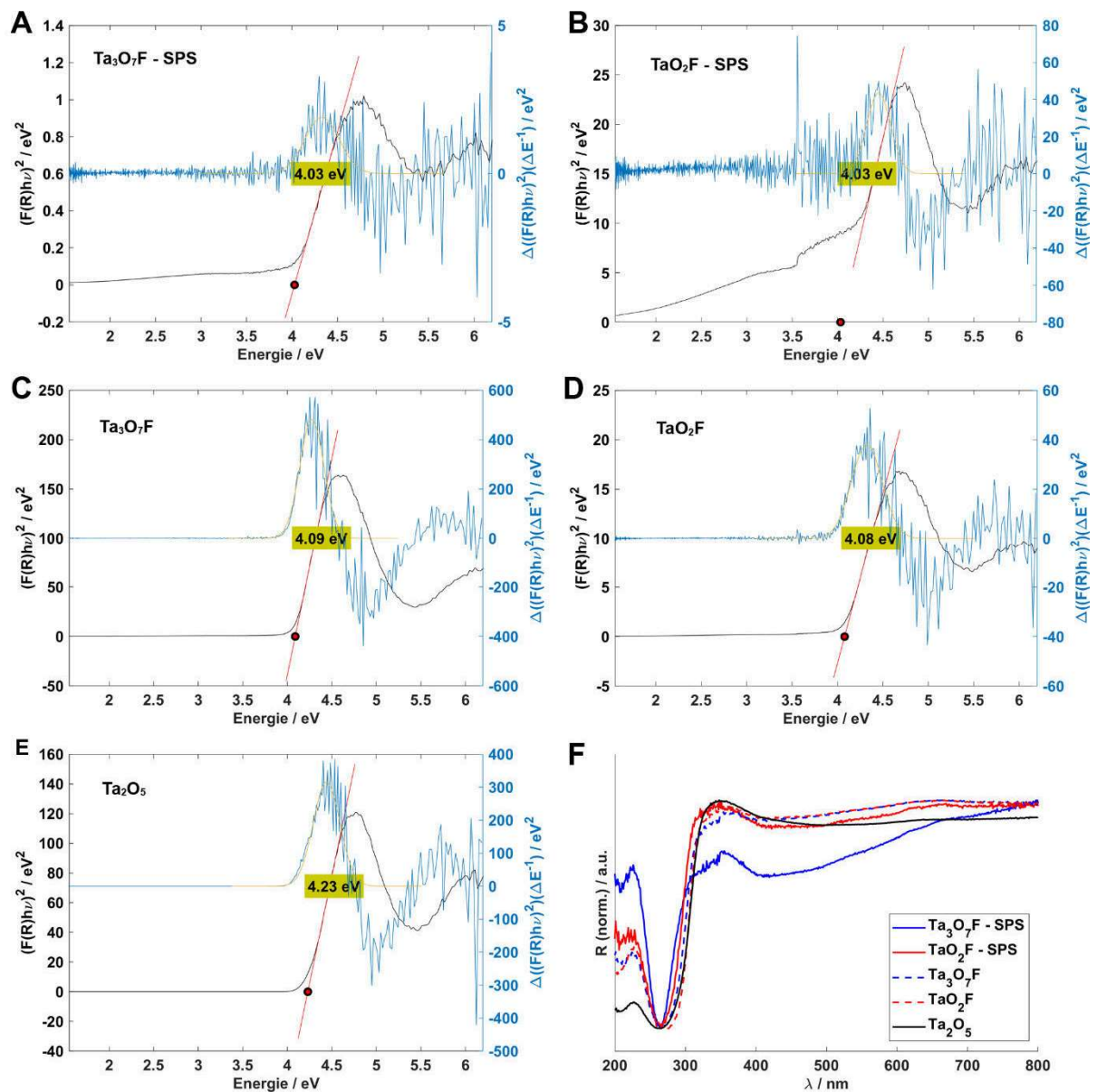


Figure 7.2.5. Kubelka-Munk plots (black line) of Ta₃O₇F, TaO₂F and reference Ta₂O₅ (E) prepared by SPS (A-B) and conventional ampoule chemistry (C-D) from UV-Vis diffuse reflectance spectra (Figure 3.5). Band-Gap values were determined by fitting the first maximum of the first derivative of the Kubelka-Munk plots (derivative - blue line, fit – yellow line) and using this value to fit the slope. Determined band gap values are highlighted yellow. (F) shows the obtained spectra from diffuse reflectance UV-Vis measurements.

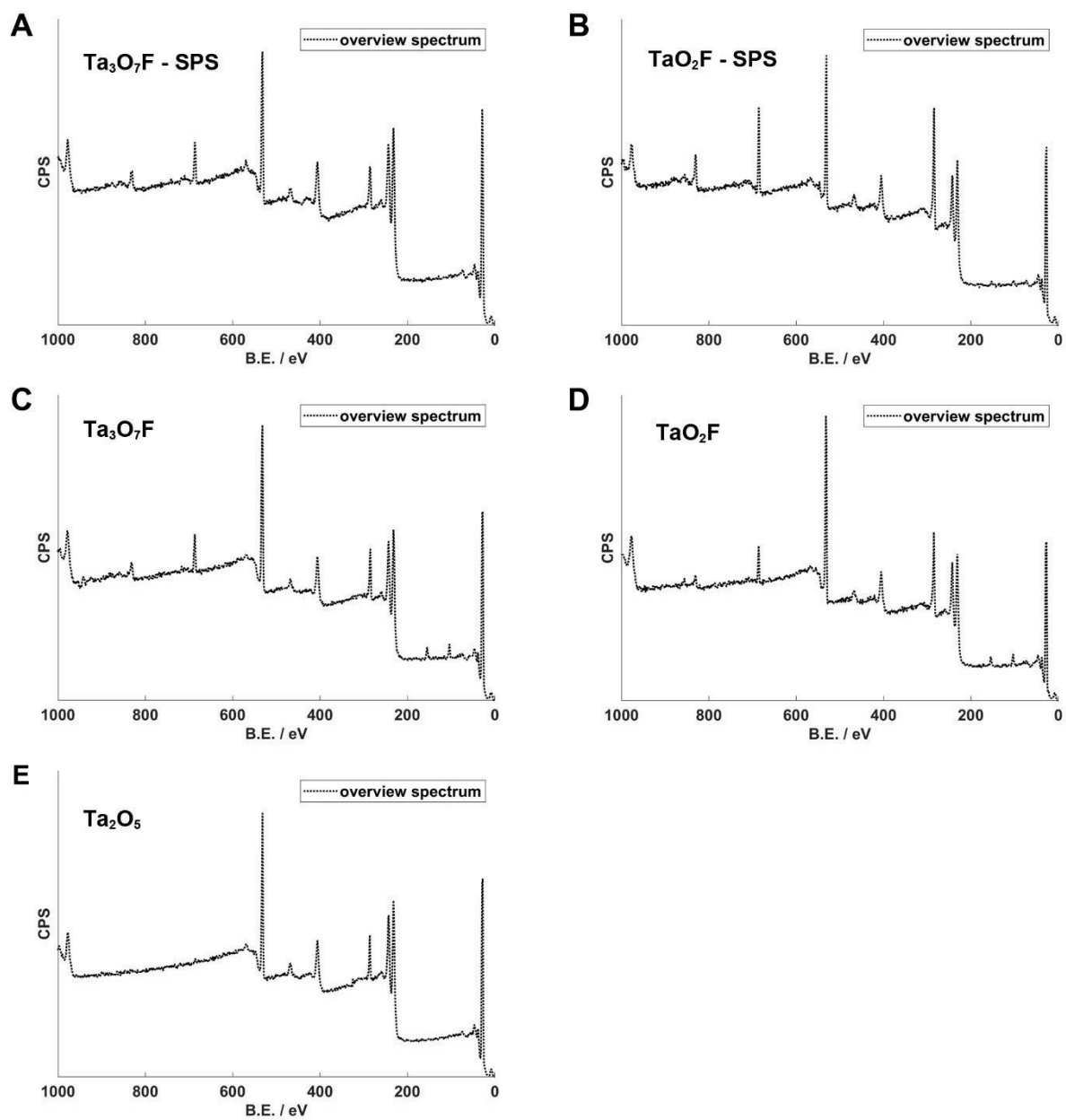


Figure 7.2.6. XPS survey of Ta₃O₇F and TaO₂F, prepared by SPS (A-B) and conventional ampoule chemistry (C-D) with fitted peaks for the respective environments. (E) shows the survey spectrum of ball-milled Ta₂O₅/PTFE reference mixture (unreacted).

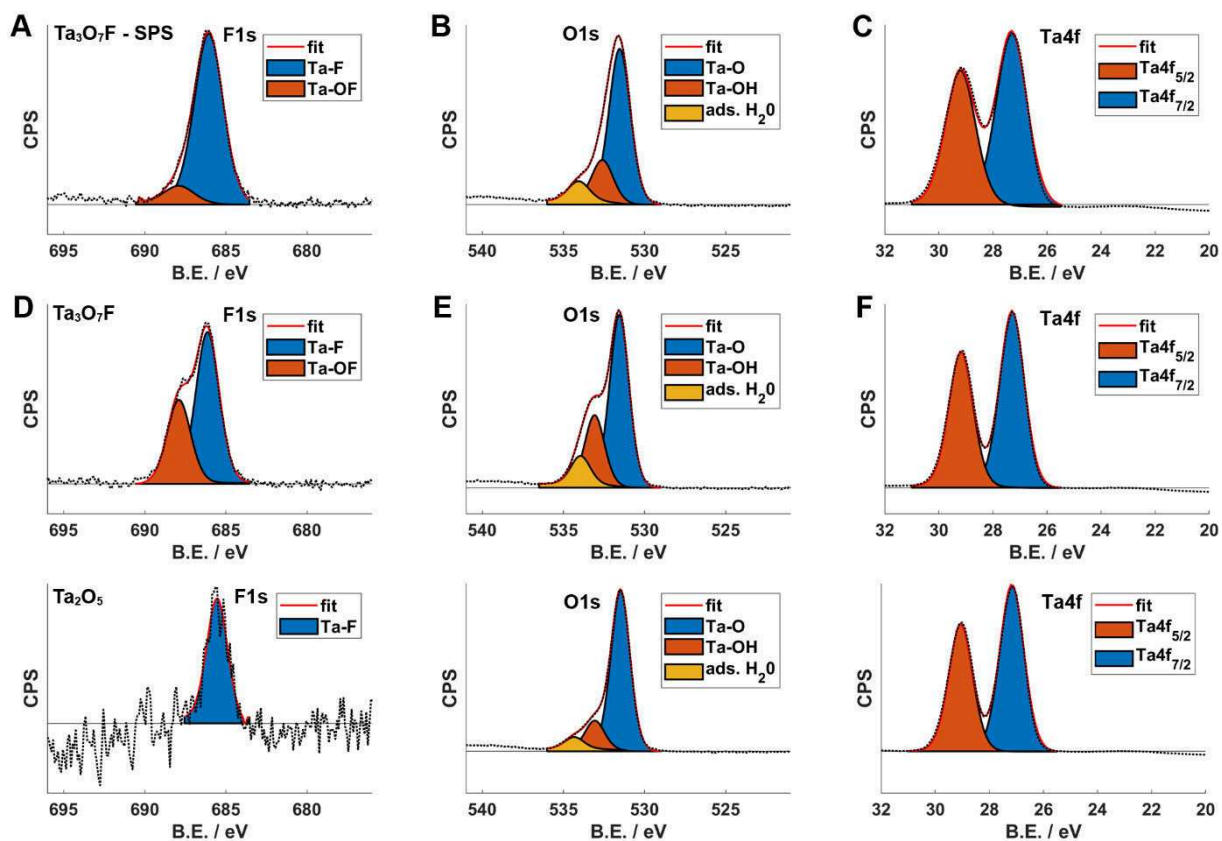


Figure 7.2.7. (A-F) XPS spectra (with F, O, and Ta sub-spectra in (A,D,G), (B,E,H) and (C,F,I)) of $\text{Ta}_3\text{O}_7\text{F}$, prepared by SPS (A-C) and conventional ampoule chemistry (D-F), together with a ball-milled Ta_2O_5 -reference mixture (unreacted) with fitted peaks for the respective environments. The ball-milled, not heated, reference shows a very small Fluorine signal attributed to PTFE near the surface.

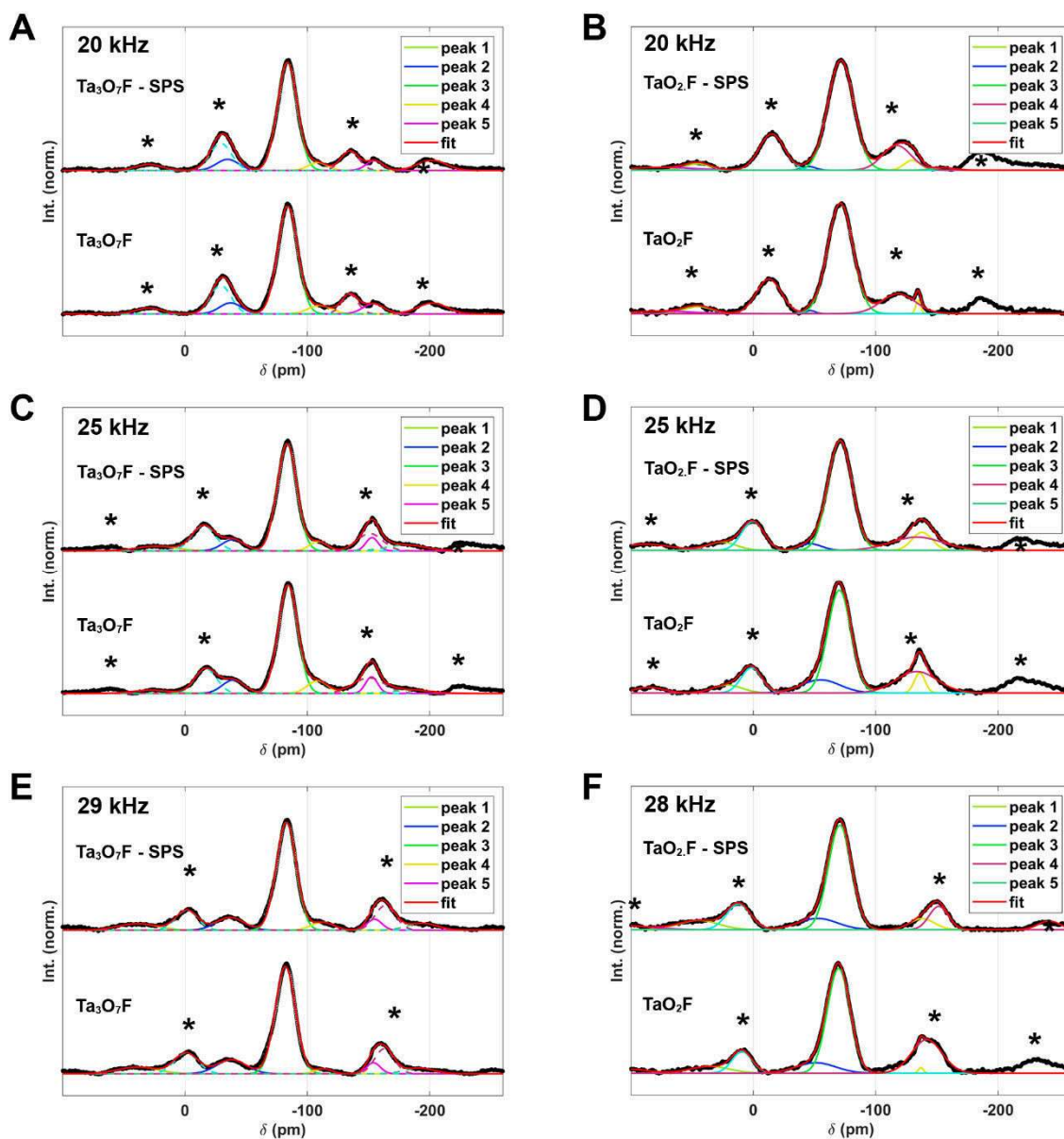


Figure 7.2.8. ^{19}F MAS-NMR spectra of $\text{Ta}_3\text{O}_7\text{F}$ (A, C, D) and TaO_2F (B, D, F). In each figure the top spectrum is derived from a SPS-prepared sample, while the spectrum at the bottom was obtained from a conventionally prepared sample of comparable composition. In case of $\text{Ta}_3\text{O}_7\text{F}$, the SPS prepared sample contains 13 % TaO_2F . Potential spinning side bands are marked with asterisks *.

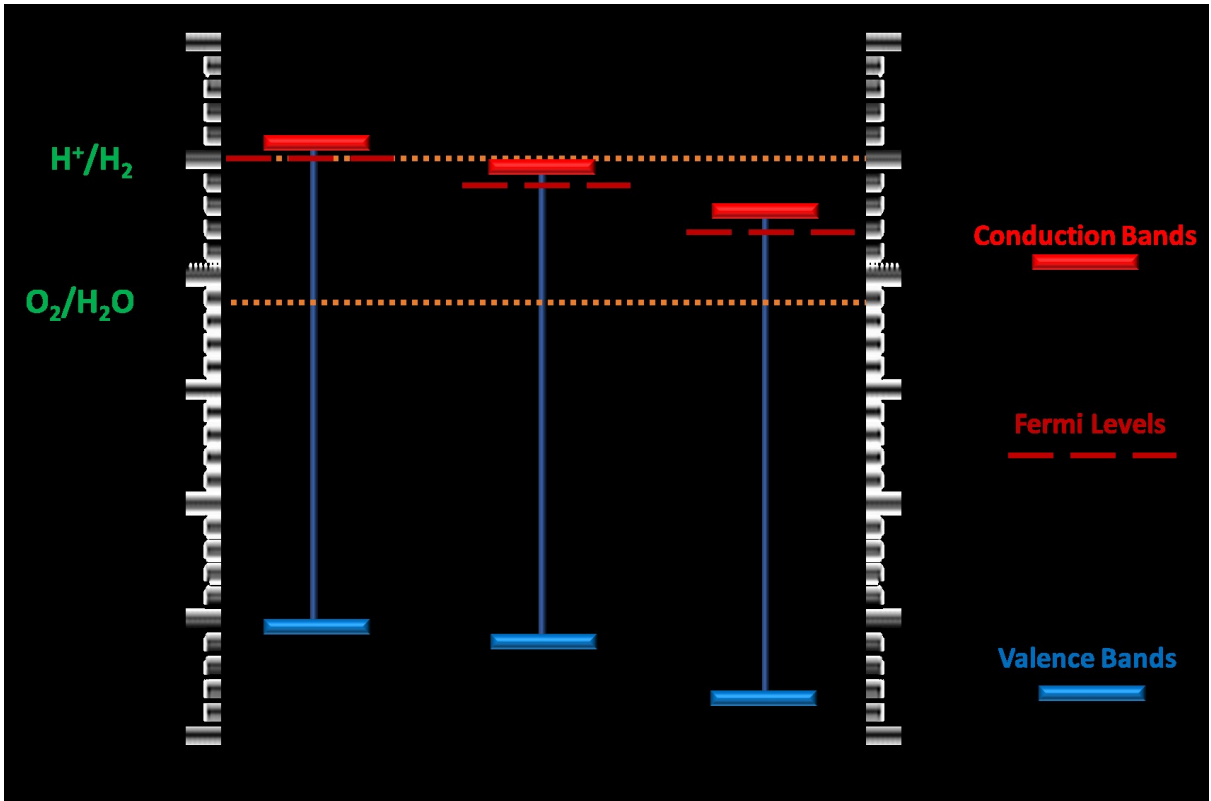


Figure 7.2.9. Graphical representation of the theoretical and calculated band edge positions (as listed in Table 7.2.4).

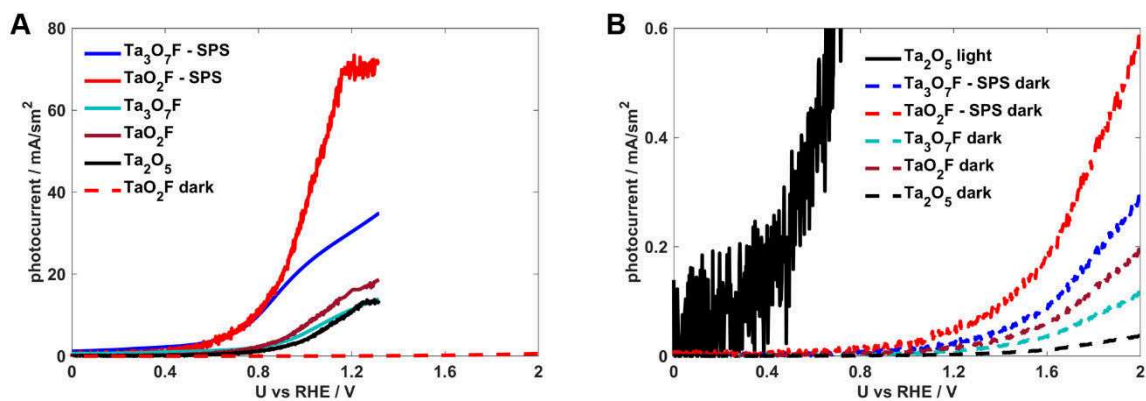


Figure 7.2.10. Comparative dark and light current plots (A) and magnified dark current plots (B). (A) shows the plot of the dark current from SPS prepared TaO₂F as comparison while (B) shows the photocurrent under light irradiation for reference Ta₂O₅ for a better comparison.

“

References

- [1] J. P. Holmberg, E. Ahlberg, J. Bergenholtz, M. Hasselöv, Z. Abbas, *J. Colloid Interface Sci.* **2013**, *407*, 168-176.
- [2] C. R. Morelock, B. K. Greve, M. Cetinkol, K. W. Chapman, P. J. Chupas, A. P. Wilkinson, *Chem. Mater.* **2013**, *25*, 1900–1904.
- [3] J. Dabachi, M. Body, C. Galven, F. Boucher, C. Legein, *Inorg. Chem.* **2017**, *56*, 5219–5232.
- [4] M. A. Lange, Y. Krysiak, J. Hartmann, G. Dewald, G. Cerretti, M. N. Tahir, M. Panthöfer, B. Barton, T. Reich, W. G. Zeier, M. Mondeshki, U. Kolb, W. Tremel, *Adv. Funct. Mater.* **2020**, *30*, 1909051.
- [5] H. Dong, J. Sun, G. Chen, C. Li, Y. Hu, C. Lv, *Phys. Chem. Chem. Phys.* **2014**, *16*, 23915-23921
- [6] A. Habibi-Yangjeh, M. Sekofteh-Gohari, *Sep. Purif. Technol.* **2017**, *184*, 334-346.
- [7] Z.H. Cui, H. Jiang, *J. Phys. Chem. C* **2017**, *121*, 3241-3251.

The contents of the following chapter are taken and partially adapted from *Dalton Transactions*, 2021, *accepted to be published*.

Authorship contributions

Category 1

Conception and design of study:

[REDACTED]

Acquisition of data:

[REDACTED] preparation of samples.
[REDACTED] – PXRD measurements.
[REDACTED] – HR-CS-GFMAS measurements.

[REDACTED] – TEM images
[REDACTED] – HR-TEM and SEM images.
[REDACTED] measurement of ^{19}F solid-state NMR.
[REDACTED] – acquisition of UV/Vis-data.
[REDACTED] – acquisition of oxygen evolution data.
[REDACTED] – acquisition of XPS data.

Analysis and/or interpretation of data:

[REDACTED] – PXRD refinement.
[REDACTED] – HR-TEM and SEM analysis.
[REDACTED] – analysis of ^{19}F solid-state NMR.
[REDACTED] interpretation of oxygen evolution data.
[REDACTED] – interpretation of HR-CS-GFMAS, ζ -potential data and XPS data.

Category 2

Drafting the manuscript:

[REDACTED]

Revising the manuscript critically for important intellectual content:



Category 3

Approval of the version of the manuscript to be published:



Figure 7.3.1: prepared by

Figure 7.3.2: prepared by

Figure 7.3.3: prepared by

Figure 7.3.4: prepared by

Figure 7.3.5: prepared by

Figure 7.3.6: prepared by

Figure 7.3.7: prepared by

Figure 7.3.8: prepared by



Chapter 7.3 Supplementary Information from Chapter 4

“

Table 7.3.1. Results of Rietveld refinements of Nb₃O₇F (*Cmmm*) and NbO₂F (*Pm-3m*) synthesized by SPS (Figure 4.2A and 2B) and by conventional high temperature chemistry (Figure 7.3.1). Because of large strain along long axis, conventionally prepared Nb₃O₇F was taken as reference for phase refinement. Phase-purity was assumed.

Sample	unit cell parameters			gof	R _{wp}	Space group	Side phase	% side phase
	a	b	c					
NbO ₂ F - SPS	3.9049(8)	-	-	3.61	3.89	<i>Pm-3m</i>	Nb ₃ O ₇ F	1.3 ± 0.1 %
Nb ₃ O ₇ F - SPS	20.693(2)	3.8387(3)	3.9383(3)	5.92	7.14	<i>Cmmm</i>	Nb ₃ O ₇ F	1.8 ± 0.2 %
NbO ₂ F	3.898(1)	-	-	1.27	5.76	<i>Pm-3m</i>	Nb ₃ O ₇ F	17.4 ± 0.5 %
Nb ₃ O ₇ F	20.677(2)	3.8316(3)	3.9237(3)	2.48	4.30	<i>Cmmm</i>	-	0% assumed

Table 7.3.2. Experimental and theoretical fluorine concentration (pure phases) and degree of fluorination for niobium oxyfluorides prepared by SPS and conventional high temperature chemistry as determined by HR-CS-GFMAS.

SPS Sample	Fluorine conc. <i>via</i> HR-CS-GFMAS (g kg⁻¹ ± sd)	Niobium conc. <i>via</i> HR-CS-GFMAS (g kg⁻¹ ± sd)	F:Nb ratio	Theoretical F:Nb ratio
NbO ₂ F - SPS	125 ± 9*	648 ± 18*	0.95±0.07:1	1:1
Nb ₃ O ₇ F - SPS	44 ± 9*	547 ± 9*	0.4 ± 0.1 :1	1:3

*n = 3

Table 7.3.3. Summary of elemental compositions and calculated F/O surface ratios determined by XPS spectroscopy.

Sample	F 1s %	O 1s %	Nb 4f %	F : O ratio
NbO ₂ F - SPS	17.6	66.8	15.6	1 : 4
Nb ₃ O ₇ F - SPS	12.0	70.9	17.7	1 : 6
NbO ₂ F	12.3	77.7	10.0	1 : 6
Nb ₃ O ₇ F	9.9	78.4	11.6	1 : 8
Nb ₂ O ₅	0.0	80.3	12.9	/

Table 7.3.4. Fit parameters of the five deconvoluted peaks from the F⁻ solid state MAS NMR of Nb₃O₇F (conventionally (bottom) and SPS-prepared (top), Figure 7.3.2A) and NbO₂F (conventionally (bottom) and SPS-prepared (top), Figure 7.3.2B).

NbO₂F - SPS (Figure 7.3.6B)	Peak 1	Peak 2	Peak 3
Peak position / Hz	-11.28	-19.66	-27.17
FWHM / Hz	6.02	2.57	6.02
Relative peak area	12.31	78.41	9.28

Nb₃O₇F - SPS (Figure 7.3.6A)	Peak 1	Peak 2	Peak 3
Peak position / Hz	-9.89	-21.05	-31.86
FWHM / Hz	3.38	3.74	4.51
Relative peak area	5.87	86.42	7.70

NbO₂F (Figure 7.3.6B)	Peak 1	Peak 2	Peak 3
Peak position / Hz	-12.39	-21.73	-28.50
FWHM / Hz	4.51	3.76	2.78
Relative peak area	15.85	68.01	16.14

Nb₃O₇F (Figure 7.3.6A)	Peak 1	Peak 2	Peak 3
Peak position / Hz	-18.99	-22.60	-29.33
FWHM / Hz	3.38	1.92	3.38
Relative peak area	36.62	56.66	6.73

Calculation of theoretical optical band positions

The conduction band (E_{CB}) and valence band (E_{VB}) potentials of semiconductors can be calculated using the following empirical quations.^[1,2,3]

$$E_{CB} = \chi - E_e - \frac{1}{2} E_g$$

$$E_{VB} = E_{CB} + E_g$$

Where E_{VB} is the valence band potential and E_{CB} the conduction band potential. E_e is the energy of free electrons of the hydrogenscale (4.5 eV), E_g is the band gap of the respective semiconductor and χ stands for the absolute electronegativity of the atom semiconductor (geometric mean of the absolute electronegativity of the constituent atoms) and is calculated according to

$$\chi = [\chi(A)^a \times \chi(B)^b \times \chi(C)^c]^{1/(a+b+c)}$$

Where a, b, c are the numbers of the respective Elements A, B, C in the chemical formular of the semiconductor. By application of these formulars, the values listed in Table 7.3.5 can be obtained and are graphically presented in Figure 7.3.8.

Table 7.3.5. Calculated Band edge position values.

Semiconductor	Absolute electronegativity (χ)	Energy of free electrons (hydrogenscale)	Band gap value (E_g)	Conduction band potential (E_{CB})	Valence band potential (E_{VB})
NbO ₂ F - SPS	6.90	4.5 eV	3.29 eV	0.76 eV	4.05 eV
Nb ₃ O ₇ F - SPS	6.46	4.5 eV	3.39 eV	0.26 eV	3.65 eV
NbO ₂ F	6.90	4.5 eV	3.36 eV	0.72 eV	4.08 eV
Nb ₃ O ₇ F	6.46	4.5 eV	3.54 eV	0.19 eV	3.73 eV
Nb ₂ O ₅	6.22	4.5 eV	3.70 eV	-0.13 eV	3.57 eV

Especially the band gap diagram shows a significant shift of the positions of the optical bands. The shift of the conduction band towards the oxygen generation potential with no overlap to the hydrogen generation potential signifies the potential efficiency of the fluorinated semiconductors related to the water oxidation reaction.

References

- [1] H. Dong, J. Sun, G. Chen, C. Li, Y. Hu, and C. Lv, *Phys. Chem. Chem. Phys.*, 2014, **16**, 23915-23921.
- [2] A. Habibi-Yangjeh, M. Sekofteh-Gohari, *Sep. Purif. Technol.* 2017, **184**, 334-346.

[3] Z.H., and H. Jiang, *J. Phys. Chem. C*, 2017, **121**, 3241-3251.

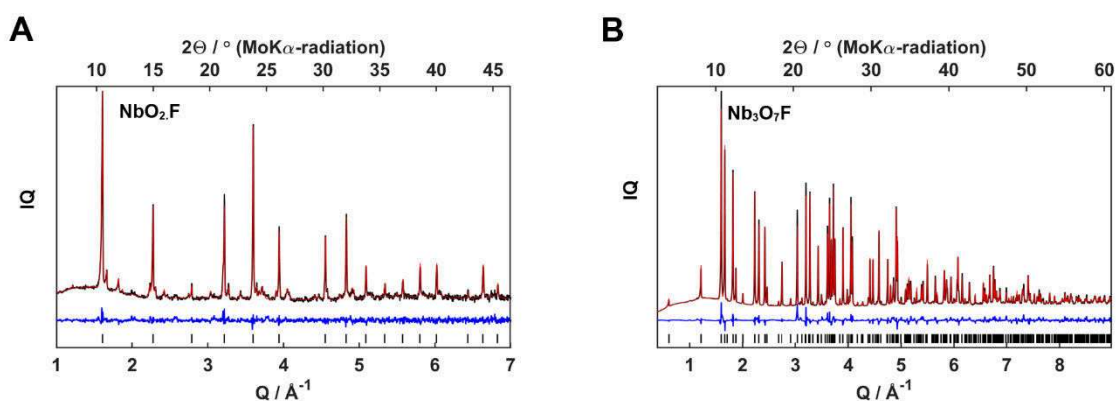


Figure 7.3.1. (A) Rietveld refinement of conventionally prepared Nb₃O₇F (red line) using X-ray powder data (83 % Nb₃O₇F, 17 % NbO₂F). (B) Rietveld refinement of conventionally prepared Nb₃O₇F (red line) using X-ray powder data. Experimental data are indicated by crosses, the calculated curve obtained after the refinement is indicated with a continuous line. The tick marks correspond to the Bragg reflections of the cubic and orthorhombic structures. The continuous blue curve under the tick marks represents the difference between the experimental data and the calculated curve.

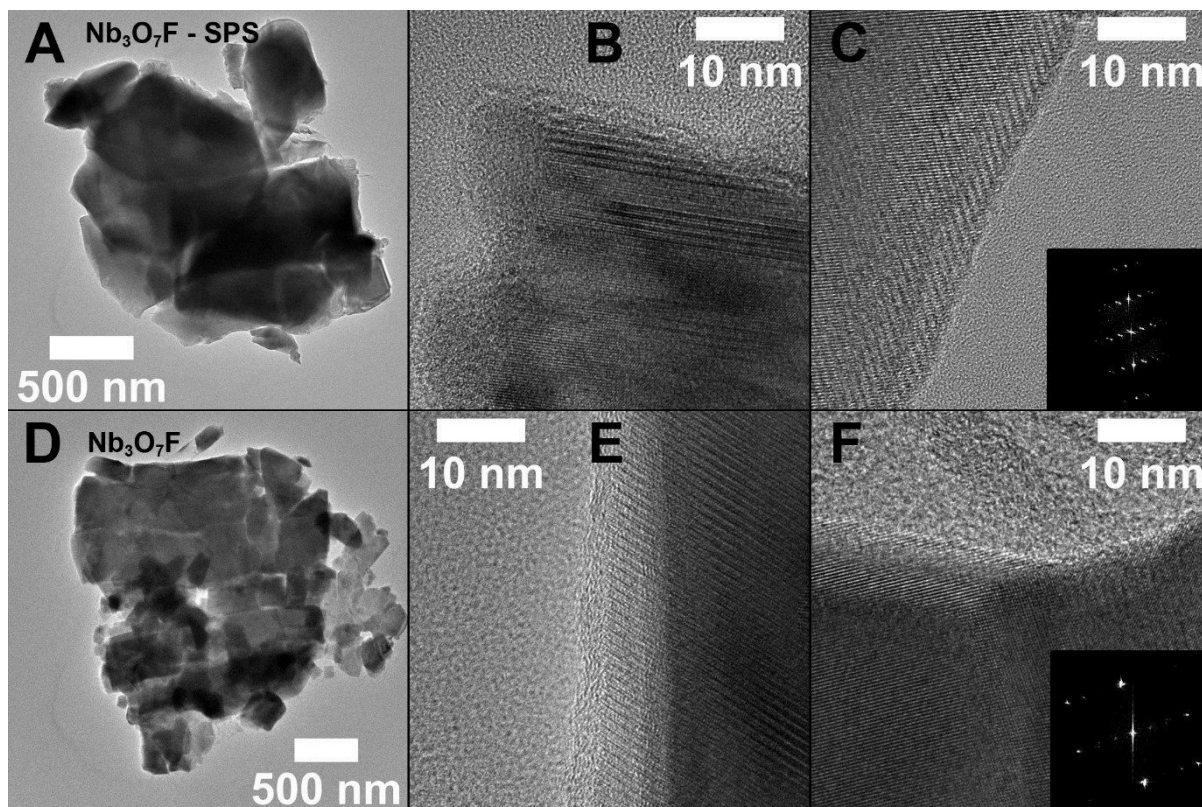


Figure 7.3.2. (A-C) (HR)TEM images of $\text{Nb}_3\text{O}_7\text{F}$ prepared by SPS, (D-F) and conventional chemistry. (A, D) show representative particles, which consist in both cases of smaller crystallites. (B, E) show a zoomed view on the edges of the layer-like particles. In case of SPS synthesis, the outer layer is larger and less crystallized than in case of conventional synthesis. (C, F) Magnified crystalline areas, which show for the SPS-prepared material less ordering and indications for twinning and disorder. The Fourier transformation (insets) exhibits diffuse intensities, which are broadened in one direction.

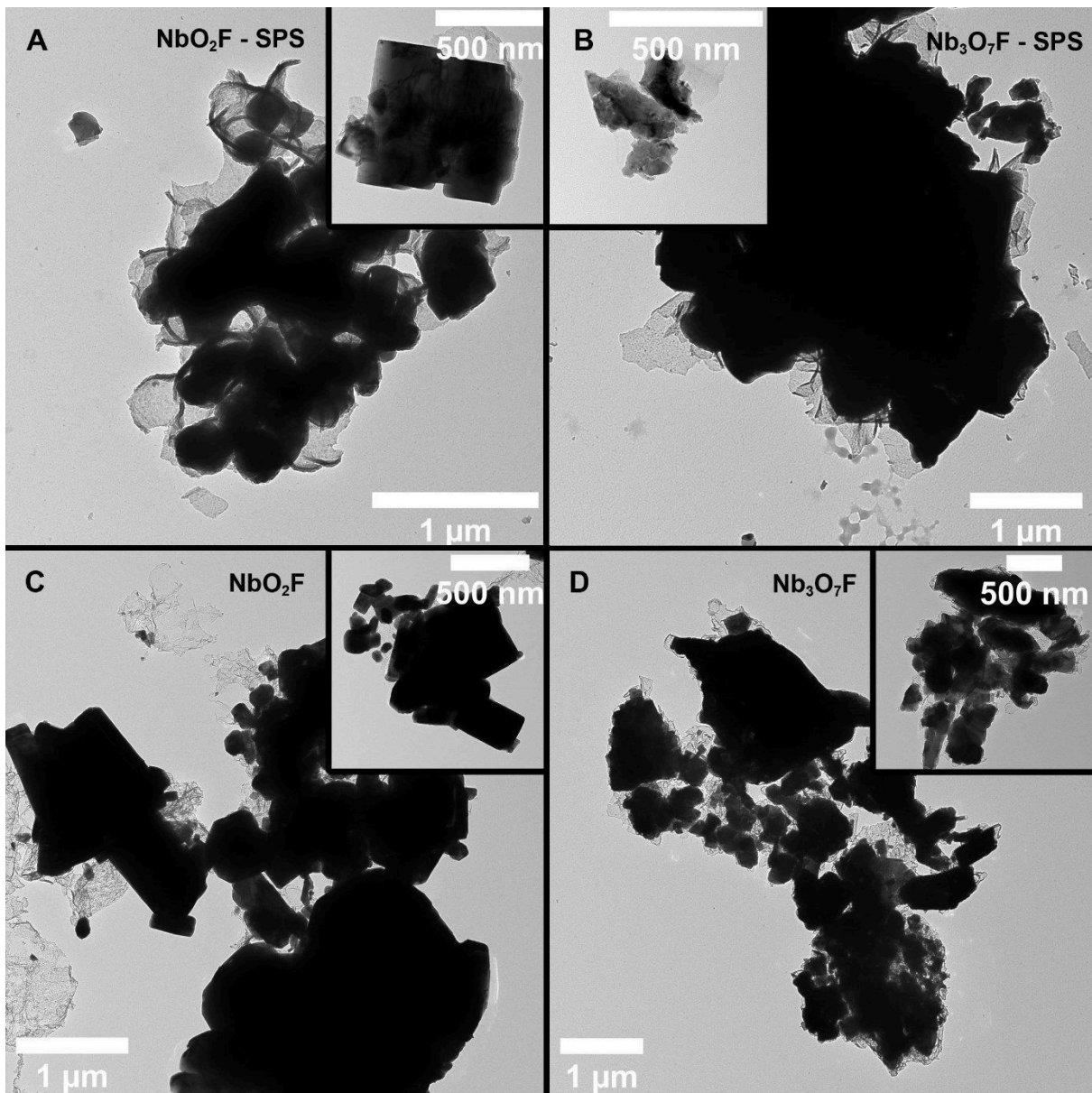


Figure 7.3.3. TEM images of NbO₂F and Nb₃O₇F prepared by SPS (A-B) and conventional ampoule chemistry (C-D). The SPS-prepared samples have similar particle size, but a more pronounced appearance of layers.

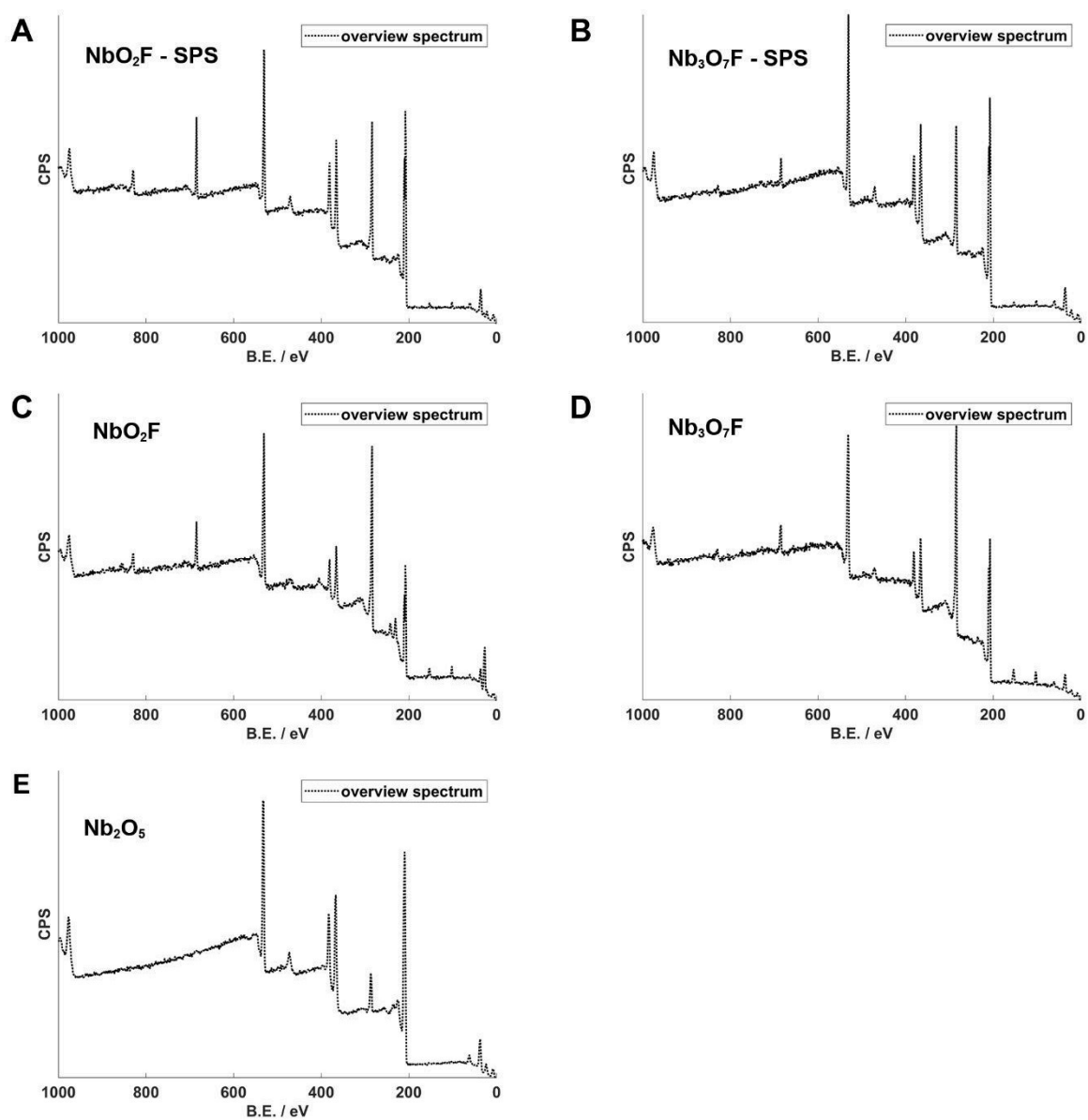


Figure 7.3.4. XPS survey spectra of NbO_2F and $\text{Nb}_3\text{O}_7\text{F}$, prepared by SPS (A-B) and conventional ampoule chemistry (C-D) with fitted peaks for the respective environments. (E) Survey spectrum of a ball-milled (unreacted) Nb_2O_5 /PTFE reference mixture.

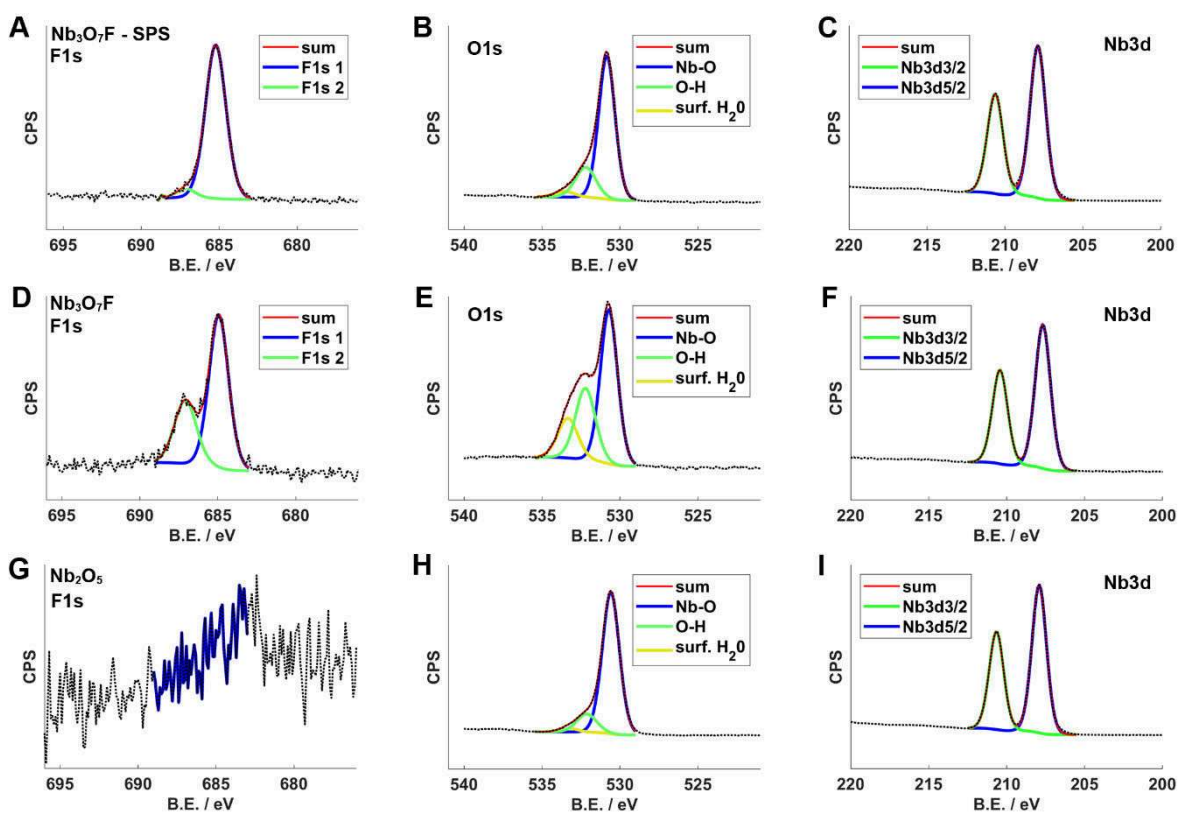


Figure 7.3.5. XPS fine spectra of F, O, and Nb regimes for $\text{Nb}_3\text{O}_7\text{F}$ prepared by SPS (A-C), conventional ampoule chemistry (D-F) and from reference Nb_2O_5 (G-I, ball milled powder treated with the same SPS program as NbO_2F) with fitted peaks for the respective environments.

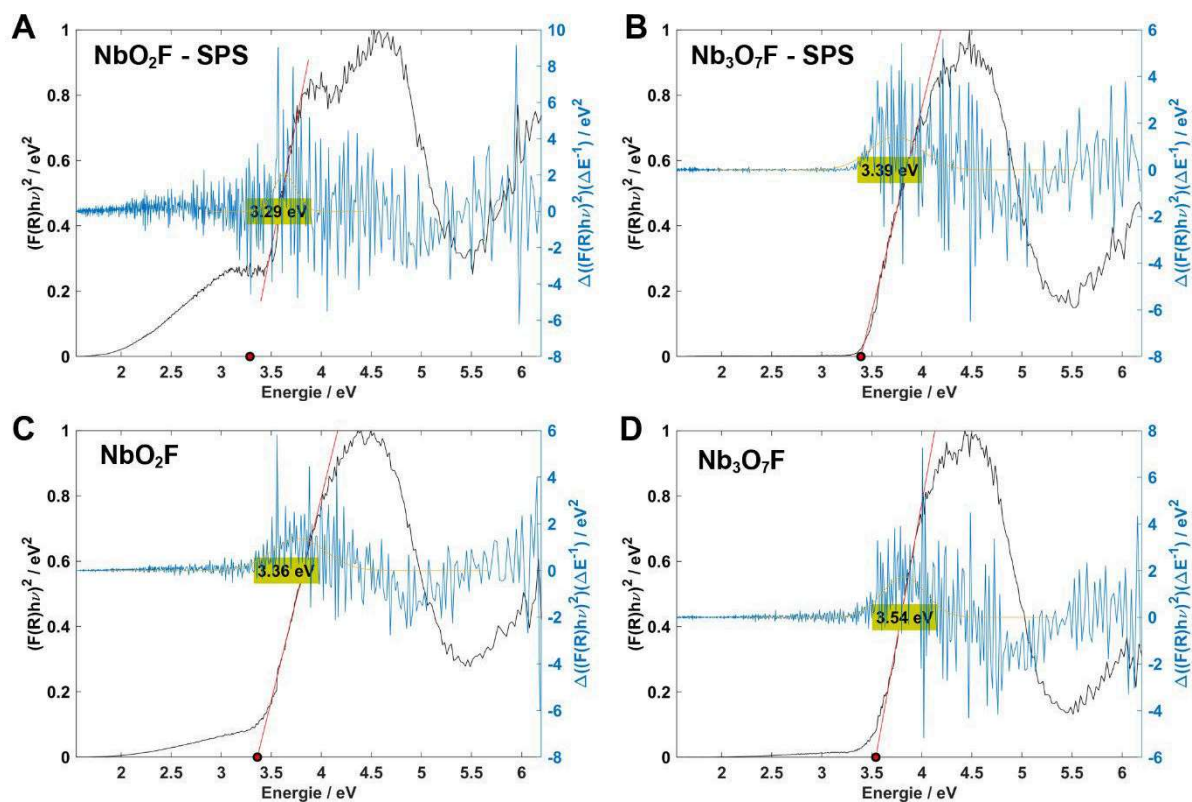


Figure 7.3.6. Kubelka-Munk plots (black line) of NbO₂F and Nb₃O₇F prepared by SPS (A-B) and conventional ampoule chemistry (C-D) from UV-Vis diffuse reflectance spectra (Figure 4.5). Band-Gap values were determined by fitting the first maximum of the first derivative of the Kubelka-Munk plots (derivative - blue line, fit – yellow line) and using this value to fit the slope. Determined band gap values are highlighted yellow.

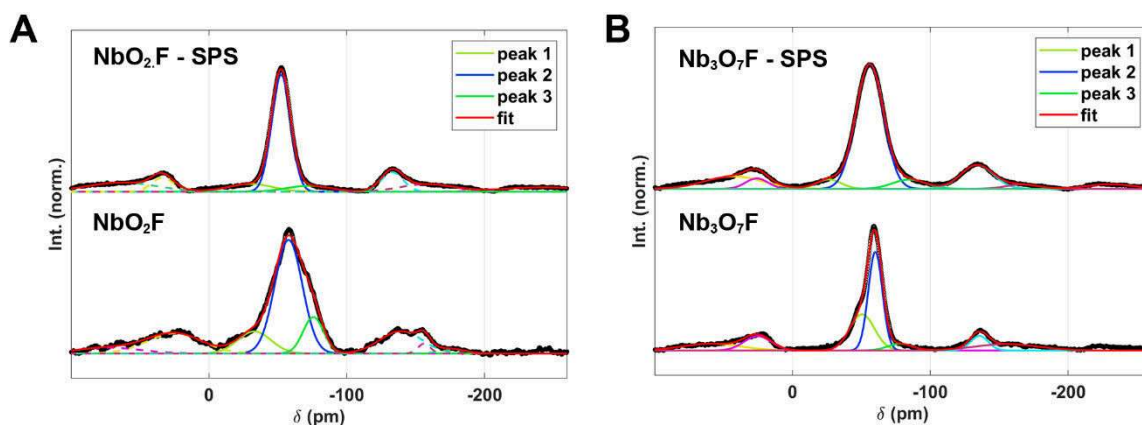


Figure 7.3.7. ^{19}F MAS-NMR spectra of $\text{Nb}_3\text{O}_7\text{F}$ (A) and NbO_2F (B). In each figure the top spectrum is obtained from a SPS-prepared sample. The bottom spectrum was obtained from a conventionally prepared sample of comparable composition. The conventional prepared NbO_2F contains 17 % $\text{Nb}_3\text{O}_7\text{F}$ as a side phase, which is the main reason for the much broader peak form since complete deconvolution of the very similar signals of both phases is impossible. Potential spinning side bands are marked with stars *.

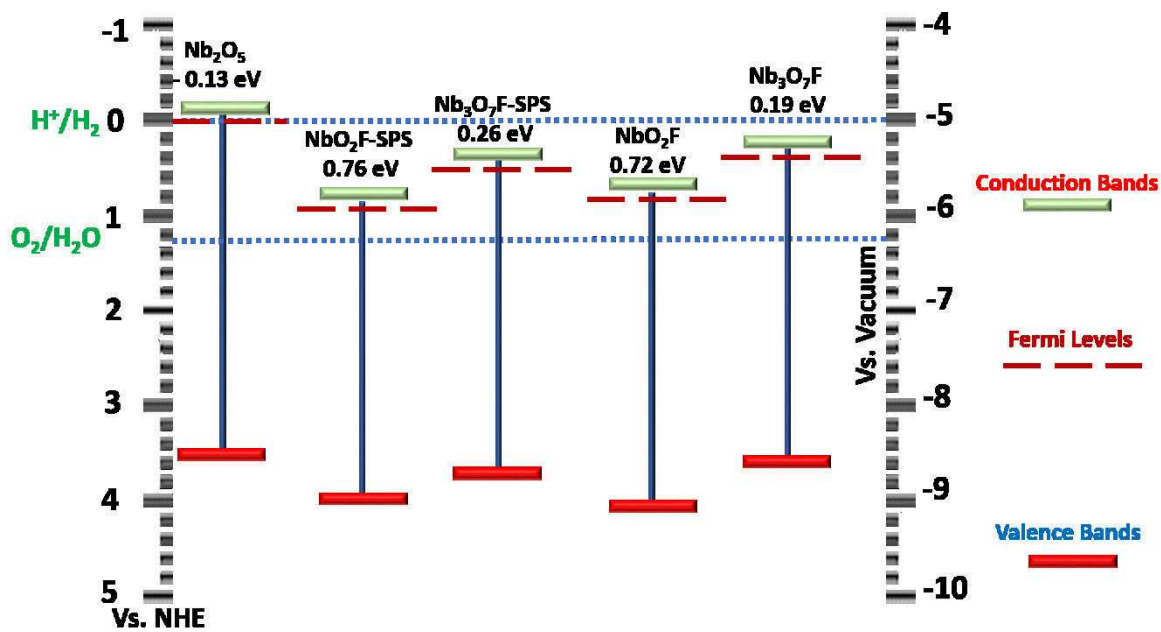


Figure 7.3.8. Graphical representation of the theoretical and calculated band edge positions as listed in Table 7.3.5.

cc

The contents of the following chapter are taken and partially adapted from *Adv. Funct. Mater.*, 2021, to be submitted.

Authorship contributions

Category 1

Conception and design of study:

[REDACTED]

Acquisition of data:

[REDACTED] – preparation of samples.
[REDACTED] – PXRD measurements.
[REDACTED] – XPS measurements.
[REDACTED] – HR-TEM and SEM images.
[REDACTED] acquisition of UV/Vis-data.
[REDACTED] – acquisition of neutron diffraction data.

Analysis and/or interpretation of data:

[REDACTED] – PXRD and neutron diffraction refinement.
[REDACTED] – HR-TEM and SEM analysis.
[REDACTED] Band-gap/UV-Vis analysis
[REDACTED] – interpretation of XPS data.

Category 2

Drafting the manuscript:

[REDACTED]

Revising the manuscript critically for important intellectual content:

[REDACTED]

Category 3

Approval of the version of the manuscript to be published:



Figure 7.4.1: prepared by
Figure 7.4.2: prepared by
Figure 7.4.3: prepared by
Figure 7.4.4: prepared by
Figure 7.4.5: prepared by
Figure 7.4.6: prepared by
Figure 7.4.7: prepared by



Chapter 7.4 Supplementary Information from Chapter 5

“

Table 7.4.1. Crystallographic data of relevant tantalum oxide and oxynitride.

Modification	Space group	CIF	<i>a</i> / nm	<i>b</i> / nm	<i>c</i> / nm	α / °	β / °	γ / °
11-f.u.-Ta ₂ O ₅ / L11-Ta ₂ O ₅	<i>Pmm2</i>	Stephenson ³	0,3888	4,029	0,6198	90	90	90
β -TaON	<i>P2₁/c</i>	Weishaupt ⁴	4,968	5,037	5,185	90	99,56	90

Table 7.4.2. Influence of different reaction parameters during FAST synthesis on the obtained phases. The main phase is marked bold.

Temperature /°C	Holding time /min	R_{wp}	GOF	Identified Phases
600	5	1.642	1.208	L11-Ta₂O₅ , Mg(OH) ₂
	30	2.412	1.817	L11-Ta₂O₅ , Mg ₃ N ₂
	180	2.212	1.649	L11-Ta₂O₅ , Mg ₄ Ta ₂ O ₉ , Ta ₃ N ₅ , TaO ₂ , TaON
750	5	2.263	1.739	L11-Ta₂O₅ , Mg ₃ N ₂
	30	2.368	1.382	L11-Ta₂O₅ , Mg(OH) ₂
	180	2.262	1.672	L11-Ta₂O₅ , Mg ₄ Ta ₂ O ₉ , MgTa ₂ O ₆ , Ta ₄ N ₅ , TaO ₂
900	5	2.247	1.845	L11-Ta ₂ O ₅ , Mg(OH) ₂
	30	2.356	1.840	L11-Ta ₂ O ₅ , Mg(OH) ₂ , TaO ₂ , TaON
	180	2.740	1.916	L11-Ta ₂ O ₅ , Mg ₄ Ta ₂ O ₉ , MgTa ₂ O ₆ , Ta ₄ N ₅

Table 7.4.3. Influence of different reaction parameters on the obtained phases during conventional solid-state synthesis for 48 hours in quartz glass ampoules. The main phase is marked bold, side products MgO and Mg(OH)₂ are not included in the percentages.

Temperature /°C	N/Ta	<i>R</i> _{wp}	GOF	Identified Phases (+ MgO or Mg(OH) ₂)
600	1	1.642	1.208	L11-Ta₂O₅
750	1	3.652	2.074	L11-Ta ₂ O ₅ (9.8%), TaON (89.4%) , TaO ₂
750	1.2	3.618	1.989	L11-Ta ₂ O ₅ (6.6%), TaON (93.4%) , TaO ₂
800	1.2	3.567	1.926	L11-Ta ₂ O ₅ (2%), TaON (97.5%) , TaO ₂
810	1.2	3.777	1.818	TaON (93.6%) , TaO ₂
900	1	2.247	1.845	Mg ₄ Ta ₂ O ₉ , Ta ₃ N ₅ , TaON , MgTa ₂ O ₆

Table 7.4.4. Results of Rietveld-refinement from XRPD data and neutron diffraction data of L11-Ta₂O₅ (Figure 7.4.1) and ε-TaON synthesized by FAST (Figure 5.2 a)+b), Figure 7.4.3, Figure 7.4.4) and β-TaON synthesized by conventional high temperature chemistry (Figure 5.2 c)) or FAST plus additional sintering (Figure 7.4.2).

Sample	unit cell parameters			gof	R _{wp}	Space group	Side phase	% side phase
	a	b	c					
X-Ray diffraction data								
L-Ta ₂ O ₅ – SPS 600°C	3.890(3)	40.27(4)	6.203(6)	2.63	4.33	<i>Pmm2</i>	/	/
L-Ta ₂ O ₅ – SPS 750°C	3.8931(8)	40.31(1)	6.202(3)	3.33	6.69	<i>Pmm2</i>	/	/
TaON – SPS + conv.	4.966(2)	5.034(2)	5.185(2)	1.93	4.56	<i>P21/c</i>	TaO ₂	4.2 ± 0.6 %
TaON	4.9677(6)	5.0374(5)	5.1882(6)	1.83	3.65	<i>P21/c</i>	L-Ta ₂ O ₅ , TaO ₂	2.0 ± 0.1 % 0.5 ± 0.1 %
L-Ta ₂ O ₅ Ref.	3.893(1)	40.31(2)	6.206(4)	1.76	4.73	<i>Pmm2</i>	/	/
<hr/>								
Neutron diffraction data								
L-Ta ₂ O ₅ – SPS 600°C	3.892(6)	40.26(5)	6.211(8)	2.36	3.42	<i>Pmm2</i>	Mg(OH) ₂	1.8 ± 0.1 %
L-Ta ₂ O ₅ – SPS 750°C	3.891(6)	40.26(5)	6.204(7)	2.81	4.73	<i>Pmm2</i>	/	/

Table 7.4.5. Refined O/N positions and occupancies from neutron diffraction data of L11-Ta₂O₅ synthesized by FAST at 600°C (Figure 7.4.3) and 750°C (Figure 7.4.4).

Position	x	y	z	Occ ₁ (O)	Occ ₁ (N)	Occ ₂ (O)	Occ ₂ (N)
O1	0.0	0	0.4902 ± 0.0706	1.00	0.00	1.00	0.00
O2	0.0	0.0300 ± 0.0114	0.2696 ± 0.0770	0.75	0.25	0.79	0.21
O3	0.0	0.0466 ± 0.0145	0.8626 ± 0.1166	1.00	0.00	0.99	0.01
O4	0.0	0.0857 ± 0.0148	0.3619 ± 0.0899	1.00	0.00	1.00	0.00
O5	0.0	0.0943 ± 0.0682	0.7314 ± 0.3763	0.00	0.25	0.00	0.25
O6	0.0	0.1366 ± 0.0149	0.1938 ± 0.0701	1.00	0.00	1.00	0.00
O7	0.0	0.1905 ± 0.0127	0.3634 ± 0.0775	0.00	1.00	0.00	1.00
O8	0.0	0.2297 ± 0.0130	0.9989 ± 0.0604	0.00	1.00	0.00	1.00
O9	0.0	0.2536 ± 0.0113	0.3776 ± 0.0652	1.00	0.00	1.00	0.00
O10	0.0	0.2774 ± 0.0116	0.7479 ± 0.0622	0.58	0.42	0.20	0.80
O11	0.0	0.3078 ± 0.0118	0.2567 ± 0.0774	0.06	0.94	0.00	1.00
O12	0.0	0.3657 ± 0.0139	0.4982 ± 0.0839	0.00	1.00	0.45	0.55
O13	0.0	0.4166 ± 0.0138	0.2977 ± 0.0850	1.00	0.00	1.00	0.00
O14	0.0	0.4745 ± 0.0103	0.3793 ± 0.0839	1.00	0.00	0.92	0.08
O15	0.0	0.4489 ± 0.0142	0.7924 ± 0.1111	0.40	0.60	0.53	0.47
O16	0.0	0.5	0.0658 ± 0.0711	1.00	0.00	0.55	0.45
O17	0.5	0	0.0650 ± 0.0958	0.01	0.99	0.36	0.64
O18	0.5	0.5	0.6354 ± 0.0982	0.04	0.96	0.24	0.76
O19	0.5	0.0857 ± 0.0098	0.0493 ± 0.0814	1.00	0.00	1.00	0.00
O20	0.5	0.1852 ± 0.0101	0.0526 ± 0.0859	0.86	0.14	0.24	0.76
O21	0.5	0.2831 ± 0.0095	0.0338 ± 0.0641	1.00	0.00	1.00	0.00
O22	0.5	0.3541 ± 0.0074	0.1617 ± 0.0720	0.50	0.50	0.04	0.96
O23	0.5	0.4481 ± 0.0073	0.1778 ± 0.0448	1.00	0.00	1.00	0.00
O24	0.5	0.0510 ± 0.0078	0.6112 ± 0.0429	1.00	0.00	1.00	0.00
O25	0.5	0.1397 ± 0.0102	0.5680 ± 0.0547	0.87	0.13	1.00	0.00
O26	0.5	0.2206 ± 0.0095	0.5716 ± 0.0627	1.00	0.00	1.00	0.00
O27	0.5	0.3175 ± 0.0119	0.5948 ± 0.0805	0.55	0.45	0.75	0.25
O28	0.5	0.4186 ± 0.0091	0.6100 ± 0.0756	1.00	0.00	1.00	0.00
O29	0.0	0.1318 ± 0.0180	0.8802 ± 0.0772	0.75	0.00	0.75	0.00
O30	0.0	0.1772 ± 0.0589	0.7472 ± 0.3047	0.00	0.25	0.00	0.25
O31	0.0	0.3234 ± 0.0644	0.9409 ± 0.2262	0.00	0.25	0.00	0.25
O32	0.0	0.3689 ± 0.0149	0.8652 ± 0.0642	0.75	0.00	0.75	0.00
O33	0.0	0.4056 ± 0.0529	0.9343 ± 0.3906	0.25	0.00	0.00	0.25

Table 7.4.6. Optical bandgaps of different samples. More are shown in Figure 7.4.7.

Sample	Direct Bandgap /eV	Indirekt Bandgap /eV
L11-Ta ₂ O ₅ before FAST synthesis	4.1	
L11-Ta ₂ O ₅ after FAST synthesis	4.0	
β-TaON after conventional synthesis (N/Ta = 1.2)		2.5

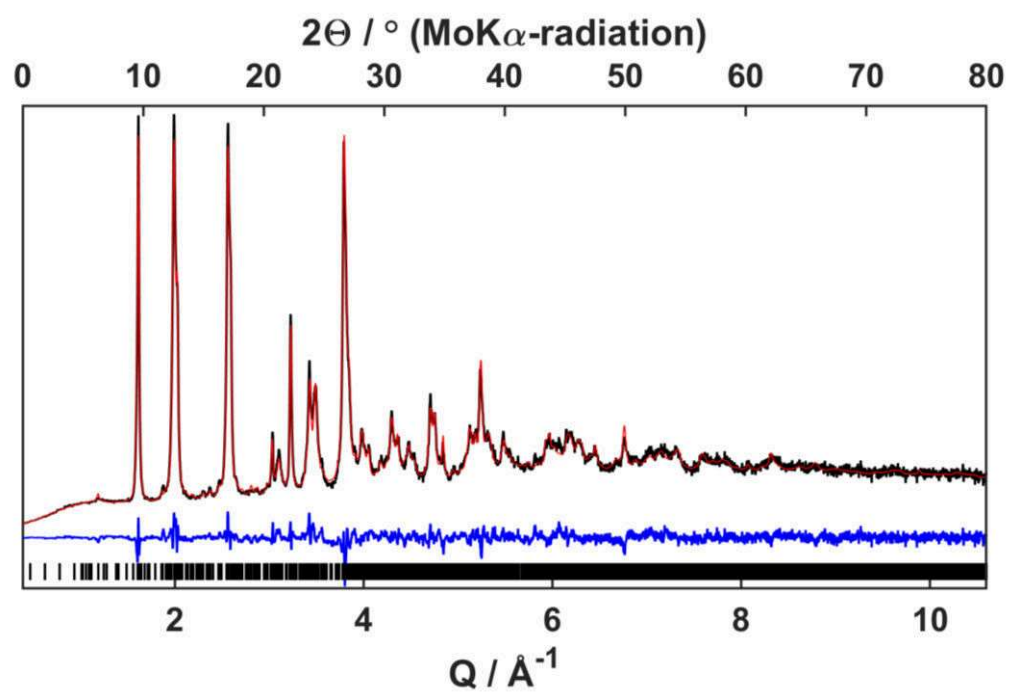


Figure 7.4.1. Rietveld refinement of the reference L11-Ta₂O₅ from XRPD data.

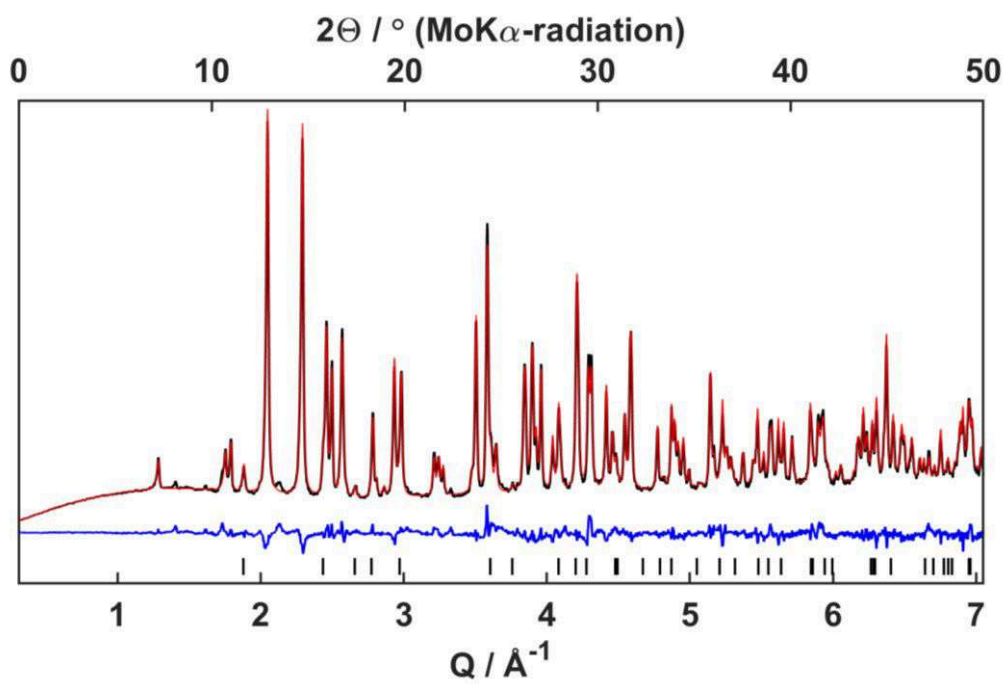


Figure 7.4.2. Rietveld refinement of β -TaON prepared by FAST synthesis plus additional sintering from XRPD data.

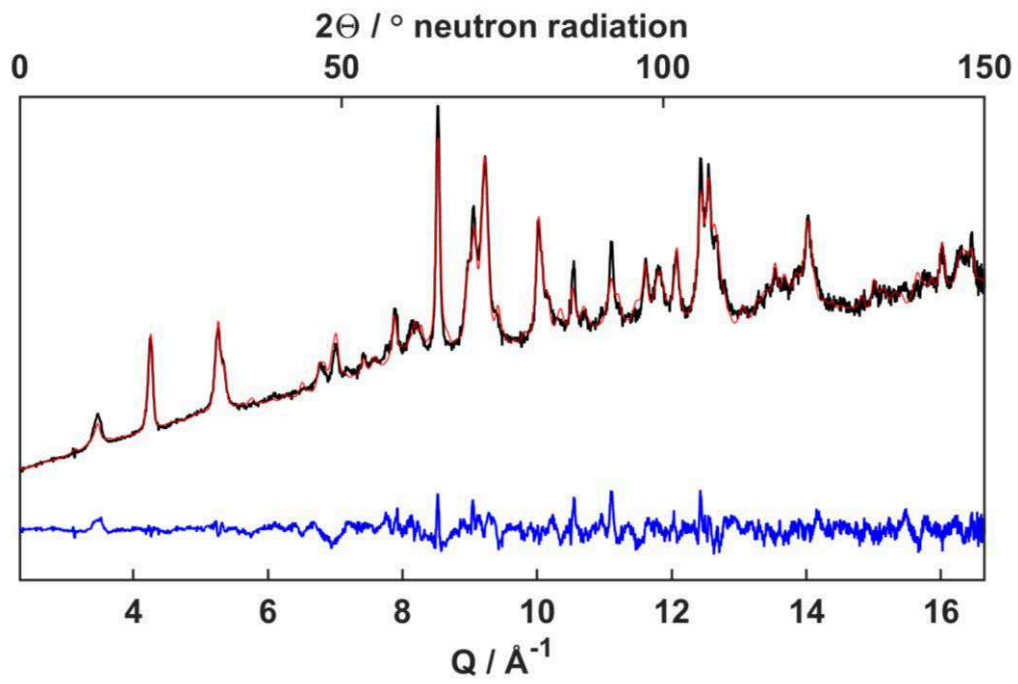


Figure 7.4.3. Rietveld refinement of $\epsilon\text{-TaO}_x\text{N}_y$ prepared by FAST synthesis at 600 °C for 5 min from neutron diffraction data.

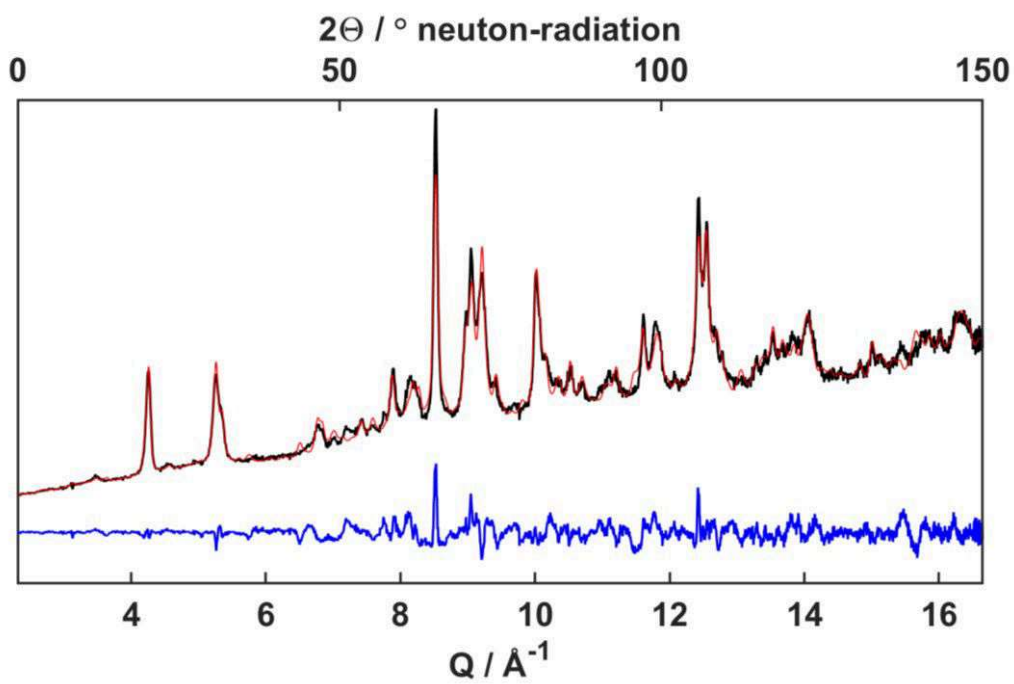


Figure 7.4.4. Rietveld refinement of ϵ -TaO_xN_y prepared by FAST synthesis at 750 °C for 5 min from neutron diffraction data

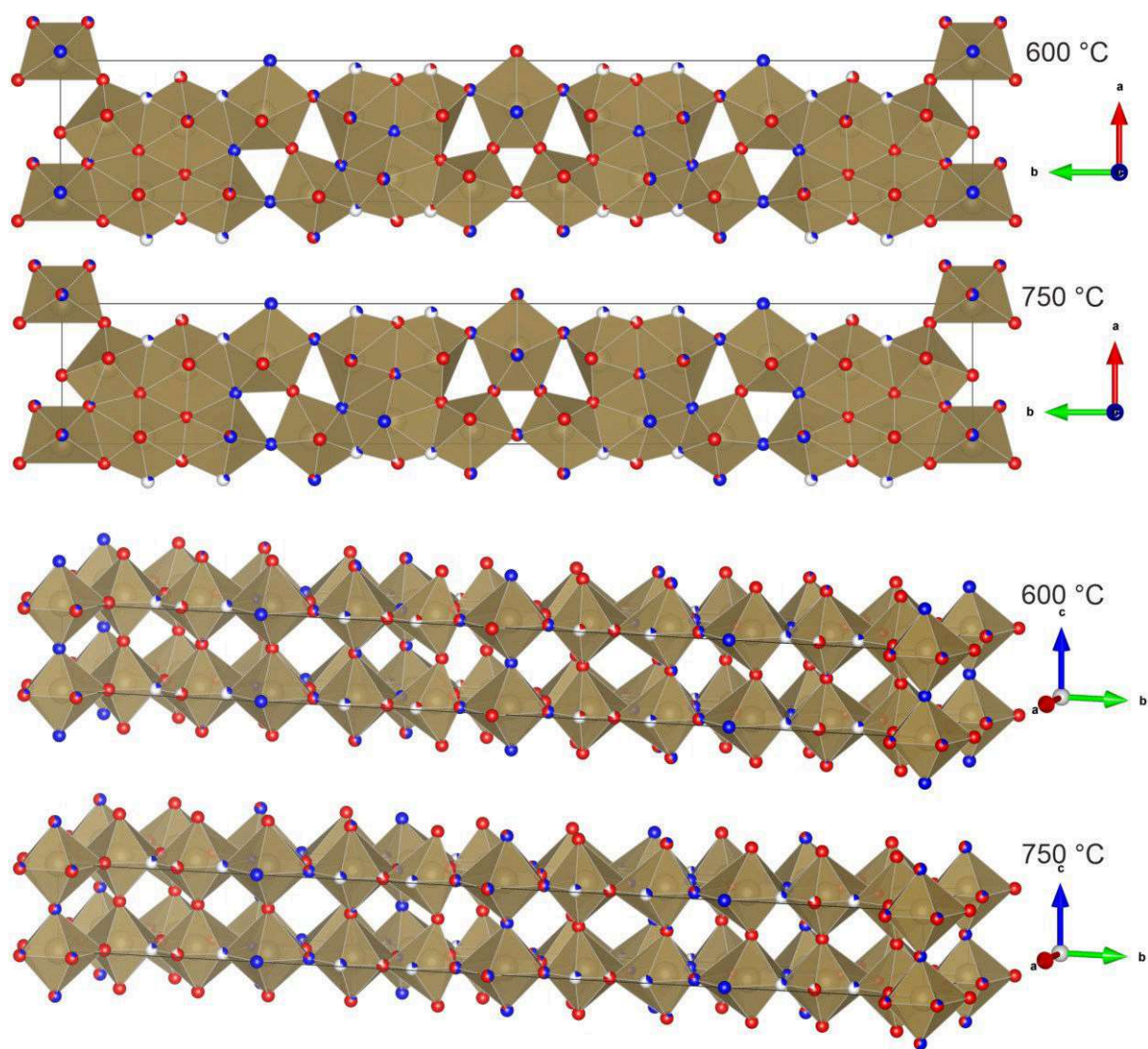


Figure 7.4.5. Structural representation of ϵ - TaO_xN_y prepared by FAST synthesis from refinement of neutron diffraction data.

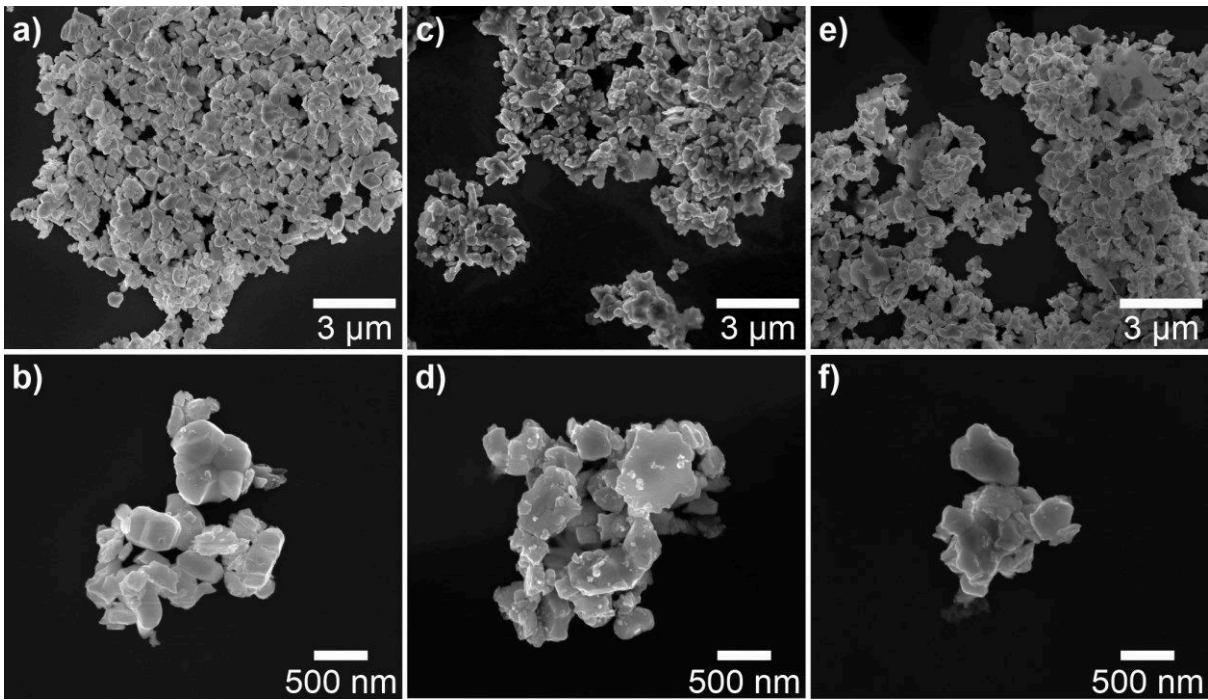


Figure 7.4.6. SEM images of samples after FAST and conventional solid-state synthesis in two magnifications. a) + b) Exemplary SEM images of a sample after FAST synthesis at 750 °C. c) + d) Exemplary SEM images of a sample after FAST synthesis at 750 °C with additional sintering at 800 °C. e) + f) Exemplary SEM images of a sample after conventional solid-state synthesis at 800 °C.

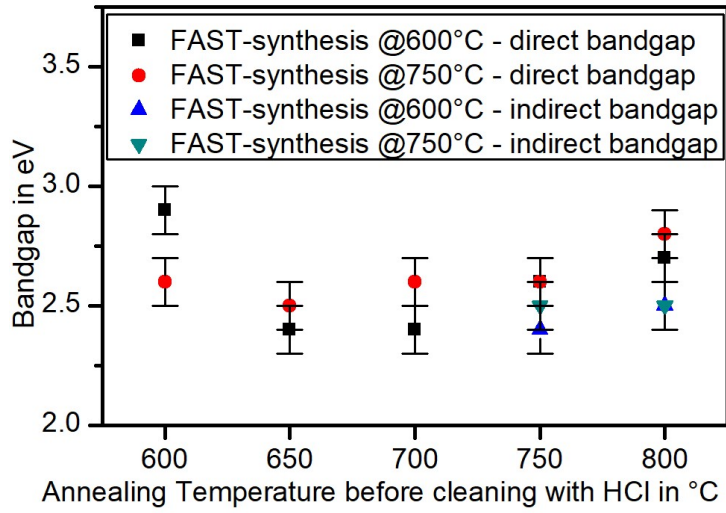


Figure 7.4.7. Direct and indirect bandgaps of different TaO_xN_y . The sample were sintered at different temperature prior cleaning with dilute HCl after by FAST synthesis at different temperatures.

“

References

- [1] Rietveld, H. M. A profile refinement method for nuclear and magnetic structures. *J. Appl. Crystallogr.* **1969**, *2*, 65–71.
- [2] Coelho, A. A. TOPAS and TOPAS-Academic: An optimization program integrating computer algebra and crystallographic objects written in C++: *An. J. Appl. Crystallogr.* **2018**, *51*, 210–218.
- [3] Stephenson, N. C.; Roth, R. S. Structural systematics in the binary system Ta₂O₅–WO₃. V. The structure of the low-temperature form of tantalum oxide L-Ta₂O₅. *Acta Crystallogr. Sect. B Struct. Crystallogr. Cryst. Chem.* **1971**, *27*, 1037–1044.
- [4] Weishaupt, M.; Strähle, J. Darstellung der Oxidnitride VON, NbON und TaON. Die Kristallstruktur von NbON und TaON. *Z. Anorg. Allg. Chem* **1977**, *429*, 261–269.

List of Figures

- Figure 1.1.** History of sintering through human history in comparison with ceramic development. Adapted from Biesuz et al.^[10] page 3
- Figure 1.2.** (A) Histogram of published papers using the term “spark-plasma sintering”, adapted from Yamanoglu and SCOPUS.^[20] (B) Scheme of a FAST process. page 4
- Figure 1.3.** Comparison of the influence of pressure assisted (squares) and pressure less (circles) sintering, shown by temperature T needed to obtain a relative density of 95% (A) of ZrO_2 and the influence on relative density in relation to observed particle grain-growth (B). Adapted from Anselmi-Tamburini et al.^[33] and Munir et al.^[35] page 6
- Figure 1.4.** Example of heat-distribution in (a) a non-conducting sample of Al_2O_3 and (b) a Cu sample, applying 100 A and 40 kN as adapted from Garay^[23] page 7
- Figure 1.5.** (A) Schematic of particle rearrangement, adapted from Garay.^[23] (B) Examples for material transport pathways between particles. page 9
- Figure 1.6.** (A) Current flow through powder sample during FAST, adapted from Wachowicz.^[58] (B+C) Current pathways along lowest resistance between powder particles, leading to neck formation.^[59] page 10
- Figure 1.7.** Schematic representation of fields of interest relevant for research of FAST synthesis and processing. Adapted from Guillon et al.^[64] page 12
- Figure 1.8.** Alternative die designs for pressureless SPS using (a) T-shaped graphite punches or (c) additional graphite pieces to avoid external pressure in comparison to (b) regular SPS pressing tools. Adapted from Yamanoglu^[20] page 16
- Figure 2.1.** (A) Illustration of the synthesis procedure. (B) Temperature profile and piston movement/densification during the SPS process. Different segments of the process are indicated by capital letters. page 31
- Figure 2.2.** (A) X-ray powder diffractograms of samples obtained by quenching the SPS reaction (B) Analysis of the phase composition of the obtained samples at several stages of the reaction showing the gradual formation of orthorhombic and cubic $WO_{3-x}F_x$. (C, D) Rietveld refinements of SPS prepared $WO_{2.90}F_{0.10}$ and $WO_{2.40}F_{0.60}$ using X-ray powder data. page 34
- Figure 2.3.** (A) View of the orthorhombic $WO_{3-x}F_x$ structure with tilted WO_6 octahedra along the b -axis. The tilt pattern corresponds to that of the tungsten oxide high-temperature ($Pbcn$) phase with the Glazer nomenclature $a^0 b^+ c^-$ (where $a < c < b$). (B) Relation of the monoclinic, orthorhombic and cubic $WO_{3-x}F_x$ lattices. (C) Reconstruction of zonal extinctions from ADT measurements. From left to right: $a - 0kl$, $b - h0l$, $c - hk0$. (D) Probability density function (in yellow) of the non-harmonic page 36
- Figure 2.4.** ^{19}F MAS-NMR spectra of orthorhombic $WO_{2.90}F_{0.10}$ (A) and cubic $WO_{2.58}F_{0.42}/WO_{2.40}F_{0.60}$ (B). page 39
- Figure 2.5.** (A) SEM-EDX image of a cross-section of a SPS-pellet of cubic $WO_{2.4}F_{0.6}$. (B) Diffuse reflectance UVVIS spectra of cubic and orthorhombic conventionally prepared $WO_{3-x}F_x$. page 41
- Figure 2.6.** Calibrated XPS sub-spectra of W 4f (A), F 1s (B), O 1s (C) and C 1s (D) of reference WO_3 (top) cubic $WO_{3-x}F_x$ prepared conventionally (middle) and by SPS (bottom). page 41
- Figure 2.7.** UV-vis spectra showing the photocatalytic degradation of RhB in aqueous solution for $WO_{2.92}F_{0.08} / WO_{2.90}F_{0.10}$ (A, C) and $WO_{2.58}F_{0.42} / WO_{2.40}F_{0.60}$ (D, B). page 43
- Figure 2.8.** (A-C) TEM (HRTEM) images acquired with underfocus (black atom contrast) of a SPS-prepared (A) and conventionally prepared (B) samples of cubic $WO_{2.40}F_{0.60}$. The ReO_3 -type structure can easily be seen. (C) HRTEM image of an SPS-prepared particle with twin boundaries. page 44
- Figure 3.1.** (A) General approach to convert Ta_2O_5 and Teflon scrap to tantalum oxyfluoride by SPS in minute intervals and enhanced photocatalytic properties. (B) Illustration of the SPS page 60

- synthesis. (C) Temperature profile (red) and piston movement/densification (blue) during the SPS process with capital letters indicating different segments of the synthesis.
- Figure 3.2.** (A) Rietveld refinement of SPS-prepared Ta₃O₇F (red line) using X-ray powder data. (B) Rietveld refinement of SPS-prepared TaO₂F (red line) using X-ray powder data. page 61
- Figure 3.3.** Microstructure of Ta₃O₇F and TaO₂F prepared by SPS and conventional solid state chemistry. (A, B) (HR)TEM images of Ta₃O₇F and TaO₂F prepared by SPS, (C, D) and conventional chemistry. Insets show a individual particles in high resolution. page 63
- Figure 3.4.** (A) Section of the reverse Monte Carlo (RMC) model of SPS prepared TaO₂F obtained from total-scattering data. (B) Reduced structure function F(Q) and the corresponding RMC fit and (C) pair distribution function (PDF) D(r) in comparison to the simulated PDF function of TaO₂F. page 64
- Figure 3.5.** (A-F) XPS spectra (with F, O, and Ta sub-spectra in (A,D), (B,E) and (C,F)) of TaO₂F, prepared by SPS (A-C) and conventional ampoule chemistry (D-F) with fitted signals for the respective environments. page 65
- Figure 3.6.** (A) Low energy region of Kubelka-Munk Plot of Ta₃O₇F (blue line) and TaO₂F (red line) prepared by SPS (solid lines) and conventional ampoule chemistry (dashed lines). (B) Mott-Schottky plot, and (C) EIS Nyquist plot spectra under illumination. page 66
- Figure 3.7.** (A, B) Linear sweep voltammograms under light and dark conditions, (C) *I*-*t* photostability curve under continuous luminescence at 1.23 V vs RHE, and (D) amperometric *I*-*t* curves at an applied potential of 1.23 V vs RHE with 20 s ON/OFF cycle. (E) Incident photon-to-current efficiencies, IPCE (%) and (F) applied bias to photo-conversion ABPE (%) for Ta₂O₅, Ta₃O₇F (SPS-prepared and conventional synthesis) and TaO₂F (SPS-prepared and conventional synthesis). page 68
- Figure 4.1.** General approach to convert Nb₂O₅ and Teflon scrap to niobium oxyfluoride photocatalysts by SPS (top) and conventional synthesis (bottom) and effect of the synthesis on photocatalytic properties. Results for SPS processing are shown in green, for conventional ampoule chemistry in red. A temperature profile of the SPS program is shown on the top right (red) including the absolute piston movement/densification (blue) during the SPS process of NbO₂F. Capital letters indicate different segments of the process. page 85
- Figure 4.2.** (A) Rietveld refinement of SPS- (red line) and conventionally prepared NbO₂F (blue line) using X-ray powder data. (B) Rietveld refinement of SPS- (red line) and conventionally prepared Nb₃O₇F (blue line) using X-ray powder data. The insets show polyhedral representations of the structures. page 86
- Figure 4.3.** (A-C) (HR)TEM images of NbO₂F prepared by SPS, (D-F) and conventional chemistry. (A, D) show representative particles. (B, E) show a zoom on the edges of the layered-like built particles. (C, F) show magnified crystalline area.. page 87
- Figure 4.4.** (A-F) XPS spectra (with F, O, and Ta sub-spectra in (A,D), (B,E) and (C,F)) of NbO₂F, prepared by SPS (A-C) and conventional ampoule chemistry (D-F) with fitted signals for the respective environments. page 88
- Figure 4.5.** (A) UV-Vis diffuse reflectance spectra of Nb₃O₇F (blue line) and NbO₂F (red line) prepared by SPS (solid lines) and conventional ampoule chemistry (dashed lines). (B) Mott-Schottky plot, and (C) EIS Nyquist plot spectra under illumination. page 90
- Figure 4.6.** (A, B) Linear sweep voltammograms under light and dark conditions, (C) *I*-*t* photostability curve under continuous luminescence at 1.23 V vs RHE, and (D) amperometric *I*-*t* curves at an applied potential of 1.23 V vs RHE with 20 s ON/OFF cycle. (E) Incident photon-to-current efficiencies, IPCE (%) and (F) applied bias to photo-conversion ABPE (%) for Nb₂O₅, Nb₃O₇F (SPS-prepared and conventional synthesis) and NbO₂F (SPS-prepared and conventional synthesis). page 93
- Figure 5.1.** a) Scheme of the FAST synthesis procedure. b) Temperature profile (blue) and piston movement/densification (red) during the FAST process. Capital letters indicate different segments of the process. c) Digital images of the products after the FAST synthesis. d) page 107

- Optical bandgaps of the products after different FAST treatments. The dashed line marks the stability border of the L11-Ta₂O₅ phase. Optical bandgaps
- Figure 5.2.** a) Rietveld refinement of product after FAST treatment at 600 °C for 5 min. b) Product after FAST treatment at 750 °C for 5 min. c) Product after conventional synthesis at 800 °C for 48 h. page 109
- Figure 5.3.** Graphical representation of the neutron diffraction results for the sample FAST treated at 750 °C for 5 min. page 111
- Figure 5.4.** Representative TEM images of a)-c) FAST-prepared ε-TaO_xN_y (T = 750 °C) and d), e) β-TaO_xN_y prepared via conventional high temperature reaction of Ta₂O₅ and Mg₃N₂ at 800°C for 48 h at different magnifications. f) Representative SEM images of FAST-prepared ε-TaO_xN_y (T = 750 °C). page 112
- Figure 5.5.** a)-c) XPS analysis of ε-TaO_xN_y prepared by FAST at 600 and 750°C, FAST at 750°C with subsequent annealing and β-TaON prepared by conventional synthesis. Reference: Ta₂O₅ (ball-milled + FAST). page 114
- Figure 7.1.1.** Observeable flakes after ball-milling of powder mixtures with high PTFE/WO₃ ratios (A+C+D) and pellet cross-section of not ball-milled precursor mixture (B). The black particles in the SEM picture consists of PTFE-remains which form when the precursors are insufficiently mixed (eg no ball-milling), likely due to incomplete decomposition/reaction with WO₃. These particle create/make up the present “pores” in reacted product-pellets. page 133
- Figure 7.1.2.** Evolution of WO_{3-x}F_x monoclinic, orthorhombic and cubic phases during the SPS reaction for two different starting compositions x = 0.15 (A + C) and x = 1.0 (B + D). page 134
- Figure 7.1.3.** Rietveld Refinements of phase pure conventional sample WO_{2.92}F_{0.08} (A) and WO_{2.60}F_{0.40} (B). Intensities are weighted with q-values. page 135
- Figure 7.1.4.** (A) ¹⁹F EXSY solid state spectrum of cubic WO_{2.6}F_{0.4} at t_{mix} = 50 ms. (B) ¹⁹F EXSY solid state spectrum of cubic WO_{2.6}F_{0.4} at t_{mix} = 250 ms. page 136
- Figure 7.1.5.** Overview TEM pictures for conventional synthesized WO_{2.58}F_{0.42} (A + B) and WO_{2.40}F_{0.60} (C + D) synthesized by SPS using the same preparation procedure by ball-milling. page 137
- Figure 7.1.6.** XPS overview spectra of conventional (C,D) and SPS (A,B) synthesized orthorhombic WO_{2.90}O_{0.10} (A,C) and cubic WO_{2.60}O_{0.40} (B,C). page 138
- Figure 7.1.7.** Fitted XPS spectra of conventionally (A-C) and SPS (D-F) prepared orthorhombic WO_{2.90}O_{0.10}. The F, O, and W sub-spectra are shown in (A,D), (B,E) and (C,F). page 139
- Figure 7.1.8.** Fitted XPS spectra of conventionally (A-C) and SPS (D-F) prepared cubic WO_{2.60}O_{0.40}. The F, O, and W sub-spectra are shown in (A,D), (B,E) and (C,F). page 140
- Figure 7.1.9.** UV–vis spectra showing the photocatalytic degradation of RhB in aqueous solution for cubic (A + B) and orthorhombic (C + D) WO_{3-x}F_x prepared by conventional solid state chemistry (A - WO_{2.60}F_{0.40}, C - WO_{2.92}F_{0.82}) and by SPS (B - WO_{2.40}F_{0.60}, D- WO_{2.90}F_{0.10}). page 141
- Figure 7.1.10.** Plots showing the concentration development of RhB during photocatalytic degradation in aqueous solution for WO_{2.55}O_{0.45} (B + D) and WO_{2.9}F_{0.1} (A + C) prepared by conventional solid state chemistry (C, D) and by SPS (A, B). page 142
- Figure 7.1.11.** UV–vis spectra showing the photocatalytic degradation of RhB in aqueous solution under dark conditions for SPS prepared orthorhombic WO_{2.90}F_{0.10} (A) and cubic WO_{2.40}F_{0.60} (B). page 143
- Figure 7.2.1.** (A) Rietveld refinement of conventional prepared Ta₃O₇F (red line) using X-ray powder data. (B) Rietveld refinement of conventional-prepared Ta₃O₇F (red line) using X-ray powder data. page 155
- Figure 7.2.2.** Diffraction image of Ta₃O₇F prepared by SPS (A). HR-TEM images of Ta₃O₇F and TaO₂F prepared by SPS (B-C) and conventional ampoule chemistry (D-F) showing presence of line defects. page 156
- Figure 7.2.3.** SEM images of Ta₃O₇F prepared by conventional synthesis (A+B) and SPS synthesis (C+D) showing the much rougher surface and less uniform areas in the material synthesized by field assistance. page 157

Figure 7.2.4.	(A) Section of the reverse Monte Carlo (RMC) model of SPS prepared Ta ₃ O ₇ F obtained from total-scattering data. (B) Reduced structure function F(Q) and the corresponding RMC fit and (C) pair distribution function (PDF) D(r) in comparison to the simulated PDF function of TaO ₂ F.	page 158
Figure 7.2.5.	Kubelka-Munk plots (black line) of Ta ₃ O ₇ F, TaO ₂ F and reference Ta ₂ O ₅ (E) prepared by SPS (A-B) and conventional ampoule chemistry (C-D) from UV-Vis diffuse reflectance spectra (Figure 3.5). (F) shows the obtained spectra from diffuse reflectance UV-Vis measurements.	page 159
Figure 7.2.6.	XPS survey of Ta ₃ O ₇ F and TaO ₂ F, prepared by SPS (A-B) and conventional ampoule chemistry (C-D) with fitted peaks for the respective environments. (E) shows the survey spectrum of ball-milled Ta ₂ O ₅ /PTFE reference mixture (unreacted).	page 160
Figure 7.2.7.	(A-F) XPS spectra (with F, O, and Ta sub-spectra in (A,D,G), (B,E,H) and (C,F,I)) of Ta ₃ O ₇ F, prepared by SPS (A-C) and conventional ampoule chemistry (D-F), together with a ball-milled Ta ₂ O ₅ -reference mixture (unreacted) with fitted peaks for the respective environments.	page 161
Figure 7.2.8.	¹⁹ F MAS-NMR spectra of Ta ₃ O ₇ F (A, C, D) and TaO ₂ F (B, D, F). In each figure the top spectrum is derived from a SPS-prepared sample, while the spectrum at the bottom was obtained from a conventionally prepared sample of comparable composition.	page 162
Figure 7.2.9.	Graphical representation of the theoretical and calculated band edge positions (as listed in Table 7.2.4).	page 163
Figure 7.2.10.	Comparative dark and light current plots (A) and magnified dark current plots (B). (A) shows the plot of the dark current from SPS prepared TaO ₂ F as comparison while (B) shows the photocurrent under light irradiation for reference Ta ₂ O ₅ for a better comparison.	page 164
Figure 7.3.1.	(A) Rietveld refinement of conventionally prepared Nb ₃ O ₇ F (red line) using X-ray powder data (83 % Nb ₃ O ₇ F, 17 % NbO ₂ F). (B) Rietveld refinement of conventionally prepared Nb ₃ O ₇ F (red line) using X-ray powder data.	page 174
Figure 7.3.2.	(A-C) (HR)TEM images of Nb ₃ O ₇ F prepared by SPS, (D-F) and conventional chemistry. (A, D) show representative particles, which consist in both cases of smaller crystallites. (B, E) show a zoomed view on the edges of the layer-like particles. (C, F) Magnified crystalline areas.	page 175
Figure 7.3.3.	TEM images of NbO ₂ F and Nb ₃ O ₇ F prepared by SPS (A-B) and conventional ampoule chemistry (C-D).	page 176
Figure 7.3.4.	XPS survey spectra of NbO ₂ F and Nb ₃ O ₇ F, prepared by SPS (A-B) and conventional ampoule chemistry (C-D) with fitted peaks for the respective environments. (E) Survey spectrum of a ball-milled (unreacted) Nb ₂ O ₅ /PTFE reference mixture.	page 177
Figure 7.3.5.	XPS fine spectra of F, O, and Nb regimes for Nb ₃ O ₇ F prepared by SPS (A-C), conventional ampoule chemistry (D-F) and from reference Nb ₂ O ₅ (G-I, ball milled powder treated with the same SPS program as NbO ₂ F) with fitted peaks for the respective environments.	page 178
Figure 7.3.6.	Kubelka-Munk plots (black line) of NbO ₂ F and Nb ₃ O ₇ F prepared by SPS (A-B) and conventional ampoule chemistry (C-D) from UV-Vis diffuse reflectance spectra (Figure 4.5).	page 179
Figure 7.3.7.	¹⁹ F MAS-NMR spectra of Nb ₃ O ₇ F (A) and NbO ₂ F (B) with indicated potential spinning side bands. In each figure the top spectrum is obtained from a SPS-prepared sample. The bottom spectrum was obtained from a conventionally prepared sample of comparable composition.	page 180
Figure 7.3.8.	Graphical representation of the theoretical and calculated band edge positions as listed in Table 7.3.5.	page 181
Figure 7.4.1.	Rietveld refinement of the reference L11-Ta ₂ O ₅ from XRPD data.	page 191
Figure 7.4.2.	Rietveld refinement of β-TaON prepared by FAST synthesis plus additional sintering from XRPD data.	page 192
Figure 7.4.3.	Rietveld refinement of ε-TaO _x N _y prepared by FAST synthesis at 600 °C for 5 min from neutron diffraction data.	page 193

- Figure 7.4.4.** Rietveld refinement of ϵ -TaO_xN_y prepared by FAST synthesis at 750 °C for 5 min from neutron diffraction data page 194
- Figure 7.4.5.** Structural representation of ϵ -TaO_xN_y prepared by FAST synthesis from refinement of neutron diffraction data. page 195
- Figure 7.4.6.** SEM images of samples after FAST and conventional solid-state synthesis in two magnifications. a) + b) Exemplary SEM images of a sample after FAST synthesis at 750 °C. c) + d) Exemplary SEM images of a sample after FAST synthesis at 750 °C with additional sintering at 800 °C. e) + f) Exemplary SEM images of a sample after conventional solid-state synthesis at 800 °C. page 196
- Figure 7.4.7.** Direct and indirect bandgaps of different TaO_xN_y. The sample were sintered at different temperature prior cleaning with dilute HCl after by FAST synthesis at different temperatures. page 197

List of Tables

Table 2.1.	Calculated F/W ratios of orthorhombic and cubic $\text{WO}_{3-x}\text{F}_x$, determined potentiometrically with a F^- sensitive electrode.	page 31
Table 2.2.	Dynamical refinement of $\text{WO}_{2.58}\text{F}_{0.42}$ and $\text{WO}_{2.90}\text{F}_{0.10}$ against ADT data.	page 33
Table 2.3.	Atomic positions (fractional units) of the $\text{WO}_{2.90}\text{F}_{0.10}$ structure refined against XRPD and ADT data.	page 33
Table 2.4.	Assignment of the ^{19}F MAS-NMR signals for orthorhombic and cubic $\text{WO}_{3-x}\text{F}_x$.	page 39
Table 3.1.	Experimental and theoretical fluorine concentration and degree of fluorination determined by HR-CS-GFMAS.	page 61
Table 3.2.	Comparison of photochemical parameters and their effect on PEC performance of $\text{Ta}_3\text{O}_7\text{F}$ and TaO_2F photoanodes	page 70
Table 4.1.	Experimental and theoretical fluorine concentration (pure phases) and degree of fluorination for niobium oxyfluoride samples from SPS and conventional synthesis as determined by HR-CS-GFMAS.	page 87
Table 4.2.	Results from water oxidation measurements	page 94
Table 7.1.1.	Unit cell parameter values obtained by averaging the lattice parameters of 12 EDT data sets from different crystals of the same sample (SPS prepared $\text{WO}_{2.90}\text{F}_{0.10}$).	page 131
Table 7.1.2.	Fit parameter of the three orthorhombic (Figure 2.4A) and four cubic (Figure 2.4B) deconvoluted peaks from the F^- solid state MAS NMR of $\text{WO}_{2.90}\text{F}_{0.08}$ (conventional synthesis)/ $\text{WO}_{2.90}\text{F}_{0.10}$ (SPS-prepared) and $\text{WO}_{2.60}\text{F}_{0.40}$ (conventional synthesis)/ $\text{WO}_{2.40}\text{F}_{0.60}$ (SPS-prepared).	page 132
Table 7.2.1.	Effect of reaction parameters during SPS preparation on the phase distribution ($50^\circ\text{C}/\text{min}$ heating and dwelling at $T = 600^\circ\text{C}$ for $t = 9$ min and under a pressure of $p = 19$ MPa) with losted side phases.	page 147
Table 7.2.2.	Results of Rietveld-Refinement of $\text{Ta}_3\text{O}_7\text{F}$ and TaO_2F synthesized by SPS (Figure 3.2A and 2B) and by conventional chemistry (Figure 7.2.1).	page 148
Table 7.2.3.	pH-dependence of the ζ potentials of $\text{Ta}_3\text{O}_7\text{F}$ and TaO_2F . All values are the average of three individual determinations at identical pH under identical conditions.	page 149
Table 7.2.4.	Summary of XPS determined elemental compositions and calculated F/O ratio on surface.	page 150
Table 7.2.5.	Fit parameter of the four to five deconvoluted peaks from the F^- solid state MAS NMR of $\text{Ta}_3\text{O}_7\text{F}$ (conventionally (bottom) and SPS-prepared (top), Figure 7.2.8E) and TaO_2F (conventionally (bottom) and SPS-prepared (top), Figure 7.2.8F), exemplary for the 28 and 29 kHz measurements.	page 151
Table 7.2.6.	Calculated Band edge position values	page 154
Table 7.3.1.	Results of Rietveld refinements of $\text{Nb}_3\text{O}_7\text{F}$ (<i>Cmmm</i>) and NbO_2F (<i>Pm-3m</i>) synthesized by SPS (Figure 4.2A and 2B) and by conventional high temperature chemistry (Figure 7.3.1).	page 169
Table 7.3.2.	Experimental and theoretical fluorine concentration (pure phases) and degree of fluorination for niobium oxyfluorides prepared by SPS and conventional high temperature chemistry as determined by HR-CS-GFMAS.	page 170
Table 7.3.3.	Summary of elemental compositions and calculated F/O surface ratios determined by XPS spectroscopy.	page 171
Table 7.3.4.	Fit parameters of the five deconvoluted peaks from the F^- solid state MAS NMR of $\text{Nb}_3\text{O}_7\text{F}$ (conventionally (bottom) and SPS-prepared (top), Figure 7.3.2A) and NbO_2F (conventionally (bottom) and SPS-prepared (top), Figure 7.3.2B).	page 172
Table 7.3.5.	Calculated Band edge position values.	page 173

Table 7.4.1.	Crystallographic data of relevant tantalum oxide and oxynitride.	page 185
Table 7.4.2.	Influence of different reaction parameters during FAST synthesis on the obtained phases.	page 186
Table 7.4.3.	Influence of different reaction parameters on the obtained phases during conventional solid-state synthesis for 48 hours in quartz glass ampoules.	page 187
Table 7.4.4.	Results of Rietveld-refinement from XRPD data and neutron diffraction data of L11-Ta ₂ O ₅ (Figure 7.4.1) and ε-TaON synthesized by FAST (Figure 5.2 a)+b), Figure 7.4.3, Figure 7.4.4) and β-TaON synthesized by conventional high temperature chemistry (Figure 5.2 c)) or FAST plus additional sintering (Figure 7.4.2).	page 188
Table 7.4.5.	Refined O/N positions and occupancies from neutron diffraction data of L11-Ta ₂ O ₅ synthesized by FAST at 600°C (Figure 7.4.3) and 750°C (Figure 7.4.4).	page 189
Table 7.4.6.	Optical bandgaps of different samples. More are shown in Figure 7.4.7.	page 190

List of Symbols and Notations

a, b, c	Lattice parameters
ABPE	Applied Bias to Photo-Conversion
AC	Alternating Current
ADP	Anisotropic Displacement Parameters
ADT	Automated Diffusion Tomography
BET	Brunauer–Emmett–Teller
C	Capacitance
c	Concentration
CCD	Charge-Coupled Device
CIF	Crystallographic Information File
δ	Chemical Shift
DC	Direct Current
DI	Deionized
$D(r)$	Pair Distribution Function
e^-	Electron
E	Energy
E_{CB}	Conduction Band Potential
EDT	Electron Diffraction Tomography
EDX	Energy-Dispersive X-ray Spectroscopy
E_{gap}	Band-Gap Energy
EIS	Electronic Impedance Spectroscopy
E_{VB}	Valence Band Potential
EXSY	Exchange Spectroscopy
FAST	Field-Activated Sintering Technique
$F(Q)$	Reduced Structure Function
$F(R)$	Kubelka–Munk Function
FTO	Fluorinated Tin Oxide
FWHM	Full-Width at Half-Maximum
gof	Goodness of Fit
HAADF	High Angular Annular Dark Field
h, k, l	Miller Indices
$h\nu$	Photon Energy
HR	high resolution
HR-CS-GFMS	high resolution-continuum source-graphite furnace molecular absorption spectrometer
I	Current

IPCE	Incident Photon-to-Current Efficiency
J_{ph}	Photocurrent Density
λ	Wavelength
LED	Light-Emitting Diode
MAS	Magic-Angle Spinning
MoK α	Molybdenum K α Radiation
NED	Non-Precession Electron Diffraction
NIR	Near-Infrared
NMR	Nuclear Magnetic Resonance
NP	Nanoparticle
<i>Occ</i>	Elemental Occupancy
<i>p</i>	Pressure
P	Power
PDF	Pair Distribution Function
PEC	Photoelectric Current
PED	Precession Electron Diffraction
PTFE	Polytetrafluorethylene
PXRD	Powder X-Ray Diffraction
Q/q	Scattering Vektor Length
<i>R</i>	Reflecance
RhB	Rhodamine-B
RHE	Reversible Hydrogen Electrode
RMC	Reverse Monte Carlo
R_{wp}	Weighted Profile R-Value
SCE	Saturated Calomel Electrode
SEM	Scanning Electron Microscopy
SPS	Spark Plasma Sintering
<i>t</i>	Time
<i>T</i>	Temperature
TEM	Transmission Electron Microscopy
<i>U</i>	Voltage
UV/Vis	Ultraviolet/Visible light
<i>V</i>	Volume
wt%	weight-percent
χ	Absolute Electronegativity
XPS	X-ray photoelectron spectroscopy
<i>Z</i>	Number of Atoms per Unit Cell

Z_{Im} Imaginary Part of Impedance
 Z_{re} Real Part of Impedance
□ Vacancy